

ATOMINRED: ATmospheric Oxidation of MIXed organic films on aqueous droplets studied by Neutron reflectometry and infra-RED reflection- absorption spectroscopy

PhD

Department of Chemistry
School of Chemistry, Food & Pharmacy

Ben Wōden

August 2019

Declaration

The following thesis represents entirely my own work, with the following specific exceptions.

RSC Advances paper: This paper forms part of the method development chapter (Chapter 3). The text of the paper was written by Dr Maximilian WA Skoda (my secondary supervisor) in consultation with Dr Christian Pfrang (my primary supervisor) and me, who are co-authors of the paper. The work underlying that paper was carried out by Dr Skoda, Dr Pfrang, and me. More details are given in the declaration that introduces that paper.

Atmosphere paper: This paper forms most of one of the results chapters (Chapter 4). The main text of the paper was written by me, in consultation with Drs Pfrang and Skoda, who are co-authors of the paper. Several small revisions to the text were requested by reviewers, and these were carried out by Drs Pfrang and Skoda, in consultation with me, as I was away on a placement at the time. More details are given in the declaration that introduces that paper.

Atmospheric Chemistry and Physics (ACP) paper: This paper forms one of the results chapters (Chapter 5). The main text of the paper was written by me, in consultation with Drs Pfrang and Skoda, who are co-authors of the paper.

Proofreading: The main thesis text outside the three included papers was read by Drs Pfrang and Skoda, who suggested a number of minor edits. Following the oral defence, some changes were suggested by Profs Ann Chippindale and Martin King. No suggested edits were included in the text without being explicitly reviewed and accepted or rejected by me. Rebecca Wöden also read over the main thesis text and checked for grammatical and typographical errors. No changes were made to the text without being explicitly reviewed and accepted or rejected by me. The final composition of the thesis text was entirely in my control.

Abstract

The following thesis describes the design and development of a pioneering reaction and analysis chamber for combining neutron reflectometry with simultaneous *in situ* Fourier transform infra-red reflection-absorption spectroscopy for studying the oxidation of mixed lipid monolayers at the air/water interface by gas-phase oxidants. The thesis then describes several bodies of work performed using the apparatus, each of which advances the field in a specific manner.

The first body of work describes the oxidation of galactocerebroside (GCB) monolayers by NO_3^\bullet radicals (the key night-time atmospheric oxidant species), both as a pure monolayer and as part of a mixed monolayer with palmitic acid and palmitoleic acid. Galactocerebroside was chosen as a model system for glycolipids, which have been found to be a key component in sea-spray aerosol. NO_3^\bullet radical oxidation did not fully remove the GCB monolayer from the surface under any conditions, suggesting that such monolayers are likely to persist under night-time atmospheric conditions.

The second body of work describes the ozonolysis of oleic acid monolayers at low temperatures. Oleic acid (OA) is a key component of anthropogenic aerosol and has been established as a reference system in this domain. The effect of cooling the system to near-freezing temperatures was selected for study as the real-life conditions in which these reactions take place are likely to be better modelled at such a temperature condition than at the room temperature conditions usually employed for such studies. A residual monolayer resistant to further oxidation persisted after OA ozonolysis at low temperatures, which could be built up by repeated deposition and ozonolysis, suggesting that the effects of an organic film, such as surface tension depression, can persist beyond the expected lifetime of the deposited film species itself.

The third body of work describes the ozonolysis of OA as part of a mixed monolayer with stearic acid (SA). Real-life aerosol will be highly heterogeneous, and so the effect of co-deposited species on the reactivity and lifetime of reactive components such as OA is important to determine. The presence of SA in the system allowed the formation of a stable residual product monolayer from OA ozonolysis even at room temperature.

Finally, possible future applications of the combined reaction and analysis chamber are developed by presenting preliminary data from a study of the oxidation of linoleic acid in a variety of mixtures and temperature conditions.

The primary implication of this work is that unsaturated fatty acid emissions could affect the physical properties of water droplets in the atmosphere longer than implied by their atmospheric lifetimes.

Table of Contents

Declaration	2
Abstract	3
Table of Contents	4
Chapter 1 – Introduction	6
1.1 – Water and the Greenhouse Effect	6
1.2 – Water and Convection	8
1.3 – Water and Aerosol: Cloud Lifetime Effects	9
1.4 – Organic Films at the Air/Water Interface	12
1.5 – Organic Films and Clouds	14
1.6 – Structure of the Thesis	16
1.7 – Bibliography (Introduction)	17
Chapter 2 – Methods	21
2.1 – Specular Neutron Reflectometry	21
2.1.1 – Reflectivity Basics	21
2.1.2 – Reflectivity from Monolayers	23
2.1.3 – Calculation of Reflectivity	25
2.1.4 – Deuteration of Monolayer Material	26
2.1.5 – Selection of Q Range	28
2.1.6 – Data Processing	29
2.2 – Fourier Transform Infra-Red Reflection-Absorption Spectroscopy	32
2.2.1 – Vibrational Spectroscopy Basics	32
2.2.2 – Absorbance of Hydrocarbon Tails	33
2.2.3 – Reflection-Absorption Geometry	34
2.2.4 – Practical Considerations	35
2.3 – Wilhelmy Plate Tensiometry	36
2.4 – Brewster Angle Microscopy	37
2.5 – Ultraviolet-Visible Spectroscopy	38
2.6 – Bibliography (Methods)	39
Chapter 3 – Method Development	41
3.1 – Introduction and <i>RSC Advances</i> Paper	41
3.2 – Improvements to Height Adjustment	49
3.3 – Atmospheric Interference Suppression	50
3.4 – Addition of Temperature Control	51
3.5 – Improvement of Temperature Control	53
3.6 – Future Improvements	58
3.7 – Acknowledgements (Method Development)	60

Chapter 4 – Oxidation of Galactocerebroside Monolayers including Fatty Acid Mixtures.....	61
4.1 – Introduction and <i>Atmosphere</i> Paper	61
4.2 – Supplementary Information	81
Chapter 5 – Low Temperature Oleic Acid Ozonolysis; <i>Atmospheric Chemistry and Physics</i> Paper	83
Chapter 6 – Ozonolysis of Mixed Monolayers of Oleic and Stearic Acids.....	124
6.1 – Introduction.....	124
6.2 – Initial Results	125
6.3 – Explaining the Anomaly.....	129
6.4 – Compression/Annealing Experiments	133
6.5 – Implications	134
6.6 – Kinetics	135
6.7 – Residual Product Monolayers	137
6.8 – Preliminary Low Temperature Experiments	138
6.9 – Conclusions and Future Work	139
6.10 – Bibliography (Mixtures).....	141
Chapter 7 – Oxidation of Linoleic Acid Monolayers including Fatty Acid and Methyl Ester Mixtures	142
7.1 – Introduction.....	142
7.2 – Oleic Acid Ozonolysis with Linoleic Acid	142
7.3 – Oxidation of Linoleic Acid.....	145
7.4 – Future Work	156
7.5 – Bibliography (Linoleic).....	158
Chapter 8 – Summary.....	159
8.1 – Introduction.....	159
8.2 – Early Exploratory Phase: INTER RB 1510605 and RB 1520459.....	159
8.3 – Focus on GCB: INTER RB 1610500	159
8.4 – Focus on Mixtures: INTER RB 1620451 and RB 1710483	160
8.5 – Focus on Temperature: INTER RB 1710483 and RB 1810793; FIGARO 9-10-1518	160
8.6 – The Final Piece of the Puzzle: SURF RB 1540015 and INTER RB 1910615.....	162
8.7 – New Frontiers: INTER RB 1910615	162
8.8 – Key Findings.....	163
Appendices.....	164
Appendix 1 – Process Code	164
A.1.1 – Introduction	164
A.1.2 – MantidPlot	164
A.1.3 – Igor	170
Appendix 2 – Oleic Acid Brewster Angle Microscopy	174
Bibliography (Appendices)	Error! Bookmark not defined.
Acknowledgements.....	175

Chapter 1 – Introduction

1.1 – Water and the Greenhouse Effect

The earth's atmosphere contains approximately $1.29 \times 10^{13} \text{ m}^3$ water¹. This is only approximately 0.001% of the water present in the entire earth's water system¹, and yet it still carries enormous climatic and meteorological significance. Water plays a role in the earth's climate via its activity as a condensable greenhouse gas, via complicating the process of convection, and via the formation of clouds and their interaction with aerosol particles.

The earth system's incoming and outgoing radiation must balance in order for the system to be in equilibrium. If incoming radiation increases relative to outgoing radiation, then the temperature of the earth's surface (T) will rise until equilibrium is restored at a higher temperature. This re-establishment of equilibrium occurs because hotter bodies emit more radiation (or have a higher luminosity (L)) in a manner that is quartically dependent on temperature thus:

$$L = 4\pi R_{\oplus}^2 \sigma T^4$$

Equation 1.1

The radius of the earth (R_{\oplus}) is a constant for our purposes at $6.38 \times 10^6 \text{ m}$ and the Stefan-Boltzmann constant (σ) is a fundamental constant at $5.67 \times 10^{-8} \text{ kg s}^{-3} \text{ K}^{-4}$. As the temperature will vary until equilibrium is established, the temperature of the earth's surface can be predicted by setting luminosity equal to incoming radiation and solving Equation 1.1 for temperature.

The earth does not absorb incoming radiation with total efficiency as it is partially reflective, so the absorbed radiation (A_r) depends on the strength of the solar radiation (S_0) and the earth's albedo (α), which is the fraction of incoming radiation that is reflected back to space, as follows:

$$A_r = \pi R_{\oplus}^2 S_0 (1 - \alpha)$$

Equation 1.2

The solar constant (S_0) is not quite constant, but varies by $\sim 0.1\%$ between solar minima and maxima. This variation, however, is smaller than the instrumental error in the best available measurements of the phenomenon, so S_0 can safely be treated as constant with a value of $1.36 \times 10^3 \text{ kg s}^{-3}$ that is stable across the timeframes necessary to achieve a steady state². The albedo of the earth can be measured by taking advantage of the great difference in temperature between the earth and the sun, and therefore the vastly different wavelength distribution of solar radiation reflected from the earth and radiation emitted directly from the earth in accordance with Equation 1.1 (hotter bodies emit at a higher frequency range). This difference allows the reflected radiation (related to albedo) to be measured independently of emitted radiation (related to surface temperature). Albedo is also not completely fixed, as changing ice cover, cloudiness, forest cover, and many other factors affect it, but it is stable at its current value of 0.29 across the kind of timescales in which the earth system can come to equilibrium through changing surface temperature³, and so can be treated as a constant in this steady state calculation.

Using these values, setting luminosity equal to absorbance (the definition of the steady state), and solving Equations 1.1 and 1.2 gives a value for the equilibrium temperature of 279 K. The actual mean surface temperature of the earth⁴ is around 278 to 288 K. This difference is due to modulation of outgoing radiation via the greenhouse effect.

Increases in the concentration of non-condensable greenhouse gases such as carbon dioxide (CO_2), methane (CH_4), sulfur hexafluoride (SF_6), and many others reduce the ability of the earth system to emit

energy in the longwave infra-red (IR) region of the electromagnetic spectrum. This decrease in the efficiency of energy loss via outgoing radiation results in an increase in surface temperature, and thus in outgoing radiation, until energy balance is restored. Disturbances to the balance between outgoing and incoming radiation such as this are known as direct forcings. Other direct forcing effects include changes to the albedo of the planet or variations in incoming solar radiation.

The warmer surface caused by these direct forcings leads to a warmer atmosphere, which in turn leads to enhanced evaporation from the surface. Enhanced evaporation then leads to a higher concentration of water vapour in the atmosphere. This water vapour further blocks outgoing longwave IR radiation, further increasing the temperature. The result of this is that water vapour acts as a positive feedback mechanism in the climate system, amplifying the extent of warming due to direct forcings.

Directly adding water vapour to the troposphere is not a forcing effect, as the excess will condense out and the system will return to equilibrium at the same temperature as before the injection. The equilibrium of the water cycle establishes itself quickly in response to perturbations when compared with the equilibrium of the earth's radiative balance, so changes in directly emitted water vapour in the troposphere are not of direct climatic significance via the greenhouse effect. However, injection of water vapour into the stratosphere, which is not in dynamic equilibrium with the troposphere and surface, will cause a direct radiative forcing effect. This is particularly notable for the case of water vapour produced by the oxidation of CH_4 in the stratosphere and for the case of contrails, which contribute radiative forcing effects of 0.07 and 0.01 kg s^{-3} respectively⁴, with an extra 0.05 kg s^{-3} from cirrus clouds formed as a result of the contrails⁵. These are still small contributions when compared with the radiative forcing attributed to anthropogenic emissions of CO_2 and other non-condensable greenhouse gases (2.83 kg s^{-3})^{4,5}.

Figure 1.1 summarises these forcings; note the large error bars on the forcing effects attributable to aerosol, particularly via the aerosol/cloud interaction. The effects of feedback via the direct greenhouse effect of water vapour (water dissolved in the atmosphere) are relatively easily factored into forcing calculations and taken account of in climate modelling, whereas the behaviour of water in its condensed form, as suspended liquid or ice particles that make up clouds, is much more complex and has proven tricky to incorporate into climate models from the very beginning.

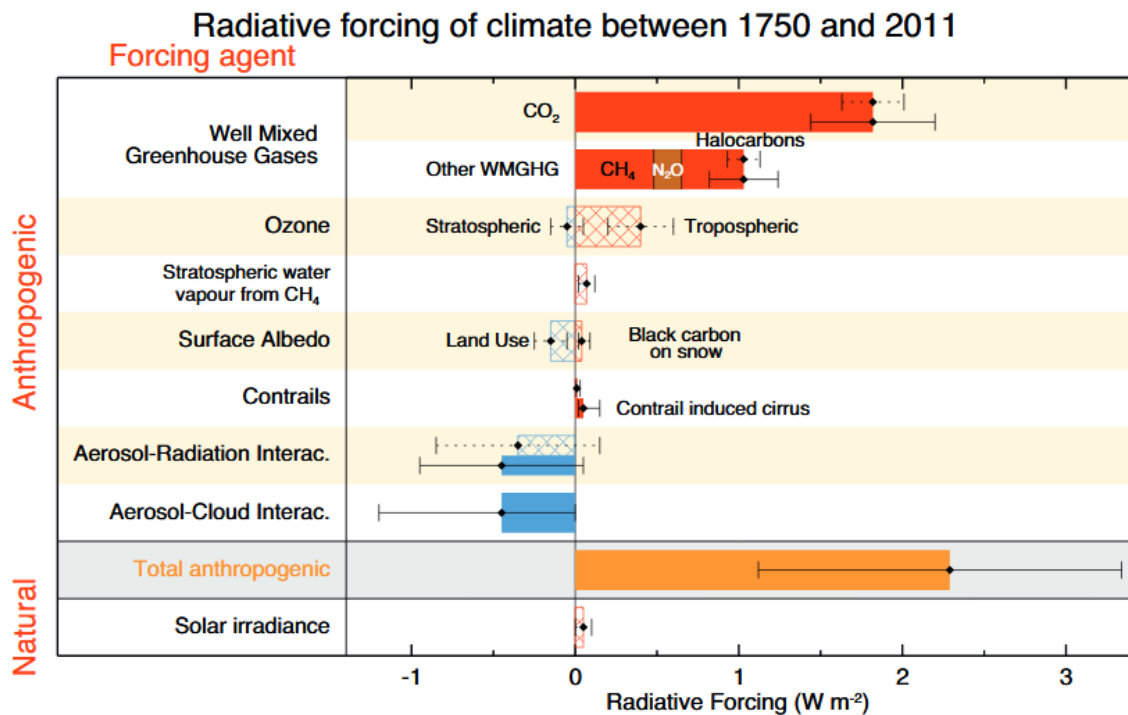


Figure 1.1 – Radiative Forcing Chart from IPCC AR5⁵. Hatched bars represent radiative forcing, solid bars represent effective radiative forcing^a, and error bars are 95% confidence intervals (dashed error bars for radiative forcing; solid error bars for effective radiative forcing).

As Figure 1.1 makes clear, the aerosol/cloud interaction could reasonably (95% confidence interval) represent a radiative forcing as significant as -1.2 kg s^{-3} , or could be negligible. This represents the most significant uncertainty in high-level climate science. The work described in this thesis represents a very small part of the efforts to better understand the aerosol/cloud interaction and therefore reduce this uncertainty.

1.2 – Water and Convection

Before moving on to discuss the aerosol/cloud interaction in more detail, a brief word will be said about the interaction between water and convection, as it provides a good background for why the troposphere is the region of interest for the majority of cloud activity, whereas the direct effect of water vapour emissions as radiative forcing is only relevant in the stratosphere. Fundamentally, the reason for this is that the stratosphere is convectively stable, whereas the troposphere is frequently convectively unstable.

As atmospheric pressure is a result of the weight of the column of air above a given point pushing down on that point, it naturally decreases with height (z). If an air parcel rises or falls through the atmosphere, then it experiences a change in pressure which, as a result of Gay-Lussac's law, manifests as a change in the temperature of the air parcel. This change in temperature is linear, and is known as the dry adiabatic lapse rate⁶ or DALR. It has a value of $9.8 \times 10^{-3} \text{ K m}^{-1}$. For sign convenience, it is defined as $-dT_{\text{parcel}}/dz$, which gives it a positive value as temperature decreases with increasing height.

^a Effective radiative forcing is a recently introduced method for estimating radiative forcing values that takes into account some perturbations that were not included in the radiative forcing calculations used previously⁵. The exact differences between radiative forcing and effective radiative forcing are beyond the scope of this introduction.

This leads to the concept of potential temperature (θ), which can be conceptualised as the temperature that a parcel of air would be if brought to some standard height. A column of air with $-dT_{\text{column}}/dz = \text{DALR}$ has a constant potential temperature with respect to height.

Hotter air is more buoyant than colder air, meaning that an air parcel that is warmer than its surroundings will rise. If $d\theta/dz$ is negative, then the disparity between the parcel and the surrounding air will only increase as the air parcel rises, causing it to rise even faster. A column of air with this potential temperature gradient is said to be convectively unstable.

Conversely, if $d\theta/dz$ is positive, then the rising parcel of air will cool more quickly than the column through which it is rising, eventually rising to a height where it has the same potential temperature as the surrounding air and staying there. A column of air with this potential temperature gradient is said to be convectively stable.

The stratosphere is convectively stable, which means that injections of water vapour into the stratosphere can result in reasonably long-lasting changes to the amount of water vapour in the stratosphere, as air is only exchanged with the troposphere (which is in a reasonably fast equilibrium with the terrestrial water system) via the overturning of planet-wide air circulation currents.

Water added to the troposphere is added to a rapidly overturning system and therefore is quickly returned to the terrestrial water system. Regions of convective stability, called inversions, do appear in the troposphere, and these manage to isolate small air masses from the overall equilibrium reasonably efficiently. These can be very unpleasant for those on the ground if there are major sources of pollution under the inverted atmospheric region, but they do not generally last for more than a few days at most.

The DALR is referred to as such because it describes the situation for a dry air parcel. Wet air (air with dissolved moisture) can depart from the simple pressure/temperature relationship of Gay-Lussac's law by releasing the latent heat of condensation of the dissolved water vapour through the formation of clouds. While unsaturated or supersaturated, a rising air parcel follows the DALR, but, once condensation has begun (the details of which will be discussed in section 1.3), the change in temperature with altitude is described by the moist adiabatic lapse rate (MALR). The MALR is nonlinear and depends on temperature, unlike the linear temperature-independent DALR. The details of the MALR are beyond the scope of this introduction, but it is always of lower magnitude (less negative) than the DALR⁶.

Columns of air in which $\text{DALR} > -dT_{\text{column}}/dz > \text{MALR}$ will be convectively stable as long as the critical supersaturation (see section 1.3) is not reached, so condensation is not occurring. Once condensation of water vapour into liquid or ice aerosol particles is underway, this air will then be convectively unstable. This instability will drive further convection, which will result in the further raising and cooling of supersaturated air, driving further condensation. This process underlies the formation of convective clouds in the troposphere, which have significant climatic impacts. It is to these impacts that this introduction now turns, as it is via effects upon these processes that the phenomena studied in this work derive their climatic impact.

1.3 – Water and Aerosol: Cloud Lifetime Effects

Clouds have a complex climatic impact, as they can represent both positive and negative radiative forcings, depending on the nature of the cloud in question. Changes in the climate also affect the prevalence and nature of clouds in turn, leading to feedback effects.

Clouds have a modulating effect on outgoing longwave radiation, as they absorb a fraction of such radiation as it propagates outwards towards space and then re-emit it back downward towards earth and outward towards space with a luminosity and frequency distribution characteristic of the

temperature of the cloud, which may be quite different from the temperature of the earth. They also reflect a portion of incoming radiation, which manifests as a shift in the planetary albedo.

High clouds have the most significant warming effect, as their cloud-top temperatures are very low, meaning that they emit radiation out to space at a considerably lower rate than would an equivalent portion of the surface of the earth. This decreases the overall efficiency of outgoing radiation in a similar manner to the greenhouse effect, and the surface temperature must rise to re-establish equilibrium.

Low clouds, on the other hand, have similar cloud-top temperatures to the surface, meaning that their modulating effect on outgoing radiation is much smaller, and they lack the positive radiative forcing associated with high clouds⁷. The main effect of these low clouds, therefore, is their raising of the planetary albedo, which is a negative forcing effect⁸. The presence of low clouds above the ocean in particular, which has a very low albedo in the absence of cloud cover, is quite a large negative forcing. The interactions of such clouds with the wider water cycle complicates this issue⁹.

The formation of clouds in the atmosphere does not occur spontaneously if water vapour saturation reaches 100%. This is due to the increase in the effective equilibrium vapour pressure associated with a convex liquid droplet as the diameter of said droplet decreases (due to the greater surface energy associated with curved surfaces). The greater the convex curvature of the droplet, the greater the supersaturation required to produce condensation. This is known as the Kelvin effect, and expresses the equilibrium vapour pressure for a droplet (p_{drop}) as a function of the diameter (D) of that droplet. The function depends on the relevant equilibrium vapour pressure for a flat surface (p_{flat}), the molar mass (M_r), density (ρ) and surface tension (γ) of the liquid, and the temperature (T) as follows⁶:

$$\ln \frac{p_{drop}(D)}{p_{flat}} = \frac{4M_r\gamma}{RT\rho D}$$

Equation 1.3

R represents the universal gas constant at $8.314 \text{ kg m}^2 \text{ s}^{-2} \text{ K}^{-1} \text{ mol}^{-1}$. Taking a limit as D tends to zero, p_{drop} tends to infinity; this means that it is not possible to precipitate droplets out of clean, supersaturated air. Water droplets must instead nucleate around tiny seed particles in the atmosphere, which partially dissolve into the droplet as it forms. The presence of these solute particles lowers the effective equilibrium vapour pressure of the droplet, allowing further condensation and growth; this is called the Raoult effect. The Raoult effect simply expresses the partial equilibrium vapour pressure (p_{part}) for a substance with a given equilibrium vapour pressure as a pure liquid (p_{pure}) in a mixed liquid phase composed of a certain mole fraction (x) of the substance in question thus:

$$p_{part} = p_{pure}x$$

Equation 1.4

Taking a limit as x tends to zero, p_{part} also tends to zero, meaning that arbitrarily small amounts of water nucleating as a cloud droplet around a solute particle can have arbitrarily low equilibrium vapour pressures as the amount of water in the droplet tends to zero. This works to promote nucleation, and counters the Kelvin effect.

The balance of the two effects is described by the Köhler equation⁶, which adds an extra term to the equation for the Kelvin effect that takes account of the number of moles of solute in the droplet (n_s):

$$\ln \frac{p_{drop}(D)}{p_{flat}} = \frac{4M_r\gamma}{RT\rho D} - \frac{6n_sM_r}{\pi\rho D^3}$$

Equation 1.5

Plotting p_{drop} against D for a particular set of conditions produces a Köhler curve, which allows the critical supersaturation to be determined. Increasing solute amounts will decrease the critical saturation and promote nucleation, meaning that increased aerosol loading promotes the formation of clouds.

However, this effect also makes the clouds produced predisposed to be composed of a larger number of smaller water droplets than would be the case in cleaner air (if nucleation is more favoured, less water vapour will end up contributing to the growth of existing particles instead of forming new ones). This makes precipitation more difficult, leading to an enhanced lifetime for the clouds¹⁰. This effect, and a raft of other secondary effects associated with it, have led to a family of ideas called 'cloud lifetime hypotheses' or 'cloud lifetime effects'⁷.

These lifetime effects work alongside the more direct 'cloud albedo effect', in which aerosol load leads to clouds that are more reflective than they otherwise would be¹¹, to create quite a substantial negative radiative forcing upon the climate system as a result of the presence of aerosol in the atmosphere and its interactions with clouds in particular.

Unfortunately, these effects are complicated and still not well understood. Cloud lifetime hypotheses in particular are very difficult to study effectively and many researchers⁷ have challenged some of the higher estimates for the forcing value that have been derived from satellite surveys, some of which¹² are as high as -8 Wm^{-2} .

The problems with these hypotheses generally revolve around one of two issues. The first concern is measurement artefacts, in which the presence of clouds causes overestimation of aerosol concentrations or vice versa, and thus causes spurious correlations^{13,14}. Other problems are related to the fact that performing controlled experiments on these systems is difficult or impossible. This means that epidemiological data from earth observations has to be used, leaving conclusions vulnerable to confounding effects: What may appear to be enhanced cloud lifetimes due to aerosol concentrations may in fact be enhanced cloud lifetimes and aerosol concentrations due to a third factor, for instance strong surface winds, which produce both heavy sea-spray (aerosol) and deep, lasting clouds^{15,16}. Measurement problems further frustrate attempts at progress in this field^{17,18}, and a study by Rauber *et al.* even hints at the opposite correlation¹⁹.

Use of climate and weather modelling systems to improve measurement and modelling of this process have been held back by limited incorporation of cloud processes into the relevant models at the temporal and spatial resolution required to provide insight on the matter²⁰⁻²³.

Further investigations have complicated this picture again by revealing buffering effects. These are similar to some of the negative feedbacks present in the climate system, in which radiative forcing in one direction produces or enhances a forcing in the other direction, thus reducing the impact of the initial forcing. These buffer effects are not climate feedbacks, as they do not operate across climatic scales, but they work on the same principle on meteorological scales⁷.

One group of buffering effects involves microphysical couplings, such as changes in the sensitivity of the induction of precipitation to cloud droplet number concentration in different cloud regimes²⁴⁻²⁷, and the suppression of linearity in the relationship between cloud droplet number and aerosol concentration caused by changes in the local supersaturation²⁸⁻³⁰. Another group involves macrophysical couplings, such as the interactions between precipitation and liquid flux through the cloud, which may cause enhanced aerosol loading to result in *more* precipitation and thus shorter-lived clouds in certain circumstances⁷. Radiative effects related to the absorption and scattering of incoming radiation by the aerosol itself and the interplay that this process has with any present clouds also contribute to the buffering of the system³¹⁻³³.

In summary, the system is exceptionally complicated, and precise knowledge of the interplay between aerosol and radiative forcing by clouds eludes the scientific community at present. A 2009 review of the subject by Stevens and Feingold⁷ places high importance on buffering processes and the associated reduction in the negative radiative forcing associated with the aerosol/cloud interaction, while still maintaining an overall cautious commitment to at least the sign and importance of the effect. Much more research is underway, and it is under the auspices of working gradually towards understanding the interactions between aerosol pollutants and water droplets in the atmosphere that this research is placed.

1.4 – Organic Films at the Air/Water Interface

In key papers in 1983³⁴ and 1999³⁵, it was noted that organic films form on the surface of aerosol particles and that the reactivity of both the aerosol particles underneath and of the species that make up the films themselves was different from what would be expected if each were encountered alone. Donaldson and Vaida published a major review in 2006³⁶ that brings together most of the large body of existing knowledge regarding the behaviour of molecular monolayer organic films at the air/water interface that are relevant to atmospheric processes. They divided the subject into two clear areas of study depending on the nature of the species at the interface. The division that they proposed is between relatively insoluble films of amphiphiles, such as fatty acids, and films of soluble surfactants that also partially partition to the interface, such as alcohols. This work deals with insoluble films, so it is upon their behaviour that this introduction will focus.

Insoluble films at the air/water interface can be described by an equation of state that is roughly analogous to the ideal gas equation³⁶. In this equation, surface pressure (Π)^b is analogous to gas pressure, and surface area per molecule (A) is analogous to volume. These are related to the temperature (T) analogous to the temperature for gaseous systems by the following equation, which also describes dependencies on the minimum area per molecule for a theoretically maximally compressed monolayer (A_0) and cohesive attractive forces between molecules in the monolayer (Π_c):

$$(\Pi - \Pi_c)(A - A_0) = k_B T$$

Equation 1.6

The Boltzmann constant (k_B) is a fundamental constant at $1.381 \times 10^{-23} \text{ kg m}^2 \text{ s}^{-2} \text{ K}^{-1}$. As minimum surface area per molecule is constant for a given system, measurement of surface pressure as a function of area at a constant temperature (commonly referred to as a Π - A isotherm measurement) can give information about cohesive attractive forces in the monolayer, as changes in this variable produce deviations from the offset hyperbolic relationship between surface area per molecule and surface pressure that would be expected if these forces were constant. This procedure is carried out by spreading a surface monolayer at a very low area per molecule and then compressing the layer between moveable barriers³⁷. A detailed treatment of the way in which surface pressure is measured and Π - A isotherms produced in this work is included in Chapter 2.

A typical Π - A isotherm produced during this research is shown in Figure 1.2, and similar data was collected by Voss *et al.*³⁸. The various phases are labelled on the graph. At high surface area values, the system is in a 2D-gas (G) phase, in which the molecules are widely separated and not significantly

^b Donaldson and Vaida use lower-case π for surface pressure, which is standard. However, some equations in the methods section of this work include surface pressure as well as the mathematical constant for the ratio between the circumference and diameter of a circle, which is universally denoted as π across all disciplines. To avoid confusion when that point arises, surface pressure is referred to using upper-case Π in this work, except where it involves reproduction of individually published papers in which surface pressure is discussed in a circumstance removed from this possible confusion with the mathematical constant, in which the traditional lower-case π is used, as there is no reason to divert from the convention in the intended publication environment of those papers.

interacting. As the area per molecule decreases, the system moves into an expanded 2D-liquid (LE) phase, in which surface pressure rises nonlinearly with decreasing area per molecule, and then a compressed 2D-liquid (LC) phase in which this relationship is linear. The boundaries between these phases are somewhat indistinct, but the transition to the 2D-solid (S) phase, at 22 mN m^{-1} , is easily noticeable as a sharp kink. Below a surface area per molecule of around 22 \AA^2 , a monolayer can no longer be maintained, leading to a broken (B) phase that quickly collapses.

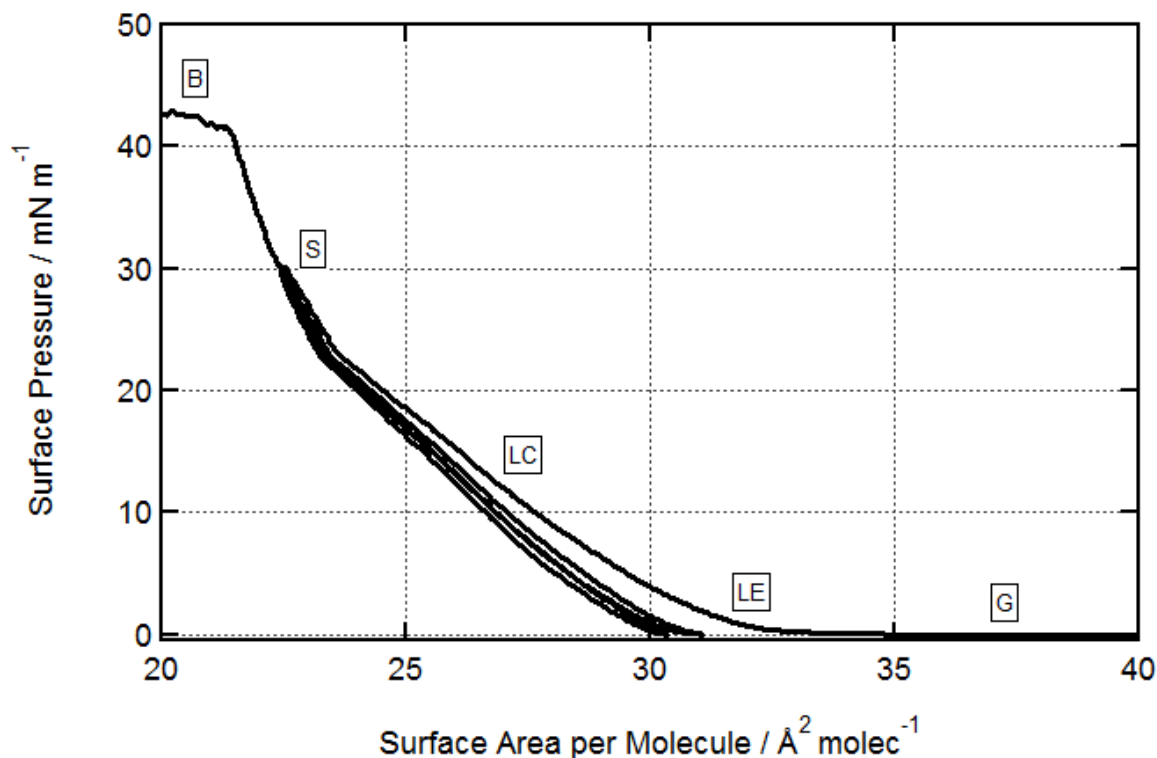


Figure 1.2 – Stearic acid pressure-area isotherm on pure water collected by compression from low-area spreading to 30 mN m^{-1} , two cycles between 30 and 0 mN m^{-1} , and a final compression to break. G = 2D-gas; LE = 2D-liquid expanded; LC = 2D-liquid compressed; S = 2D-solid; B = broken monolayer. Boundaries of LE phase are somewhat indistinct.

A cyclic compression/decompression collection protocol is used, as described in the caption, in order to ensure that the system is stable and that significant quantities of material are not being lost from the surface during the experiment (which can be a problem if vibrations are not adequately dampened or the barriers are not sufficiently clean). The offset of the first compression from the others is reproducible across systems and represents a pseudo-annealing process in which the first compression/decompression cycle reliably records slightly higher surface pressures for any given surface area per molecule. The slight offset between the second and third cycles is due to small losses of material from the system that cannot be entirely avoided. Compression/decompression cycle hysteresis is also common.

Isotherms such as these facilitate the preparation of monolayers for use in the oxidation experiments that make up the bulk of this work. For instance, the isotherm in Figure 1.2 suggests that targeting a surface area per molecule of 25 \AA^2 would be an appropriate way to prepare an LC phase stearic acid monolayer for an oxidation study.

Many of the monolayers studied this work are more disordered than the stearic acid example shown in Figure 1.2, and do not easily access LC or S phases as a result. In these cases, the main purpose of gathering the isotherms is to determine a maximum spreading amount for a given surface area to produce an LE phase monolayer without risking overspreading.

1.5 – Organic Films and Clouds

Many anthropogenic and biogenic organic compounds emitted into the atmosphere have surfactant activity and therefore can partition to the air/water interfaces that form the surfaces of cloud droplets^{34–36}. Such behaviour has been established, and various properties of the films and their reactivity has been probed, for the fatty acids^{38–43} and glycolipids⁴³ studied in this work, as well as for fatty acid methyl esters⁴⁴.

The oxidation of these organic species to form secondary organic aerosol (SOA) has been studied extensively in the past^{45–48}, and the SOA thereby produced will have climatic effects of the sort discussed in the section on cloud lifetime effects (section 1.3). However, the partitioning of these species into monolayers at the surfaces of cloud droplets has been observed to affect their reactivity^{38–41,44}. This could result in changes in rates of SOA production and therefore the extent of aerosol-induced cloud lifetime extension via enhancement of the Raoult effect as described in section 1.3. Perhaps more significant, though, are the effects that the presence of a surface monolayer has directly on the cloud droplets themselves.

All sorts of cloud formation, growth, evaporation, and rainout processes have a critical dependence upon surface tension as a result of the Kelvin effect⁶. The presence of insoluble organic films at the air/water interface has a lowering effect on the surface tension of the resultant water aerosols as described in section 1.4, and the knock-on effects in terms of interactions with clouds, and with cloud lifetime effects, is only just beginning to be understood³⁶. The lowering of the surface tension associated with the presence of a monolayer would seem, via a weakening of the Kelvin effect, to suppress the destabilising of small droplets and resultant suppression of nucleation that the Kelvin effect produces. On this basis, the presence of these surfactant species within the aerosol loading could promote nucleation via reducing the surface tension of the droplets thereby nucleated. Additionally, the presence of such monolayers on the surface of existing droplets enhances their stability at lower diameters compared to the situation that would obtain without them. This enhancement of nucleation and comparative stabilisation of lower diameter droplets could lead to increased cloud lifetimes via a similar route to the enhancement of the Raoult effect by increased aerosol loading that was discussed in section 1.3. Two studies, however, have thrown some doubt upon this and these will be discussed in turn.

A 2004 study⁴⁹ found that increased surfactant partitioning to the surface enhanced the stability of larger particles and depressed nucleation, which completely contradicts the hypothesis laid out in the previous paragraph. However, the study was performed using soluble surfactants, which contribute to both the Raoult (while partitioned to the bulk) and Kelvin (while partitioned to the surface) effects, and compared models in which partitioning was altered between the bulk and the surface. The reason given by the study for this behaviour is that increased partitioning of material away from the bulk towards the surface did more to weaken the Raoult effect through reduction in dissolved solute than it did to weaken the Kelvin effect through lowering of surface tension, leading to an overall trend of increased critical supersaturation and therefore a preference for larger particles and a reduction in nucleation activity. The surfactant monolayers studied in this work are all insoluble, with little to no material partitioned to the bulk. Only the weakened Kelvin effect, and not the weakened Raoult effect, is relevant for insoluble monolayers, meaning that the conclusions drawn from the 2004 paper cannot be used to predict the nucleation and particle stabilisation effects of insoluble monolayers.

A 2005 study⁵⁰, in which coatings of oleic, stearic, and *cis*-pinonic acid were formed around salt particles that were then used as cloud condensation nuclei, could not clearly attribute any enhanced nucleation behaviour to a lowering of surface tension via the Kelvin effect (although the study did record enhanced nucleation behaviour for thicker coatings of oleic and *cis*-pinonic acid, but reduced nucleation behaviour for thicker stearic acid coatings). Abbatt *et al.* attributed the reduced nucleation behaviour to the

shielding of the soluble salt particle from water vapour due to slow diffusion of water through stearic acid, and the enhanced nucleation behaviour for oleic and *cis*-pinonic acid to an increasing of the effective size of the droplet. However, the study was clear that it is difficult to be quantitative about these effects without better knowledge of the hygroscopic and diffusion behaviour of the substances. This makes it difficult to draw too many conclusions about the effects of organic monolayer coatings on small water droplets from this study. The hypothesis that nucleation would be promoted is weakly challenged, but the hypothesis that the stability of smaller droplets will be enhanced via reduced surface tension is not challenged, as it is not clear to what degree the study was able to assess such an effect.

In summary, though the enhancement of nucleation that would be expected from a simple lowering of the surface tension term in Equation 1.5 might be somewhat doubtful based on the experimental observations of Abbatt *et al.*⁵⁰, the reduction in the degree to which larger diameter particles are favoured that would also be expected from that surface tension reduction has not been challenged for insoluble monolayers (though does appear to be outweighed by other considerations for soluble monolayers⁴⁹). Therefore, a contribution of insoluble organic surfactants to cloud lifetime effects via a weakened Kelvin effect route is likely.

In addition to this effect, there exists a number of other routes via which the presence of a monolayer film on the surface of a cloud droplet has important consequences for atmospheric chemistry. On the one hand, such films can act as a barrier to mass transport between the water droplet and the atmosphere. Many studies have shown that insoluble films at the interface are able to significantly retard both the evaporation of the water droplet itself and the transport of oxygen (O₂), ozone (O₃), ammonia (NH₃), and many other important atmospheric species between the water droplet bulk phase and the atmospheric bulk phase^{51–58}. This inhibition of cross-interfacial transport could hinder the progress of atmospheric reactions that are carried out inside water aerosols and thus rely heavily on mass-transport steps across the air/water boundary⁵⁹.

On the other hand, the surface film itself can act as a '2D solvent' for species from the atmosphere, thus allowing the dissolution of species that would not normally dissolve in a water droplet, or altering the solvation behaviour of species that normally would dissolve in the droplet^{60–64}. This effect may play an important role in the transport of various species by water droplets, as it allows species that would not normally be transported by water droplets to be adsorbed at the coated interface and transported thus³⁶. These changes in solvation behaviour at the interface could impact the rates and even natures of atmospheric reactions that occur heterogeneously at the surface of such particles. Studies of some reactions have shown a reduction in reaction rates, such as the rate of the production of nitric acid (HNO₃) from dinitrogen pentoxide (N₂O₅) and water^{65,66} (a key atmospheric process for the redistribution of nitrogen amongst various species in the atmosphere) as a result of the presence of these coatings³⁶. The complexity of this effect is demonstrated by the existence of cases in which the opposite is true (situations in which organic coatings enhance heterogeneous reaction rates), such as the case of halide proton exchange reactions⁶⁷.

In sum, the reactivity and properties of these films deserve serious study, as they likely have a vast range of effects that are of climatic and meteorological significance, be that by affecting the reactivity of the film components and associated SOA production (with all the downstream effects that implies), by weakening the Kelvin effect and thus extending the lifetime of reflective clouds, or by modifying key atmospheric chemical processes that involve adsorption to the surface of or diffusion into the bulk of water droplets.

1.6 – Structure of the Thesis

This chapter has established the importance of organic films at the air/water interface generally. This thesis aims to extend the state of the art for study of the oxidation of these films by gas-phase oxidants in both a technical and scientific sense. The work consists in part of development of an apparatus and method for *in situ* deployment of Fourier transform infra-red reflection-absorption spectroscopy (FT-IRRAS) on a neutron reflectometry beamline (the technical component), and in part of reports of experiments performed using this apparatus (the scientific component). Chapter 2 introduces these two major methods and several complementary methods that have also been used for this work. Chapter 3 describes the work done to integrate *in situ* FT-IRRAS with neutron reflectometry, extending a 2017 paper produced by this research group outlining development of this system to an earlier prototype⁶⁸.

The following four chapters then detail the four main avenues of work pursued via the use of this apparatus. Each of these extends existing knowledge in this domain in a particular direction.

First, the oxidation of glycolipids, which have recently been identified as a major component of biogenic marine aerosol⁴³, is investigated in Chapter 4. A model glycolipid, galactocerebroside (GCB) is studied as a pure film, as a binary mixture with palmitic acid, and as a binary mixture with palmitoleic acid, each oxidised by NO_3^\bullet (nitrate) radicals, the major atmospheric oxidant present at night⁴¹.

Secondly, the effect of temperature on the oxidation of oleic acid is described in Chapter 5. Oleic acid has been established as a benchmark system for long-chain unsaturated fatty acids³⁶. Its oxidation by O_3 , the primary day-time oxidant³⁹, was studied early in the development of this field^{38,39}, with a study of oxidation by NO_3^\bullet radicals published more recently⁴⁰. This makes it a good candidate for studying at more atmospherically realistic temperatures.

Thirdly, in Chapter 6, mixed films of oleic and stearic acid are studied, in order to elucidate the effects of co-deposition of a comparatively unreactive (to ozone) film component on the oxidation of oleic acid. This takes great advantage of the *in situ* FT-IRRAS capabilities (as do the GCB mixtures reported in Chapter 4) to track multiple film components simultaneously.

Fourthly, Chapter 7 reports preliminary results from an exploratory experiment into the oxidation of linoleic acid by ozone, building on recent work that showed two competing oxidation mechanisms^{69,70}. This chapter presents data from only one beamline experiment performed at the very end of the time spent collecting data for this thesis. It is by its nature incomplete, leaving several questions still unanswered, and is presented only as preliminary data pointing the way towards further investigations.

Chapter 4 is formed mostly of an existing published paper describing the relevant body of work⁷¹, with a small supplementary section specific to the thesis providing additional information on the underlying neutron reflectometry data. Chapter 5 is formed entirely of a paper⁷² and supplement⁷² that are currently in peer review. As a result, these two chapters carry their own introductions and methods sections, which briefly repeat some of the key points of this general introduction before bringing in specific introductory material relevant to that particular portion of work. Chapters 6 and 7 are presented as traditional thesis results chapters.

Therefore, more specific introductory material, justifying the importance of the specific work carried out, is not repeated here, but will be presented at the start of each respective experimental chapter (either as part of the paper or as a section of the chapter). The introduction to the first chapter to use ozonolysis (Chapter 5) introduces the ozonolysis mechanism, which also applies to Chapters 6 and 7.

Finally, a summary is presented, in which the work is discussed chronologically, so that the interleaving of the technical developments discussed in Chapter 3 and the scientific progress discussed in Chapters 4 to 7 can be understood as a coherent whole. This chapter ends with a short summary of the key findings of the project.

1.7 – Bibliography (Introduction)

- 1 P. H. Gleick, in *Encyclopedia of Climate and Weather, Second Edition*, ed. S. H. Schneider, T. L. Root and M. D. Mastrandrea, Oxford University Press, Oxford, 2011, vol. 2, pp. 817–823.
- 2 G. Kopp and J. L. Lean, *Geophysical Research Letters*, **38**, L01706.
- 3 G. L. Stephens, D. O’Brien, P. J. Webster, P. Pilewski, S. Kato and J. Li, *Reviews of Geophysics*, 2015, **53**, 141–163.
- 4 IPCC, *Climate Change 2014: Synthesis Report. Contribution of Working Groups I, II and III to the Fifth Assessment Report of the Intergovernmental Panel on Climate Change [Core Writing Team, R.K. Pachauri and L.A. Meyer (eds.)]*, IPCC, Geneva, Switzerland, 2014.
- 5 IPCC, *Global warming of 1.5 °C. An IPCC Special Report on the impacts of global warming of 1.5 °C above pre-industrial levels and related global greenhouse gas emission pathways, in the context of strengthening the global response to the threat of climate change, sustainable development, and efforts to eradicate poverty. [V. Masson-Delmotte, P. Zhai, H. O. Pörtner, D. Roberts, J. Skea, P.R. Shukla, A. Pirani, W. Moufouma-Okia, C. Péan, R. Pidcock, S. Connors, J. B. R. Matthews, Y. Chen, X. Zhou, M. I. Gomis, E. Lonnoy, T. Maycock, M. Tignor, T. Waterfield (eds.)]*, IPCC, Geneva, Switzerland, 2018.
- 6 M. H. P. Ambaum, *Thermal Physics of the Atmosphere*, Wiley-Blackwell, Reading, 2010.
- 7 B. Stevens and G. Feingold, *Nature*, 2009, **461**, 607–613.
- 8 D. L. Hartmann and D. Doelling, *Journal of Geophysical Research*, 1991, **96**, 869–891.
- 9 M. Tiedtke, *Monthly Weather Review*, 1989, **117**, 1779–1800.
- 10 B. A. Albrecht, *Science*, 1989, **245**, 1227–1230.
- 11 S. Twomey, *Journal of the Atmospheric Sciences*, 1977, **34**, 1149–1152.
- 12 Y. J. Kaufman, I. Koren, L. A. Remer, D. Rosenfeld and Y. Rudich, *Proceedings of the National Academy of Sciences of the United States of America*, 2005, **102**, 11207–11212.
- 13 R. J. Charlson, A. S. Ackerman, F. A. M. Bender, T. L. Anderson and Z. Liu, *Tellus, Series B: Chemical and Physical Meteorology*, 2007, **59**, 715–727.
- 14 I. Koren, L. A. Remer, Y. J. Kaufman, Y. Rudich and J. V. Martins, *Geophysical Research Letters*, 2007, **34**, L08805.
- 15 N. G. Loeb and G. L. Schuster, *Journal of Geophysical Research*, 2008, **113**, D14214.
- 16 M. A. Matheson, J. A. Coakley and W. R. Tahnk, *Journal of Geophysical Research*, 2005, **110**, D24204.
- 17 L. Avey, T. J. Garrett and A. Stohl, *Journal of Geophysical Research*, 2007, **112**, D10S33.
- 18 T. Várnai and A. Marshak, *Geophysical Research Letters*, 2009, **36**, L06807.
- 19 R. Rauber, *Bulletin of the American Meteorological Society*, 2007, **88**, 1912–1928.
- 20 U. Lohmann and J. Feichter, *Atmospheric Chemistry and Physics Discussions*, 2004, **4**, 7561–7614.

- 21 C. Hoose, J. E. Kristjánsson, T. Iversen, A. Kirkevåg, Ø. Seland and A. Gettelman, *Geophysical Research Letters*, 2009, **36**, L12807.
- 22 T. Storelvmo, J. E. Kristjánsson, U. Lohmann, T. Iversen, A. Kirkevåg and Ø. Seland, *Environmental Research Letters*, 2008, **3**, 045001.
- 23 L. D. Rotstayn, *Journal of Geophysical Research*, 1999, **104**, 9369–9380.
- 24 A. Seifert and K. D. Beheng, *Atmospheric Research*, 2001, **59–60**, 265–281.
- 25 A. Sorooshian, G. Feingold, M. D. Lebsock, H. Jiang and G. L. Stephens, *Geophysical Research Letters*, 2009, **36**, L13803.
- 26 M. C. vanZanten, B. Stevens, G. Vali and D. H. Lenschow, *Journal of the Atmospheric Sciences*, 2005, **62**, 88–106.
- 27 R. Wood, *Journal of Geophysical Research*, 2006, **111**, D21205.
- 28 G. M. Martin, D. W. Johnson and A. Spice, *Journal of the Atmospheric Sciences*, 1994, **51**, 1823–1842.
- 29 C. D. O’Dowd, J. A. Lowe, M. H. Smith and A. D. Kaye, *Quarterly Journal of the Royal Meteorological Society*, 1999, **125**, 1295–1313.
- 30 V. Ramanathan, P. J. Crutzen, J. T. Kiehl and D. Rosenfeld, *Science*, 2001, **294**, 2119–2124.
- 31 A. S. Ackerman, *Science*, 2000, **288**, 1042–1047.
- 32 G. Feingold, H. Jiang and J. Y. Harrington, *Geophysical Research Letters*, 2005, **32**, 1–4.
- 33 I. Koren, Y. J. Kaufman, L. A. Remer and J. V. Martins, *Science*, 2004, **303**, 1342–1345.
- 34 P. S. Gill, T. E. Graedel and C. J. Weschler, *Reviews of Geophysics*, 1983, **21**, 903–920.
- 35 G. B. Ellison, A. F. Tuck and V. Vaida, *Journal of Geophysical Research*, 1999, **104**, 11633–11641.
- 36 D. J. Donaldson and V. Vaida, *Chemical Reviews*, 2006, **106**, 1445–1461.
- 37 A. W. Adamson and A. P. Gast, *Physical Chemistry of Surfaces*, 6th Edition, Wiley, Hoboken, 1997.
- 38 L. F. Voss, M. F. Bazerbashi, C. P. Beekman, C. M. Hadad and H. C. Allen, *Journal of Geophysical Research*, 2007, **112**, D06209.
- 39 M. D. King, A. R. Rennie, K. C. Thompson, F. N. Fisher, C. C. Dong, R. K. Thomas, C. Pfrang and A. V. Hughes, *Physical Chemistry Chemical Physics*, 2009, **11**, 7699–7707.
- 40 F. Sebastiani, R. A. Campbell, K. Rastogi and C. Pfrang, *Atmospheric Chemistry and Physics*, 2018, **18**, 3249–3268.
- 41 F. Sebastiani, PhD Thesis, University of Reading, 2014.
- 42 W. R. Barger and W. D. Garrett, *Journal of Geophysical Research*, 1970, **75**, 4561–4566.
- 43 E. Adams and H. Allen, *Atmosphere*, 2013, **4**, 315–336.
- 44 C. Pfrang, F. Sebastiani, C. O. M. Lucas, M. D. King, I. D. Hoare, D. Chang and R. A. Campbell, *Physical Chemistry Chemical Physics*, 2014, **16**, 13220–13228.
- 45 M. K. Shrivastava, R. Subramanian, W. F. Rogge and A. L. Robinson, *Atmospheric Environment*, 2007, **41**, 9353–9369.

- 46 H.-M. Hung and C.-W. Tang, *The Journal of Physical Chemistry A*, 2010, **114**, 13104–13112.
- 47 A. K. Y. Lee and C. K. Chan, *The Journal of Physical Chemistry A*, 2007, **111**, 6285–6295.
- 48 K. E. Huff Hartz, E. A. Weitkamp, A. M. Sage, N. M. Donahue and A. L. Robinson, *Journal of Geophysical Research*, 2007, **112**, D04204.
- 49 R. Sorjamaa, B. Svenningsson, T. Raatikainen, S. Henning, M. Bilde and A. Laaksonen, *Atmospheric Chemistry and Physics*, 2004, **4**, 2107–2117.
- 50 J. Abbatt, K. Broekhuizen and P. Pradeepkumar, *Atmospheric Environment*, 2005, **39**, 4767–4778.
- 51 G. T. Barnes, *Colloids and Surfaces A: Physicochemical and Engineering Aspects*, 1997, **126**, 149–158.
- 52 G. L. Gaines, *Insoluble Monolayers at the Liquid Gas Interface*, Interscience Publishers, Geneva, 1966.
- 53 V. K. La Mer, *Retardation of Evaporation by Monolayers: Transport Processes*, Academic Press Inc., London, 1962.
- 54 V. K. La Mer, *Journal of Colloid Science*, 1964, **19**, 673–684.
- 55 I. Benjamin, *Chemical Reviews*, 1996, **96**, 1449–1476.
- 56 W. D. Garrett, *Journal of the Atmospheric Sciences*, 1971, **28**, 816–819.
- 57 A. K. Ray, B. Devakottai, A. Souyri and J. L. Huckaby, *Langmuir*, 1991, **7**, 525–531.
- 58 E. K. Rideal, *The Journal of Physical Chemistry*, 1924, **29**, 1585–1588.
- 59 B. Daumer, R. Niessner and D. Klockow, *Journal of Aerosol Science*, 1992, **23**, 315–325.
- 60 J. B. Gilman, T. L. Eliason, A. Fast and V. Vaida, *Journal of Colloid and Interface Science*, 2004, **280**, 234–243.
- 61 J.-H. A. Lo and W.-M. G. Lee, *Chemosphere*, 1996, **33**, 1391–1408.
- 62 B. T. Mmereki, S. R. Chaudhuri and D. J. Donaldson, *The Journal of Physical Chemistry A*, 2003, **107**, 2264–2269.
- 63 B. T. Mmereki and D. J. Donaldson, *Physical Chemistry Chemical Physics*, 2002, **4**, 4186–4191.
- 64 M. Tomoaia-Cotisel and D. Allan. Cadenhead, *Langmuir*, 1991, **7**, 964–974.
- 65 M. Folkers, Th. F. Mentel and A. Wahner, *Geophysical Research Letters*, 2003, **30**, 1644.
- 66 J. A. Thornton and J. P. D. Abbatt, *The Journal of Physical Chemistry A*, 2005, **109**, 10004–10012.
- 67 J. R. Lawrence, S. V Glass, S.-C. Park and G. M. Nathanson, *The Journal of Physical Chemistry A*, 2005, **109**, 7458–7465.
- 68 M. W. A. Skoda, B. Thomas, M. Hagreen, F. Sebastiani and C. Pfrang, *RSC Advances*, 2017, **7**, 34208–34214.
- 69 Y. Chu, T. F. Cheng, M. Gen, C. K. Chan, A. K. Y. Lee and M. N. Chan, *ACS Earth Space Chem.*, 2019, **3**, 779–788.

- 70 U. Molteni, M. Simon, M. Heinritzi, C. R. Hoyle, A.-K. Bernhammer, F. Bianchi, M. Breitenlechner, S. Brilke, A. Dias, J. Duplissy, C. Frege, H. Gordon, C. Heyn, T. Jokinen, A. Kürten, K. Lehtipalo, V. Makhmutov, T. Petäjä, S. M. Pieber, A. P. Praplan, S. Schobesberger, G. Steiner, Y. Stozhkov, A. Tomé, J. Tröstl, A. C. Wagner, R. Wagner, C. Williamson, C. Yan, U. Baltensperger, J. Curtius, N. M. Donahue, A. Hansel, J. Kirkby, M. Kulmala, D. R. Worsnop and J. Dommen, *ACS Earth and Space Chemistry*, 2019, **3**, 873–883.
- 71 B. Woden, M. W. A. Skoda, M. Haggren and C. Pfrang, *Atmosphere*, 2018, **9**, 471.
- 72 B. Woden, M.W.A Skoda, A. Milsom, A. Maestro, J. Tellam and C. Pfrang, *Atmospheric Chemistry and Physics*, Under Review: Preprint at doi.org/10.5194/acp-2020-717

Chapter 2 – Methods

2.1 – Specular Neutron Reflectometry

2.1.1 – Reflectivity Basics

Neutron reflectometry is one of a family of techniques that takes advantage of the differential refractive indices (η)^c characteristic of a certain particle's travel through various media. A reflected beam of these particles is compared with an incident beam in order to make inferences about the media under study. For neutron reflectometry, this particle is the neutron. Such reflection occurs when a beam of incident radiation passes from a medium with a higher refractive index to a medium with a lower refractive index. The refractive index of the various media with respect to the particle in question is determined by interaction between the particle and the various media. The measured property of reflectivity (R)^d is defined as the intensity of reflected radiation (I_{ref}) normalised to the intensity of incident radiation (I_{inc}). Specular (or regular) reflectometry deals in particular with radiation reflected at an angle with respect to the interface (θ_{ref})^e that is equal to the angle of the incident beam (θ_{inc}).

The refractive index of a material with respect to neutrons is determined by the interactions of the neutrons with that material. Neutrons interact with atomic nuclei and indirectly with unpaired electrons. Both of these interactions are weak, which means most refractive indices are close to 1, and reflection is weak apart from at low θ . Interaction with unpaired electrons (magnetic scattering) is dependent on the polarisation of the incident neutron beam. The technique that makes use of this interaction, polarised neutron reflectometry, will not be discussed further here. This work makes use only of the interaction between neutrons and atomic nuclei. The strength of the interaction between neutrons and nuclei depends on the atomic number, mass number, and orientation of nuclear spin with respect to the angular momentum of the incident neutron (for nuclei with a nonzero nuclear spin).

For a medium containing just one type of nucleus with no spin, the scattering of neutrons by nuclei is described by the characteristic scattering length (b) of the nucleus, upon which scattering has a quadratic dependence. For a medium containing just one type of nucleus with nonzero nuclear spin, the scattering will be composed of coherent and incoherent components. For the purposes of unpolarised specular neutron reflectometry, only coherent scattering matters and it can be calculated by weighting the scattering lengths of the antiparallel (b^-) and parallel (b^+) nuclear spin orientations in accordance with a weighting factor (w^- , w^+) dependent on the nuclear spin quantum number to produce an ensemble averaged scattering length for that nucleus, upon which coherent scattering has a quadratic dependence. For a medium containing multiple types of nucleus, the scattering has a quadratic dependence on a simple linear average of the scattering lengths of the nuclei present (averaged across b^- and b^+ contributions according to w^- and w^+ if necessary), weighted by the number concentration (n) of each nucleus.

The incoherent component of the total scattering is more complex. Total scattering scales with the linear average of the square of the scattering lengths of individual nuclei (rather than with the square of

^c Refractive index is commonly denoted by n instead of by η , but the latter is employed here in order to avoid confusion with the use of n to denote number concentration in Equation 2.1.

^d R was used to denote the universal gas constant in Chapter 1. Generally, efforts have been made to avoid re-using the same letter to refer to more than one concept. However, sometimes this is not possible without making the work hard to reconcile with other literature. When two concepts habitually given the same letter designation (such as refractive index and number concentration as discussed in footnote c) are used either in the same equation or equations in the same section of the thesis, one of them will be given an alternative designation and this will be made clear. Where confusion of two concepts is considered less likely, and no clear alternative can be found (as in this case), the same letter designation will be used, and the shift in usage will be explained.

^e θ was used in section 1.2 to indicate potential temperature, whereas here it denotes angle of incidence.

the linear average, as for coherent scattering) and the incoherent scattering is the ‘missing’ scattering that makes up the difference between coherent and total scattering. Incoherent scattering does not contribute to specular reflection (it is non-directional), and is therefore irrelevant to specular neutron reflectometry except as a contribution to background scattering.

This convenient linear combination property for coherent scattering allows the assignment of scattering length values to molecules that are simply the sum total of the scattering lengths of the component nuclei. It also allows the description of media by a scattering length density (ρ) parameter, which is dependent upon the number concentration and scattering length of the species present, and which can be calculated with b and n values for atoms or molecules (or even for other units of interest such as supramolecular complexes):

$$\rho = \sum_i b_i n_i$$

Equation 2.1

The refractive index (η) of a medium with respect to neutrons can then be expressed as a function of the wavelength of the neutrons (λ) and the scattering length density of the medium:

$$\eta = \sqrt{1 - \frac{\lambda^2 \rho}{\pi}}$$

Equation 2.2

The reflectivity of an interface between media with different refractive indices is dependent upon the angle of incidence and on the difference between the refractive indices, which themselves depend upon the scattering length density (SLD) values of the media and the wavelength of the neutrons. It is helpful for neutron reflectivity to combine the angle of incidence and wavelength into a single parameter, momentum transfer (Q)^f thus:

$$Q = \frac{4\pi \sin \theta}{\lambda}$$

Equation 2.3

This parameter represents the transfer of momentum from a reflected neutron to the media by specular reflection at an interface. Reflectivity is therefore dependent on momentum transfer and on the SLD of the layers. The neutron reflectometry experiments performed here are white beam time-of-flight (TOF) experiments, in which a fixed angle of incidence is used and a range of Q values is probed by illuminating the media with a white beam of neutrons made up of neutrons spanning a range of wavelengths. The wavelength of a neutron is related to its mass (m) and velocity (v) via Planck’s constant ($h = 6.626 \times 10^{-34} \text{ m}^2 \text{ kg s}^{-1}$) as expressed in the de Broglie relation:

$$\lambda = \frac{h}{mv}$$

Equation 2.4

Velocity is measured by TOF via the method of allowing pulses made up of neutrons spanning a range of wavelengths to enter the instrument at very precisely defined times by the use of a series of rotating

^f Momentum transfer is often denoted as κ rather than Q , particularly in the review by Lu *et al.*¹. The latter has been chosen for this work as it seems to be in more common use now, and is the convention used by the MOTOFIT² fitting software used throughout this work and explained in more detail in section 2.1.6.

choppers and then measuring the time taken to traverse the known distance to the detector in order to calculate the wavelength of any given detected neutron.

If a greater Q range is desired than that which is accessible by the range of neutron wavelengths available, then the same system can be studied at various different values of θ , producing multiple datasets of a variety of Q ranges, which can then be stitched together into one overall R vs Q plot.

The three neutron reflectometry instruments used here (INTER, SURF, and FIGARO) are based at two different neutron sources (ISIS in Oxfordshire houses INTER and SURF; the Institute Laue Langevin (ILL) in Grenoble houses FIGARO), which generate their neutrons in two different ways. At ISIS, neutrons are generated by colliding pulses of high-energy protons generated by a synchrotron into a tungsten target, causing spallation of neutrons out of the target. These neutrons are, therefore, already provided bunched into pulses and the role of the chopper assembly is to 'shape' the pulse by cutting out undesired wavelengths and preventing 'frame overlap', in which fast neutrons from a later pulse catch up with slow neutrons from an earlier pulse. At the ILL, neutrons are generated continuously from a nuclear reactor. In this situation, the choppers must create the pulses as well as shaping them. In either situation, the precise timings of the choppers affects the size of these pulses, which introduces uncertainty into the calculation of Q due to uncertainty in the exact time at which any given neutron in a pulse left the neutron source. This uncertainty is expressed as dQ/Q .

A further contribution to dQ/Q is caused by variation in the path any neutron might take through the entire process between the point at which the pulse is generated and assigned a timestamp, and the point at which it is detected and the velocity calculated from the elapsed time between these event. Some of this uncertainty in path length comes from the fact that a neutron beam must be of some specific width, so any given neutron can travel a variety of paths of slightly different lengths within this defined beam path. The width of the beam is determined by a series of cadmium slits placed along the beam path. Narrower slits reduce the uncertainty in path length but correspondingly reduce neutron flux. The appropriate trade-off between flux and dQ/Q will vary depending on the requirements of the experiment. An additional contribution to dQ/Q comes from the fact that the neutron source itself is not a point, but has some defined size, and neutrons can be produced from any point within the source, some of which are further away from the detector than others. This means that, even for an arbitrarily narrow beam, some path length uncertainty will remain.

2.1.2 – Reflectivity from Monolayers

The relationship between Q and R for an interface between media of differing SLD values is composed of two parts. Below a certain critical Q (analogous to a critical angle for a fixed wavelength neutron beam), total reflection is achieved ($R = 1$). This critical Q is calculated as follows:

$$Q_{crit} = \sqrt{16\pi\Delta\rho}$$

Equation 2.5

Above this critical Q, R falls off quartically with Q according to a complex formula that, with the application of a simplifying assumption that holds for Q ranges that are not close to Q_{crit} (see Lu *et al.* 2000¹ for a full treatment), reduces to the following:

$$R \simeq \frac{16\pi^2(\Delta\rho)^2}{Q^4}$$

Equation 2.6

A monolayer at an interface, of the sort studied in this work, results in a system with three layers with their own SLD values and a defined distance between the two interfaces, or monolayer thickness (τ).

The reflectivity from this whole system comes from an interference pattern between reflections from two interfaces:

$$R \simeq \frac{16\pi^2}{Q^4} ((\rho_1 - \rho_0)^2 + (\rho_2 - \rho_1)^2 + 2(\rho_1 - \rho_0)(\rho_2 - \rho_1) \cos(Q\tau))$$

Equation 2.7

This can be extended for systems with more layers, and the SLD and thickness values for each layer, along with an SLD for semi-infinite ‘fronting’ and ‘backing’ layers can be fitted numerically to a measured R vs Q profile. R vs Q data cannot easily (or, in many cases, at all) be directly transformed into values for SLD and thickness by solving these equations analytically, which is why numerical curve fitting is required. The cosine dependence of R on Q produces oscillations in the quartic decay of R with Q (Kiessig fringes) which, in a manner analogous to Bragg diffraction peaks, are spaced in Q (which has units of reciprocal length) in a manner reciprocal to the thickness of the layer. Systems with multiple layers produce complicated and ambiguous R vs Q relationships that are often difficult to fit and are vulnerable to overfitting, in which ever more and more layers, and thus parameters, can be added to the model in order to marginally improve the goodness of fit without corresponding to anything physical.

Fitting of this kind of data requires some assumptions to be made about the structure of the system. Co-refinement of multiple datasets, for instance on two subphases with different known SLD values to be included as ‘backing’ in the fit, can help constrain the model and avoid overfitting.

The SLD of air is essentially zero, due to its low number concentration. This means that Equation 2.7 can be simplified. Further simplification can be achieved for monolayers at an air/water interface by the use of null-reflecting water (NRW; also known as air-contrast matched water or ACMW), which also has an SLD of zero. NRW is composed of an 8.8% v/v solution of D₂O (deuterated water) in H₂O. This exploits the fact that protium (¹H) has a negative scattering length (b = -3.74 fm) whereas deuterium (²H) has a positive scattering length (b = 6.67 fm), so the correct balance between them (also taking into account b = 5.80 fm for O (weighted average of naturally occurring isotopes)) can produce a solution with b = 0 fm. The relationship between R and Q then only depends on the SLD and thickness of the monolayer thus:

$$R \simeq \frac{16\pi^2}{Q^4} (2\rho^2 - \rho^2 \cos(Q\tau))$$

Equation 2.8

It is important to note at this stage that these approximate relations, which hold for values of Q that are sufficiently above Q_{crit}, are provided in order to aid explanation of the general shape of the R vs Q relation for reflection from various interfaces, how interference patterns are produced by multiple interfaces, and how the system is greatly simplified and thus models more easily fitted by the use of NRW as a subphase for monolayers at the air/water interface. The fitting algorithms actually used make use of more complicated expressions of the R vs Q relation that hold for all values of Q.

These expressions also take into account reductions in reflectivity due to surface roughness. No surface is completely smooth: Even a completely uncontaminated surface has atomic roughness, and clean liquid surfaces cannot be completely free of small (capillary) waves and disturbances caused by thermal motion. Roughness suppresses specular reflectivity by essentially introducing a mismatch between θ as defined between an incident beam and the overall orientation of the surface, and θ as experienced by each individual neutron as the angle of incidence between its direction of travel and the orientation of the interface at the exact point of contact that, for a surface with any roughness, will not always exactly match the overall orientation of the interface (which is what roughness is). Micro-level specular

reflection events are therefore slightly blurred outside the precisely defined specular scattering angle at the macro level.

The fitting also takes into account background scattering, which is mostly Q-independent and due to incoherent scattering (which is not Q-dependent). If the Q range of the dataset extends to high enough Q values that ‘true’ reflectivity is essentially zero, and all detected neutrons are from Q-independent background scattering, then a Q-independent background scattering parameter can be fitted. If not, then such a parameter has to be measured via a reflectivity experiment using an air/NRW interface, and then fixed at a suitable value inferred from this experiment in the fitting of other R vs Q plots.

2.1.3 – Calculation of Reflectivity

Reflectivity is not trivial to measure, as the sensitivity of neutron detectors is not constant as a function of λ , and therefore of Q. Neither are the detectors used to measure the incident beam of the same overall sensitivity, or sensitivity with respect to Q, as the detectors used to measure the reflected beam. The monitors (incident beam detectors) are designed to be low efficiency, so as to remove as little flux as possible from the incident beam. Scintillating glass bead arrays are used for this purpose. The main detectors are designed to be much more sensitive, in order to improve counting statistics, and are composed of helium-3 (^3He) tubes.

In order to effectively measure reflectivity, then, it is necessary to run a transmission experiment in which a neutron beam is directed through the monitors and main detectors without being reflected by a sample in the interim. With intensity as a function of Q measured for the detector and the monitor in transmission and sample runs, reflectivity as a function of Q is calculated thus:

$$R(Q) = \frac{I_{det,sample}(Q)I_{mon,trans}(Q)}{I_{mon,sample}(Q)I_{det,trans}(Q)}$$

Equation 2.9

The beam is also passed through any experimental apparatus through which the beam will have to pass during measurement runs, in order to correct for any beam attenuation effects such apparatus might have (though this is generally kept to a minimum). The performance of transmission runs also takes account of the fact that the white beam does not contain a flat distribution of flux with respect to λ , and therefore with respect to Q, as well as automatically normalising for variations in incident neutron flux during an experiment (except in certain configurations discussed later in this section).

The remaining effect of the differential flux and detector sensitivity with respect to Q is simply that dR/R is greater in regions of Q with lower flux and sensitivity. The distribution of flux with respect to λ is fixed for any one neutron source (though the overall flux can be adjusted by manipulating chopper timings, which also affects dQ/Q as explained in section 2.1.1), but as Q depends on λ and θ , choice of θ allows adjustment of the Q range over which maximum flux is distributed.

Even after this normalisation, it is possible that sample data may end up mis-scaled due to differences in experimental geometry between transmission and sample runs. This tends to happen because the reflected beam is more divergent than the transmission beam. The detector sits close behind a cadmium slit (one of four used to shape the beam and balance flux against dQ/Q), and so additional beam loss from the more divergent reflected beam can be significant. In principle, this could be corrected by extending any R vs Q plot to low enough Q that total reflection, which is then Q-independent for Q equal to or lower than Q_{crit} , is definitively observed. R at $Q < Q_{crit}$ can then be assumed to be 1, and the R vs Q dataset scaled accordingly (or a scale factor parameter allowed to float during fitting). In practice, sufficient (or any) neutron flux at a low enough Q is often unavailable. This is true for the vast majority of this work. In these cases, a calibration with an air/D₂O interface, whose Q_{crit} is within the Q range at which the relevant instruments have high flux, must be performed. A parameter for scaling inferred

from this data is then fixed when fitting experimental R vs Q datasets collected under the same conditions.

2.1.4 – Deuteration of Monolayer Material

Equation 2.6 makes clear that greater reflectivity is achieved from an interface with a large change in SLD. Equation 2.8 shows how this translates to a very simple dependency for a monolayer at an air/NRW interface: The greater the SLD and thickness of the monolayer, the greater the reflectivity. This work involves the study of monolayers of fatty acids such as oleic acid, and glycolipids such as galactocerebroside. These molecules have b values of around -20 to -40 fm. When spread as a monolayer of around 20 Å thickness (roughly the thickness of these monolayers determined by ellipsometry³) and a surface area per molecule of around 35 Å² (about as closely packed as is feasible for oleic acid, and a common benchmark surface concentration used throughout this work), this would produce a layer with an SLD of approximately $-0.4 \times 10^{-6} \text{ \AA}^{-2}$. This is possibly strong enough to detect, but much of this work deals with tracking reactions that involve deletion of the monolayer, and often requires detection of residual monolayers of around an order of magnitude lower surface concentration than this benchmark for the concentrations of initial reactant films. For such experiments, the scattering of these fatty acids and glycolipids is far too weak to allow meaningful work to proceed.

In order to be measurable with neutron reflectometry, the fatty acids and glycolipids studied in this work are deuterated. This means that they are prepared by specialist organic synthesis teams to have some or all of their hydrogen atoms replaced with deuterium (²H; $b = 6.67 \text{ fm}$). The natural abundance of deuterium (0.02%) is low enough that naturally occurring non-deuterated versions can be assumed to essentially have no deuterium, with all hydrogen atoms being protium (¹H; $b = -3.74 \text{ fm}$).

d_{34} -Oleic acid, an example of such a deuterated fatty acid, has a scattering length of 328 fm, which, under the same spreading thickness and area per molecule (20 Å and 35 Å², respectively), gives a layer SLD of approximately $5 \times 10^{-6} \text{ \AA}^{-2}$. This is well within the range of detection of the current generation of neutron reflectometry instruments. Therefore, in the correct geometric configuration and with sufficient count times, precise measurement of surface concentration values an order of magnitude lower than this, which is necessary for some of this work, can be performed.

It is important to note that, if acidic hydrogen atoms are deuterated (as in d_{34} -oleic acid, where the hydrogen bound to the carboxylic acid group is one of the 34 deuterated), then they can, depending on the level of acidity, undergo exchange with hydrogen in the NRW subphase. As only 8.8% of hydrogen atoms in NRW are deuterated, this will reduce the degree of deuteration of the species of interest slightly. For molecules in which a reasonable fraction of hydrogen atoms are acidic, this could introduce a significant problem. However, of all the species studied in this work, the highest fraction of hydrogen atoms that are at all acidic is the 1/34 or 3% for d_{34} -oleic acid. It was also established by Dluhy and Cornell in 1985⁴ that the carboxylic group of oleic acid remains protonated when spread as a monolayer at an air/water interface, which implies that any exchange is likely to be slow. The other notably acidic protons encountered in this work are located on the carboxylic acid groups of other fatty acids of similar chain lengths to oleic acid, and therefore are likely to behave in a similar manner with regards to proton exchange behaviour. Any exchange of acidic hydrogen atoms with NRW can therefore safely be ignored, as even total exchange would have a minor effect on results, and exchange is likely to be slow.

Figures 2.1 and 2.2 show the fatty acids and glycolipids studied in this work, in non-deuterated and deuterated forms, respectively. There is not an exact 1:1 correspondence between the two, as palmitoleic acid was only used as a non-deuterated component, and two deuterated forms of oleic acid were used. The deuteration of the acidic hydrogen was inconsistent across suppliers, so, for instance, d_{34} -oleic acid and d_{33} -oleic acid were both used. The difference between these two is considered slight enough that they are not considered separate compounds under study, and only one variant is displayed in Figure 2.2 in each relevant case.

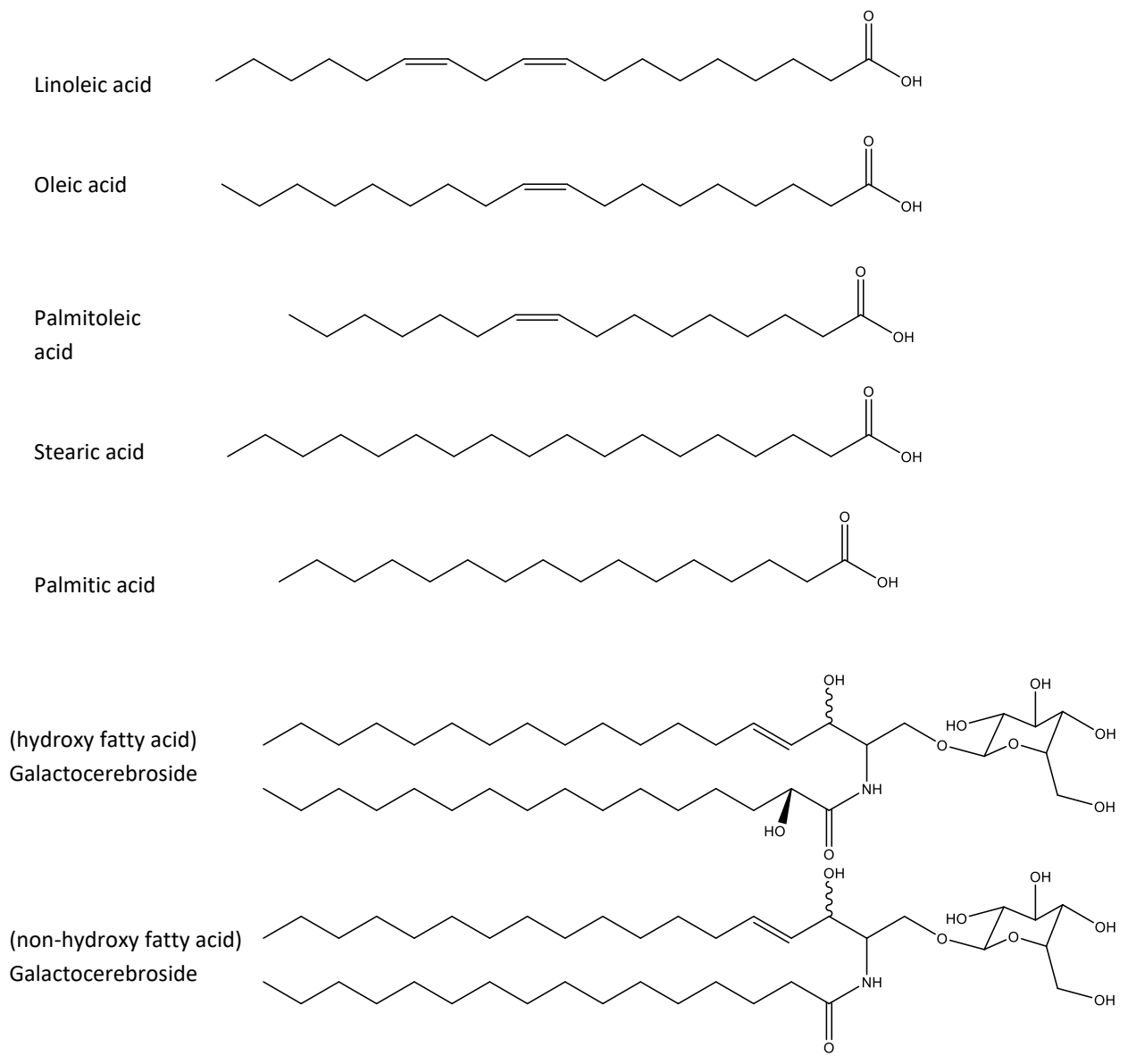


Figure 2.1 – Non-deuterated fatty acids and glycolipids.

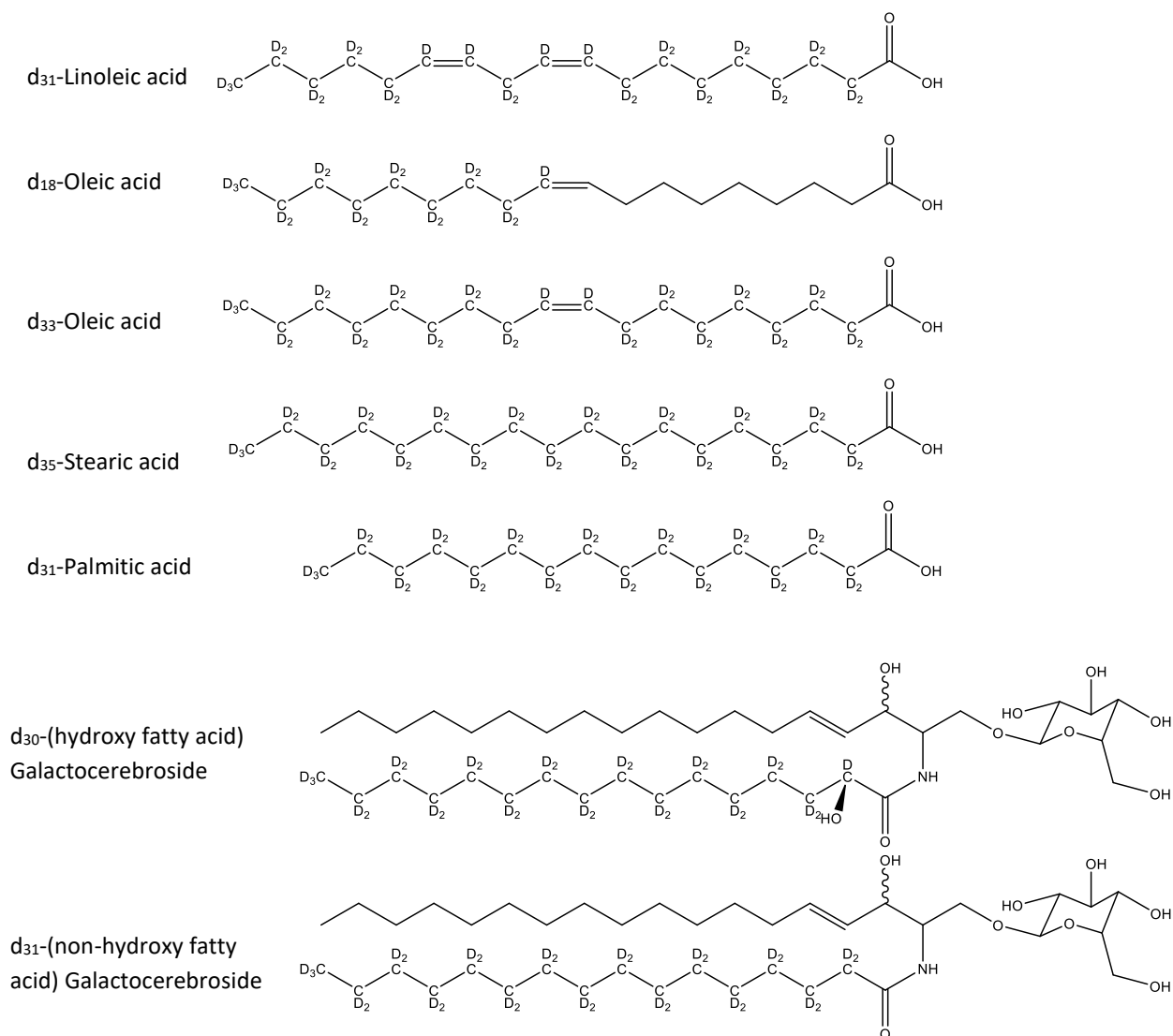


Figure 2.2 – Deuterated fatty acids and glycolipids.

2.1.5 – Selection of Q Range

Despite the reasonably high SLD values for these monolayers, they are thin enough ($\tau \approx 20 \text{ \AA}$) that Q_{crit} is below the Q threshold of the current generation of reflectometry instruments. The rapid fall-off (quartic dependency) of R on Q means that only the tail of the R vs Q curve is observable, with R values around 10^{-2} at $Q_{\text{min}} \approx 0.01 \text{ \AA}^{-1}$ and undetectable from a largely Q-independent background above $Q \approx 0.25 \text{ \AA}^{-1}$. This Q range is not accessible all at once and, depending on the requirements of the experiment in question, different Q ranges are measured.

For kinetic experiments, where the system is changing rapidly and so a high time resolution is required, a low Q range (approximately 0.01 to 0.1 \AA^{-1} is typical) is employed in order to achieve the highest possible flux at the detector (by measuring higher R regions of the R vs Q curve). When using INTER at ISIS, this allows for count times of around 20 seconds. For very fast kinetics, the higher flux of FIGARO at the ILL allows for count times as low as 5 seconds. This higher flux is accessible due to the continuous beam source, which can be shaped into long, closely spaced pulses using very relaxed chopper timings for this purpose. Such behaviour creates very high dQ/Q values of $\sim 10\%$. However, the rather featureless R vs Q curve produced by a very thin monolayer at an air/NRW interface is devoid of Kiessig fringes that require precise Q resolution, so this poor Q resolution is not as detrimental to the fitting as would be the case for more complex systems.

The weakness of measuring in such a low Q domain, however, is that no part of the Q range is dominated by Q-independent background scattering, and so, for very weakly reflective systems, it can be difficult to distinguish between signal and background. This means that measured air/NRW systems have to be used to inform the fixing of a Q-independent background scattering parameter in the fit. There is some natural drift in the background scattering over time, meaning that this is not always sufficient for measurement of very weakly reflective systems.

Some of this work has required precise measurement of systems in which the scattering signal is very close to the background, and measurement across this low Q range and fitting with a measured and fixed background parameter has not been found to be suitable. For these systems, in which the most important consideration is reliable measurement of very small signals and reliable discernment between background and signal, use of a higher θ experimental geometry and therefore a higher Q range (typically around 0.03 to 0.3 \AA^{-1}) is necessary. This Q range includes the point at which reflectivity from the system has subsided to be essentially nothing but background scattering, meaning that a Q-independent background parameter can be fitted to each individual measurement, allowing variation in background to be taken into account. The trade-off here is with flux at the detector, as higher Q regions of the spectrum that have significantly lower reflectivity and therefore higher count times (often 5 minutes or more for weakly reflective systems) are required to produce data of sufficient statistical quality for fitting. This means that this geometry is poorly suited to measuring kinetic parameters for fast reactions.

A data collection paradigm that came into effect at ISIS during the course of this work has provided new options for the manipulation of some of these trade-offs. Event Mode data collection involves making no up-front decision about the amount of time to count each frame. Instead, each experiment is collected as one long frame, which can then be sliced into frames of any desired length (including mixed lengths across an experiment) in the course of data processing. This removes the need to estimate beforehand how much count time is required to achieve sufficient statistical data quality for good fitting, and has allowed for much more precise use of high-Q data.

2.1.6 – Data Processing

The various normalisations and fitting processes described in sections 2.1.1 to 2.1.5 can be broken down into two distinct groups that are handled by two different software packages. The interpretation of raw neutron counts from detectors and monitors, normalisation to transmission runs, and slicing of Event Mode data into frames forms the first group of processes, the output of which is a series of R vs Q curves for each frame. The second process involves the fitting of model parameters to these R vs Q curves, and correcting for scaling and Q-independent background scattering.

For INTER data, a Python-based development and data visualisation environment, MantidPlot⁵, is used. The basic function that slices one frame out of an Event Mode dataset and processes it into an R vs Q is a facility standard, and wrappers have been written as part of this work⁶ that call that function iteratively with the appropriate parameters (which vary according with different θ setups) and export the R vs Q curves. For early INTER data collected before Event Mode was introduced, the slicing component is absent. For FIGARO data (for which Event Mode is unavailable as the system has not yet been introduced at the ILL), the relevant software package for the processing of neutron detector data into R vs Q curves is COSMOS, part of the LAMP analysis package⁶.

Once these R vs Q curves have been produced, a number of tools exist for fitting model parameters to the curves and correcting for scaling and Q-independent backgrounds (or fitting the same, as desired). For this work MOTOFIT² has been utilised. This package is written in the data analysis focused high-level

⁵ These are included in full in Appendix 1, along with functions written for other parts of this analysis.

language Igor and designed to run as an extension in the development and visualisation environment Igor Pro.

For all this work, fitting scale factor corrections is not possible because $Q_{crit} < Q_{min}$ always obtains. Instead, an R vs Q curve for an air/D₂O interface is fitted, with all model parameters held at values that are known for this system and only the scale factor allowed to float. This fitted scale factor is then fixed for all other fitting from the same experimental session.

Some of this work requires a similar process (with an air/NRW interface) to be run to obtain a Q-independent background parameter that is then fixed for other fitting for experiments run with the same batch of NRW subphase. However, some of this work uses R vs Q curves with a high enough Q_{max} that, across a sufficient Q range, only background reflectivity is measured. In these cases, the Q-independent background parameter can be fitted as part of the fitting procedure for the sample data itself, and does not need to be held constant at a value fitted to a separate air/NRW background measurement. This improves accuracy somewhat, as background scattering is not entirely constant.

Roughness parameters (one each for the two interfaces either side of the monolayer) are highly correlated with $\tau\rho$ for these systems and so cannot be fitted, but are instead assumed to be roughly equivalent to values fitted to an air/D₂O system.

When fitting τ and ρ parameters to a measured R vs Q dataset, τ and ρ turn out to be multiplicatively dependent variables, meaning that it is the value of $\tau\rho$, rather than the individual values of τ and ρ , which affect the fit. This means that, if an R vs Q curve is defined by a certain pair of τ and ρ parameters ($\tau = y$; $\rho = x$), then an identical curve will be defined by the parameters ($\tau = y/n$; $\rho = xn$). This is true for values of τ and ρ that are reasonably close to their fitted minimum, though unphysically low, high, or negative values for either parameter will break down this relation.

As a result of this, if τ is set to an arbitrary value within sensible bounds (the bounds will be set by the nature of the fitting algorithm: Negative or absurdly high values could cause the fit to fail), then ρ will be dependent on the chosen value of τ . If the fit is repeated with the value of τ n times higher, then all the fitted values of ρ will be scaled by $1/n$, leaving $\tau\rho$ completely unchanged. It would be equally mathematically viable, though somewhat physically vexing, to set ρ to an arbitrary yet vaguely realistic value and use τ as the fitted parameter. The values of $\tau\rho$ would be no different.

This multiplicative dependence means that it is really a $\tau\rho$ parameter, rather than a τ or ρ parameter, which is fitted by the minimisation algorithm. The fitting cannot distinguish between two model layers, one of which is twice as thick but half as dense as the other. Values of 20 Å are used for τ throughout this work, as that has been indicated to be approximately appropriate for these systems by earlier investigations^{3,7}, but it does not affect the fitted $\tau\rho$ values if this is not quite physically realistic.

Indeed, it does not actually affect the fitting if the slab-like monolayer model itself is not entirely physically realistic. Lu *et al.* demonstrate that the shape of the distribution of ρ in the z -direction is more reasonably described by a Gaussian function, but also demonstrate that this does not affect the derived $\tau\rho$ ¹.

This fitted parameter $\tau\rho$, which has units of inverse length, can be conceptualised as a 2D concentration of scattering length, analogous to ρ but for a surface, rather than bulk, concentration. This measured $\tau\rho$ parameter is related to the surface concentration (Γ) of a single species with a known scattering length by the following simple relation:

$$\Gamma = \frac{\tau\rho}{b}$$

Equation 2.10

This is appropriate if the experiment is following the evolution of a single-component film at the interface. However, when a reaction is occurring at the interface, any products that remain at the interface will also contribute to $\tau\rho$. As a first approximation, for the fatty acid and glycolipid systems studied in this work, $\tau\rho$ can be taken to be tracking the presence of deuterated species at the interface. This is because non-deuterated hydrocarbons have scattering lengths quite close to zero, as the negative scattering length of ^1H and the positive scattering length of carbon (C) mostly cancel each other out, whereas deuterated hydrocarbons have strongly positive scattering lengths. For most situations, the contribution of non-deuterated species can be ignored. This allows for the use of partially deuterated reactants in order to investigate the partitioning to the surface (or lack of it) for various reaction products.

Situations in which multiple species contribute significantly to $\tau\rho$ require more careful treatment. These systems can only be disentangled by making certain assumptions about the system. In these cases, $\tau\rho$ can be expressed as a function of multiple contributions thus:

$$\tau\rho = \sum_i \Gamma_i b_i$$

Equation 2.11

Disentangling the various contributions will, in many cases, not be possible, but an example of a situation in which it is possible, and which is used in this work, is one in which only one reactive component is present amongst any number of inert components, and in which products of the reaction with a significant scattering length can safely be assumed not to be present in significant quantities at the interface (as is often the case at least early in a reaction). A single scattering length parameter for the modelled unified unreactive components can be calculated from their scattering lengths and their total and individual surface coverages, which are assumed to be constant throughout the reaction in progress and calculated as follows:

$$b_{inert} = \sum_{i=1}^n \frac{b_i \Gamma_i}{\Gamma_{inert}}$$

Equation 2.12

The surface coverage of the reactive compound can then be calculated thus:

$$\Gamma_{reactive} = \frac{\rho\tau - \Gamma_{inert} b_{inert}}{b_{reactive}}$$

Equation 2.13

For more complex systems, explicit numerical modelling of the process must be carried out. Models that describe the kind of reactions studied in this work, and then calculate R vs Q curves across the course of the reactions that can be compared with experimental data, do exist (and exist for much more complex systems than a single monolayer reacting with a gas-phase oxidant). These models, namely KM-SUB⁸, K2-SUB⁹, and KM-GAP¹⁰, may be used in simplified forms to inform interpretation of some of the neutron reflectometry data collected in the course of this work. These models also take into account reflectivity contributions from surface-partitioned products, which allows use of the whole timeframe of a reaction for the calculation of kinetic parameters.

2.2 – Fourier Transform Infra-Red Reflection-Absorption Spectroscopy

2.2.1 – Vibrational Spectroscopy Basics

Infra-red (IR) spectroscopy is a long-established technique for qualitative and quantitative chemical analysis. The fundamental principle of IR spectroscopy is the absorbance of photons in the mid-IR spectral region (400 to 4000 cm^{-1}) by molecules with a matching resonant vibrational frequency and the subsequent excitation of the relevant vibrational mode to a more excited state. The vibrational modes which exhibit these resonant frequencies are generally covalent bonds (stretching modes) or combinations thereof (such as two-bond three-atom rocking modes). The fundamental absorbance wavenumber (ω) of a particular vibrational mode for a stretching mode is a function of the spring constant for the bond (k), the reduced mass (μ) of the system, and the speed of light in a vacuum ($c = 3 \times 10^8 \text{ m s}^{-1}$):

$$\omega = \frac{1}{2\pi c} \sqrt{\frac{k}{\mu}}$$

Equation 2.14

The reduced mass is a function of the individual masses of the atoms:

$$\mu = \frac{m_1 m_2}{m_1 + m_2}$$

Equation 2.15

This gives the characteristic wavenumber for the transition from the vibrational ground state ($v = 0$)^h to the first excited state ($v = 1$). Overtones, which are transitions from the ground state to higher excited states ($v > 1$), would be predicted by a simple harmonic oscillator approximation to be observed at integer multiples of the fundamental frequency. The simple harmonic approximation becomes less and less valid at more excited states, where a Morse potential, which more precisely describes the energy profile of a chemical bond with respect to internuclear distance, must be used instead. A Morse potential model predicts that overtone bands will be observed at lower wavenumbers than simple integer multiples of the fundamental wavenumber, with greater deviation from simple multiples as one moves further from the ground state. This is because the evenly-spaced energy levels of the simple harmonic approximation deviate further from the energy levels of a Morse potential with increasing energy, as Morse energy levels eventually converge to a limiting value (the energy necessary to break the bond).

However, these overtones are generally very weak due to the selection rule for IR absorbance, which only permits IR transitions with particular symmetry properties and requires a change in dipole moment for the transition to be allowed. The physical justification for the IR selection rule is complex and is of no concern here; the relevant outcome is that overtones are completely forbidden in the harmonic oscillator approximation, but are, in practice, weakly observed due to the departure of the more realistic Morse potential from the harmonic oscillator approximation¹¹.

Hot bands (transitions from states above the ground state, for instance from $v = 1$ to $v = 2$) would be predicted by a simple harmonic approximation to occur at the same wavenumber as the fundamental wavenumber or the overtone wavenumber that represents a step of the same number of energy levels. However, the gradually converging energy levels of the Morse potential, which is more realistic, predict that hot bands will be observed at slightly lower wavenumbers than the fundamental wavenumber or

^h For IR purposes, v is used to denote the vibrational energy state, rather than velocity (as in the TOF equations in section 2.1.1).

corresponding overtone. Fortunately, hot bands are rarely observed, as the population of excited states at or below room temperature is almost zero.

As a result of the weakness of overtones and hot bands, IR spectroscopy of the large molecules studied in this work is dominated by absorbance at the fundamental frequency.

2.2.2 – Absorbance of Hydrocarbon Tails

The IR spectroscopy carried out in this work focuses on one particular absorbance band – that associated with C–H stretching vibrations. This band is heavily represented in the fatty acid and glycolipid molecules studied in this work, which consist of either a carboxylic acid or sugar head group and one or more hydrocarbon tails. It is these tails, made up almost exclusively of $-\text{CH}_2-$ groups, which account for this absorbance.

This C–H absorbance is split into multiple absorbance bands. In order to understand this, it is necessary to conceptualise the vibrational transition not as being undergone by a single C–H bond, but by the entire $-\text{CH}_2-$ group. Strictly, vibrational transitions are undergone by the entire molecule, which has $3n-5$ vibrational modes, where n represents the number of atomsⁱ. This holds unless the molecule is linear, in which case it has one fewer vibrational mode and one more rotational mode; this is only a formal distinction as rotational and vibrational modes are both simply combinations of atomic movements classified by group theory. However, the vibrational modes that are relevant to IR spectroscopy generally apply to groups of three or four atoms within the molecule, so a functional group-based conceptualisation is appropriate¹².

C–H bonds within fatty acids and glycolipids can be classified as part of $=\text{CH}-$, $-\text{CH}_2-$, or $-\text{CH}_3$ functional groups. $=\text{CH}_2$ groups and triple-bonded groups are possible, but do not occur in any of the species studied in this work. For the large saturated or mono-unsaturated molecules studied in this work, $-\text{CH}_2-$ groups greatly outnumber $-\text{CH}_3$ groups (present only at tail termini) and $=\text{CH}-$ groups (present only on unsaturated tail groups and only accounting for two C–H bonds per mono-unsaturated tail). The practical result of this is that the dominant contribution to the C–H absorbance band is from $-\text{CH}_2-$ groups, $=\text{CH}-$ bands are too weak to be visible, and $-\text{CH}_3$ bands are not significantly differentiated from $-\text{CH}_2-$ bands due to their similar absorbance frequency and low abundance in the molecules under study.

The $-\text{CH}_2-$ absorbance, however, is split into two distinct bands. This is because there are two stretching vibrational modes associated with the group: symmetric and asymmetric. These two vibrational modes absorb at different enough frequencies to split the $-\text{CH}_2-$ absorbance peak in two. The change in dipole moment associated with the asymmetric stretching mode is larger, and this means that this band is stronger. This produces the two distinct $-\text{CH}_2-$ stretching peaks that are used in this work to measure the presence of fatty acids and glycolipids. The $-\text{CH}_3$ stretch is sometimes observable as a shoulder on the $-\text{CH}_2-$ asymmetric peak. In principle, each distinct $-\text{CH}_2-$ group on the molecule could be said to produce a separate peak, as each will absorb at a marginally different frequency due to its position relative to other functional groups on the molecule. In practice, this difference is small and manifests as a broadening, rather than splitting, of the peaks.

IR absorbance bands also exhibit a strong isotopic dependence, particularly for hydrogen. Equation 2.13 shows that the absorbance frequency depends on the reduced mass of the relevant atoms. Equation 2.14 shows how the reduced mass depends on the individual atomic masses. The atomic mass of deuterium is close to double that of protium. Carbon is many times heavier than either isotope of hydrogen, meaning that the denominator of the reduced mass fraction increases only slightly on the

ⁱ Rather than number concentration, as n represents in the earlier discussion of neutron reflectometry in section 2.1.

isotopic substitution of protium for deuterium, but the numerator doubles. This means that the reduced mass is nearly doubled by such an isotopic substitution.

This results in significantly different IR absorbance wavenumbers for deuterated versus non-deuterated hydrocarbon tails. $\text{-CH}_2\text{-}$ symmetric and asymmetric vibrational modes absorb at around 2850 and 2920 cm^{-1} respectively, whereas the corresponding $\text{-CD}_2\text{-}$ modes absorb at around 2100 and 2200 cm^{-1} . The $\text{-CD}_2\text{-}$ bands are also generally weaker than their corresponding $\text{-CH}_2\text{-}$ bands.

Carbon occurs naturally in ^{12}C and ^{13}C isotopes. The natural abundance of $\sim 1\%$ for ^{13}C , along with the relatively small effect on the reduced mass of this isotopic difference, means that the peaks are not observed to split at the levels of resolution used in this work. Rather, this is just another broadening effect.

The sensitivity of IR to C–H bonds provides a strong complement to the sensitivity to deuterium exhibited by neutron reflectometry. This allows for the study of monolayers made up of two components, one of which is deuterated and the other of which is not. The non-deuterated component will be invisible or near-invisible to neutron reflectometry due to the similarity of SLD between such components and air/NRW, meaning that the neutron reflectometry data will near-exclusively allow measurement of the deuterated component. Simultaneously, the FT-IRRAS data will allow for tracking of the non-deuterated component, as well as providing an additional supporting dataset for tracking the deuterated component if required. IR spectroscopy also provides the ability to study the molecular environment, as it is fundamentally a molecular technique, which ideally complements the nuclear focus of neutron reflectometry.

2.2.3 – Reflection-Absorption Geometry

Traditional IR experiments are performed in transmission geometry, in which the substance to be measured is spread upon or somehow incorporated within a substrate that is transparent to IR in the spectral regions of interest. Measuring monolayers at the air/water interface with such a configuration is not feasible, as water strongly absorbs IR radiation.

This problem was overcome in 1985 by Dluhy and Cornell, who demonstrated for the first time the measurement of monolayers at the air/water interface using reflection-absorption geometry⁴. The technique takes advantage of the fact that monolayer films at the air/water interface reflect around 6% of mid-IR radiation incident upon their surface from the air side¹³. Using an array of mirrors (one planar and one spherical) to direct and focus a beam of IR radiation on the interface, and another array of mirrors (one spherical and one parabolic) to return the reflected radiation to a parallel beam and refocus it onto a detector, a single beam spectrum of reflectance (R)^j as a function of wavenumber can be collected.

The measurement of this spectrum is performed using a white beam of mid-IR radiation, which is passed through a Michelson interferometer. The interferometer splits the beam into two beam paths, one of which is reflected off a stationary mirror, and the other off a moveable mirror, before recombining the two paths and passing the resultant combined beam on to a detector. The moveable mirror is then swept through a continuous range of positions with respect to the beam-splitter, and the intensity of radiation incident upon the detector is measured as a function of the difference in length between the two paths, producing an interferogram. The IR radiation will interfere constructively or destructively to various degrees with itself as a function of the relationship between the wavenumber of the radiation and the path length difference. As a result of this, performing a Fourier transform on the interferogram results in a spectrum of reflectance as a function of wavenumber.

^j Reflectance is the same concept as reflectivity (as discussed in the context of neutrons in section 2.1), but the term 'reflectance' is more common in IR spectroscopy.

This single beam reflectance spectrum must then be compared with a reference single beam reflectance spectrum for a clean air/water interface (R_0) in order to produce a reflectance-absorbance spectrum (RA) as a function of wavenumber for the monolayer:

$$RA(\omega) = -\log \frac{R(\omega)}{R_0(\omega)}$$

Equation 2.16

The absorbance bands for $-\text{CH}_2-$ and $-\text{CD}_2-$ stretches observed in this work have the unusual quality of being negative. That is, absorbance is actually lower at the characteristic absorbance wavenumber for the vibrational transition than in the reference spectrum, rather than higher, as would be expected from the basic picture of photons being absorbed by the molecule in order to facilitate the excitation of the vibrational mode in question. This peculiarity arises from the reflection-absorption geometry because of the low attenuation constant of the surface monolayer, which results in a suppressed imaginary component of its complex refractive index¹⁴ (the physics behind which is out of scope here). These negative absorbance bands were observed by Dluhy and Cornell in their pioneering experiment⁴ and had previously been observed on a metallic reflective substrate¹⁵.

The reflection-absorption geometry has been signified by a number of abbreviations and acronyms by different research groups, with no one candidate able to emerge as a clear favourite. RAIRS has been recommended by IUPAC¹⁶, but IRRAS is common in the literature^{13,17}. Incorporating the Fourier transform element to give FT-IRRAS is the preferred formalism for this work.

2.2.4 – Practical Considerations

Due to the weak signal all-round (which is a result of the fact that only ~6% of the incident beam is reflected by the interface), the thinness of the monolayer, and the low extinction coefficients of the large molecules studied in this work, a highly sensitive Hg-Cd-Te alloy (commonly referred to as MCT, from Mercury, Cadmium, Telluride) detector is required. This has to be kept cold using a regularly refreshed liquid nitrogen (N_2) reservoir.

The setup is very sensitive to the precise focusing of the incident beam on the interface, and the effective parallelisation and refocusing of the reflected beam onto the detector. The set of four moveable mirrors of various geometries (not counting the moveable mirror in the Michelson interferometer, which is electronically controlled as it has to be repeatedly swept throughout measurement), combined with the vertical position of the interface with respect to the mirror assembly and the position and rotation of the MCT detector and IR source (which cannot be relied upon to be sufficiently collimated for such an extended path length), gives the system a total of 19 practical degrees of freedom, many of which are coupled in unintuitive ways.

The complex nature of this setup and the ensuing difficulty of integrating it into many experimental configurations means that the technique is still not routine (except in the case of measurements of static systems in small quantities (monolayer areas of only a few tens of cm^2 in most cases) for which some standardised inserts for FT-IR spectrometers are available), and it generally falls to the individual researcher to adapt the method to their circumstances and deploy the relevant equipment in order to do so¹⁷. Performing this development task for the study of the reaction of monolayers with gas-phase oxidants as part of an *in situ* experiment with neutron reflectometry makes up a large part of this work, and is covered in detail in the method development chapter (Chapter 3).

Suppression of atmospheric interference is a significant challenge for FT-IRRAS experiments. CO_2 and H_2O in the atmosphere absorb strongly in the mid-IR region, and very slight changes in the concentration of these in the region through which the beam passes between R and R_0 measurements, such as those caused by breathing, will produce strong signals in the RA spectrum. This can be avoided

by placing the entire setup in a dry purged environment such as a flow of N₂. However, the presence of the water subphase means that this will still not fully eliminate H₂O from the atmosphere, and its concentration over the subphase may still be somewhat variable, especially as the IR beam can heat the surface¹⁸.

One solution to this is a dual-trough shuttle system developed by Flach *et al.* in 1994¹⁹, in which a subphase-only reference trough, from which R₀ can be measured, is moved in and out of the beam at regular intervals throughout measurement, allowing R and R₀ to be collected in near-identical humidity conditions, but this further increases the size and complexity of the setup and so may not be practical in all cases. Another method for suppression of all gas-phase interference is that of polarisation modulation (PM-FT-IRRAS or simply PM-IRRAS). This method involves fast modulation between p- and s-polarised IR beams and the calculation of a resultant spectrum via combination of the multiple spectra produced. The details of the calculations are of no concern here (see Blaudez *et al.*²⁰ and Buffeteau *et al.*²¹ for more information); the outcome is the suppression of signal from all randomly-oriented species at a particular wavenumber, and gradually decreasing efficiency of suppression with difference from this wavenumber. This suppresses gas-phase contributions but also suppresses contributions from randomly-oriented surface species, which makes the technique unsuitable for the measurement of surface species that do not exhibit a reasonable degree of order at the interface, including some studied in this work. The approach taken to atmospheric interference and humidity considerations in this work will be covered in the method development chapter (Chapter 3).

2.3 – Wilhelmy Plate Tensiometry

Wilhelmy plate tensiometry was used routinely for various experiments throughout this work, most of which were conducted off the neutron beamline, to characterise surface films and determine appropriate spreading volumes for the preparation of monolayer films for NR/FT-IRRAS experiments. It was also used to check that the behaviour of the films, particularly at low temperatures or on salt water subphases, was within expected bounds and that various assumptions made during the interpretation of data from NR/FT-IRRAS experiments remained valid across the range of conditions that were studied. This was integrated with Brewster angle microscopy measurements (discussed in section 2.4) and some FT-IRRAS experiments.

Wilhelmy plate tensiometry allows for the measurement of the surface tension (γ) of an air/water interface. For measurement of interfacial monolayers, the measurement of interest is surface pressure (Π)^k of the monolayer, which is the difference in surface tension between the clean interface (γ_0) and the interface bearing the monolayer thus:

$$\Pi = \gamma_0 - \gamma$$

Equation 2.17

This is generally calculated automatically by the measurement and control software, providing that it has previously been used to measure a clean interface to establish a zero point.

The measurement is performed by suspending a small thin object (a Wilhelmy plate) of a defined thickness (d) and width (w) above the interface and lowering it until it is partially submerged within the subphase and a contact meniscus has formed, then raising it until the bottom of the plate is roughly aligned with the undisturbed interface. The force (F) exerted by the meniscus on the plate is then measured by a tensiometer, and the surface tension is calculated as follows:

^k As mentioned in section 1.4, lower-case π is commonly used to denote surface pressure, but it is denoted with the upper-case letter Π here in order to avoid confusion with the mathematical constant π employed in Equation 2.19 and elsewhere.

$$\gamma = \frac{F}{(2w + 2d) \cos \theta}$$

Equation 2.18

For water subphases, the contact angle (θ)^l is generally assumed to be zero, which represents the limiting case of total wetting²². For the paper Wilhelmy plates commonly used, it is necessary to allow the system to equilibrate for some time in order to reach a state where this assumption is valid. This can largely be avoided by using a more expensive torched platinum rod in place of a paper Wilhelmy plate. The width and depth considerations relevant for the cuboidal plate are then replaced by a radius (r) dependency for the cylindrical rod:

$$\gamma = \frac{F}{(2\pi r) \cos \theta}$$

Equation 2.19

The measurement of interest for monolayer films at the air/water interface is generally that of the variation of Π as a function of surface area per molecule (A). This function is a Π - A isotherm^m, and contains significant information about the structure of the monolayer at various surface concentrations. Measurement of this isotherm is achieved using a Langmuir trough equipped with electronically controlled partial barriers and a Wilhelmy plate tensiometer. The control software calculates Π from a measured γ (and a measured reference γ_0) and records it as A is gradually varied by sweeping the barriers across the subphase and therefore compressing and expanding the interface under measurement as required.

2.4 – Brewster Angle Microscopy

Brewster angle microscopy (BAM) is a microscopy technique used to image thin films adsorbed at interfaces in a manner which reveals the density of material at the interface and some information about its packing and orientation. It is used in this work, in concert with Wilhelmy plate tensiometry, to study the structure of monolayer fatty acid and glycolipid films at air/water interfaces, particularly mixed films, and provide additional information for interpretation of neutron reflectometry and FT-IRRAS data that otherwise eludes simple explanation.

BAM takes advantage of the fact that, at a particular characteristic angle called the Brewster angle (θ_B), which is a function of the refractive indices (η)ⁿ of the subphases, p-polarised light passing from subphase 1 to subphase 2 is entirely transmitted, therefore reflectivity is zero²³. This angle can be calculated from the refractive indices thus:

$$\theta_B = \arctan \left(\frac{\eta_2}{\eta_1} \right)$$

Equation 2.20

In 1991, Hönig and Möbius²⁴ took advantage of this in order to produce microscopy images of surface monolayers of 1,2-bis(dimethylphosphino)ethane (DMPE) at an air/water interface. By illuminating the surface with p-polarised laser light at the air/water Brewster angle (53.15°), they acquired a reflected image that was sensitive only to the presence of DMPE at the interface, for which the Brewster angle is different, and which therefore was not being illuminated under Brewster angle conditions and exhibited

^l θ was used in section 1.2 to indicate potential temperature, whereas here it denotes contact angle. This is a similar concept to angle of incidence, which was denoted θ in section 2.1.

^m Commonly π - A instead of Π - A isotherm, but the latter is used here (see footnote k).

ⁿ Refractive index is commonly denoted by n instead of by η , but the latter is employed here in order to maintain consistency with section 2.1, which uses η in order to avoid confusion with number concentration (see footnote c).

some reflectivity. Building on this work, Cohen Stuart *et al.* developed a compact and economical BAM that could be constructed from standard optical components²⁵.

The combination of an illuminating laser and a microscope to focus detection on a small region of the interface means that BAM images tend to be bright enough to be collected real-time, and can even be recorded as video. Focusing trade-offs may have to be made, however, as the proximity of the objective lens to the interface at a non-normal angle means that the focal length is only correct at one particular line across the interface. For photos, the focus can be swept across a small range as the image is recorded in order to correct for this, but this is more problematic for video recording.

2.5 – Ultraviolet-Visible Spectroscopy

Ultraviolet-visible (UV-Vis) spectroscopy is a chemical analysis technique that works in an analogous way to IR spectroscopy, except that electronic, rather than vibrational, excitations are measured²⁶. UV-Vis spectroscopy is used in this work in a routine manner to calibrate the ozonisers that are used to produce O₃ for use as a gas-phase oxidant or a precursor to such oxidants. A simple transmission geometry is utilised, in which absorption (a)^o is calculated from the intensity of sample (I) and reference (I₀) beams of UV light at 254 nm (a characteristic absorbance wavelength for O₃). This is used to deduce the concentration (c) of O₃ produced by the ozoniser in various states via the Beer-Lambert law, which relates absorption to concentration, path length (l) and extinction coefficient (ε) thus:

$$a = -\log \frac{I}{I_0} = \epsilon cl$$

Equation 2.21

For this work, ε is taken as 1.13 × 10⁻¹⁷ cm⁻² from Daumont *et al.*²⁷.

Calibration proceeds by measuring the concentration at various settings on the ozoniser, and calibrating using a simple straight-line fitting. An example of a calibration plot is shown in Figure 2.3.

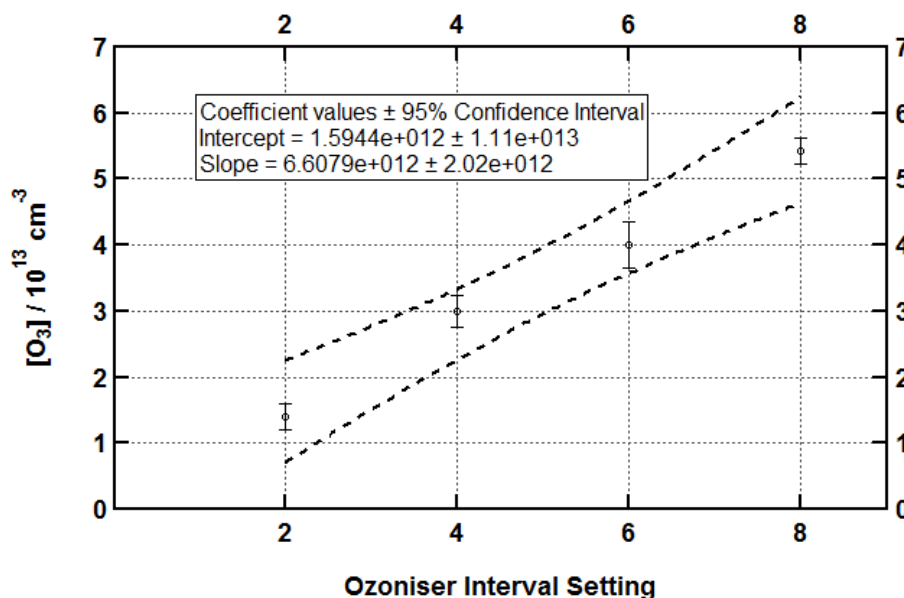


Figure 2.3 – Example of an ozoniser calibration plot.

^o Absorption is normally represented by an upper-case A, but the lower-case a is used here to avoid confusion with the usage of upper-case A to denote surface area throughout the rest of the thesis.

2.6 – Bibliography (Methods)

- 1 J. R. Lu, R. K. Thomas and J. Penfold, *Advances in Colloid and Interface Science*, 2000, **84**, 143–304.
- 2 A. Nelson, *Journal of Applied Crystallography*, 2006, **39**, 273–276.
- 3 F. Sebastiani, PhD Thesis, University of Reading, 2014.
- 4 R. A. Dluhy and D. G. Cornell, *The Journal of Physical Chemistry*, 1985, **89**, 3195–3197.
- 5 O. Arnold, J. C. Bilheux, J. M. Borreguero, A. Buts, S. I. Campbell, L. Chapon, M. Doucet, N. Draper, R. Ferraz Leal, M. A. Gigg, V. E. Lynch, A. Markvardsen, D. J. Mikkelsen, R. L. Mikkelsen, R. Miller, K. Palmen, P. Parker, G. Passos, T. G. Perring, P. F. Peterson, S. Ren, M. A. Reuter, A. T. Savici, J. W. Taylor, R. J. Taylor, R. Tolchenov, W. Zhou and J. Zikovsky, *Nuclear Instruments and Methods in Physics Research Section A: Accelerators, Spectrometers, Detectors and Associated Equipment*, 2014, **764**, 156–166.
- 6 D. Richard, M. Ferrand and G. J. Kearley, *Journal of Neutron Research*, 1996, **4**, 33–39.
- 7 C. Pfrang, F. Sebastiani, C. O. M. Lucas, M. D. King, I. D. Hoare, D. Chang and R. A. Campbell, *Physical Chemistry Chemical Physics*, 2014, **16**, 13220–13228.
- 8 M. Shiraiwa, C. Pfrang and U. Pöschl, *Atmospheric Chemistry and Physics*, 2010, **10**, 3673–3691.
- 9 C. Pfrang, M. Shiraiwa and U. Pöschl, *Atmospheric Chemistry and Physics*, 2010, **10**, 4537–4557.
- 10 M. Shiraiwa, C. Pfrang, T. Koop and U. Pöschl, *Atmospheric Chemistry and Physics*, 2012, **12**, 2777–2794.
- 11 S. Califano, *Vibrational States*, Wiley, Hoboken, 1976.
- 12 P. Atkins, *Elements of Physical Chemistry Fifth Edition*, Oxford University Press, Oxford, 2009.
- 13 R. Mendelsohn, G. Mao and C. R. Flach, *Biochimica et Biophysica Acta*, 2010, **1798**, 788–800.
- 14 J. D. E. McIntyre, *Advances in Electrochemistry and Electrochemical Engineering*, 1973, **9**, 61–166.
- 15 D. L. Allara, A. Baca and C. A. Pryde, *Macromolecules*, 1978, **11**, 1215–1220.
- 16 P. Hollins, in *Encyclopedia of Analytical Chemistry: Applications, Theory, and Instrumentation*, ed. R. A. Meyers, Wiley, Hoboken, 2000, DOI: 10.1002/9780470027318.a5605.
- 17 R. Mendelsohn and C. R. Flach, in *Handbook of Vibrational Spectroscopy*, ed. P. Griffiths and J. M. Chalmers, Wiley, Hoboken, 2006, pp. 1028–1041.
- 18 H. Sakai and J. Umemura, *Langmuir*, 1997, **13**, 502–505.
- 19 C. R. Flach, J. W. Brauner, J. W. Taylor, R. C. Baldwin and R. Mendelsohn, *Biophysical Journal*, 1994, **67**, 402–410.
- 20 D. Blaudez, T. Buffeteau, J. C. Cornut, B. Desbat, N. Escafre, M. Pezolet and J. M. Turllet, *Thin Solid Films*, 1994, **242**, 146–150.
- 21 T. Buffeteau, B. Desbat and J. M. Turllet, *Applied Spectroscopy*, 1991, **45**, 380–389.
- 22 H. J. Butt, K. Graf and M. Kappl, *Physics and Chemistry of Interfaces*, Wiley, Hoboken, 2006.

- 23 E. Hecht, *Optics, 4th Edition*, Addison-Wesley, New York, 2002.
- 24 D. Hoenig and D. Moebius, *The Journal of Physical Chemistry*, 1991, **95**, 4590–4592.
- 25 M. A. Cohen Stuart, R. A. J. Wegh, J. M. Kroon and E. J. R. Sudhölter, *Langmuir*, 1996, **12**, 2863–2865.
- 26 D. A. Skoog, S. R. Crouch and F. J. Holler, *Principles of Instrumental Analysis*, Thomson Brooks/Cole, Belmont, 2007.
- 27 D. Daumont, J. Brion, J. Charbonnier and J. Malicet, *Journal of Atmospheric Chemistry*, 1992, **15**, 135–155.

Chapter 3 – Method Development

3.1 – Introduction and *RSC Advances* Paper

A large part of the work undertaken throughout this PhD project consisted in the design, manufacture, and testing of the bespoke reaction and analysis chamber. The early period of development on this chamber was reported in a technical paper published in *RSC Advances* in 2017. The paper forms the bulk of this method development chapter.

It is important to note that, unlike the papers presented in Chapters 4 and 5, the text of this paper was not authored by me. This introduction is intended to also serve as a declaration of my contribution to the work that is described in the paper.

The initial idea for the combination of neutron reflectometry and Fourier transform infra-red reflection-absorption spectroscopy (NR/FT-IRRAS) was conceived by Dr Maximilian WA Skoda (the paper author and principal beamline scientist at the INTER white beam reflectometry instrument at ISIS) and Dr Christian Pfrang (the research programme leader). Drs Skoda and Pfrang developed an early prototype of the reaction chamber by modifying an example of the standardised reflectometry trough chamber used at ISIS for air/water interface experiments and making some preliminary measurements on INTER (experiment RB 1510605). Armed with proof of concept, and with another period of beamline access on INTER already granted (experiment RB 1520459) they undertook to take on a PhD student (me) in order to develop the concept further and put it to use as a tool for studying oxidation reactions at the air/water interface.

Experience from experiment RB 1520459 on INTER and offline testing and experimentation with the original prototype eventually led to the development of the reaction and analysis chamber, plus the array of adjustable mirrors, described in the *RSC Advances* paper. The designing of the chamber was performed by Dr Skoda, Jacob Simms of the ISIS workshop, and me, based on information and ideas gleaned from my experimentation with the prototype and decisions as to what major changes needed to be made in order to increase the quality of the IR spectroscopy data, combined with Dr Skoda's and Mr Simms's extensive existing experience with designing and deploying bespoke analysis solutions for neutron science applications. The data presented in the *RSC Advances* paper as case studies of the technique in action was collected during experiment RB 1520459 by Dr Skoda, Dr Pfrang, and me, with additional preparatory support from Dr Kunal Rastogi. The processing of the data was carried out by Dr Skoda and me. The interpretation of the mixed layer data in section 3.3 of the paper was based on an idea generated by Dr Skoda. The Brewster angle microscopy images in Figure 5 of the paper were obtained by Dr Federica Sebastiani during her work with Dr Pfrang and Dr Richard Campbell at the ILL in Grenoble.

What follows is the *RSC Advances* paper in its entirety. The introduction briefly covers some of the ground already covered in the preceding methods chapter (Chapter 2); the rest of the paper is focused on describing the precise details of the method as far as it had been developed at the time of publication, and briefly touches on some case study data, some of which will be revisited in later results chapters (Chapters 4 to 7). After the publication of this paper, I took more firm responsibility for the ongoing development of the experimental setup, and worked closely with the ISIS workshop and design teams in order to develop several later iterations. These iterations are described in the rest of this method development chapter. The reaction and analysis chamber as described in the *RSC Advances* paper was used for experiment RB 1610500 on INTER at ISIS.

At the time of this paper's publication, I was using the surname 'Thomas'.

Cite this: *RSC Adv.*, 2017, 7, 34208

Simultaneous neutron reflectometry and infrared reflection absorption spectroscopy (IRRAS) study of mixed monolayer reactions at the air–water interface†

 Maximilian W. A. Skoda,¹ Benjamin Thomas,¹ Matthew Hagreen,² Federica Sebastiani¹ and Christian Pfrang¹

The simultaneous application of neutron reflectometry (NR) and infrared reflection absorption spectroscopy (IRRAS) to the study of the oxidation kinetics of organic monolayers at the air–water interface is described for the first time. This advance was possible thanks to the development of a new sample environment that includes a gas-delivery system and is compatible with *in situ* application of the two techniques within the constraints of short-term neutron beam-line access. We studied the oxidation of monolayers of the mono-molecular film palmitoleic acid and of a binary mixture of oleic (OA) and stearic (SA) acids by gas-phase ozone. We contrast the two highly complementary techniques and demonstrate that IRRAS provides key additional insight into the alignment of surfactant molecules at the air–water interface. We highlight the potential of the more economical and widely available IRRAS technique to complement NR studies. We also found an apparent increase of the NR signal upon oxidation of a mixed SA/OA monolayer, as well as evidence of slow intensity fluctuations of the SA-generated IRRAS signal. We demonstrate how simultaneous NR-IRRAS substantially enhances future studies of increasingly complex surfactant mixtures and their atmospheric surface reactions.

Received 1st May 2017
Accepted 23rd June 2017

DOI: 10.1039/c7ra04900e

rsc.li/rsc-advances

1 Introduction

Organic monolayers at the air–water interface serve as model systems for a variety of natural and artificial surface films.^{1,2} Surfactant monolayers are relevant to a wide range of practical systems and processes, including detergency, paint manufacture, corrosion control, and foaming/de-foaming applications.³ In recent years, awareness has grown of potential roles for surfactants and long chain carboxylic acids in atmospheric aerosol.^{4–7} Surfactants in the atmosphere can originate from the sea-surface microlayer or can be associated with biomass burning and other combustion processes. Atmospheric aerosols in turn are of great interest, since they influence cloud formation and earth's global radiation budget. Although it is known that aerosols contain a mix of organic and inorganic material, the exact composition of aerosol particles and the partitioning of surfactants, for instance within the aerosol and on its surface,

is not well established. Even less well understood is the effect of oxidative processes initiated by nitrate radicals (NO₃), hydroxyl radicals (OH), and ozone, (O₃) on surfactant composition.^{4,8–10} Our interest lies in understanding the kinetics of such processes, as well as in identifying the fate of the reaction products. A common and powerful technique for studying such reactions at the air–water interface is neutron reflectometry (NR).¹¹ This non-destructive method enables the absolute determination of the adsorbed amount of a certain molecular species at the interface. Furthermore, by selective isotopic exchange of hydrogen atoms by deuterium it is possible to highlight one species in a mixture, or indeed to determine the fate of reaction products by deuterating only one part of a molecule. This approach has been successfully used by our group and others.^{12–14} With NR alone however, it is not possible to quantify the absolute adsorbed amount of each surfactant in a mixed monolayer consisting of two or more different species. Recent work by our group combined NR with ellipsometry off-line (Sebastiani *et al.*, 2015).¹⁵ However, a method linked to NR on-line would have obvious advantages such as simultaneous observations on a single system without the need for assumptions about reproducibility of off- and on-line conditions/systems. One way of achieving this is to use a different surface-sensitive technique, such as Fourier Transform Infrared Reflection Absorption Spectroscopy (FT-IRRAS, or

¹ISIS Pulsed Neutron and Muon Source, Science and Technology Facilities Council, Rutherford Appleton Laboratory, Harwell, Oxfordshire OX11 0QX, UK. E-mail: maximilian.skoda@stfc.ac.uk

²Department of Chemistry, University of Reading, P.O. Box 224, RG6 6AD, Reading, UK. E-mail: c.pfrang@reading.ac.uk

† Electronic supplementary information (ESI) available. See DOI: 10.1039/c7ra04900e

‡ Current address: CR Competence AB, P.O. Box 124, 22100 Lund, Sweden.



IRRAS). Voss *et al.* have demonstrated the use of sum frequency generation spectroscopy and IRRAS to observe the oxidation of oleic acid monolayers on water.¹⁶ A further advantage of IRRAS is its potential to show changes – evidenced by peak shifts – in the molecular environment during the oxidation process. These changes could be caused by reorganisation of the monolayer, changing surface pressure, level of hydration or cleavage of bonds. In order to obtain comprehensive information about the desorption behaviour of mixed, multi-component surfactant monolayers, we employed these two complementary techniques in parallel. An earlier set-up, using Attenuated Total Reflection (ATR) geometry, was deployed at the BioRef instrument at the Helmholtz-Zentrum Berlin (HZB).¹⁷ Due to the vertical sample geometry and space constraints of this set-up, it is only possible to measure solid(–liquid) samples. Furthermore, the accessible mid-IR region is restricted to above 1400 cm⁻¹ due to absorption by the silicon substrate. In contrast, we developed a set-up allowing, for the first time, measurements on monolayers at the air–water interface in IRRAS geometry in a fully controlled gas-phase environment above the Langmuir trough allowing observation of complex reactions at the air–water interface with these two techniques simultaneously. The accessible mid-IR range is 4000–900 cm⁻¹. By exploiting isotopic substitution (*i.e.* selective deuteration), we were able to obtain structural information from NR, as well as molecular level information about both deuterated and non-deuterated monolayer components at the same time. While NR provides accurate information about the surface excess and to some extent about changes in the layer thickness, IRRAS is able to record changes in the molecular environment within the monolayer (*via* shift in the characteristic absorption bands of the respective species), as well as detecting the presence of reaction products at the interface. This is especially important when studying mixed monolayers, where one of the components is not deuterated and therefore a determination of the surface excess from NR is not possible due to low contrast. Our set-up has the potential to be used for a broad range of monolayer or thin film systems, including protein adsorption in complex environments,¹⁸ polyelectrolyte/surfactant systems¹⁹ and many others. In this article we present two case studies in order to illustrate the capabilities of our set-up and to outline its key advantages.

2 Materials and methods

2.1 Materials

Partially deuterated (d₁₄; the alkyl chain between double bond and carboxylic acid group is deuterated) palmitoleic acid (dPOA) was provided by the Oxford Deuteration Facility. Deuterated stearic acid (dSA, product no. 448249), deuterated oleic acid (dOA, product no. 683582), deuterated palmitic acid (dPA, product no. 366897), stearic acid (hSA, product no. 366897) and oleic acid (hOA, product no. O1008) were purchased from Sigma-Aldrich. All fatty acids were dissolved in chloroform to produce spreading solutions with the following concentrations: hSA – 1.12 mg mL⁻¹, dOA – 1.18 mg mL⁻¹, dPOA – 1.85 mg mL⁻¹, dSA – 1.5 mg mL⁻¹. The sub-phase was a mixture of 8.1% by volume D₂O (Sigma-Aldrich 99.9 atom% D) in pure H₂O

(generated using a Millipore purification unit, 18.2 MΩ cm), known as air contrast matched water (ACMW). Chloroform (Sigma-Aldrich, >99.8%) and O₂ (Air Liquide, France, >99.9%) were used as supplied.

2.2 Gas set-up

Ozone, O₃, was produced by flowing pure O₂ through a commercial ozoniser (UVP Pen-Ray continuous flow generator, UK). The O₃ concentration was regulated by changing the exposure to the UV lamp. A flow of O₃ in O₂ was then admitted to the reaction chamber and the organic monolayer was oxidised at a rate that was determined by the O₃ concentration. The flow rate of O₂ was 1.2 L min⁻¹, leading to a range of [O₃]_v from (3.6 ± 0.3) × 10¹⁵ cm⁻³ to (9.6 ± 0.6) × 10¹⁵ cm⁻³. Measurements of O₃ absorption at 253.7 nm were carried out using UV-visible spectroscopy to establish the volume concentration, [O₃]_v (in molecule per cm³), and its uncertainty. The surface concentration, [O₃]_s (in molecule per cm²), of ozone that dissolves into the organic layer at the air–water interface is calculated from [O₃]_v, assuming that the surface concentration is constant in time and is equal to Henry's law solubility following the approach of Smith *et al.*²⁰

2.3 Neutron reflectometry

Specular neutron reflectometry (NR) measurements were carried out using the white beam INTER reflectometer at the Rutherford Appleton Laboratory (Oxfordshire, UK), using neutron wavelengths from 2.0 to 17.0 Å. The reflected intensity was measured at an incident angle of 0.8° (using a non-polarising supermirror at 0.75°) as a function of the momentum transfer, $q = (4\pi \sin \theta)/\lambda$, where λ is wavelength and θ is the incident angle. Data were collected at a resolution ($\Delta q/q$) of 7%, yielding a total illuminated length of 165 mm. The width of the beam was set to 50 mm in order to avoid meniscus effects. Time-resolved measurements were acquired over minutes and up to several hours with a time resolution of 20 s. The sample stage was equipped with passive and active anti-vibration control. The reaction chamber was mounted on the sample stage and interfaced with the gas setup. The PTFE trough was filled with 90 mL of ACMW. Monolayers were spread using 20–40 μL of the spreading solutions in chloroform, leaving a monolayer of the dissolved species after evaporation of the solvent. Data were recorded for a few minutes before O₃ was admitted into the chamber. The air–liquid interface was aligned with respect to the neutron beam using a “Keyence” laser displacement sensor (model no. LK-G402), which was coupled into the sample chamber *via* a quartz window to allow automated height adjustment during the measurements. NR measures the reflected intensity as a function of the momentum transfer vector q . For a monolayer at the air–ACMW interface the reflected intensity (or reflectivity) R can be expressed as:

$$R \cong \frac{16\pi^2}{q^4} 4b^2 n^2 \sin^2\left(\frac{qd}{2}\right), \quad (1)$$

where b is the scattering length, in Å, n is the number density, in Å³, d is the thickness of the layer in Å, and $bn = \rho$ is the



scattering length density in \AA^{-2} .⁴⁴ Due to the use of ACMW, the reflectivity data do not show a critical edge and the neutrons are only sensitive to the surface monolayer. The monolayer is too thin to generate any Kiessig oscillations in the observable q -range. Using a single layer model fit, the product of ρ and d was determined for each kinetic measurement. Once ρd was determined the surface excess, Γ , was calculated by:

$$\Gamma = \frac{1}{\text{APM}} = \frac{\rho d}{b}, \quad (2)$$

where APM is the area per molecule. Although the individual values for monolayer thickness and density are correlated, their product can be determined with high confidence, as it is not very sensitive to specific model assumptions. By changing the thickness or density of the film within reasonable boundaries, the effect on the value of the surface excess was assessed and resulted in an uncertainty of <1% monolayer coverage.

2.4 *In situ* infrared reflection absorption spectroscopy

The *in situ* spectra were recorded with a Thermo Scientific Nicolet iS50 FT-IR Spectrometer in the spectral range $900\text{--}4000\text{ cm}^{-1}$ at a spectral resolution of 4 cm^{-1} , using a liquid-nitrogen-cooled MCT (Mercury-Cadmium-Telluride) detector. The acquisition time was 5 min (1024 co-added spectra and an optical velocity of 1.8988) unless otherwise stated. An external infra-red beam was obtained by using the right-hand-side custom port. The infra-red light's optical path through the reaction chamber is outlined in Fig. 1a. All external optical components, as well as the reaction chamber, were mounted on a $600\text{ mm} \times 600\text{ mm}$ optical breadboard (ThorLabs). This way, the entire set-up could be pre-aligned prior to the NR experiment, thus substantially reducing on-beam set-up time. The collimated light from the spectrometer's right-hand-side port was deflected up by using a 45° flat gold coated mirror ($10\text{ cm} \times 15\text{ cm}$), which could be adjusted along the IR beam path making it possible to align its reflection with the first spherical mirror. Two adjustable, symmetrically positioned spherical mirrors with focal length $f = 150\text{ mm}$ (protected gold, Edmund Optics) created a focal point on the liquid surface. Both spherical mirrors were mounted on gimbal mounts allowing fine adjustment. These were in turn located on a set of custom-made goniometer stages, which allowed each mirror to be individually rotated around the focal point. A final gold coated 90° parabolic mirror with an effective focal length of 101.6 mm (Edmund Optics) focused the light into the external MCT detector, which was mounted on a linear stage and a rotating collar to allow fine alignment. The parabolic mirror was also mounted on a linear stage for alignment with the second spherical mirror, and could also be rotated to allow fine control of the focal point relative to the MCT detector. The incident angle of the IR beam on the water surface was chosen to be 48° (it could be varied from 42° to 55°). This angle was found to yield the best signal-to-noise ratio. This is close to the Brewster angle (53°) and similar to angles reported elsewhere.²¹ Immediately before each measurement, a background spectrum of at least 1024 co-added spectra was acquired from a bare water surface. These

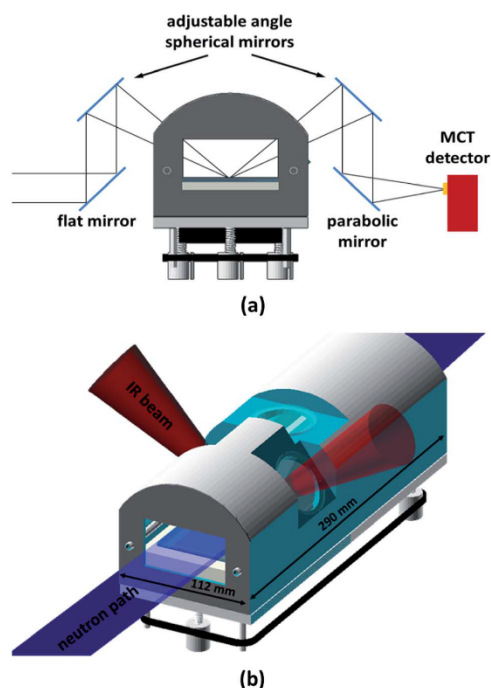


Fig. 1 (a) Optical path for the infra-red beam obtained from the right-hand-side port of the iS50 spectrometer. The beam was focused on the air-liquid interface using $3''$ gold coated spherical mirrors with a focal length of 150 mm . The incident angle of the IR beam with respect to the surface normal was chosen to be 48° , but could be varied between 42° and 55° . (b) Sketch of reaction chamber with neutron and IR beam paths indicated.

background spectra were used to normalise the sample spectra. The spectrometer, with a footprint of approximately $600\text{ mm} \times 600\text{ mm}$, was mounted on a 2.5 m long structural rail (X95, ThorLabs) directly attached to the INTER sample position in such a way that the spectrometer and optics set-up could be moved as a whole in order to fine-adjust the trough position with respect to the neutron beam without disturbing the alignment of the spectrometer with respect to the optics, MCT detector, and reaction chamber.

2.5 Reaction chamber design

A purpose-built gas flow cell was designed for studying oxidation reactions in mixed monolayers (Fig. 1b). The flow cell with a volume of approximately 1.5 L accommodates a liquid trough with inner dimensions of $238\text{ mm} \times 70\text{ mm}$ and provides two CaF_2 windows (CrysTran) of 1.5 mm thickness to allow ingress and egress of the IR light. The clear aperture of these windows is 45 mm . The windows are mounted at an angle of 48° with respect to the vertical, to enable normal or near-normal incidence for the IR beam in an angular range of 42 to 55° . A third



circular quartz window with a clear aperture of 50 mm is mounted above the centre of the liquid trough to allow the height laser to monitor the liquid surface. This window is tilted by 5° from the horizontal in order to avoid a secondary reflection into the height laser.

The neutron beam enters and exits the chamber through rectangular quartz windows (50 mm × 68 mm) at either end of the reaction chamber. The main requirements for the reaction chamber were dictated by fitting the NR and FTIR beam geometries, minimising the chamber volume for rapid gas-mixing, and ensuring good flow characteristics by avoiding dead volumes. As a compromise between NR signal (illuminated area) and chamber volume, the outer dimensions were chosen to be 290 mm × 112 mm. To allow gas flow through the chamber, four push-fit-style bulkhead connectors are used, accepting 6 mm diameter PTFE tubing. Gas is admitted to the chamber by inserting an end-capped PTFE tube with 2 mm diameter holes drilled at 1 cm intervals into one of the push fit connectors, as described in Sebastiani *et al.*¹⁵ This design provides optimised homogenous flow and gas diffusion. The liquid trough is supported at three kinematic mounting points; the supporting adjustable screws can be synchronously adjusted from the outside using a belt drive, allowing for fine adjustment of the vertical location of the air-water interface within the gas-flow cell. This adjustment capability allows the maximisation of the FTIR signal independently of the alignment of the interface with respect to the neutron beam.

3 Results and discussion

3.1 Performance of the external IRRAS set-up

In order to assess the performance of the set-up, a representative spectrum containing both CH and CD absorption bands was baseline-corrected and the signal-to-noise ratio (SNR) was calculated as follows: first, the amplitude of the strongest and weakest band was determined (Fig. 2); then, by analysing a region without absorption bands (3415–3019 cm⁻¹ – not shown here) the RMS noise was determined and compared with the signal from the reference spectrum. The resulting SNR values were 30.6 and 17.1 for CH and CD bands, respectively. Since the spectrum above arose from a mixture of perdeuterated palmitic acid and hydrogenous oleic acid (1 : 1 mixing ratio), for some single component measurements the SNR is better than the values quoted above. When using saturated compounds, such as stearic acid or lipids, which form tightly packed, well oriented monolayers, the obtained signal-to-noise is further improved, and count times of 30 s (rather than several minutes for unsaturated components) are achievable.

3.2 Single-component monolayers

Partially deuterated POA. In order to determine the sensitivity of our set-up, a single component monolayer consisting of partially deuterated (d₁₄) palmitoleic acid (15 μL spreading solution) was oxidised *in situ* and the reaction followed both with 20 s time resolution NR scans and 5 min time resolution

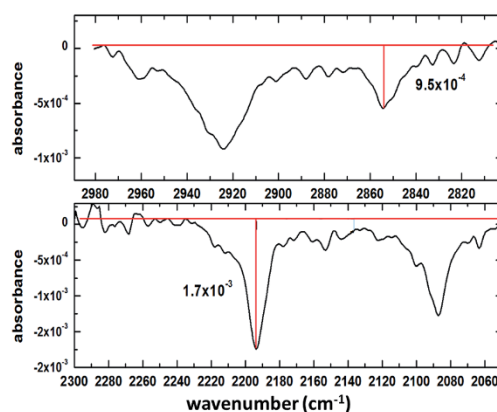


Fig. 2 Mixed monolayer of 1 : 1 deuterated palmitic acid and hydrogenous oleic acid: determination of the peak heights of the weakest (CH stretch of oleic acid, top) the strongest (CD stretch of palmitic acid, bottom) absorption bands.

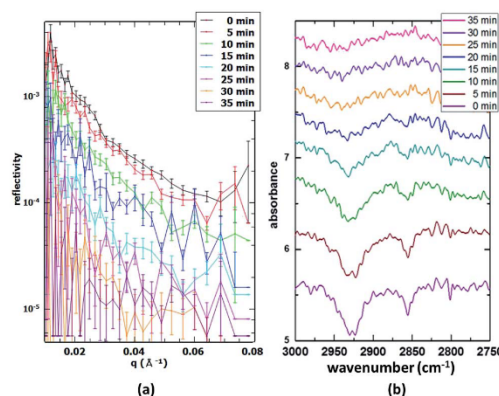


Fig. 3 (a) Time-resolved NR data (30 s acquisition time in 5 min intervals) during the oxidation of a partially deuterated palmitoleic acid monolayer; (b) simultaneous *in situ* IRRAS data (5 min acquisition time) obtained from the same monolayer.

IRRAS scans. Fig. 3 illustrates the comparison of the simultaneous NR and IRRAS data obtained. The much longer IRRAS acquisition time was necessary due to the comparatively low signal-to-noise caused by the disordered nature of the unsaturated fatty acid monolayer. These results also denote to some extent the sensitivity limit, as saturated fatty acids or lipids form well-ordered monolayers which generally lead to better signal-to-noise ratios than unsaturated compounds such as this species. The stability of the monolayer was assessed by monitoring the IRRAS and NR signals over several hours (data not shown). The slight decay in surface coverage can then be



accounted for, leading to a precise determination of the coverage during the oxidation process.

3.3 Two-component monolayers

Stearic acid/deuterated oleic acid. The main strength of the presented method lies in the ability to follow the desorption of multiple components in mixed monolayers simultaneously in real time. For this purpose, one of the components is deuterated, while the other is not. This means that the NR signal will arise almost solely from the surface excess of the deuterated species, while the IRRAS signal will contain both CD and CH absorption bands and therefore will provide information for both species. An example of a mixed stearic acid and deuterated oleic acid system (1 : 1 mixing ratio) is presented in Fig. 4. The mixed monolayer was spread using 26 μL of a 1 : 1 mixture of the two spreading solutions and was oxidised using an O_3 concentration of $1.2 \times 10^{13} \text{ cm}^{-3}$. The reaction was followed both with 20 s time resolution NR scans and 5 min time resolution IRRAS scans. The NR data show a fast drop in intensity, indicating the removal of dOA from the interface. In parallel, the FTIR spectra show the weakening of CD bands ($2000\text{--}2200 \text{ cm}^{-1}$), while the CH bands (originating from the hSA) maintain a constant intensity; however, complementary runs with a lower proportion of unsaturated surfactants (a better mimic for atmospheric aerosol composition) showed disappearance of CH bands suggesting an orientation dependent IR signal loss (data not shown). The difference in peak shape and intensity between CH and CD bands has several causes. Firstly, the saturated SA tends to form domains or islands due to strong van-der-Waals interactions of the alkane chains (see Brewster-Angle Microscopy (BAM) images obtained for the mixture of hSA and hOA in Fig. 5; the pressure-area isotherm for this mixture is given in the ESI†). These BAM images clearly illustrate the immiscibility of the two components recorded at three

Open Access Article. Published on 07 July 2017. Downloaded on 8/20/2019 10:53:06 AM.
This article is licensed under a Creative Commons Attribution 3.0 Unported Licence.

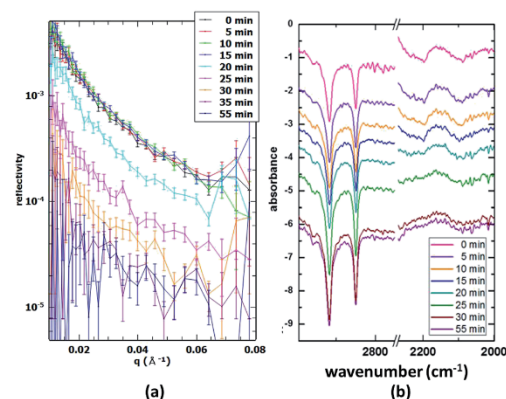


Fig. 4 Time-resolved NR and IRRAS data during the oxidation of a 1 : 1 mixed monolayer of stearic acid and deuterated oleic acid. Both CH and CD stretching vibrations are visible at about $2850\text{--}2920$ and $2000\text{--}2200 \text{ cm}^{-1}$, respectively.

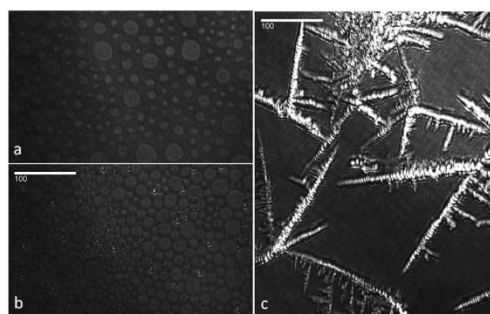


Fig. 5 BAM images of the hOA-hSA monolayer at $25 \text{ }^\circ\text{C}$ on a pure water sub-phase recorded at three pressures: (a) 0 mN m^{-1} : the layer shows circular domains; (b) 32 mN m^{-1} : collapsing points start to be visible between the circular domains; (c) 40 mN m^{-1} : the layer is collapsed and domains became rod-like. The white bar corresponds to $100 \mu\text{m}$.

different surface pressures. Fig. 5a shows the presence of separated domains. Just before the pressure plateau (32 mN m^{-1} ; see Fig. S.1†), condensation nuclei appear while the circular domains are still visible (Fig. 5b). At the maximum pressure, 40 mN m^{-1} , rod-like domains are distinguishable from a uniform background (Fig. 5c), and the morphology of the collapsed structure is different from the previous morphologies. Within these domains the chains are well aligned and this results in sharp CH bands. The unsaturated OA chains, on the other hand, are disordered and the resulting CD bands are broad and weak by comparison. As can be seen in Fig. 4, NR and CD band intensity both decrease during the oxidation process, while the CH bands remain visible, indicating the presence of the SA monolayer throughout the reaction.

It is worth mentioning that the oxidation of OA in the films mixed with SA leads to an unusual increase in the measured neutron reflectivity signal when SA is deuterated instead of OA. This is mostly due to the reorganisation of the remaining SA from islands into an homogeneous monolayer. When measuring the same mixed system, but with this reverse deuteration configuration (dSA/hOA), the NR signal started increasing as soon as oxidation of OA commenced (Fig. 6). The most likely explanation for this behaviour is the effect of the lateral coherence length of the neutron beam: if a significant proportion of the initial SA islands have a size greater than the coherence length of the neutron beam (typically of the order of microns),²² then the neutrons scattered by the islands do not interfere coherently with those scattered by the surrounding material. As a consequence, the scattered signal, rather than being an average of scattering length densities (SLDs) of dSA and hOA, arises solely from the dSA. The dSA islands however, cover only about 50% of the surface, leading to an overall reduction of the scattered signal in the initial state. Upon oxidation of hOA, the dSA islands spread to form a uniform monolayer covering the entire surface. This leads to an apparent increase in the scattering signal. For mixed monolayers where

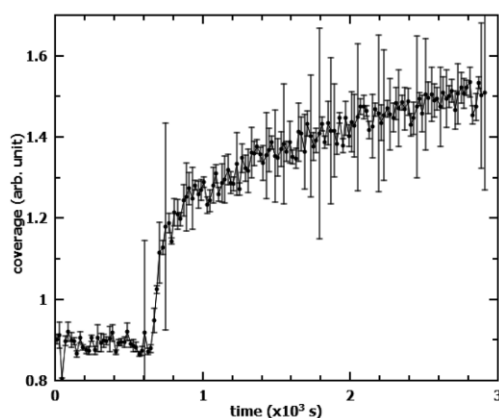


Fig. 6 Evolution of NR signal from a dSA/hOA monolayer during oxidation with a time resolution of 20 s. O_3 at a concentration of $1.2 \times 10^{13} \text{ cm}^{-3}$ is admitted to the reaction chamber at $t = 640 \text{ s}$. The scattering arose solely from the deuterated component (SA), which underwent re-ordering on the surface.

the two components are miscible, the scattered signal will always be a function of the average of the SLDs of the different species. If the oxidisable component is null-reflecting (same SLD as air and the sub-phase), then no change in the scattered intensity will be observed if the stable component remains on the surface. This signal increase could be misinterpreted, especially if measuring in the reverse deuteration, where it would lead to an apparent reduction in the reaction rate as well as a “residual” signal. This effect strongly depends on island size and could be used as indirect measure of island size distribution. To corroborate this explanation of the signal increase we have also measured the scattered intensity on a linear detector (data not shown). There was no discernible difference before and after the oxidation in the amount of off-specular scattering. This finding excludes the possibility of increased roughness due to the islands in the initial state.

4 Conclusions and outlook

We have described an experimental set-up for performing simultaneous NR and IRRAS within a specially designed reaction chamber for the study of atmospherically relevant chemical reactions in thin films at the air–water interface. To our knowledge this is the first on-beam IRRAS set-up for studying liquid interfaces. This flexible set-up is available for use on the INTER reflectometer at the ISIS spallation neutron source. We have demonstrated that we can obtain complementary information regarding thin-film structure and molecular environment with good SNR and short acquisition times in an optimised set-up. This set-up is applicable to a range of monolayer and thin film (kinetic) studies, *e.g.* protein adsorption, protein-monolayer interactions, surfactant monolayers and mixtures, as well as our core interest of atmospheric

chemistry. The *in situ* IRRAS set-up provides additional information: it shows the presence and relative concentration (if corrected for the natural strength of various absorption bands, for instance by comparing with a known standard) of molecules invisible to NR (contrast matched) at the same time as the NR signal provides structural information of the highly contrasting species. IRRAS also gives molecular environment information in addition to structural information from NR. We are continuing to apply the strengths of our approach to determining the fate of reaction products upon oxidation. As atmospheric aerosols will typically contain a complex mixture of surfactants (saturated and unsaturated), our combined techniques are ideally suited to give us detailed insight into the oxidation process. Unraveling the fate of individual components within a complex mixture will inevitably further our understanding of the very complex life cycle of atmospheric aerosols.

Acknowledgements

MWAS would like to thank J. Simms for help with the technical drawings for the reaction chamber. The authors gratefully acknowledge studentship funding from the following sources: NERC for MH, NERC SCENARIO and ISIS for BT, Institut Laue-Langevin (ILL) and University of Reading for FS. We also thank the Partnership for Soft Condensed Matter at ILL for providing access to BAM. Access to the neutron reflectometer INTER and use of the on-beam FTIR was provided by ISIS (experiments RB1510605 and RB1520459).

References

- 1 S. Fuzzi, M. O. Andreae, B. J. Huebert, M. Kulmala, T. C. Bond, M. Boy, S. J. Doherty, A. Guenther, M. Kanakidou, K. Kawamura, V.-M. Kerminen, U. Lohmann, L. M. Russell and U. Pöschl, *Atmos. Chem. Phys.*, 2006, **6**, 2017–2038.
- 2 J. Pérez-Gil, *Biochim. Biophys. Acta, Biomembr.*, 2008, **1778**, 1676–1695.
- 3 M. S. Aston, *Chem. Soc. Rev.*, 1993, **22**, 67–71.
- 4 A. D. Estillore, J. V. Trueblood and V. H. Grassian, *Chem. Sci.*, 2016, **7**, 6604–6616.
- 5 R. E. Cochran, O. S. Ryder, V. H. Grassian and K. A. Prather, *Acc. Chem. Res.*, 2017, **50**, 599–604.
- 6 P. K. Quinn, D. B. Collins, V. H. Grassian, K. A. Prather and T. S. Bates, *Chem. Rev.*, 2015, **115**, 4383–4399.
- 7 B. Graham, P. Guyon, P. E. Taylor, P. Artaxo, W. Maenhaut, M. M. Glovsky, R. C. Flagan and M. O. Andreae, *J. Geophys. Res.: Atmos.*, 2003, **108**, 2156–2202.
- 8 R. C. Chapleski, Y. Zhang, D. Troya and J. R. Morris, *Chem. Soc. Rev.*, 2016, **45**, 3731–3746.
- 9 I. J. George and J. P. D. Abbatt, *Nat. Chem.*, 2010, **2**, 713–722.
- 10 U. Pöschl and M. Shiraiwa, *Chem. Rev.*, 2015, **115**, 4440–4475.
- 11 J. Lu, R. Thomas and J. Penfold, *Adv. Colloid Interface Sci.*, 2000, **84**, 143–304.



Open Access Article. Published on 07 July 2017. Downloaded on 8/20/2019 10:53:06 AM.
This article is licensed under a Creative Commons Attribution 3.0 Unported Licence.



- 12 M. D. King, A. R. Rennie, K. C. Thompson, F. N. Fisher, C. C. Dong, R. K. Thomas, C. Pfrang and A. V. Hughes, *Phys. Chem. Chem. Phys.*, 2009, **11**, 7699–7707.
- 13 M. D. King, A. R. Rennie, C. Pfrang, A. V. Hughes and K. C. Thompson, *Atmos. Environ.*, 2010, **44**, 1822–1825.
- 14 C. Pfrang, F. Sebastiani, C. O. M. Lucas, M. D. King, I. D. Hoare, D. Chang and R. A. Campbell, *Phys. Chem. Chem. Phys.*, 2014, **16**, 13220–13228.
- 15 F. Sebastiani, R. A. Campbell and C. Pfrang, *RSC Adv.*, 2015, **5**, 107105–107111.
- 16 L. F. Voss, M. F. Bazerbashi, C. P. Beekman, C. M. Hadad and H. C. Allen, *J. Geophys. Res.: Atmos.*, 2007, **112**, D06209.
- 17 M. Strobl, R. Steitz, M. Kreuzer, M. Rose, H. Herrlich, F. Mezei, M. Grunze and R. Dahint, *Rev. Sci. Instrum.*, 2011, **82**, 055101.
- 18 J. Seeliger, F. Evers, C. Jeworrek, S. Kapoor, K. Weise, E. Andreetto, M. Tolan, A. Kapurniotu and R. Winter, *Angew. Chem., Int. Ed.*, 2012, **51**, 679–683.
- 19 I. Varga and R. A. Campbell, *Langmuir*, 2017, **33**, 5915–5924.
- 20 G. D. Smith, E. Woods, C. L. DeForest, T. Baer and R. E. Miller, *J. Phys. Chem. A*, 2002, **106**, 8085–8095.
- 21 C. R. Flach, Z. Xu, X. Bi, J. W. Brauner and R. Mendelsohn, *Appl. Spectrosc.*, 2001, **55**, 1060–1066.
- 22 C. F. Majkrzak, C. Metting, B. B. Maranville, J. A. Dura, S. Satija, T. Udovic and N. F. Berk, *Phys. Rev. A*, 2014, **89**, 033851.

3.2 – Improvements to Height Adjustment

The preparation of an air/water interface involves decanting approximately 80 mL of water subphase into the trough, followed by cleaning the surface using a vacuum pump. The variable amount of water removed in the cleaning process leads to slight variations in the amount of water in the trough for any given experiment, which means that the vertical position of the air/water interface is not reproducible between experiments. Both neutron reflectometry and infra-red reflection-absorption spectroscopy are highly sensitive to the vertical position of the interface, so the apparatus must be moved so that the interface is returned to a reproducible position with respect to the neutron and IR beams.

Height adjustment for the purposes of neutron reflectometry is routine, and can be performed using a height measurement laser (Keyence LK-G402 on INTER at ISIS) zeroed to an aligned position and then adjusting the height of the measurement table in order to compensate for any measured deviation in interface height. This laser beam couples into the reaction and analysis chamber through a quartz window as described in the *RSC Advances* paper. For work on the FIGARO reflectometer at the ILL, height adjustments were made by scanning over a small height range before each experiment and optimising for reflected signal, as the available height laser struggled to reliably locate the interface.

However, the movement of the entire sample environment to compensate for variations in interface position also moves the whole FT-IRRAS analysis setup (source, mirrors, and detector), and thus does nothing to restore the interface to the correct position with respect to the IR beam. The spherical mirrors of the FT-IRRAS setup are intended to focus the IR beam to a small spot on the interface, so even small variations in the height of the interface significantly affect signal strength and quality. In order to correct the height of the interface for both IR and neutron beams, the interface must first be adjusted in the vertical direction independent of the FT-IRRAS apparatus until it is optimised with respect to the IR signal, and then the whole system, including the FT-IRRAS apparatus, must be adjusted to the optimal position with respect to the neutron beam.

The reaction and analysis chamber described in the *RSC Advances* paper achieved this by simple mounting upon a manual height stage, which was then adjusted in order to maximise IR signal before allowing automatic adjustment of the INTER sample environment to optimise for neutron signal. The problem with this approach was the fact that, as the whole chamber was adjusted up and down with respect to the FT-IRRAS apparatus, the calcium fluoride (CaF_2) windows through which the IR beam achieved ingress to and egress from the chamber were also shifted up and down with respect to that apparatus. The eventual result, when all corrections were complete, was that the windows ended up in slightly different positions with respect to everything else, as they were the one piece of the entire NR/FT-IRRAS assemblage that could not be adjusted freely with respect to the interface. Thus, a lower than usual subphase volume resulted in higher window position, and vice versa.

CaF_2 windows do introduce some attenuation to the IR beam, and their finite thickness means that non-perpendicular ingress and egress of the beam through said windows results in increased attenuation. Small reflection and refraction artefacts were also a concern for non-perpendicular beam ingress and egress, and, in the worst-case scenario, the windows could be so shifted from their ideal position that some of the IR beam would be incident upon the aluminium window frame, rather than the CaF_2 window. This latter situation would cause severe attenuation as well as a number of reflection, absorbance, and interference artefacts, which were in fact observed on several occasions.

In order to address these problems, the first modification made to the reaction and analysis chamber after the development covered in the *RSC Advances* paper was the decoupling of the vertical position of the subphase trough from the vertical position of the CaF_2 windows. This was achieved by allowing the steel baseplate upon which the polytetrafluoroethylene (PTFE) subphase trough was mounted to move freely up and down its steel mounting pins, while supporting the baseplate on three new steel pins that were inserted through the aluminium base of the reaction and analysis chamber while still maintaining a

gas-tight seal. These three pins were equipped with a screw thread of a very shallow pitch, so that they could be rotated in order to adjust their vertical position with respect to the base of the chamber. The three pins were further equipped with cog wheels on the outside of the chamber. These three cog wheels, along with two extra cog wheels connected only to the chamber base, were linked together with a belt and tensioner, so that the height of the three pins could be adjusted in concert. One of the cog wheels was then outfitted with an adjustment point, so that it could be rotated in order to control the height of the trough with respect to the chamber and therefore, crucially, the CaF₂ windows. This system is demonstrated visually in Figure 3.1.

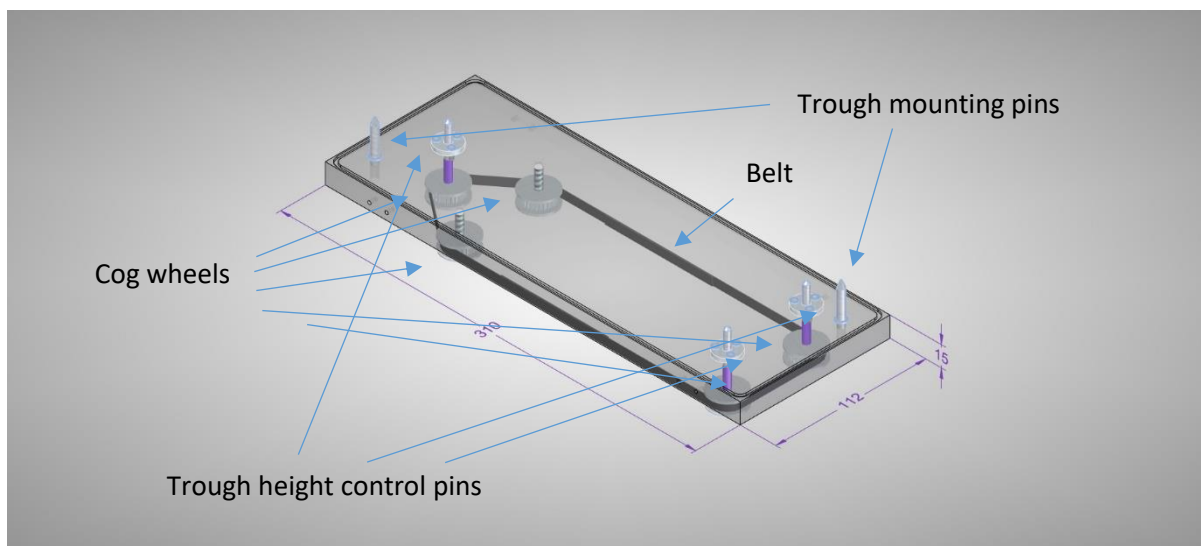


Figure 3.1 – 3D translucent projection of height adjustment system (measurements in mm). Credit: J. Simms, ISIS.

The entire chamber was still mounted on a manual height stage, which then served as a way to adjust the entire chamber at the start of a series of experiments in order to achieve optimal alignment of the CaF₂ windows with respect to the FT-IRRAS apparatus. Variations in interface height from experiment to experiment could then be corrected using the new cog wheel adjustment system, which only moved the interface, and not the windows, with respect to the IR beam. The whole FT-IRRAS setup would then be adjusted to the optimal height for neutron signal. This greatly simplified and accelerated the process of re-aligning the system between experimental runs compared with the system as described in the *RSC Advances* paper. That system already improved upon the prototype, whose smaller CaF₂ windows severely limited the range of interface height with respect to the chamber over which reasonable IR throughput could be obtained. The larger, better located windows of the iteration described in the *RSC Advances* paper was a large step forward, but the following iteration's decoupling of window and interface position in the vertical direction represented further progress in the effective integration of FT-IRRAS into neutron reflectometry experiments.

The reaction and analysis chamber as described here was used for experiment RB 1620451 on INTER at ISIS.

3.3 – Atmospheric Interference Suppression

The reaction and analysis chamber is itself gas-tight, as it needs to be in order for oxidation experiments to be carried out within it. However, the IR beam path also travels through the atmosphere after it leaves the source until it enters the chamber, and after it exits the chamber until it enters the detector. The atmosphere inside the experimental blockhouse of INTER is regulated by air conditioning, but this is not sufficient to dampen the variations in levels of CO₂ and H₂O induced by the presence of experimenters in the blockhouse during experimental setup.

Plans were made to deal with atmospheric interference by enclosing the entire IR beam path inside a Perspex cuboid. This cuboid was outfitted with windows to allow the ingress and egress of the height laser beam and the neutron beam, and equipped with a port to connect an IR ingress point on the box with the beam egress point on the FT-IR spectrometer. Only IR beam ingress, not egress, was required for the box, as the IR detector was situated within the box.

This box could then be purged with dry air in order to reach a stable and reproducible atmospheric composition under which experiments could be performed, removing the concern of varying CO₂ and H₂O levels and their effects on IR absorbance spectra. The interior optics of the FT-IR spectrometer are already purged with dry air, and this airflow could also be utilised for purging the beam path outside the spectrometer.

In practice, this suppression method was not used for any of the experiments reported upon in this thesis. The improvements in control over relative window positioning described in section 3.2 removed some sources of IR interference that had originally been supposed to be atmospheric, but were in fact due to attenuation, refraction, and interference from the window and window frames. These interference bands were of most concern to measuring the C–H and C–D stretches of interest for this work.

The FT-IRRAS measurements would still be slightly improved by use of a purge box, but testing revealed that the physical constraints introduced by the outer casing made effective alignment more difficult and time-consuming. Further, the time needed to purge the box, which would need to be done twice for each measurement (once for an FT-IRRAS background on subphase only, and once for the experiment itself), would reduce the number of experiments that could be performed in any given amount of neutron beamtime.

As a result of these considerations, the purge box was not utilised for the fatty acid oxidation experiments discussed in this thesis. It was not yet available for the glycolipid oxidation experiments, which were carried out only on experiment INTER RB 1610500, and were at an earlier stage of apparatus development before the purge box was built. The purge box remains part of the experimental apparatus housed at ISIS available for these sorts of experiments, and would be very useful for studying systems in which other IR absorbance bands, particularly amide bands (which are completely occluded by H₂O interference) are of interest.

3.4 – Addition of Temperature Control

Early in the project, as the first apparatus was under development, the focus was on room temperature experiments. As the experimental setup matured and improved, the project began to focus on more novel, low temperature experiments. For this, a system of temperature control was developed.

Initial discussions between Dr Pfrang, Dr Skoda, and me revolved around whether to use liquid or solid thermoelectric cooling. The main concern was to avoid icing, as, particularly for experiments using NO₃[•] radicals as the oxidising gas, this can complicate the chemistry of the environment. Liquid cooling would be simpler and easier, but might be more prone to icing.

Tests were carried out with a copper cooling plate of a style available at ISIS for general applications that simply requires a large heat sink, and icing was not found to be a problem within the temperature and humidity ranges desired. As a result, liquid cooling was pursued.

The steel baseplate that rests upon the height adjustment pins described in section 3.2 was modified, and a recess hollowed into the PTFE subphase trough in order to allow the sandwiching of a custom steel plate incorporating soldered copper cooling pipes between the two. Copper pipes protruded from this plate, and were connected to ports machined into the base of the reaction and analysis chamber

using polycarbonate tubing designed to be long enough to allow the height of the trough to be adjusted without placing undue strain on the connections.

Figure 3.2 shows the cooling plate and pipes, and Figure 3.3 shows the modified underside of the PTFE trough that housed them.

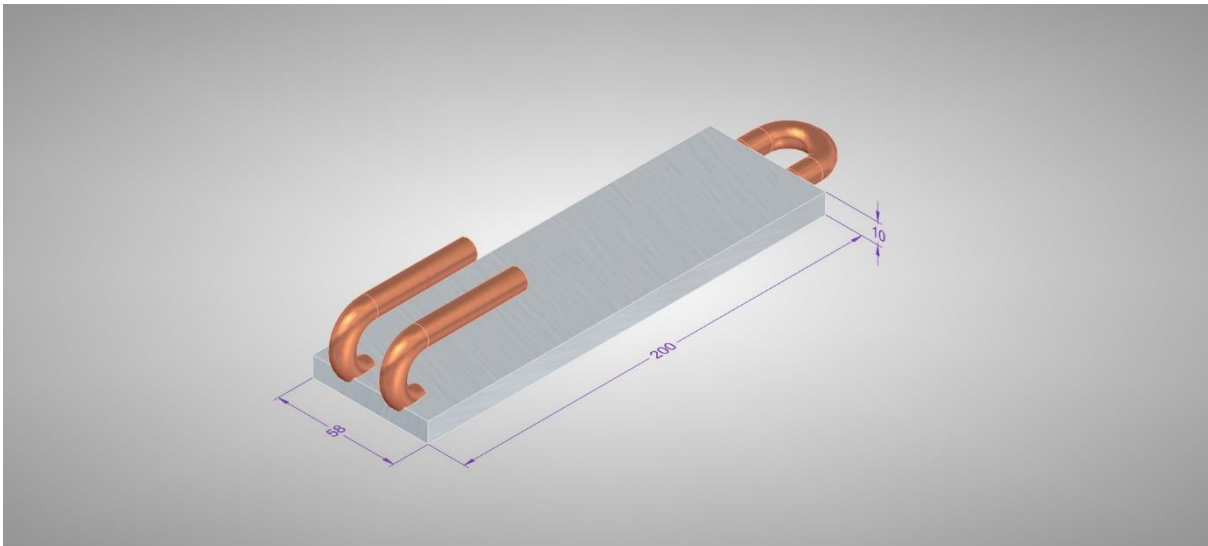


Figure 3.2 – Cooling plate and pipes (measurements in mm). Credit: J. Simms, ISIS.

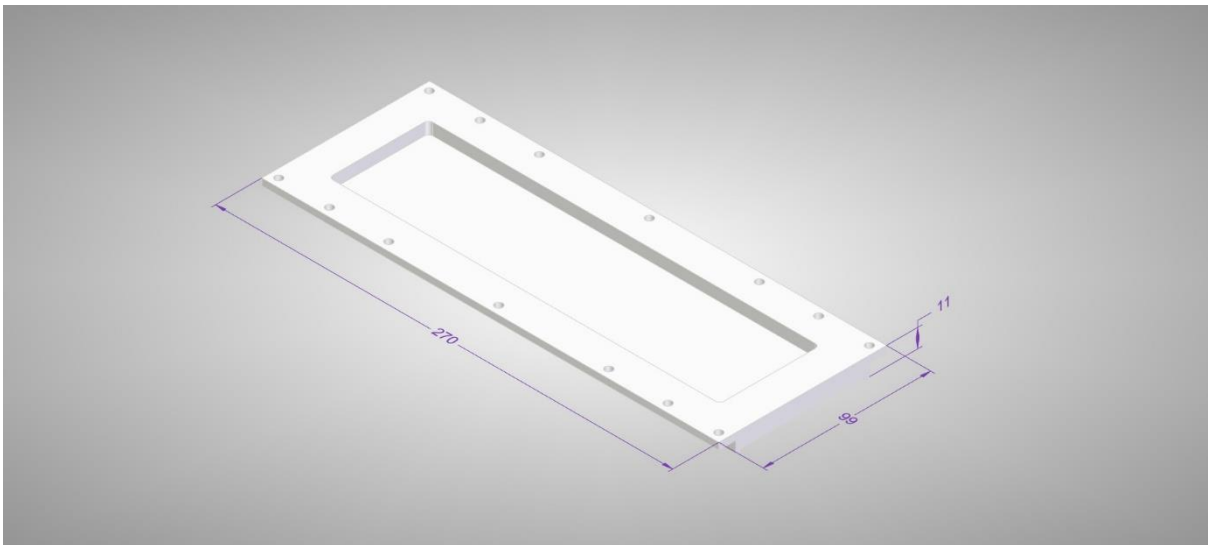


Figure 3.3 – Underside of PTFE trough (measurements in mm). Credit: J. Simms, ISIS.

There was not room inside the chamber for these ports to be mounted vertically, so complementary recesses were machined into the base of the chamber from the inside and outside, leaving a section of vertical chamber wall between them, through which horizontal ports could be placed. Figure 3.4 shows the base section of the chamber with the relevant recess.

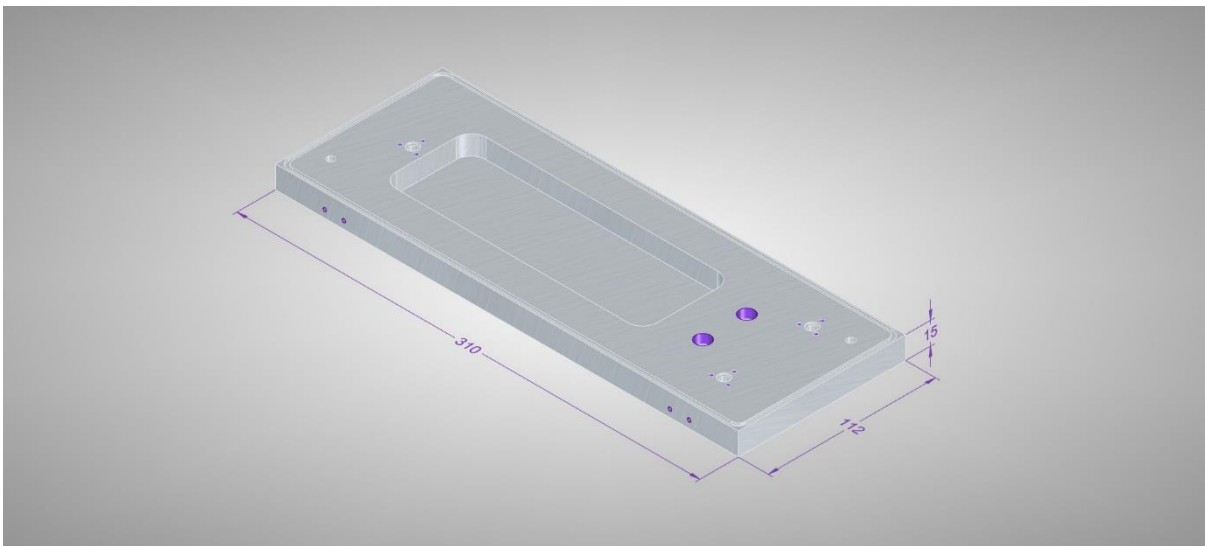


Figure 3.4 – Chamber base with recess for cooling pipe connections (measurements in mm). Credit: J. Simms, ISIS.

The reaction and analysis chamber as described here was used for experiment RB 1710483 on INTER at ISIS. It allowed for access to the required temperature ranges, but was somewhat hard to control, with up to 5 °C variation in temperature across the trough. The trough also suffered from warping at times.

3.5 – Improvement of Temperature Control

The issues suffered by the first temperature-controlled setup were diagnosed as mostly due to the choice of a steel and copper mix for the cooling plate, and the limited area of contact between the cooling plate and the trough.

Copper, with its higher heat conductivity, would have been an ideal choice for the whole plate from a purely thermal perspective, but copper's reactivity, particularly towards oxidants, made it a poor choice and it was limited to use only for the pipes where its flexibility made it indispensable. Stainless steel was chosen for the remainder despite its low conductivity as it is easy to solder to copper and is relatively unreactive towards oxidants. The limited area of contact between the plate and the trough was due to the difficulty in incorporating the curved sections of pipe into the steel plate.

These two compromises made in design contributed to the steep temperature gradient across the trough and to the warping of the same due to uneven heating. As a result, after the first iteration, the decision was made to proceed with some of the more difficult manufacturing challenges that it was now clear were necessary to achieve a temperature control system that would function as desired.

The steel baseplate, steel cold plate, and PTFE trough were individually dispensed of and replaced with a single aluminium piece to improve thermal conductivity. This aluminium piece was PTFE-coated on its top face, and copper coolant pipes were directly attached to the underside using steel clips. In order to ensure good contact between the aluminium and copper, as soldering was not feasible, the single aluminium piece had to be manufactured to a high degree of precision, especially around the bend in the copper pipe, which had previously not been in contact with anything but air.

Figures 3.5 and 3.6 show this single aluminium piece from below and above, respectively.

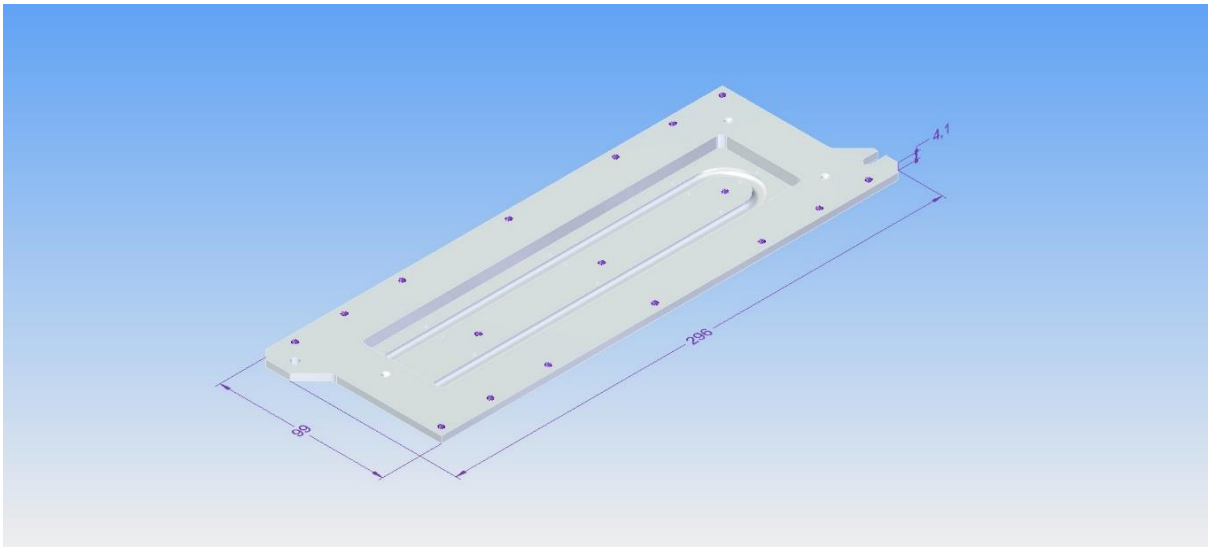


Figure 3.5 – Single-piece cooling assembly, underside (measurements in mm). Credit: J. Simms, ISIS.

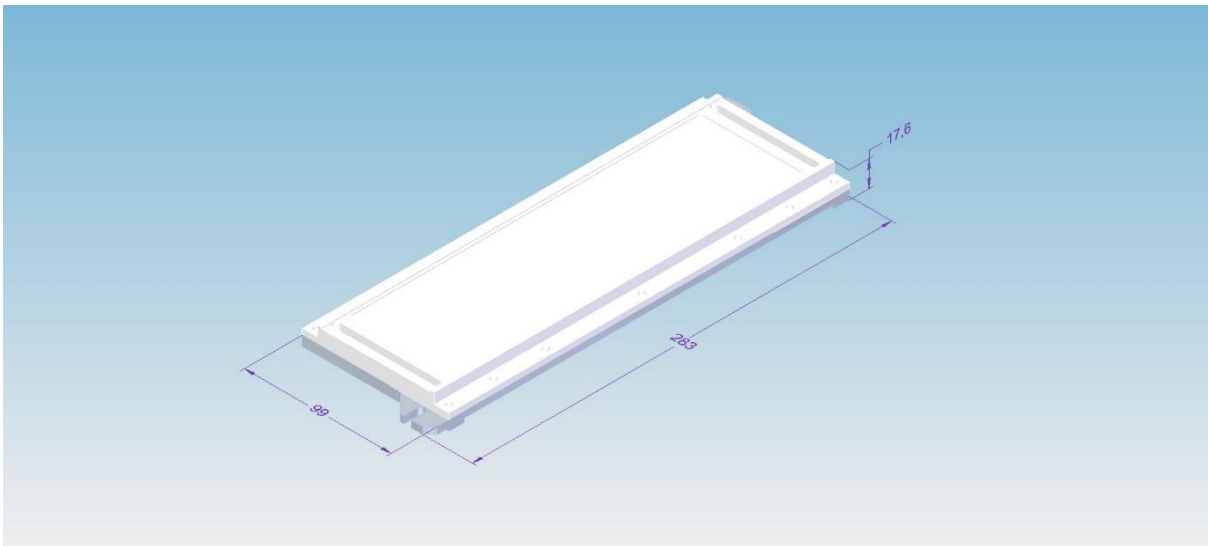


Figure 3.6 – Single-piece cooling assembly, topside (measurements in mm). Credit: J. Simms, ISIS.

The height of the assembly also needed to be reduced in order to solve an additional problem which had arisen with the initial cooling system, which was that the height adjustment system described in section 3.2 could not sweep through a sufficient vertical displacement in order to correct for the range of interface positions that was encountered. This was resulting in the trough assembly resting upon the copper pipes in some situations, which then resulted in tilting of the trough and occasional catastrophic loss of subphase material into the reaction and analysis chamber. Figure 3.7 shows the new positioning of the copper pipes, which have been crossed over to reduce the overall height they occupy by a factor of $\sqrt{2}$ without tightening the radius of the curves any further.

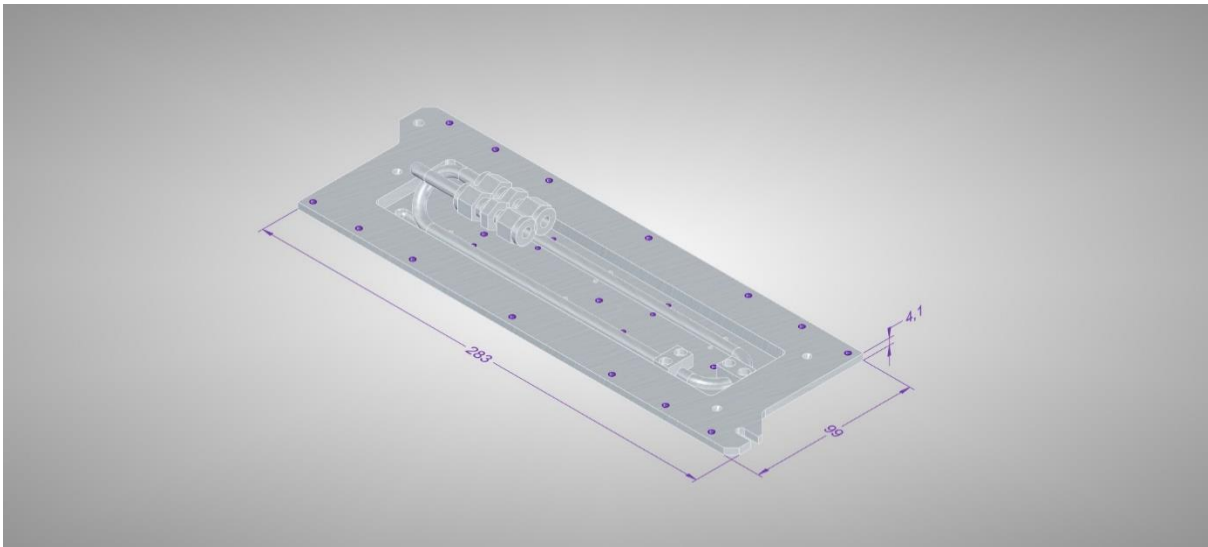


Figure 3.7 – Single-piece cooling assembly, underside with piping (measurements in mm). Credit: J. Simms, ISIS.

In order to have a contingency plan in case PTFE-coating of the single aluminium piece proved to be problematic or if the resultant trough turned out to be unsuitable, another single aluminium piece was constructed to replace just the baseplate and cold plate. This could then be used with the existing PTFE trough from the previous temperature-controlled apparatus. Additionally, a standalone aluminium trough was PTFE-coated and prepared for use with that base unit if desired, to provide redundancy if the PTFE-coated single piece were to fail.

As a result, 2 units are available. The first, a single-piece temperature-controlled unit with a PTFE trough surface, provides the best cooling performance due to its unified construction. The second, a slightly less high-performing (due to less than perfect contact between base unit and trough) unit, has added versatility due to the fact that a new trough could be manufactured for it and take the place of the PTFE-coated trough if were some other trough surface material than PTFE were required for some future application. This would be much cheaper, faster, and easier than manufacturing an entire new single-piece unit. This flexibility, along with availability of the purge box for detection of additional IR absorbance bands described in section 3.3, means that the equipment remaining at ISIS as a result of this project has the potential to be put to a wide variety of uses in the future.

Experiment RB 1810793 on INTER at ISIS was carried out with the improved cooling baseplate (standalone) and a PTFE trough top piece. The final iteration of the chamber, using the full PTFE-coated single aluminium baseplate/trough piece was used for experiment RB 1910615 on INTER at ISIS and experiment 9-10-1518 on FIGARO at the ILL. Figures 3.8 to 3.10 show the chamber and associated FT-IRRAS apparatus being set up for use on INTER, as well as the crane used to place the FT-IR spectrometer next to the setup.

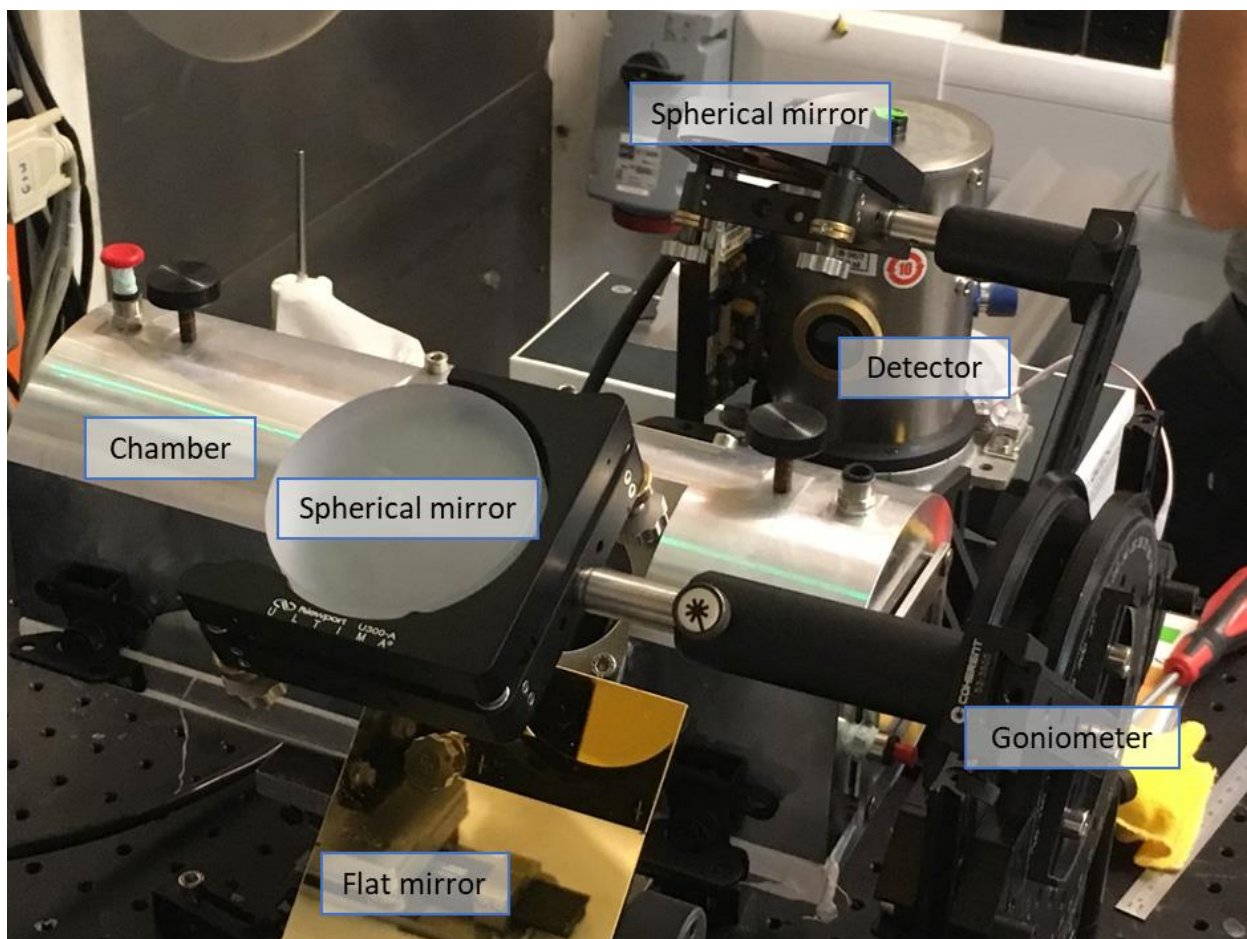


Figure 3.8 – Reaction and analysis chamber, FT-IRRAS mirrors, and MCT detector in place on INTER; neutron beam enters the chamber at the left of shot and exits through the window and circular goniometer at the bottom right; the parabolic mirror is hidden behind the chamber when viewed from this angle.

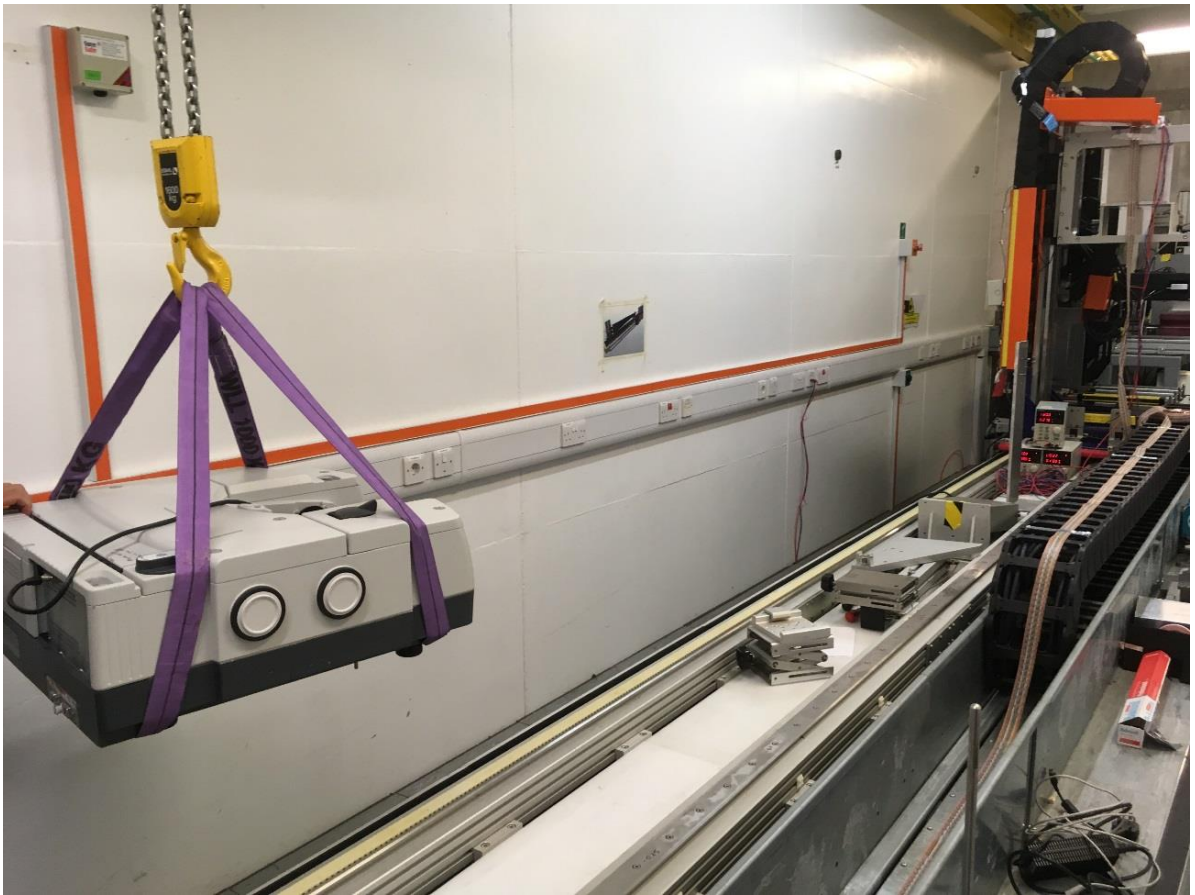


Figure 3.9 – Crane in use to move FT-IR spectrometer to the sample environment end of the INTER blockhouse at ISIS.

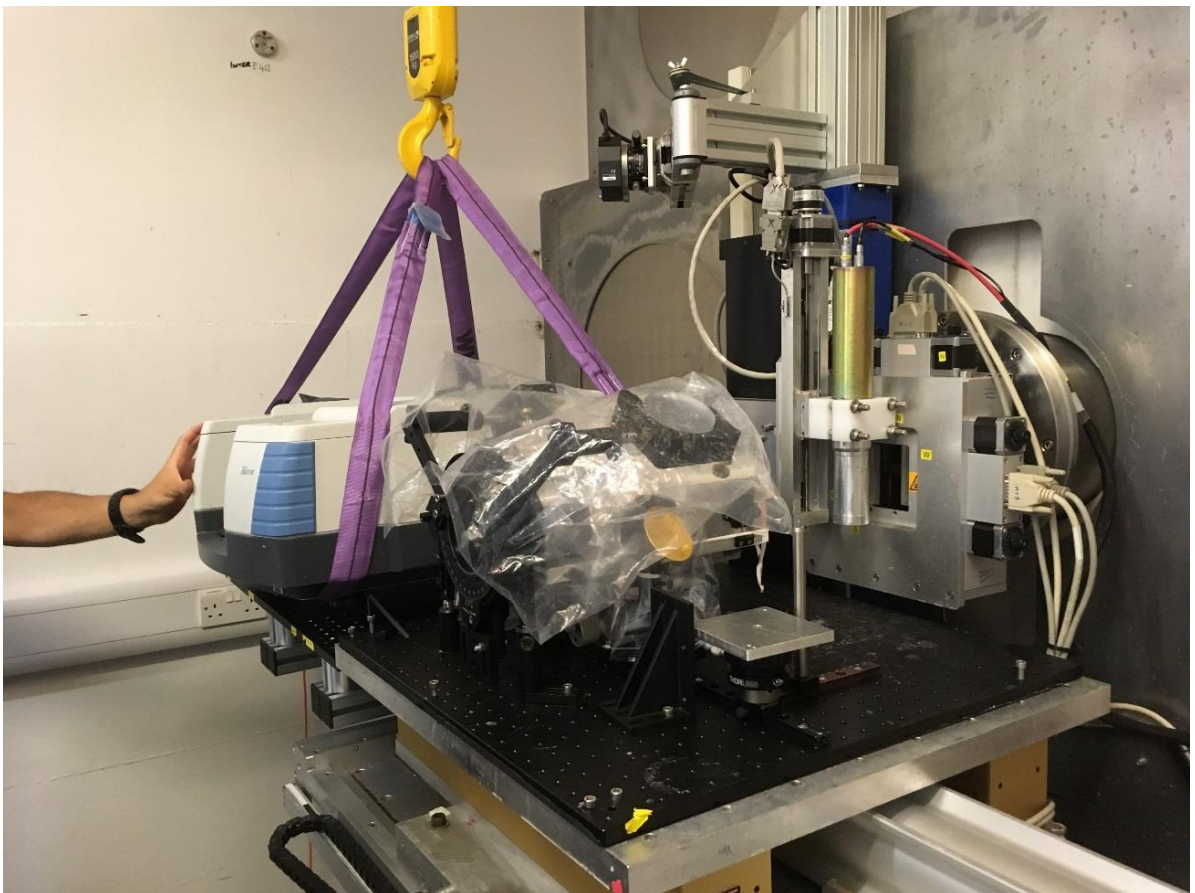


Figure 3.10 – The FT-IR spectrometer is lifted into position adjacent to the chamber and mirrors seen in Figure 3.8. The detector, situated inside the FT-IR spectrometer for normal operation, has not yet been placed on its external mount as in Figure 3.8.

Both of these setups reduce the variation in temperature across the subphase to 1 °C or less on a typical run at near-freezing temperatures. The highest temperatures are measured at either end of the trough, with the lowest temperatures in the middle. This was judged precise enough to allow quantitative work to proceed (during beamline experiments RB 1910615 and RB 1810793 on INTER at ISIS, as well as 9-10-1518 on FIGARO at the ILL) on the effects of temperature on the oxidation reactions reported upon throughout this thesis and in its associated publications. Data from beamline experiment INTER RB 1710483, which was carried out with the first temperature control system, was not deemed of publishable quality alone and is not reproduced in this thesis or in associated publications. Two runs from that beamline experiment that were directly replicated (with improved temperature control) in runs from a later beamline experiment are referenced as additional support for a conclusion in the paper on the effects of temperature on oleic acid ozonolysis presented in Chapter 5.

3.6 – Future Improvements

There are a number of areas in which the apparatus could be improved further, and some of these are briefly laid out here, along with the challenges they pose, as a possible guide for future work on continuing to develop the equipment.

One much discussed but ultimately not yet implemented feature is functionality for compressing and expanding the surface area of the system using moveable barriers, while measuring surface pressure with a Wilhelmy plate tensiometer. This is commonly employed for experiments on monolayers and other interfacial systems. However, it would not be trivial to integrate into the current reaction and analysis chamber. There is a number of reasons why this is the case.

Ozone has been observed to damage the pressure sensors employed on Langmuir troughs for this purpose. Other reactive gases likely pose a similar hazard. It would be possible to not use a sensor, and run ‘blind’, compressing and expanding the system with reference to externally measured pressure-area isotherms, but the benefits of this would be limited, and the danger of accidentally breaking a monolayer without any way of knowing this had occurred would be high.

Furthermore, the mechanical equipment required to smoothly move the barriers is quite bulky, and the barriers are generally kept clear of the neutron footprint and beam path. Including such barriers would have required making the chamber significantly larger, making it harder to control and model the ozone (or other reactive gas) concentration in the chamber and more difficult to integrate the FT-IRRAS apparatus. The bulkiness could be reduced by using a quartz barrier, which could be placed in the neutron beam path without problems, as quartz is transparent to neutrons. Alternatively, manual barrier movement could be used, but the chance of breaking a monolayer using manual barrier positioning is higher than with smooth, slow, motor-driven positioning, making the lack of a pressure sensor an even greater concern.

So far, the lack of a pressure sensor and area controls has been manageable, as the systems that have been studied have been fairly simple, and no attempts have been made to study the fine-grained impact of surface tension or monolayer phase on oxidation behaviour. In one experiment (RB 1540015 on SURF at ISIS) moveable barriers and a pressure sensor were absolutely required, but no oxidation was performed and no FT-IRRAS data was required, so a standard Langmuir trough was used instead of our bespoke apparatus. However, finding some way to integrate an area control and pressure measurement solution would expand the range of applications for the apparatus, and therefore it represents a logical next step in development, now that the basic design has been refined and temperature control introduced.

As it is not advisable to expose the tensiometer itself to reactive gases, it would have to be mounted on a nearby post, from which it could be rotated into position for measurement and then rotated away again before the chamber was sealed for oxidation. A basic form of this idea was set up and trialled in

offline experiments at one stage, but the lack of a moveable barrier meant only the facility of pressure measurement, not area (and hence pressure) control was added by this, and the additional complexity and clutter it introduced into the apparatus was not deemed worth this limited benefit. Combining this solution with a single manual-wind quartz barrier (which could likely be integrated with only limited redesign of the trough) would facilitate pressure and area control (though without any possibility for automation or operation at a distance), and this might be worth the additional complexity for some applications.

A second area for improvement emerges from a small inconsistency in kinetic measurements that is introduced by the fact that adjusting the height of the interface (using the fine adjustment system implemented after the initial full-chamber height adjustment was judged unsuitable as described in section 3.2) moves the position of the interface relative to the oxidant gas ingress pipe, which is fixed relative to the chamber. This is not a problem as long as the position of the interface is adjusted to maximise FT-IRRAS interferogram signal before each measurement and the position of the chamber is not moved relative to the FT-IRRAS apparatus, which is the intended mode of operation. As long as the chamber and FT-IRRAS mirrors, source, and detector do not move between runs, then the height to which the interface will be adjusted in order to maximise interferogram signal will be constant with respect to the ingress pipe. However, if more significant changes are made to the setup, either because a mirror is displaced and the whole FT-IRRAS setup requires realignment as a result, or because the apparatus has been removed from the beamline, packed down, and then re-deployed for another beamline experiment, then there is no guarantee that the position of the chamber, and therefore of the ingress pipe, will remain constant. This means that the ingress pipe could be in a slightly different position with respect to the interface in different experiments.

The reasons this poses a problem are complex and related to the time evolution of oxidant gas concentration gradients inside the chamber within the first minute of the reaction (see section S3 of the supplement to the *Atmospheric Chemistry and Physics (ACP)* paper presented in Chapter 5 for a full discussion). The implication is a possible slight incommensurability between rate constants derived under slightly different offsets between interface height and ingress pipe height. Affixing the inlet pipe to the trough, rather than the chamber wall, would not necessarily solve this problem, as the height of the interface is not consistent with respect to the trough either, which is why the trough height must be adjustable in the first place. Currently, the best approach is to always fill the trough with the same amount of subphase, and be as consistent as possible in aspirating the surface, making sure that the height of the trough does not have to be too radically adjusted between runs used for kinetic parameter fitting. This is far from perfect, and introduces some uncertainty into these fitted kinetic parameters. Finding a solution to this problem would improve the usefulness of the apparatus for quantitative kinetic measurements.

A third possible area for development would be to make the FT-IRRAS apparatus simpler, easier to use, faster to set up, and more reproducible by the replacement of the mirror assembly with a fibre optic solution. This was judged prohibitively expensive for the applications in this work, as the mirror setup does produce useful data, is reproducible and is not too difficult to use once the user has had some practice. In future, however, more precise, perhaps even fully quantitative, FT-IRRAS measurements could be gathered if desired through the use of a fibre optic solution.

Finally, the chamber deliberately has space for additional pairs of CaF_2 windows to be added at different angles with respect to the interface. Additional window pairs could widen the applicability of the system to other interfaces besides air/water, or allow the use of polarisation modulation FT-IRRAS (PM-FT-IRRAS or PM-IRRAS), which requires a grazing angle of incidence on an air/water interface. PM-FT-IRRAS allows for complete suppression of atmospheric interference at a particular wavenumber, which would allow the measurement of IR bands currently obscured by H_2O and CO_2 . Such additional FT-IRRAS options would require additional beam paths, meaning that the mirror setup would have to be

reworked for each option. However, the use of a fibre optic solution could allow for easy switching between FT-IRRAS incidence angles through different window pairs, or even for multiple simultaneous measurements at various angles of incidence. This could be useful for gathering detailed structural information about molecules at the air/water interface.

These suggested developments, and surely many others not discussed here, could expand the usefulness of this NR/FT-IRRAS reaction and analysis apparatus into many new domains.

3.7 – Acknowledgements (Method Development)

The development of the reaction and analysis chamber was performed in concert with the design and workshop groups at ISIS. Particular thanks to the following individuals is warranted.

Dr Maximillian WA Skoda (secondary PhD supervisor) was closely involved with the design of the chamber and many ideas were developed in back-and-forth discussions with him. He also produced the original technical drawings used for the first iteration of the chamber and modified thereafter.

Jacob Simms translated my sketches and hand-drawing into technical drawings and liaised with manufacturers for production of the parts that were not built by the in-house team. He also assisted with building the height adjustment system and assembling the cooling system.

Richard Haynes performed the difficult copper-to-aluminium attachment step, as well as assisting in the assembly of the rest of the cooling system.

Andy Church, Jeff Vine, Tom Charleston, and John Crawford also supported various stages of the development, testing, and assembly of various iterations of the equipment.

Group 4 Engineering and The Machining Centre were the outside manufacturing groups employed for the machining of many of the metal pieces used in the construction of the equipment.

Plastic Coatings Limited were employed to provide PTFE coating for trough tops and the single unified aluminium baseplate/trough piece.

Chapter 4 – Oxidation of Galactocerebroside Monolayers including Fatty Acid Mixtures

4.1 – Introduction and *Atmosphere* Paper

Experiment RB 1610500 on INTER at ISIS focused on the oxidation of pure monolayers of galactocerebroside and mixed monolayers of galactocerebroside and fatty acids. The basic idea behind the experiment was conceived by Dr Christian Pfrang and Dr Maximillian WA Skoda at the very start of the PhD project, and the proposal for INTER beamline access was written by the two of them, using some preliminary FT-IRRAS data that I had gathered in my first few months. The results formed a strong self-contained scientific story that stood somewhat separate from the rest of the work performed in the PhD, and were published as a paper in the journal *Atmosphere*.

The experiment itself was planned and performed by Dr Pfrang, Dr Skoda and me, with support from Dr Matthew Hagreen. I performed all the data analysis and produced all the figures seen in the paper. I wrote the text of the paper with input from Drs Pfrang and Skoda. A few of the changes to the text of the paper requested by reviewers were handled by Drs Pfrang and Skoda under discussion with me, as I was on a secondment at the time.

The paper itself follows and forms the bulk of this results chapter. Following the paper, a few supplementary issues relevant to the finer details of the neutron reflectometry data are included, which were not considered sufficiently relevant to the reader of *Atmosphere* to be included in the paper. The introduction briefly covers some of the topics covered in the earlier expanded introduction chapter (Chapter 1), as well as providing justification for the study of this system and providing some background specific to it.

Article

Night-Time Oxidation of a Monolayer Model for the Air–Water Interface of Marine Aerosols—A Study by Simultaneous Neutron Reflectometry and in Situ Infra-Red Reflection Absorption Spectroscopy (IRRAS)

Ben Woden ¹, Maximilian W. A. Skoda ², Matthew Hagreen ¹ and Christian Pfrang ^{3,*}

¹ Department of Chemistry, University of Reading, Reading, Whiteknights RG6 6AD, UK; rt011604@pgr.reading.ac.uk (B.W.); matthew_hagreen@hotmail.co.uk (M.H.)

² ISIS Pulsed Neutron and Muon Source, Science and Technology Facilities Council (STFC), Rutherford Appleton Laboratory, Didcot, Oxfordshire OX11 0QX, UK; maximilian.skoda@stfc.ac.uk

³ School of Geography, Earth and Environmental Sciences, University of Birmingham, Birmingham, Edgbaston B15 2TT, UK

* Correspondence: c.pfrang@bham.ac.uk; Tel.: +44(0)-121-4145-519

Received: 12 September 2018; Accepted: 24 November 2018; Published: 30 November 2018



Abstract: This paper describes experiments on the ageing of a monolayer model for the air–water interface of marine aerosols composed of a typical glycolipid, galactocerebroside (GCB). Lipopolysaccharides have been observed in marine aerosols, and GCB is used as a proxy for these more complex lipopolysaccharides. GCB monolayers are investigated as pure films, as mixed films with palmitic acid, which is abundant in marine aerosols and forms a stable attractively mixed film with GCB, particularly with divalent salts present in the subphase, and as mixed films with palmitoleic acid, an unsaturated analogue of palmitic acid. Such mixed films are more realistic models of atmospheric aerosols than simpler single-component systems. Neutron reflectometry (NR) has been combined in situ with Fourier transform infra-red reflection absorption spectroscopy (IRRAS) in a pioneering analysis and reaction setup designed by us specifically to study mixed organic monolayers at the air–water interface. The two techniques in combination allow for more sophisticated observation of multi-component monolayers than has previously been possible. The structure at the air–water interface was also investigated by complementary Brewster angle microscopy (BAM). This study looks specifically at the oxidation of the organic films by nitrate radicals ($\text{NO}_3\bullet$), the key atmospheric oxidant present at night. We conclude that $\text{NO}_3\bullet$ oxidation cannot fully remove a cerebroside monolayer from the surface on atmospherically relevant timescales, leaving its saturated tail at the interface. This is true for pure and salt water subphases, as well as for single- and two-component films. The behaviour of the unsaturated tail section of the molecule is more variable and is affected by interactions with co-deposited species. Most surprisingly, we found that the presence of CaCl_2 in the subphase extends the lifetime of the unsaturated tail substantially—a new explanation for longer residence times of materials in the atmosphere compared to lifetimes based on laboratory studies of simplified model systems. It is thus likely that aerosols produced from the sea-surface microlayer at night will remain covered in surfactant molecules on atmospherically relevant timescales with impact on the droplet’s surface tension and on the transport of chemical species across the air–water interface.

Keywords: aerosol; monolayer; nitrate radical; cerebroside; palmitic acid; palmitoleic acid; neutron; reflectivity; infra-red; Brewster angle microscopy

1. Introduction

In papers published in 1983 [1] and 1999 [2], it was noted that organic films formed on the surface of atmospheric aerosol particles and that the reactivity both of the aerosol particles underneath and of the species that make up the organic films themselves were different from what would be expected if each were encountered individually in the atmosphere. Donaldson and Vaida published a seminal review in 2006 [3] which brought together the subset of the body of scientific knowledge regarding the behaviour of molecular monolayer organic films at the air–water interface relevant to atmospheric processes.

The role of atmospheric aerosols in cloud formation is a topic of key importance for climate science. The relationship between aerosol concentrations and the radiative forcing attributable to clouds is exceptionally complex, poorly understood, and difficult to measure [4]. The study of these organic films at the air–water interface may form a key part of solving this puzzle. Many organic compounds will oxidise in the atmosphere to form secondary organic aerosol (SOA). Changes in these reactions due to the partitioning of the relevant reactants to the surface of water droplets in the atmosphere will, therefore, affect the manner in which SOA is formed and distributed. The films' effects on the physical nature of the water droplets onto which they partition is also of vital importance, as the surface tension of the droplets is lowered by the presence of these films [3], meaning that the removal of such films by oxidation can cause an increase in surface tension. The surface tension of water droplets plays a key role in regulating the growth of clouds [5]. The water droplets on which these organic films form are thus atmospherically important and are modified by virtue of their interaction with each other in a monolayer at the air–water interface. The film coating can also act as a barrier to water uptake by and evaporation of the droplet and can inhibit the transport of various atmospheric species from the gas to the aqueous phase [6–13]. Conversely, the film can act as a “2D solvent” for atmospheric species that would not normally partition to the aqueous phase, or can alter the solvation behaviour of those that would [14–18]. Very recently, Forestieri et al. [19] studied the surface tension effects on sea spray aerosol mimics (oleic, palmitic, myristic acids, and their mixtures) using a surface film model to establish the properties that surface-active organic molecules must have to substantially impact on the aerosol's activation efficiency. They found that the properties of surface-active marine-derived organic molecules must differ substantially from the simple fatty acids they studied e.g., by having larger molecular areas.

While the discussion here is focused on the presence of thin organic films on particles, it should be noted that particles have been shown to be phase separated and may contain 3D organic surface layers or even more complex 3D self-assembled structures, leading to particle morphologies that may differ substantially from the construct of a monolayer or sub-monolayer film on an electrolyte subphase [20–22].

The present study investigates the oxidation of model marine aerosol systems via reaction with nitrate radicals ($\text{NO}_3\bullet$), the key atmospheric oxidant present at night [23,24]. This oxidant takes over in the absence of sunlight from the dominant day-time initiator of atmospheric oxidation, $\text{OH}\bullet$, together with the less reactive ozone (O_3) that is present throughout the day and night (e.g., [25,26]). $\text{NO}_3\bullet$ primarily reacts with organic species by attacking carbon-carbon double bonds (e.g., [23,27–29]) and oxidising the new terminal groups to produce a variety of carboxylic acid and aldehyde fragments [23]. These reactions may be important in the production of atmospheric SOA, so changes to their nature and kinetics could be important in their own right, however their key relevance comes in that they determine the lifetime and ageing of the monolayer and, thus, the extent to which the water droplet is affected by all the physical and chemical changes detailed above that are due to the presence of that monolayer. Most monolayer studies to date (e.g., [30–33]) have focused on the less reactive initiator of the atmospheric oxidation ozone (O_3) that is known to be unreactive towards saturated surfactants (e.g., [34]). However, saturated surfactants have recently been shown to be of particular atmospheric importance [35], therefore processes that can attack saturated organic compounds are of particular interest. Understanding the night-time atmospheric ageing by $\text{NO}_3\bullet$, in addition to the chemistry of the dominant day-time oxidant $\text{OH}\bullet$ (e.g., [36]) and photochemical

reactions that have recently received lots of attention (e.g., [37]) is therefore an important focus of current research. It is thus essential to investigate the $\text{NO}_3\bullet$ chemistry at the air–water interface given the scarcity of previous studies [38,39].

Marine aerosols are highly variable in composition. Saturated fatty acids have been detected in abundance, particularly palmitic acid (PA) [40]. PA is commonly used as a proxy for marine aerosols [41]. Lipopolysaccharides have been discovered both in the sea surface microlayer [42] and in atmospheric aerosol [43]. Facchini et al. [43] found that sea water microgels, mainly composed of lipopolysaccharides, are preferentially transferred to the submicron aerosol size fraction during bubble bursting. Cerebrosides provide a good proxy species for the more complex lipopolysaccharides at the air–water interface [41], therefore the present study focuses on the oxidation of the glycolipid galactocerebroside (GCB).

We investigated the reaction of GCB with $\text{NO}_3\bullet$ both as a pure monolayer and in a mixed monolayer with the saturated and thus less reactive PA as a pair of proxies for marine aerosol monolayers containing lipopolysaccharides. A mixed monolayer of GCB and the unsaturated analogue of PA, palmitoleic acid (POA), was also oxidised in order to test how the introduction of a double bond affects the interaction between GCB and the fatty acid. Unlike saturated PA that is only subject to slow hydrogen abstraction [23,39], the double bond in POA reacts quickly with $\text{NO}_3\bullet$ [39], so this system should behave rather differently.

A 2013 study [41] found that the PA/GCB film mixture is fully miscible and that the components are attracted to each other and produce an enhanced film stability as a mixture, and also found that Ca^{2+} and, to a lesser extent, Mg^{2+} cations in the subphase increase acyl chain ordering. In order to investigate whether this has any effect on the oxidation, we used both pure water and CaCl_2 solution subphases.

Based on the results mentioned above with regards to the stability of the GCB/PA mixture and the lack of a double bond for fast oxidation in PA, we expected that at least part of the GCB/PA monolayer would remain at the surface after oxidation. The fate of the pure GCB monolayers will depend on whether any product from the reaction is sufficiently surface active to remain partitioned to the interface.

2. Experiments

2.1. Neutron Reflectivity (NR)

This research was performed on the specular neutron reflectometry instrument INTER at the ISIS Neutron and Muon Source. A comprehensive summary of the use of neutron reflectometry for the study of organic films at the air–water interface was provided by a review paper by Lu et al. in 2000 [44], which details the physics of neutron reflectivity and the mathematical manipulations required to convert reflectivity data into coverage data using fitting models. In short, specular NR typically determines the thickness, density, and roughness of thin layers stacked in the out-of-plane direction of a flat sample. In the present work, the only quantity extracted was the time evolution of the surface coverage of deuterated moieties that were present in the system. Purely hydrogenous moieties do not contribute to the NR signal, however the relative change in their coverage (as well as that of deuterated moieties) was monitored by simultaneous IRRAS. Since 2000, the number of models and methods for dealing with this data has increased significantly, and a recent paper by Campbell et al. [45] provides a review of the existing methods and an optimum model validation. The brief section that follows here will give a simplified introduction to the technique from a physical perspective and will only focus on the techniques and models required for a simple monolayer system (also see our recent method paper for further details [46]). More complex physical systems naturally require more complex modelling approaches that are not covered here.

The intensity of the reflected neutron beam depends on the differences between concentrations of nuclei with different neutron scattering lengths in the layers of the material stacked in the z-direction

(vertical). Simplifications of the complex equations that govern the relationship between neutron wavelength and reflected intensity are possible when investigating just one layer (for instance, an organic monolayer) at the air–water interface. This is because air has such a low number density of atoms that it essentially has a scattering length density of zero and an “air-contrast matched” or “null-reflecting” water subphase with a scattering length density of zero can be prepared by mixing D₂O 8.8% *v/v* in H₂O such that the surfactant at the air–water interface is the only component with a non-zero scattering length density.

According to the simplified equation that applies for this system (a single monolayer at the interface between air and a null-reflecting subphase), the reflectivity, *R*, varies as a function of the energy of the incident neutrons (expressed as momentum transfer, *Q*, and measured by white-beam time-of-flight) and the scattering length density, ρ , and thickness, τ , of the monolayer according to the following equation:

$$\frac{Q^4 R}{16\pi^2} \cong 4\rho^2 \sin^2 \frac{Q\tau}{2} \quad (1)$$

The layer thickness and scattering length density for the system can then be inferred from the relationship between the reflectivity and momentum transfer measured. These two parameters cannot be fitted independently (as they are multiplicatively dependent), however instead they must be fitted as a combined $\rho\tau$ variable, which corresponds to a surface concentration of scattering length, from which the surface concentration, or “coverage”, Γ , of the relevant surfactant species can be determined (as the scattering lengths, *b*, of the species are known):

$$\Gamma = \frac{\rho\tau}{b} \quad (2)$$

If multiple components are deuterated, however only one is being considered possibly reactive (as in the GCB/PA systems studied), then a contribution to $\rho\tau$ attributed to a known initial amount of the unreactive co-surfactant (PA) must be accounted for in converting a fitted $\rho\tau$ for the system to a Γ value specific to the surfactant of interest (GCB):

$$\Gamma_{\text{GCB}} = \frac{\rho\tau - \Gamma_{\text{PA}} b_{\text{PA}}}{b_{\text{GCB}}} \quad (3)$$

Reflectivity curves of *Q* vs. *R* are collected at intervals of 20 s throughout the reaction and each curve is fitted using MOTOFIT [47], an extension to the Igor Pro data manipulation and visualisation environment, to produce values for surface coverage at 20-s time intervals. These coverage values have the advantage of being absolute and, thus, are comparable between experiments as well as within one experiment (the latter alone is the case for IRRAS).

In order to achieve measurable scattering length density contrasts between the subphase and monolayer, the film components of interest for each experiment were deuterated to give a high positive scattering length density. Specifically, 18.2 MΩ cm water with D₂O from Sigma Aldrich (99.9% atom D) and CaCl₂ from Fisher Scientific (General Purpose Grade) was used to prepare null-reflecting water and 0.1 M CaCl₂ null-reflecting solution subphases. Of the two tail chains that were present in GCB, the saturated chain was deuterated by Avanti Lipids in a custom synthesis specifically for the present study to produce *d*-GCB. Deuteration of the unsaturated chain is more synthetically complicated and was not feasible within our timeframe and budget. *d*₃₁-PA was acquired from Sigma Aldrich (98% atom D; 99%). Hydrogenous GCB (≥ 97%), PA (≥ 99%), and POA (≥ 98.5%) were also acquired from Sigma Aldrich. All film components were spread from dilute CHCl₃ solutions, with CHCl₃ acquired from Sigma Aldrich (99.4%) using a 50 μL spade-ended Hamilton syringe.

The GCB used (both deuterated and hydrogenated) was a mixture of NFA (non-hydroxylated fatty acid) and HFA (hydroxylated fatty acid) forms and, thus, *d*-GCB is a mixture of *d*₃₁-(NFA)GCB and *d*₃₀-(HFA)GCB (see Figures 1 and 2 for details).

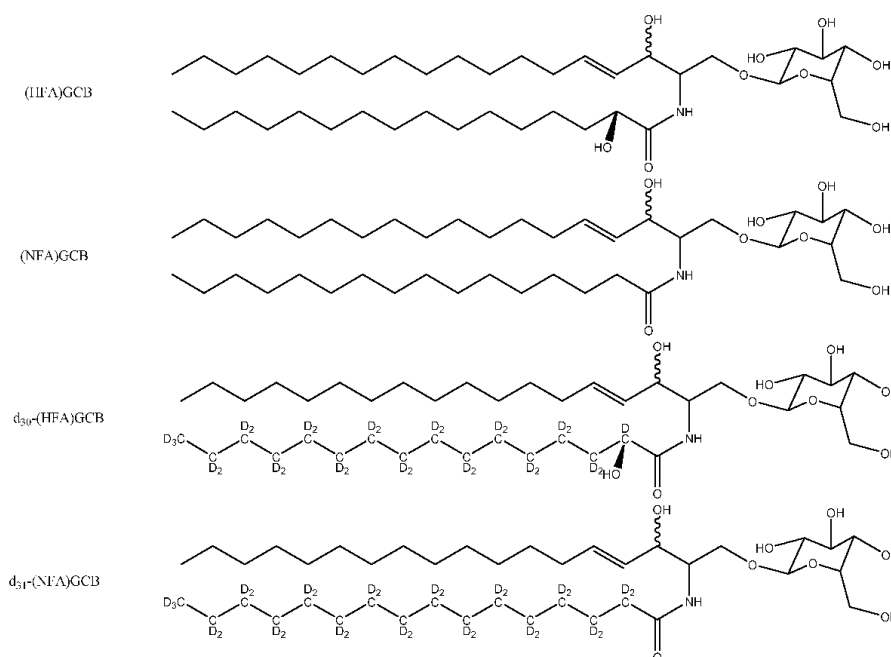


Figure 1. Molecular structures of the galactocerebroside (GCB) species employed; the deuterated GCB species were custom-synthesised for the present study.

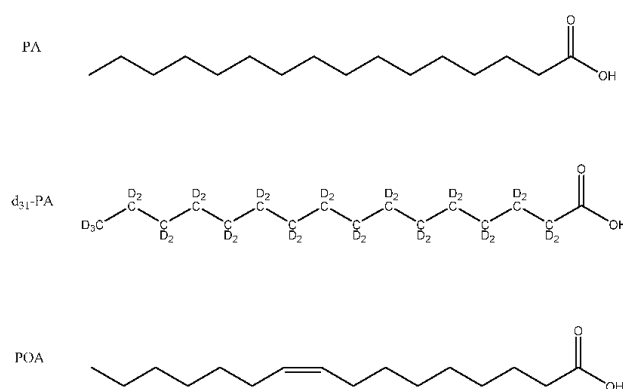


Figure 2. Molecular structures of the fatty acid species employed in the present study.

Due to the need to spread from a CHCl_3 solution (in which GCB is sparingly soluble) rather than the more convenient $\text{CHCl}_3/\text{CH}_3\text{OH}$ solution (in which GCB is much more soluble), in order to achieve reliable monolayer production (the mixed chloroform/methanol solution may not evaporate evenly from the interface and could leave methanol behind in the system which would not be at all realistic as an atmospheric proxy) and considering the need to spread only a small volume ($< 100 \mu\text{L}$) of solution in order to ensure rapid evaporation of the carrier solvent, we spread from a saturated solution of GCB, for which the analysis of the NR data gave a concentration of $\sim 1 \text{ mg mL}^{-1}$. This corresponded to an area per molecule of $\sim 30 \text{ \AA}^2$, and a surface pressure of $\sim 25 \text{ mN m}^{-1}$.

2.2. Fourier Transform Infra-Red Reflection Absorption Spectroscopy (IRRAS)

The integration of in situ Fourier transform infra-red reflection absorption spectroscopy (IRRAS) is logistically complex and makes use of a bespoke reaction and analysis chamber developed by us. This equipment and the setup that was required for conducting these experiments is laid out in detail in a method paper [46]. The general setup for this experiment aligns with that in the method paper apart from where specifically noted. The FTIR spectrometer that was used was a Thermo-Nicolet iS50. We used a purpose-built gas flow cell (volume: ca. 1.5 L) containing a liquid trough (238 mm × 70 mm) and two CaF₂ windows (CrysTran) of 1.5 mm thickness to allow ingress and egress of the IR light. The windows were mounted at an angle of 48° with respect to the vertical to enable normal or near-normal incidence for the IR beam in an angular range of 42 to 55°. A third circular quartz window was mounted above the centre of the liquid trough to allow the height laser to monitor the liquid surface. This window was tilted by 5° from the horizontal in order to avoid a secondary reflection into the height laser. The neutron beam entered and exited the chamber through rectangular quartz windows (50 mm × 68 mm) at either end of the reaction chamber.

Baseline-corrected integrations under CH and CD peaks (a symmetric and asymmetric stretch for each, typically 2110–2070 cm⁻¹ and 2208–2178 cm⁻¹ for CD bonds and 2868–2833 cm⁻¹ and 2945–2898 cm⁻¹ for CH bonds, though small surface interaction effects may cause a slight chemical shift in the location of these bands in some cases) provide a series of peak area against time traces for each reaction, which reflects the presence or absence of CH or CD chains at the surface and follows their evolution throughout the reaction. Due to the IRRAS geometry deployed, the peaks are inverted in the Fourier-transformed spectra, appearing as regions of depressed absorbance. This means that the baseline-corrected integrated peak areas are negative.

The absolute intensity values of these absorbance bands vary significantly between experiments due to slight changes in the geometry of the focusing setup, so no absolute coverage data can be determined from any one experiment. The IRRAS data are strictly semi-quantitative: they allow the inference of trends in the concentration of CH and CD bonds at the surface across one experiment, however not absolute determination of surface concentrations for any one run or meaningful comparisons of concentrations between experiments. The asymmetric stretches are habitually stronger than the symmetric stretches (particularly for CH bonds) in these spectra due to complex quantum chemistry effects that are not the subject of the current study. The shift of the CD stretches to much lower wavenumber ranges than the CH stretches is due to the larger reduced mass of the bonding interaction given the greater mass of the deuterium nucleus.

2.3. Physical Setup and Gas Handling

NO₃• was produced as described previously by Sebastiani et al. [39] through a gas flow system by the reaction of an excess of NO₂ (Scientific and Technical Gases Ltd.; 1000 ppm in air ± 2%) with O₃ in a 5 L reaction bulb. O₃ was generated from O₂ (BOC; 99.999%) using a pen-ray ozoniser (model: SOG-2; Ultra-Violet Products Ltd., Cambridge, UK). An equilibrium mixture of the gases NO₂, NO₃•, and N₂O₅ (in a stream of O₂) was established and then fed into the reaction chamber. The O₂ flow was kept constant at 1.2 L min⁻¹, and the NO₂ flow could be adjusted to achieve the desired [NO₃•] for each experiment. [NO₂] was kept in large excess for all conditions to ensure that O₃ was consumed well before the gas mixture entered the reaction chamber. In previous work, we have shown that NO₂ does not remove organic films from the air–water interface on timescales relevant to our experiments, however it is able to slowly isomerise carbon–carbon double bonds [48]. All plots for the reactions were time-normalised so that $t = 0$ s refers to the point at which oxidant gas was admitted from the mixing bulb holding the equilibrium mixture through a short polytetrafluoroethylene (PTFE) tube into the reaction chamber. This equipment was located within the INTER blockhouse so that the neutron beam had to be blocked with shutters in order to allow the safe ingress and egress of personnel when starting the reaction. As a result, a few of the 20-s time interval data points were always missing from

either side of the start of the reaction. Other gaps in the NR data stem from occasional short-term beam loss at the neutron facility.

2.4. Offline Brewster Angle Microscopy (BAM) with Surface Tension Measurements

Film characterisation for GCB on water, GCB/PA on water, and GCB/PA on an aqueous solution containing CaCl_2 was performed using a Langmuir trough with moveable barriers and a Wilhelmy plate surface pressure measurement system driven by a NIMA IU4 serial interface in order to provide a visual assessment of the nature of the film with a Brewster angle microscope (BAM)—which is particularly interesting for the mixed films—as well as a pressure-area isotherm for the system.

The BAM technique allows the direct observation of ultrathin organic films on transparent dielectric substrates. It is based on the effect that from the clean surface no reflection occurs for *p*-polarized incoming light under the Brewster angle. The technique allows the characterisation of morphological features of monolayers during compression/decompression. Brewster angle microscopy images at characteristic phase transitions of the surface pressure-area isotherm give valuable information on the structural and orientational changes in the monolayer. For instance, the conformation of unsaturation, such as *cis* or *trans*, induces observable differences in domain morphology of fatty acids of the same length. Here, we use the BAM images in a qualitative way, e.g., to demonstrate the effect of Ca^{2+} ions in the subphase on the monolayer morphology.

These monolayers were prepared in the same manner as the films that were used for the neutron reflectometry and IRRAS measurements. The Brewster angle microscope and associated Langmuir trough were made available at the Diamond Light Source. The microscope that was used was an Accurion Nanofilm EP³-096 ellipsometer and BAM operated with the EP³ control software. The Langmuir trough was a NIMA DLS1140 with a variable surface area of between 700 cm² and ~70 cm² (the minimum surface area is limited by the type of barriers used due to the proximity of the BAM objective lens)—a compression ratio of ~10. Due to a small flaw in the objective lens, a banding artefact can be observed in some images. This can normally be corrected by subtracting a clean surface background image from the film images, however, if the brightness of the sample film is substantially different to the brightness of a clean water surface so that images of the two cannot be gathered with the same gain settings, as is the case for the GCB/PA on water system, then this correction is not possible. However, for the cases when this occurred for images that were taken as part of the present study, we believe that the film surface features are on a sufficiently different scale to be visually differentiable from the banding artefact.

All neutron reflectivity, infra-red spectroscopy, and microscopy raw data is available in a data repository (Woden et al., 2018) [49].

3. Results and Discussion

3.1. BAM Film Characterisation

Figure 3 shows a film of GCB on the surface of a pure water subphase. The strong acyl chain van-der-Waals interactions between the GCB molecules cause them to form islands (of less than ca. 15 μm) at low surface pressures. As the surface pressure increases, the film spreads to cover the surface more evenly.

Figure 4 shows a film of a GCB/PA (1:1 *w/w*) monolayer on the same subphase. Due to the BAM setup discussed in the methods section and the unusually bright nature of this film, these pictures are affected by a banding artefact that cannot be fully suppressed with background correction. For similar reasons related to the different gain settings required to gather this set of images, no conclusions can be drawn by comparing the absolute brightness of these images to that of those in Figure 3. What can be determined, however, is that a situation similar to that observed for the pure GCB monolayer, in which islands can be seen at low surface pressures (up to ~10 mN m⁻¹) which are not seen at higher

pressures, holds for this mixed system as well. The effect is weaker than for pure GCB, however is still observed here.

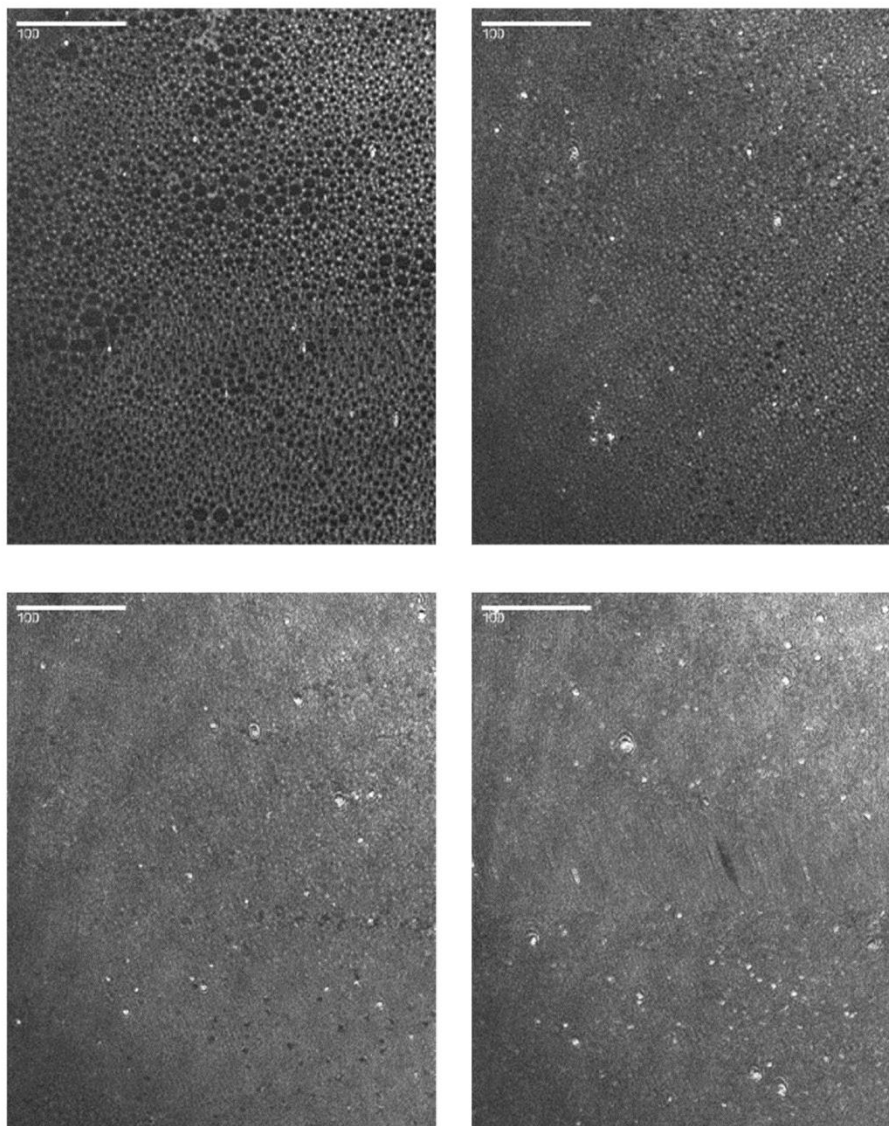


Figure 3. BAM images of a GCB monolayer on water at various surface pressures—scale bar represents 100 μm ; top left, top right, bottom left, bottom right: 1, 5, 10, 25 mN m^{-1} .

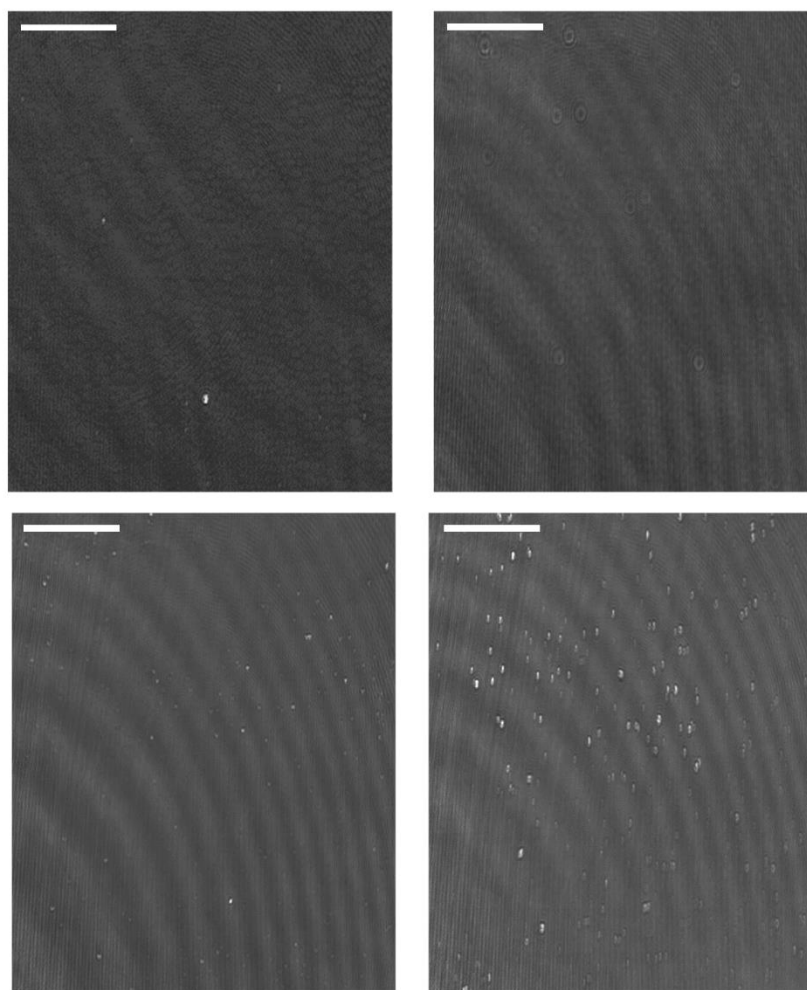


Figure 4. BAM images of a two component (GCB/palmitic acid (PA)) monolayer on water at various surface pressures—scale bar represents 100 μm ; top left, top right, bottom left, bottom right: 1, 5, 10, 25 mN m^{-1} .

Figure 5 shows the same film composition as Figure 4, but now on 100 mM CaCl_2 (aq) instead of pure water. Here, the formation of islands at low surface pressures is much less pronounced, with only a slight mottling showing. This is in line with the observation by Adams and Allen [41] that Ca^{2+} ions stabilise this mixed film through cross-chain interactions.

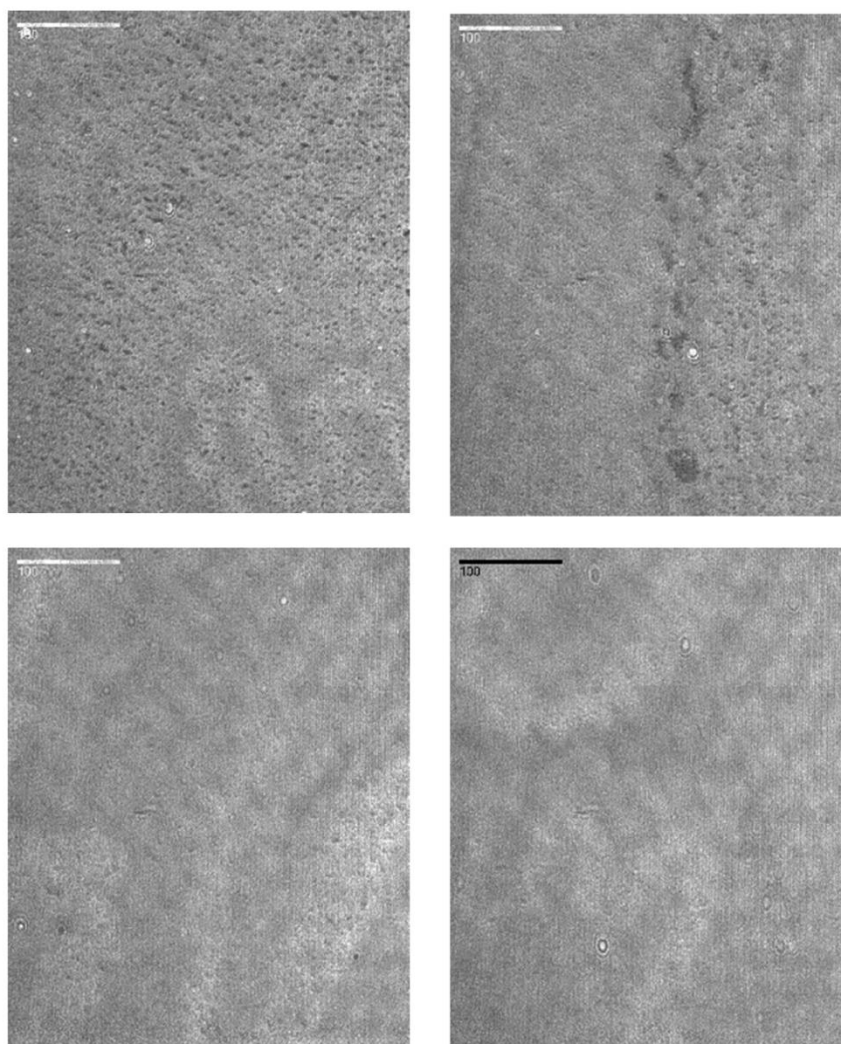


Figure 5. BAM images of a two component (GCB/PA) monolayer on CaCl_2 (aq; 100 mM) at various surface pressures—scale bar represents 100 μm ; top left, top right, bottom left, bottom right: 1, 5, 10, 25 mN m^{-1} .

3.2. Single Component (GCB) Monolayer Oxidation

Figure 6 shows both neutron reflectometry (NR) and IRRAS data from the oxidation of a GCB film on pure water. The injection of $\text{NO}_3\bullet$ into the reaction chamber at $t = 0$ s does not have a noticeable effect on the NR signal (see black symbols and left ordinate). A reflectivity signal in keeping with what was observed at the start of the reaction still remains at the end (the data gap is due to beam down time). It should be noted that this does not mean that no reaction has taken place. The measured neutron signal is only sensitive to the deuterated part of the molecule (i.e., the saturated chain in our case). A reaction at the double bond that removes the unsaturated tail chain from the GCB molecule

is consistent with this neutron signal. The complementary IRRAS data support this hypothesis, as detailed below.

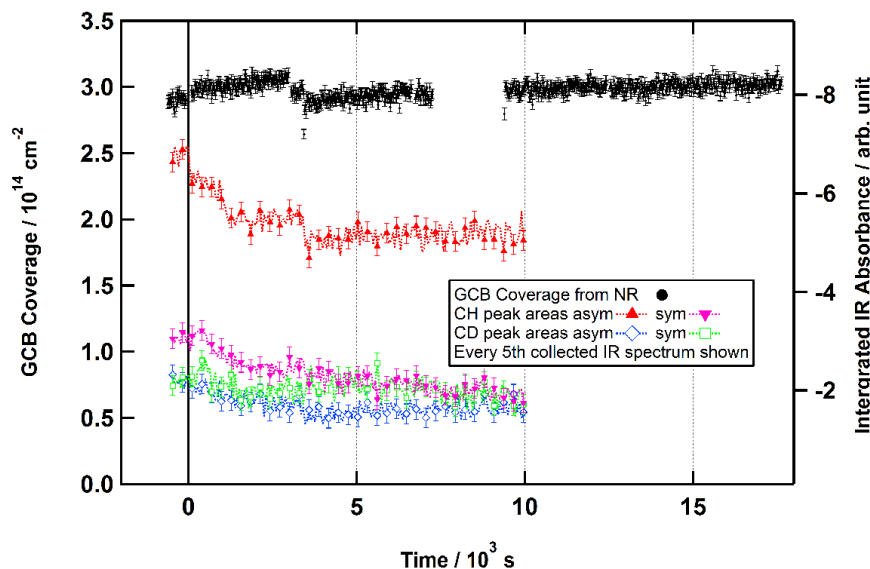


Figure 6. Oxidation of a GCB monolayer on pure water—neutron reflectometry (NR) (black circles and left ordinate) and infra-red reflection absorption spectroscopy (IRRAS) (coloured symbols and right ordinate) data as a function of time. We spread a monolayer of $\sim 6.5 \times 10^{-5}$ L from a $\sim 1 \text{ g L}^{-1}$ spreading solution of *d*-GCB in CHCl_3 . $\text{NO}_3\bullet$ was admitted at $t = 0$ s at a concentration of $\sim 4.4 \times 10^9 \text{ cm}^{-3}$. The integrated absorbance areas for the IRRAS data were calculated for 2110–2070 cm^{-1} and 2208–2178 cm^{-1} for CD bonds (one symmetric and one asymmetric stretch; coloured squares and diamonds) and for 2868–2833 cm^{-1} and 2945–2898 cm^{-1} for CH bonds (one symmetric and one asymmetric stretch; coloured triangles).

IRRAS data (shown as coloured symbols in Figure 6) were collected simultaneously with the neutron data. The IRRAS data run only to around 10,000 s (a little short of 3 h) because movement of the position of the interface due to evaporation makes the IRRAS data unusable due to increasingly poor focussing of the IR beam. This evaporation effect is corrected for in the case of the NR data by continuously reading the location of the air–water interface with a height laser and adjusting the position of the experimental stage upwards to ensure that the NR data remains unaffected. Unfortunately, for technical reasons and due to space limitations at the beamline sample area, the movement of the experimental stage also moves the IRRAS assembly upwards so that the IRRAS signal cannot be recovered from the effects of interfacial drift in this way (the IRRAS signal can only be brought back into focus by manually adjusting the trough height which would lead to the loss of the NR data). However, neutron reflectometry data were collected for a 5 h period for this system, and no significant NR signal reduction was seen over this period (the NR signal varied by a maximum of 10%), as can be seen in Figure 6.

The simultaneous IRRAS data in Figure 6 show that the CD signal remains constant within experimental error, which is in line with the neutron data in Figure 6, however the CH signal does show a reduction over time, which is consistent with an oxidation reaction taking place at the double bond on the hydrogenous chain that would be invisible when relying on NR data alone. A significant CH signal remains, however, which suggests that some hydrogenous material is retained at the air–water interface together with the entire deuterated chain.

Oxidations of GCB monolayers were also carried out on a CaCl_2 (aq) subphase. This did not seem to have an effect on the reaction within experimental uncertainties. The NR and IRRAS data showed very similar patterns to the pure water case, except that the CH signal dropped significantly more (by around 50%) in the salt subphase case. This data is available in the repository (Woden et al., 2018) [49].

3.3. Two Component (GCB/PA) Monolayer Oxidation

To provide a model for cerebrosides distributed in marine aerosols more generally, and to investigate the effects of the attractive surface interaction between PA and GCB described by Adams and Allen [41] on the oxidation, mixed monolayers of d_{31} -PA and d -GCB (1:1 mass ratio) were prepared and oxidised by $\text{NO}_3\bullet$ in the same manner as were the pure d -GCB monolayers. In this case, the neutron reflectometry was sensitive to the deuterated portion of d -GCB and to d_{31} -PA, and IRRAS was sensitive to these in the CD band and additionally to the hydrogenous portion of d -GCB in the CH band.

Figure 7 shows the neutron reflectometry data for this oxidation (black circles and left ordinate), and no significant reduction in the NR signal is observed. PA does not have a double bond and so is not susceptible to rapid attack by $\text{NO}_3\bullet$ as are unsaturated species, therefore it would not be expected to react quickly on the timescales of our experiment (compare the stability of stearic acid monolayers to $\text{NO}_3\bullet$ recently reported by Sebastiani et al. [39]). The lack of any change in neutron reflectometry signal indicates that, as in the case of the single component GCB monolayer, the deuterated (saturated) chain remains at the surface.

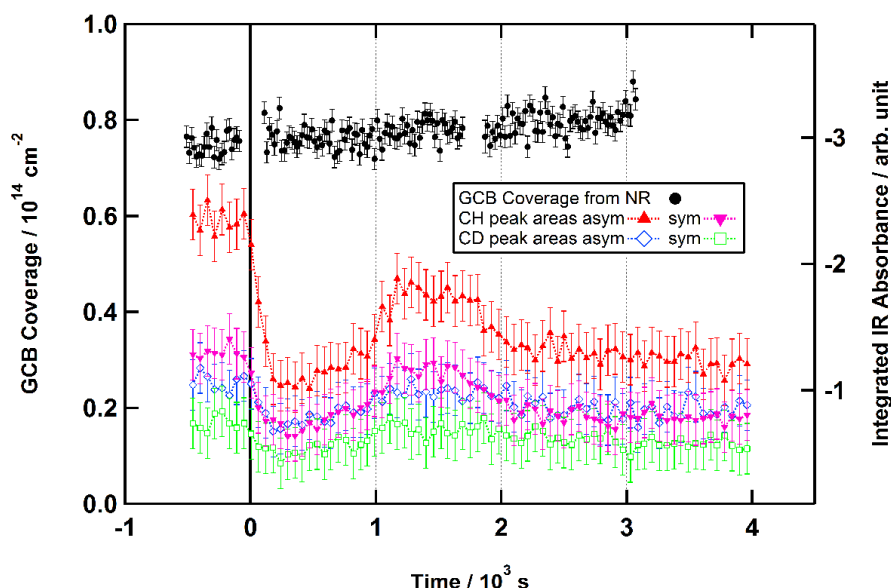


Figure 7. Oxidation of a two component (GCB/PA) monolayer on pure water—NR (black circles and left ordinate) and IRRAS (coloured symbols and right ordinate) data as a function of time. We spread a monolayer of $\sim 6.5 \times 10^{-5}$ L from a spreading solution containing $\sim 0.5 \text{ g L}^{-1}$ of d -GCB and $\sim 0.5 \text{ g L}^{-1}$ of d -PA in CHCl_3 . $\text{NO}_3\bullet$ was admitted at $t = 0$ s at a concentration of $\sim 4.4 \times 10^9 \text{ cm}^{-3}$. The integrated absorbance areas for the IRRAS data were calculated for 2110–2070 cm^{-1} and 2208–2178 cm^{-1} for CD bonds (one symmetric and one asymmetric stretch coloured squares and diamonds) and for 2868–2833 cm^{-1} and 2945–2898 cm^{-1} for CH bonds (one symmetric and one asymmetric stretch; coloured triangles).

The simultaneous IRRAS data for this reaction (shown in Figure 7 as coloured symbols) also show a similar pattern to the GCB monolayer oxidation. The CD peak areas remain constant within experimental error, whereas the CH peak areas decline over the course of the reaction, however do not disappear entirely. The trend is not as clear as for the single component GCB monolayer (after the initial reaction, the peak areas rise slightly again before falling back to their final values), which we attribute to the fact that the GCB/PA system will be rearranging at the air–water interface as the oxidation of the double bond in the hydrogenous GCB tail chain occurs. The IRRAS signal is sensitive to the orientation of molecules at the interface, so some variation due to rearrangements during the reaction is not unexpected.

These data suggest overall that the behaviour of the two component (GCB/PA) monolayer during $\text{NO}_3\bullet$ -initiated oxidation is similar to that of the single component (GCB) monolayer. PA is unreactive, and the double bond in the unsaturated chain of GCB is attacked by the $\text{NO}_3\bullet$, leaving part of that chain and the rest of the molecule (head and saturated chain) at the surface. The longest oxidation carried out for the two-component (GCB/PA) monolayer was 3 h, with a maximum of 15% signal variation during the run (no consistent trend, just variation in signal probably due to rearrangements at the air–water interface). These additional data are available in the repository (Woden et al., 2018) [49].

Adams and Allen [41] reported increased stability for these mixed monolayers with Ca^{2+} in the subphase. We therefore tested oxidation on a CaCl_2 solution subphase as well.

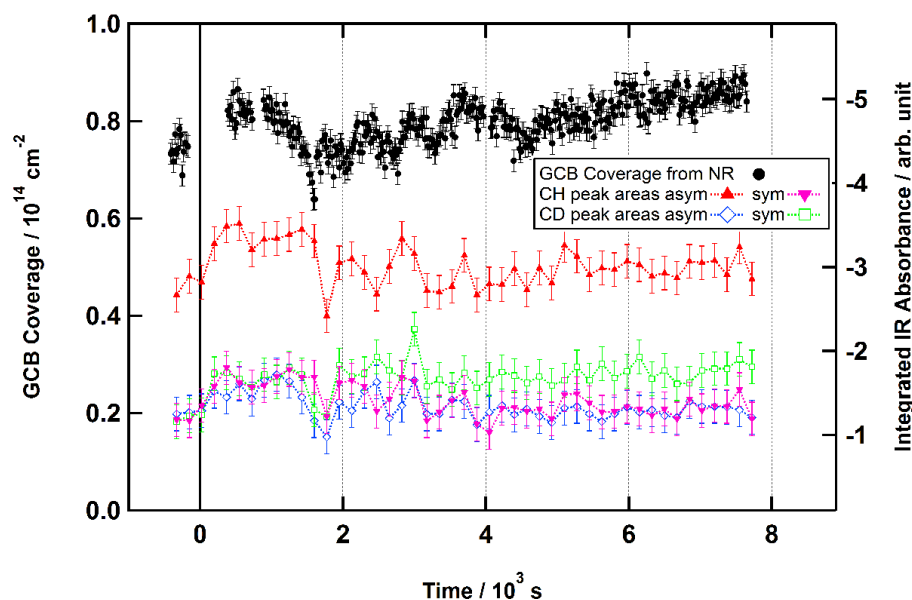


Figure 8. Oxidation of a two component (GCB/PA) monolayer on CaCl_2 aqueous solution—NR (black circles and left ordinate) and IRRAS (coloured symbols and right ordinate) data as a function of time. We spread a monolayer of $\sim 6.5 \times 10^{-5}$ L from a spreading solution containing ~ 0.5 g L^{-1} of *d*-GCB and ~ 0.5 g L^{-1} of *d*-PA in CHCl_3 . $\text{NO}_3\bullet$ was admitted at $t = 0$ s at a concentration of $\sim 4.4 \times 10^9$ cm^{-3} . The integrated absorbance areas for the IRRAS data were calculated for $2110\text{--}2070$ cm^{-1} and $2208\text{--}2178$ cm^{-1} for CD bonds (one symmetric and one asymmetric stretch; coloured squares and diamonds) and for $2868\text{--}2833$ cm^{-1} and $2945\text{--}2898$ cm^{-1} for CH bonds (one symmetric and one asymmetric stretch; coloured triangles).

Figure 8 shows the neutron reflectometry data for oxidation in the presence of Ca^{2+} in the subphase (black circles and left ordinate) and, although a signal oscillation can be seen which likely indicates

surface reorganisation (the formation of domains at the surface can cause inaccuracies in the calculation of surface coverage by a uniform monolayer model as reported by Lu et al. [44]), there is no general trend up or down, suggesting that, once again, the saturated part of GCB and the PA component remain at the surface after oxidation. Simultaneous IRRAS data (shown in Figure 8 as coloured symbols) demonstrate a similar signal variation with no trend up or down from CD or CH traces, suggesting that the attractive interactions between the chains when Ca^{2+} is present in the subphase are sufficient to largely prevent even the unsaturated part of GCB from being oxidised. Indeed, it appears that surprisingly, almost no reaction at all is occurring here—at least not one that is removing significant material from the interface. The longest timescale attempted for this system was slightly short of 3 h, and no removal of material from the interface was observed over this timescale, though the signal was significantly less stable than for the other systems, with around 30% variability between the extremes (coloured symbols in Figure 8), however no more than 10% loss between the starting conditions and the signal after 10,000 s (extended neutron data from the experiment illustrated in Figure 8 are available in the repository, Woden et al., 2018) [49]. A similarly surprising protection of a surfactant from attack by a different oxidant at the air–water interface has very recently been reported by Zhang et al. [50] for $\text{OH}\bullet$ -initiated oxidation of monolayers of 1,2-dipalmitoyl-sn-glycero-3-phosphocholine (DPPC) and 1-palmitoyl-2-oleoyl-sn-glycero-3-phospho-(1'-rac-glycerol) (POPG): cholesterol that is present in the lipid layer appears to be able to increase the order of lipid packing and lower the permeability and hinder subsequent oxidation of the lipid layers by $\text{OH}\bullet$ at the air–water interface.

3.4. Two Component (GCB/POA) Monolayer Oxidation

Introducing a double bond into GCB's co-component by using POA instead of PA should disrupt the formation of a regular, stable film structure. In addition, POA is itself reactive towards $\text{NO}_3\bullet$, as it has a double bond (the reaction of a single component POA monolayer with $\text{NO}_3\bullet$ has recently been reported by us [39]). A *d*-GCB/*h*-POA contrast (1:1 mass ratio) was chosen, since deuterated POA is not readily commercially available and is not the main focus of the present study. Therefore, the neutron reflectometry data (and the CD trace from the IRRAS data) will follow the saturated part of GCB, and the unsaturated part of GCB, as well as the reactive POA, will be represented in the CH trace of the IRRAS data.

Figure 9 shows the neutron reflectometry data from this experiment (black circles and left ordinate) and, once again, the lack of any trend downward suggests that the saturated portion of GCB remains at the interface after oxidation. The fate of the unsaturated portion of GCB is difficult to disentangle from that of the POA component as both contribute to the same IRRAS band and are invisible in the NR data. The longest neutron reflectivity data collection for this system was just below 3 h, with significant signal fluctuations (similar to those seen in Figure 8) of around 40% between the extremes, however no discernible downward trend (a maximum of 10% loss between starting conditions and the signal after 10,000 s); these extended neutron data are available in the repository (Woden et al., 2018) [49].

The IRRAS data in Figure 9 show that the CH peak areas decay to almost unmeasurable levels (only the CH symmetric stretch still registers at the end of the experiment), and this could mean that the unsaturated chain of GCB has been removed from the surface completely. This would contrast with the results from single component (GCB) monolayers, where some CH signal remains. However, there is less GCB overall in this system than in the single component GCB system, and the IRRAS signal is highly dependent upon surface orientation at low concentrations. It is thus possible that there was not a measurable amount of CH signal attributable to GCB unsaturated chains at the start of the reaction, and that the IRRAS data in Figure 9 simply show the reaction of POA. It is generally more difficult to detect IRRAS signals from disordered monolayers such as this [46] (indeed, as mentioned in the caption for Figure 9, only the asymmetric stretch was detectable for the CD bonds in this experiment and, in a repeat experiment, no CD bands were detectable at all). The fact that the CD trace drops when there is no change in the neutron reflectivity signal suggests that a re-orientation of GCB at the surface may occur after POA reacts, making GCB harder to detect by IRRAS. It is thus not possible to say from

the IRRAS data alone whether or not the greater reduction in CH signal for this system indicates any difference in the reaction of the unsaturated chain of GCB. Custom synthesis of different deuteration contrasts could shed light on this: e.g., the study of two component (*d*-POA/*d*-GCB) monolayers would allow a more detailed exploration of this effect, however these compounds are currently not commercially available. Deuteration of the unsaturated tail of GCB would also allow for experiments to probe in greater detail the fate of that part of the molecule.

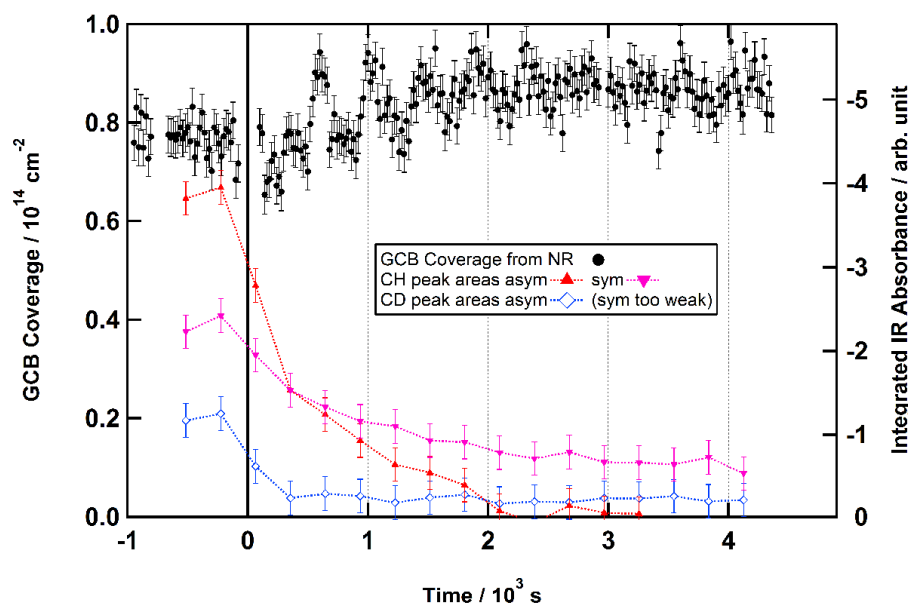


Figure 9. Oxidation of a two component (GCB/POA) monolayer on pure water—NR (black circles and left ordinate) and IRRAS (coloured symbols and right ordinate) data as a function of time. We spread a monolayer of $\sim 6.5 \times 10^{-5}$ L from a spreading solution containing ~ 0.5 g L $^{-1}$ of *d*-GCB and ~ 0.5 g L $^{-1}$ of *h*-POA in CHCl $_3$. NO $_3$ • was admitted at $t = 0$ s at a concentration of $\sim 4.4 \times 10^9$ cm $^{-3}$. The integrated absorbance areas for the IRRAS data were calculated for 2110–2070 cm $^{-1}$ for CD bonds (one asymmetric stretch as blue diamonds; the symmetric stretch was too weak) and for 2868–2833 cm $^{-1}$ and 2945–2898 cm $^{-1}$ for CH bonds (one symmetric and one asymmetric stretch; coloured triangles).

In summary, the neutron reflectometry signal is consistently unmoved by the introduction of the oxidant NO $_3$ •. While the signal is seen to change during the reaction of the mixed GCB/PA film on CaCl $_2$ aqueous solution and of the mixed GCB/POA film on pure water, the reflectivity is not significantly altered between the pre-oxidation and post-oxidation states. This finding suggests the occurrence of re-organisation of the multi-component film surfaces during the reaction. The IRRAS data show different behaviour for the CH and CD stretches, demonstrating the usefulness of our approach of simultaneous observation by NR and IRRAS. The CH stretches show a reduction, though not to zero, for the reactions of pure GCB and for GCB/PA monolayers on pure water, while they show surprisingly no reduction during the reaction of mixed GCB/PA monolayers on CaCl $_2$ aqueous solution. The CH stretches show a reduction to zero for GCB/POA on pure water. The CD stretches are generally weaker and more difficult to reliably detect. However, they are sensitive to the same parts of the molecules as NR, so this is not a significant issue in our experimental system. They do not, within experimental error, show a decrease in signal across the reactions, except for the mixed

GCB/POA monolayers where we have a mixture of two unsaturated surfactants that are both expected to undergo changes during $\text{NO}_3\bullet$ -initiated oxidation.

4. Conclusions

Our neutron reflectometry data clearly show that the key night-time atmospheric oxidant, $\text{NO}_3\bullet$, is unable to remove (or significantly reduce the surface concentration of) a model lipopolysaccharide monolayer (both as a pure monolayer and as a model mixed monolayer with palmitic acid) from either a pure water or salt water subphase on the timescales investigated. These timescales were 5 h for the single component GCB monolayers on a pure water system, and 3 h for the other systems that were investigated. No measurable decrease was observed over these timescales within the margin for error of the measurement. These experimental uncertainties account for the maximum possible losses reported (we have not observed any measurable loss of material from the surface, however simply cannot rule out low loss rates within the margin for error of our experiments). Indeed, $\text{NO}_3\bullet$ is known to have another route to reaction with organic species other than attacking a carbon–carbon double bond [23]: it can abstract hydrogen atoms via a homolytic process to create nitric acid, leaving a free radical on the carbon chain, which can then engage in back-biting reactions and attack O_2 in order to produce a range of oxidised products. However, these alternative reactions are not significantly removing deuterated material from the air–water interface over the timescales that we have studied. We cannot rule out that these reactions are occurring as it is possible that early products from these processes are being produced yet remain at the interface. Nevertheless, in terms of atmospheric consequences, we can confidently state that $\text{NO}_3\bullet$ oxidation does not remove our model marine aerosol monolayers at a rate that is sufficient to render the monolayers atmospherically irrelevant. This imperviousness to removal via oxidative attack on carbon–carbon double bonds is something that has also been observed in samples of aerosols bearing organic surface monolayers that have been collected in the field [35].

Our IRRAS data suggest that some reaction does occur, and that the unsaturated tail of the lipopolysaccharide monolayer is reacting with the oxidant. Surprisingly though, such an oxidative decay is not observed for the mixed monolayer on a CaCl_2 subphase, probably due to the stabilisation of the system by enhanced chain–chain interactions. We are not aware of previous reports of unsaturated surfactants being protected from attack by atmospheric oxidants at the air–water interface via chain–chain interactions induced by ions in the subphase. This is a particularly interesting finding, since it is very likely that in atmospheric conditions a range of ions will be present in the aerosol droplets; therefore this process may provide an alternative explanation [22,51,52] for extended atmospheric residence times that have been found for reactive species and may have important health implications [53].

Both IRRAS and neutron data together are unequivocal that the saturated tail remains at the air–water interface despite exposure to $\text{NO}_3\bullet$. We thus conclude that it is likely that aerosols produced from the sea-surface microlayer at night will remain covered in surfactant molecules on atmospherically relevant timescales; extended atmospheric lifetimes of these molecules may reduce the droplet's surface tension and may also affect the transport of species across the air–water interface.

Author Contributions: B. Woden (née Thomas): experimental setup, design, and assembly; off-line experiments; neutron beam time experiments; data processing and handling; manuscript writing; production of figures. M. Hagreen: neutron beam time experiments. M.W.A. Skoda: initial idea for study; experimental setup, design, and assembly; neutron beam time experiments; manuscript editing; neutron beamline operation. C. Pfrang: initial idea for study; experimental setup, design, and assembly; neutron beam time experiments; manuscript editing; project oversight.

Funding: This research was funded by NERC (National Environmental Research Council), STFC (Science and Technology Facilities Council) and ISIS Neutron and Muon Source (INTER experiment RB 1620451, doi:10.5286/ISIS.E.84424054).

Acknowledgments: The experimental setup was built and assembled in concert with the workshop, soft matter, and sample environment teams at the ISIS Neutron and Muon Source; the Brewster angle microscope was made available by Diamond Light Source.

Conflicts of Interest: The authors declare no conflict of interest. The funders had no role in the design of the study; in the collection, analyses, or interpretation of the data; in the writing of the manuscript; or in the decision to publish the results.

References

1. Gill, P.S.; Graedel, T.E.; Weschler, C.J. Organic films on atmospheric aerosol particles, fog droplets, cloud droplets, raindrops, and snowflakes. *Rev. Geophys.* **1983**, *21*, 903. [[CrossRef](#)]
2. Ellison, G.B.; Tuck, A.F.; Vaida, V. Atmospheric processing of organic aerosols. *J. Geophys. Res.* **1999**, *104*, 11633–11641. [[CrossRef](#)]
3. Donaldson, D.J.; Vaida, V. The influence of organic films at the air-aqueous boundary on atmospheric processes. *Chem. Rev.* **2006**, *106*, 1445–1461. [[CrossRef](#)] [[PubMed](#)]
4. Stevens, B.; Feingold, G. Untangling aerosol effects on clouds and precipitation in a buffered system. *Nature* **2009**, *461*, 607–613. [[CrossRef](#)] [[PubMed](#)]
5. Ambaum, M.H.P. *Thermal Physics of the Atmosphere*, 1st ed.; Wiley-Blackwell: Reading, UK, 2010; ISBN 9780470745151.
6. Barnes, G.T. Permeation through monolayers. *Colloids Surf. A Physicochem. Eng. Asp.* **1997**, *126*, 149–158. [[CrossRef](#)]
7. Gaines, G.L. *Insoluble Monolayers at the Liquid Gas. Interface*; Interscience Publishers: Geneva, Switzerland, 1966.
8. La Mer, V.K. *Retardation of Evaporation by Monolayers: Transport. Processes*; Academic Press Inc.: London, UK, 1962.
9. La Mer, V.K. The transport of water through monolayers of long-chain n-paraffinic alcohols. *J. Colloid Sci.* **1964**, *19*, 673–684. [[CrossRef](#)]
10. Benjamin, I. Chemical Reactions and Solvation at Liquid Interfaces: A Microscopic Perspective. *Chem. Rev.* **1996**, *96*, 1449–1476. [[CrossRef](#)] [[PubMed](#)]
11. Garrett, W.D. Retardation of Water Drop Evaporation with Monomolecular Surface Films. *J. Atmos. Sci.* **1971**, *28*, 816–819. [[CrossRef](#)]
12. Ray, A.K.; Devakottai, B.; Souyri, A.; Huckaby, J.L. Evaporation characteristics of droplets coated with immiscible layers of nonvolatile liquids. *Langmuir* **1991**, *7*, 525–531. [[CrossRef](#)]
13. Rideal, E.K. On the Influence of Thin Surface Films on the Evaporation of Water. *J. Phys. Chem.* **1924**, *29*, 1585–1588. [[CrossRef](#)]
14. Gilman, J.B.; Eliason, T.L.; Fast, A.; Vaida, V. Selectivity and stability of organic films at the air-aqueous interface. *J. Colloid Interface Sci.* **2004**, *280*, 234–243. [[CrossRef](#)] [[PubMed](#)]
15. Lo, J.-H.A.; Lee, W.-M.G. Effect of surfactant film on solubility of hydrophobic organic compounds in fog droplets. *Chemosphere* **1996**, *33*, 1391–1408. [[CrossRef](#)]
16. Mmerekki, B.T.; Chaudhuri, S.R.; Donaldson, D.J. Enhanced Uptake of PAHs by Organic-Coated Aqueous Surfaces. *J. Phys. Chem. A* **2003**, *107*, 2264–2269. [[CrossRef](#)]
17. Mmerekki, B.T.; Donaldson, D.J. Laser induced fluorescence of pyrene at an organic coated air-water interface. *Phys. Chem. Chem. Phys.* **2002**, *4*, 4186–4191. [[CrossRef](#)]
18. Tomoaia-Cotisel, M.; Cadenhead, D.A. The interaction of procaine with stearic acid monolayers at the air/water interface. *Langmuir* **1991**, *7*, 964–974. [[CrossRef](#)]
19. Forestieri, S.D.; Staudt, S.M.; Kuborn, T.M.; Faber, K.; Ruehl, C.R.; Bertram, T.H.; Cappa, C.D. Establishing the impact of model surfactants on cloud condensation nuclei activity of sea spray aerosol mimics. *Atmos. Chem. Phys.* **2018**, *18*, 10985–11005. [[CrossRef](#)]
20. Ruehl, C.R.; Davies, J.F.; Wilson, K.R. An interfacial mechanism for cloud droplet formation on organic aerosols. *Science* **2016**, *351*, 1447–1450. [[CrossRef](#)] [[PubMed](#)]
21. Ovadnevaite, J.; Zuend, A.; Laaksonen, A.; Sanchez, K.J.; Roberts, G.; Ceburnis, D.; Decesari, S.; Rinaldi, M.; Hodas, N.; Facchini, M.; et al. Surface tension prevails over solute effect in organic-influenced cloud droplet activation. *Nature* **2017**, *546*, 637–641. [[CrossRef](#)] [[PubMed](#)]
22. Pfrang, C.; Rastogi, K.; Cabrera, E.; Seddon, A.M.; Dicko, C.; Labrador, A.; Plivelic, T.; Cowieson, N.; Squires, A.M. Complex Three-Dimensional Self-Assembly in Proxies for Atmospheric Aerosols. *Nat. Commun.* **2017**, *8*, 1724. [[CrossRef](#)] [[PubMed](#)]

23. Wayne, R.P.; Barnes, I.; Biggs, P.; Burrows, J.P.; Canosa-Mas, C.E.; Hjorth, J.; Le Bras, G.; Moortgat, G.K.; Perner, D.; Poulet, G.; et al. The nitrate radical: Physics, chemistry, and the atmosphere. *Atmos. Environ.* **1991**, *25*, 1–203. [[CrossRef](#)]
24. Khan, M.A.H.; Cooke, M.C.; Utembe, S.R.; Archibald, A.T.; Derwent, R.G.; Xiao, P.; Percival, C.J.; Jenkin, M.E.; Morris, W.C.; Shallcross, D.E. Global modeling of the nitrate radical (NO₃) for present and pre-industrial scenarios. *Atmos. Res.* **2015**, *164–165*, 347–357. [[CrossRef](#)]
25. Pfrang, C.; King, M.D.; Canosa-Mas, C.E.; Wayne, R.P. Correlations for gas-phase reactions of NO₃, OH and O₃ with alkenes: An update. *Atmos. Environ.* **2006**, *40*, 1170–1179. [[CrossRef](#)]
26. Chapleski, R.C., Jr.; Zhang, Y.; Troya, D.; Morris, J.R. Heterogeneous chemistry and reaction dynamics of the atmospheric oxidants, O₃, NO₃, and OH, on organic surfaces. *Chem. Soc. Rev.* **2016**, *45*, 3731–3746. [[CrossRef](#)] [[PubMed](#)]
27. Pfrang, C.; Martin, R.S.; Canosa-Mas, C.E.; Wayne, R.P. Gas-phase reactions of NO₃ and N₂O₅ with (Z)-hex-4-en-1-ol, (Z)-hex-3-en-1-ol (leaf alcohol), (E)-hex-3-en-1-ol, (Z)-hex-2-en-1-ol and (E)-hex-2-en-1-ol. *Phys. Chem. Chem. Phys.* **2006**, *8*, 354–363. [[CrossRef](#)] [[PubMed](#)]
28. Pfrang, C.; Martin, R.S.; Nalty, A.; Waring, R.; Canosa-Mas, C.E.; Wayne, R.P. Gas-phase rate coefficients for the reactions of nitrate radicals with (Z)-pent-2-ene, (E)-pent-2-ene, (Z)-hex-2-ene, (E)-hex-2-ene, (Z)-hex-3-ene, (E)-hex-3-ene and (E)-3-methylpent-2-ene at room temperature. *Phys. Chem. Chem. Phys.* **2005**, *7*, 2506–2512. [[CrossRef](#)] [[PubMed](#)]
29. Pfrang, C.; Baeza Romero, M.T.; Cabanas, B.; Canosa-Mas, C.E.; Villanueva, F.; Wayne, R.P. Night-time tropospheric chemistry of the unsaturated alcohols (Z)-pent-2-en-1-ol and pent-1-en-3-ol: Kinetic studies of reactions of NO₃ and N₂O₅ with stress-induced plant emissions. *Atmos. Environ.* **2007**, *41*, 1652–1662. [[CrossRef](#)]
30. King, M.D.; Rennie, A.R.; Thompson, K.C.; Fisher, F.N.; Dong, C.C.; Thomas, R.K.; Pfrang, C.; Hughes, A.V. Oxidation of oleic acid at the air–water interface and its potential effects on cloud critical supersaturations. *Phys. Chem. Chem. Phys.* **2009**, *11*, 7699–7707. [[CrossRef](#)] [[PubMed](#)]
31. Thompson, K.C.; Rennie, A.R.; King, M.D.; Hardman, S.J.O.; Lucas, C.O.M.; Pfrang, C.; Hughes, B.R.; Hughes, A.V. Reaction of a Phospholipid Monolayer with Gas-Phase Ozone at the Air–Water Interface: Measurement of Surface Excess and Surface Pressure in Real Time. *Langmuir* **2010**, *26*, 17295–17303. [[CrossRef](#)] [[PubMed](#)]
32. Pfrang, C.; Sebastiani, F.; Lucas, C.O.M.; King, M.D.; Hoare, I.D.; Chang, D.; Campbell, R.A. Ozonolysis of methyl oleate monolayers at the air–water interface: Oxidation kinetics, reaction products and atmospheric implications. *Phys. Chem. Chem. Phys.* **2014**, *16*, 13220–13228. [[CrossRef](#)] [[PubMed](#)]
33. Sebastiani, F.; Campbell, R.A.; Pfrang, C. Complementarity of neutron reflectometry and ellipsometry for the study of atmospheric reactions at the air–water interface. *RSC Adv.* **2015**, *5*, 107105–107111. [[CrossRef](#)]
34. Stewart, D.J.; Almabrok, S.H.; Lockhart, J.P.; Mohamed, O.M.; Nutt, D.R.; Pfrang, C.; Marston, G. The kinetics of the gas-phase reactions of selected monoterpenes and cyclo-alkenes with ozone and the NO₃ radical. *Atmos. Environ.* **2013**, *70*, 227–235. [[CrossRef](#)]
35. Jones, S.H.; King, M.D.; Ward, A.D.; Rennie, A.R.; Jones, A.C.; Arnold, T. Are organic films from atmospheric aerosol and sea water inert to oxidation by ozone at the air–water interface? *Atmos. Environ.* **2017**, *161*, 274–287. [[CrossRef](#)]
36. Huang, Y.; Barraza, K.M.; Kenseth, C.M.; Zhao, R.; Wang, C.; Beauchamp, J.L.; Seinfeld, J.H. Probing the OH Oxidation of Pinonic Acid at the Air–Water Interface Using Field-Induced Droplet Ionization Mass Spectrometry (FIDI-MS). *J. Phys. Chem. A* **2018**, *122*, 6445–6456. [[CrossRef](#)] [[PubMed](#)]
37. Rossignol, S.; Tinel, L.; Bianco, A.; Passananti, M.; Brigante, M.; Donaldson, D.J.; George, C. Atmospheric photochemistry at a fatty acid-coated air–water interface. *Science* **2016**, *353*, 699–702. [[CrossRef](#)] [[PubMed](#)]
38. Gross, S.; Iannone, R.; Xiao, S.; Bertram, A.K. Reactive uptake studies of NO₃ and N₂O₅ on alkenoic acid, alkanolate, and polyalcohol substrates to probe nighttime aerosol chemistry. *Phys. Chem. Chem. Phys.* **2009**, *11*, 7792–7803. [[CrossRef](#)] [[PubMed](#)]
39. Sebastiani, F.; Campbell, R.A.; Rastogi, K.; Pfrang, C. Nighttime oxidation of surfactants at the air–water interface: Effects of chain length, head group and saturation. *Atmos. Chem. Phys.* **2018**, *18*, 3249–3268. [[CrossRef](#)]
40. Tervahattu, H.; Juhanoja, J.; Kupiainen, K. Identification of an organic coating on marine aerosol particles by TOF-SIMS. *J. Geophys. Res.* **2002**, *107*, 4319. [[CrossRef](#)]

41. Adams, E.; Allen, H. Palmitic Acid on Salt Subphases and in Mixed Monolayers of Cerebrosides: Application to Atmospheric Aerosol Chemistry. *Atmosphere* **2013**, *4*, 315–336. [[CrossRef](#)]
42. Laß, K.; Friedrichs, G. Revealing structural properties of the marine nanolayer from vibrational sum frequency generation spectra. *J. Geophys. Res.* **2011**, *116*, C08042. [[CrossRef](#)]
43. Facchini, M.C.; Rinaldi, M.; Decesari, S.; Carbone, C.; Finessi, E.; Mircea, M.; Fuzzi, S.; Ceburnis, D.; Flanagan, R.; Nilsson, E.D.; et al. Primary submicron marine aerosol dominated by insoluble organic colloids and aggregates. *Geophys. Res. Lett.* **2008**, *35*, L17814. [[CrossRef](#)]
44. Lu, J.R.; Thomas, R.K.; Penfold, J. Surfactant layers at the air/water interface: Structure and composition. *Adv. Colloid Interface Sci.* **2000**, *84*, 143–304. [[CrossRef](#)]
45. Campbell, R.A.; Saaka, Y.; Shao, Y.; Gerelli, Y.; Cubitt, R.; Nazaruk, E.; Matyszewska, D.; Lawrence, M.J. Structure of surfactant and phospholipid monolayers at the air/water interface modeled from neutron reflectivity data. *J. Colloid Interface Sci.* **2018**, *531*, 98–108. [[CrossRef](#)] [[PubMed](#)]
46. Skoda, M.W.A.; Thomas, B.; Hagreen, M.; Sebastiani, F.; Pfrang, C. Simultaneous neutron reflectometry and infrared reflection absorption spectroscopy (IRRAS) study of mixed monolayer reactions at the air–water interface. *RSC Adv.* **2017**, *7*, 34208–34214. [[CrossRef](#)]
47. Nelson, A. Co-refinement of multiple-contrast neutron/X-ray reflectivity data using MOTOFIT. *J. Appl. Crystallogr.* **2006**, *39*, 273–276. [[CrossRef](#)]
48. King, M.D.; Rennie, A.R.; Pfrang, C.; Hughes, A.V.; Thompson, K.C. Interaction of nitrogen dioxide (NO₂) with a monolayer of oleic acid at the air–water interface—A simple proxy for atmospheric aerosol. *Atmos. Environ.* **2010**, *44*, 1822–1825. [[CrossRef](#)]
49. Woden, B.; Skoda, M.W.A.; Hagreen, M.; Pfrang, C. Electronic Supplementary Information for the Manuscript “Night-Time Oxidation of a Monolayer Model for the Air–Water Interface of Marine Aerosols—A Study by Simultaneous Neutron Reflectometry and in Situ Infra-Red Reflection Absorption Spectroscopy (IRRAS)”. 2018. Available online: <http://researchdata.reading.ac.uk/168/15/Readme.txt> (accessed on 12 September 2018).
50. Zhang, X.; Barraza, K.M.; Beauchamp, J.L. Cholesterol provides nonsacrificial protection of membrane lipids from chemical damage at air–water interface. *Proc. Natl. Acad. Sci. USA* **2018**, *115*, 3255–3260. [[CrossRef](#)] [[PubMed](#)]
51. Pfrang, C.; Shiraiwa, M.; Pöschl, U. Chemical ageing and transformation of diffusivity in semi-solid multi-component organic aerosol particles. *Atmos. Chem. Phys.* **2011**, *11*, 7343–7354. [[CrossRef](#)]
52. Shiraiwa, M.; Ammann, M.; Koop, T.; Pöschl, U. Gas uptake and chemical aging of semisolid organic aerosol particles. *Proc. Natl. Acad. Sci. USA* **2011**, *108*, 11003–11008. [[CrossRef](#)] [[PubMed](#)]
53. Socorro, J.; Lakey, P.S.J.; Han, L.; Berkemeier, T.; Lammel, G.; Zetzsch, C.; Pöschl, U.; Shiraiwa, M. Heterogeneous OH Oxidation, Shielding Effects, and Implications for the Atmospheric Fate of Terbutylazine and Other Pesticides. *Environ. Sci. Technol.* **2017**, *51*, 13749–13754. [[CrossRef](#)] [[PubMed](#)]



© 2018 by the authors. Licensee MDPI, Basel, Switzerland. This article is an open access article distributed under the terms and conditions of the Creative Commons Attribution (CC BY) license (<http://creativecommons.org/licenses/by/4.0/>).

4.2 – Supplementary Information

As *Atmosphere* is very much an atmospheric chemistry focused journal, the neutron reflectometry data was presented purely as processed time series, with no presentation of underlying reflectivity data as might be expected if it had been presented to a more physical chemistry minded audience, or as a direct thesis chapter. For the same reason, discussion of the exact scattering length calculations involved and finer points of the fitting of monolayer parameters to reflectivity data were covered only in outline in the method section, and treated somewhat as a black box in the main body of the paper, to focus the discussion on the atmospherically relevant material. Slightly more quantitative discussion of the reflectometry side of the matter would be expected in a thesis, so this small supplementary section provides some example data and a discussion of the fitting model used.

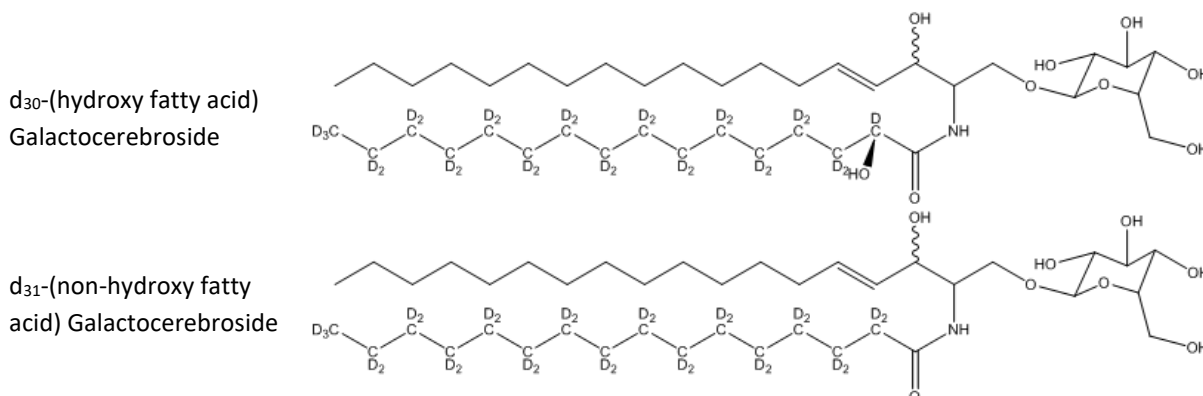


Figure 4.1 – Deuterated galactocerebroside molecules.

The partially deuterated form of GCB used in these experiments (see Figure 4.1) has a head and two tails, one of which is deuterated. The head is $C_6H_{11}O_6$, the ‘main’ h-tail is $C_{18}H_{34}O$, and the ‘side’ d-tail is $C_{16}H_2D_{30}O_2N$ in the hydroxy form, and $C_{16}HD_{31}ON$ in the non-hydroxy form. This leads to full formulae of $C_{40}H_{47}D_{30}O_9N$ and $C_{40}H_{46}D_{31}O_8N$ for those two forms respectively. Averaging across the two forms, this leads to scattering lengths (b) of 33.6 fm for the head, -1.71 fm for the h-tail, and 322 fm for the d-tail.

Clearly the d-tail dominates the neutron scattering, and is what will primarily be detected in the reflectometry signal. The h-tail has a scattering length of <1% the magnitude of the whole molecule, and so changes in it (such as the removal of most of it via cleavage at its double-bond that we propose is the only reaction taking place in our experiments) would be undetectable via neutron reflectometry.

Fitting monolayer parameters to reflectivity data for these systems is not entirely trivial, as the GCB layer might well be expected to have some structure in the z -direction in terms of scattering length, which would affect the reflectivity. The scattering length of the head group is large enough that the system might be better modelled by a bilayer, with a thin head-layer of $b \approx 33.6$ fm immediately above the null-reflecting water, a thicker tails-layer of $b \approx 320$ fm above that, and (null-reflecting) air as the top semi-infinite layer.

A bilayer model of this nature and a monolayer model with one layer of $b \approx 354$ fm were both used to fit the data, and the monolayer model worked significantly better. It was not that the bilayer model failed to fit, but that it didn’t predict substantially different reflectivity data than did the monolayer model, and the greater number of parameters available in the bilayer model made it harder to converge on a fit.

Fixing thickness parameters and assuming the head layer did not react would have allowed for calculation of GCB surface concentration values that matched those calculated using the monolayer model, but this would only have been justified had the data required the more complex bilayer model to be used in order to achieve a good fit. As the monolayer model also fit the data, it was preferentially

used as it was the simpler model, and the more complex model added nothing in terms of predictive value, and only introduced more parameters.

Physically, this makes sense as the GCB molecules would have to be tightly and regularly packed for the system to resemble a bilayer, and this would not be expected in all conditions. Indeed, the BAM images in the paper for pure GCB show significant disorder, with light and dark domains (characterised as 'islands' in the paper due to their structure) present at various surface pressures. The enhanced stability of the mixed GCB/PA on CaCl_2 (aq) system (see *Atmosphere* paper in section 4.1 and Adams *et al.*, reference 41 of said paper) means a more bilayer-like situation may have obtained during those runs, but it was still not sufficiently defined to make the bilayer model a better fit than the monolayer model.

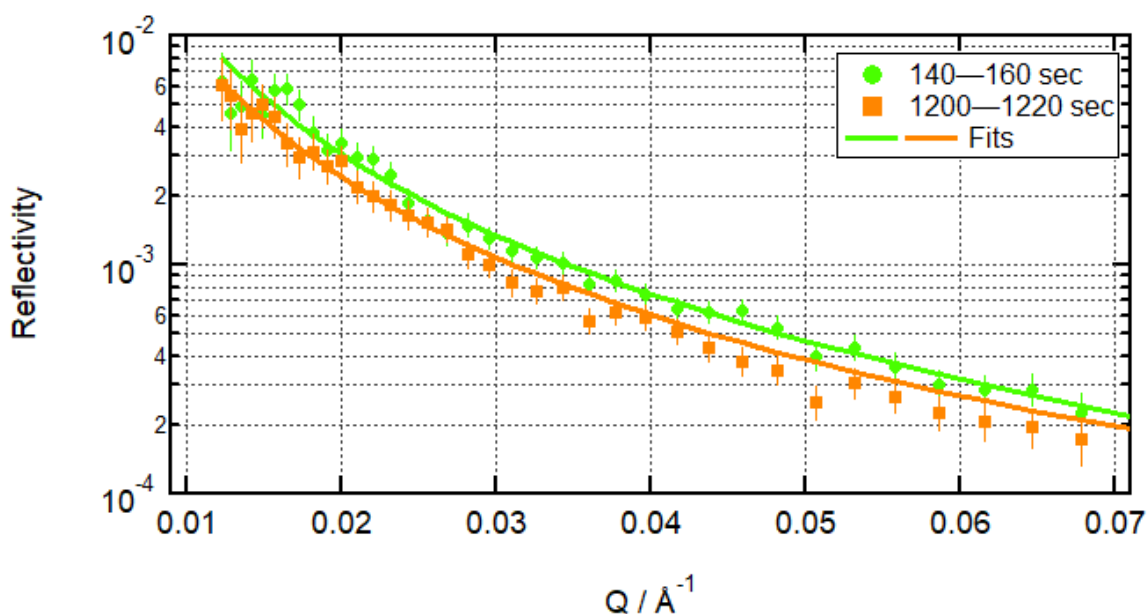


Figure 4.2 – Exposure of a mixed $d_{30/31}$ -GCB/ d_{31} -PA monolayer on CaCl_2 (aq) subphase to NO_3^* radicals; R vs Q reflectivity plots at two points in the exposure selected for maximum range of reflectivity.

Figure 4.2 shows the quality of the monolayer fit, which does not display a significant enough oscillation to allow for good fitting of a bilayer model. These reflectivity curves are taken from the experiment shown in Figure 8 of the paper, which was the experiment that displayed the most variability in neutron reflectivity signal. These two reflectivity curves are taken from a high and a low point in the fit. As the only reaction occurring was the removal of the h-tail beyond the double bond (see sections 3.2 to 3.4 of the *Atmosphere* paper in section 4.1), no experiment showed decay of reflectivity over time, so this is the largest range of different reflectivity data available.

This more detailed explanation for the choice of a monolayer, rather than bilayer, model for fitting, and more quantitative explanation for why the h-tail cannot be observed through neutron reflectometry data, should supplement the more high-level discussion of these matters in the *Atmosphere* paper, and should satisfy a reader more familiar with neutron scattering than the journal's intended audience.

Chapter 5 – Low Temperature Oleic Acid Ozonolysis; *Atmospheric Chemistry and Physics* Paper

One of the most important developments in the capabilities of the apparatus used for the work underpinning this thesis was the introduction of temperature control. This facilitated the study of reactions at temperatures that more realistically mimic those commonly experienced in the troposphere than is possible without temperature control, where room temperature (not at all representative temperature for much of the troposphere) is the only accessible thermal condition.

Work on ozonolysis of pure oleic acid monolayers at low temperatures produced a number of interesting findings, which were written up into a paper that has been submitted for publication in *Atmospheric Chemistry and Physics (ACP)*. That paper forms this chapter. Like the paper focused on GCB, it contains its own introduction and methods section which are pared down analogues of the extended introduction and methods chapters (Chapters 1 and 2) of this thesis that focus on justifying work on a particular system. As the paper has not yet completed peer review and been published, it is possible that the finally published format will differ slightly from the draft form presented here. An electronic supplement that accompanies the paper is also reproduced here.

I wrote this paper and the supplement, and I will be the first author credited in publication. Dr Christian Pfrang (primary PhD supervisor) and Dr Maximilian Skoda (secondary PhD supervisor and INTER beamline scientist) provided input on the draft and the figure presentation, as well as suggesting the split between the main paper and the supplement. The work described in the paper was led by me, with assistance and guidance from Drs Pfrang and Skoda. Practical assistance on the beamline experiments on INTER at ISIS and FIGARO at the ILL was provided by Evita Hartmane of the University of Reading, Curtis Gubb and Adam Milsom of the University of Birmingham, and Sophie Ayscough of the University of Edinburgh. The FIGARO beamline scientist was Dr Armando Maestro of the ILL. Some of the deuterated material used in the experiments was synthesised by Dr James Tellam of ISIS.



Ozonolysis of fatty acid monolayers at the air–water interface: organic films may persist at the surface of atmospheric aerosols.

Ben Woden^{1,2}, Max W. A. Skoda², Adam Milsom³, Armando Maestro⁴, James Tellam² and Christian Pfrang^{3,5}.

¹Department of Chemistry, University of Reading, Whiteknights, Reading, RG6 6AD, UK.

²ISIS Neutron and Muon Source, Science and Technology Facilities Council, Rutherford Appleton Laboratory, Didcot, OX11 0QX, UK.

³School of Geography, Earth and Environmental Sciences, University of Birmingham, Edgbaston, Birmingham, B15 2TT, UK.

⁴Institut Laue Langevin (ILL), 71 Avenue des Martyrs, Grenoble, 38000, France.

⁵Department of Meteorology, University of Reading, Whiteknights Road, Reading, RG6 6BG, UK.

Correspondence to: Christian Pfrang (c.pfrang@bham.ac.uk)

Abstract. Ozonolysis of fatty acid monolayers was studied to understand the fate of organic-coated aerosols under realistic atmospheric conditions. Specifically, we investigated the effects of temperature and salinity on the degradation of oleic acid at the air–water interface and the persistence of the aged surfactant film at the surface. The presence of a residual film is of atmospheric importance, as surface monolayers affect the physical properties of the droplets and because of the role they play in cloud formation. This occurs via several effects, most notably via surface tension reduction. The interplay between atmospheric aerosol loading and the formation, nature, and persistence of clouds is a key uncertainty in climate modelling. Our data show that a residual surface film, which we suspect to be formed of nonanoic acid and a mixture of azelaic and 9-oxononanoic acids, is retained at the interface after ozonolysis at near-freezing temperatures, but not at room temperature. Given the low temperature conditions used here are atmospherically realistic, the persistence of a product film must be considered when assessing the impact of unsaturated fatty acid partitioned to the air–water interface. The presence of stable (non-oxidisable) reaction products also opens the possibility of build-up of inert monolayers during the aerosol life-cycle with potential implications for cloud formation. Furthermore, we measured the kinetic behaviour of these films and found that the reactions are not significantly affected by the shift to a lower temperature with rate coefficients determined to be $(2.2 \pm 0.4) \times 10^{-10} \text{ cm}^2 \text{ s}^{-1}$ at $21 \pm 1 \text{ }^\circ\text{C}$, and $(2.2 \pm 0.2) \times 10^{-10} \text{ cm}^2 \text{ s}^{-1}$ at $2 \pm 1 \text{ }^\circ\text{C}$.

30

1 Introduction

Organic films are formed at the surfaces of aerosol particles in the atmosphere (Gill et al., 1983; Ellison et al., 1999; Sareen et al., 2013; Noziere et al., 2014; Kroflic et al., 2018; Gerard et al., 2019), and the partitioning of organic components in this manner changes the physical properties of the aerosol particle and its chemical reactivity (Ruehl et al., 2016; Ovadnevaite et



35 al., 2017). A key review (Donaldson and Vaida, 2006) has brought together various emerging trends in the study of these
films and their relevance to atmospheric processes. An important area of interest regarding these films concerns the
interactions between atmospheric aerosol particles and clouds. This relationship is complex and difficult to measure or
predict (Stevens and Feingold, 2009), and resolving the role played by organic monolayers at the surface of aerosol particles
is part of solving this puzzle. The organic species that are contained in these surface films oxidise in the atmosphere and may
40 produce low volatility products that form secondary organic aerosols. If the oxidation of these species is prevented,
accelerated, or otherwise modified by the partitioning of the reactant into a surface monolayer, then this will have
implications for the contribution of that reactant to aerosol loading. More importantly, the presence of a surface monolayer
changes the physical and chemical properties of the aerosol particle itself.

This study focuses on monolayers at the air–water interface as would be seen on aqueous aerosol droplets, but the concept is
45 likely broadly transferrable to any aerosol particle with an organic film coating. These monolayers are relevant, as they
decrease the surface tension of water (Donaldson and Vaida, 2006; Ambaum, 2010); the surface tension of aqueous droplets
plays a key role in the growth and formation of clouds (Ambaum, 2010; Ovadnevaite et al., 2017). Furthermore, the
monolayer can act as a barrier to water uptake, retard droplet evaporation, and inhibit the transfer of atmospheric species
between the air and water phases (Rideal, 1924; La Mer, 1962, 1964; Gaines, 1966; Garrett, 1971; Ray et al., 1991;
50 Benjamin, 1996; Barnes, 1997; Li et al., 2019). It can also act as a ‘2D solvent’ for normally water-insoluble species that
could not partition to a water aerosol or modify the solvation behaviour of soluble species (Tomoaia-Cotisel and Cadenhead,
1991; Cohen Stuart et al., 1996; Mmereki and Donaldson, 2002; Mmereki et al., 2003; Gilman et al., 2004).

This catalogue of effects upon the aerosol particle caused by the presence of an organic monolayer coating shows the
importance of establishing the lifetime and ageing of these monolayers in the atmosphere, and this has been the focus of
55 previous research (e.g. Hung et al., 2005; Knopf et al., 2005; Voss et al., 2007; Gross et al., 2009; King et al., 2009; Pfrang et
al., 2014; Sebastiani et al., 2018).

Oleic acid has been a monolayer component of particular interest, as it is a major contributor to both anthropogenic organic
emissions (it is mostly produced by meat cooking (Shrivastava et al., 2007) and is the dominant component of such
emissions (Allan et al., 2010)) and biogenic marine aerosols (Tervahattu et al., 2002; Fu et al., 2013). Its ubiquity in such
60 aerosols has allowed it to serve as a benchmark molecule for more complex mixtures of organic surfactant produced by such
anthropogenic activity (Zahardis and Petrucci, 2007). While there are numerous studies of pure oleic acid or high oleic acid
content droplets and their oxidation reactions (e.g. King et al., 2004; Voss et al., 2007; Last et al., 2009; Pfrang et al., 2017),
work on the oxidation of an oleic acid monolayer at the air–water interface in particular has been comparatively scarce (King
et al., 2009; Skoda et al., 2017; Sebastiani et al., 2018)

65 Ozone (O_3) and nitrate radicals (NO_3^{\cdot}) are important night-time oxidants (e.g. Hung et al., 2005; Gross et al., 2009;
Sebastiani et al., 2018; Woden et al., 2018), while O_3 and hydroxyl radicals ($^{\cdot}OH$) are the key day time oxidants (see Chen et
al., 2020 for a recent study of heterogeneous OH reactions on organic aerosols). Of these three primary atmospheric oxidants
 O_3 is the only one present during the day and night and the present study is focused on ozonolysis, i.e. oxidation by O_3 .



The initial reaction of O_3 with oleic acid is chemically well understood, and is laid out in Scheme 1 (compare King et al., 2009; see also Gallimore et al., 2017). It proceeds via an attack on the carbon–carbon double-bond at the centre of the molecule. The two reaction pathways resulting from the two possible collapses of the molozonide lead to a total of four initial reaction products. These products are nonanoic acid, nonanal, 9-oxononanoic acid, and azelaic acid (Zahardis and Petrucci, 2007). The fate of these products after the ozonolysis of an oleic acid monolayer is the subject of debate (Voss et al., 2007; King et al., 2009).

75 The presence of a product partitioned to the interface after reaction is the most important question for atmospheric impact, as a monolayer remaining after ozonolysis may perpetuate the modifications to the properties of an aerosol droplet due to the persistence of the organic character at the air–water interface even after ozonolysis (Ellison et al., 1999; Donaldson and Vaida, 2006).

The aim of this study is to extend the understanding of oleic acid monolayer ozonolysis in atmospherically relevant conditions by investigating the impact of low temperatures and saline subphases. King et al. (2009) investigated a variety of saline subphases, but did not study differences in ozonolysis behaviour between the monolayers spread upon them at room temperature, and to our knowledge no studies have yet investigated the effects of near-freezing temperatures which are common in the lower troposphere (Grotjahn, 2015), where these reactions occur. Our study also incorporates simultaneous characterisation by infrared reflection absorption spectroscopy (IRRAS) as a secondary analysis technique, using a bespoke reaction/analysis chamber recently developed for this purpose (Skoda et al., 2017).

2 Methodology

This research was performed on the specular neutron reflectometry instruments INTER at the ISIS Neutron and Muon Source and FIGARO at Institut Laue Langevin (ILL) and builds on previous work by this research group on the oxidation of floating monolayers at the air–water interface performed at these facilities (Pfrang et al., 2014; Sebastiani et al., 2015; Skoda et al., 2017; Sebastiani et al., 2018; Woden et al., 2018).

2.1 Neutron Reflectometry

A review paper (Lu et al., 2000) details how neutron reflectometry can be used to determine the surface concentration of organic films present as a monolayer at the air–water interface. In short, neutron reflectivity depends on the differences between concentrations of atoms with a characteristic neutron scattering length in adjacent thin layers of material. Simplifications of the equations describing this system are possible when studying just one layer (the organic monolayer) at the interface between air (which essentially has a scattering length density (SLD) of zero) and a ‘null reflecting’ or ‘air-contrast matched’ subphase (a subphase prepared to have a neutron SLD of zero, matching that of air). Null reflecting matched water was prepared as a solution of D_2O (99.9 % Atom D; Sigma-Aldrich) 8.8 % v/v in 18.2 MΩ H_2O . Null



reflecting sodium chloride solution subphase was prepared with 35 g NaCl (< 99 %, Sigma-Aldrich) in 900 mL H₂O and 58
100 mL D₂O. This preparation compensates for the scattering length of the salt ions with a slightly different H₂O/D₂O ratio.

The reflectivity (fraction of incident neutrons reflected; R) varies as a function of the energy and reflection angle of the incident neutrons (expressed as momentum transfer (Q)) and the SLD (ρ) and thickness (τ) of the monolayer as expressed in Eq. (1) (based on Lu et al., 2000).

$$\frac{Q^4 R}{16\pi^2} \cong 4\rho^2 \sin^2 \frac{Q\tau}{2} \quad (1)$$

105 The SLD and layer thickness characteristic of the system can then be inferred from the relationship between reflectivity and momentum transfer as measured by the instrument. The two parameters are fitted as a combined $\rho\tau$ value, which corresponds to a surface concentration of scattering length, from which the surface concentration of oleic acid can be determined as the scattering length of oleic acid is known ($b = 315$ fm). Reflectivity curves of R vs Q are collected at 20 s intervals throughout the reaction and fitted using MOTOFIT (Nelson, 2006), to give $\rho\tau$ values for each timeslice. These fitted $\rho\tau$ values can be
110 converted into surface concentration (Γ) values for oleic acid (Eq. (2), based on Lu et al., 2000).

$$\Gamma = \frac{\rho\tau}{b} \quad (2)$$

In order for the layer to stand out sufficiently from the other phases, a deuterated form, d_4 -oleic acid, was used. Spreading onto an aqueous subphase will cause the acidic deuterium to be exchanged with the subphase, so we use the scattering length of oleic acid with 33 deuterium atoms (315 fm) to calculate the surface concentration from $\rho\tau$ values. For product
115 identification studies, we used custom-synthesised half-deuterated d_{18} -oleic acid.

2.2 Reaction chamber for simultaneous infrared reflection absorption spectroscopy (IRRAS)

The reactions were carried out in a bespoke chamber developed by this research group. The chamber is designed to provide a controlled and confined environment in which the monolayer can be oxidised by a gas phase oxidant while under analysis by both neutron reflectometry and IRRAS. The integration of IRRAS analysis *in situ* during the neutron reflectometry
120 experiment is non-trivial, and the entire analysis and reaction setup is described in detail in a method paper (Skoda et al., 2017). For this study it had been further developed to allow for cooling of the subphase, in order to access relevant atmospheric temperature conditions. IRRAS integration is primarily intended to facilitate the study of mixed monolayers, in which one component can be deuterated (for neutron reflectometry) and the other left non-deuterated (and thus easily measurable by IRRAS). This work focuses on a film composed solely of oleic acid, so the IRRAS analysis served as an
125 additional semi-quantitative method to follow the oleic acid component, rather than as a method to follow non-deuterated film components (Skoda et al., 2017). During experiments using d_{18} -oleic acid, IRRAS data were sensitive to the deuterated and non-deuterated halves of the molecule (via the C–D and C–H absorption bands, respectively). The IRRAS equipment was only available at the INTER beamline, given the large and flexible sample environment available at that instrument.



130 Baseline-corrected integrations under C–D peaks (symmetric and asymmetric stretch) provide a series of peak area against
time traces for each reaction, which reflect the presence or absence of CD chains at the surface and traces their evolution
throughout the reaction.

While IRRAS can measure deuterated components (the IR absorbance bands are shifted to a lower wavenumber,
distinguishing them from the absorbance bands associated with non-deuterated components), the sensitivity in this region is
135 much lower, as these bands are weaker and more affected by the gas-phase atmosphere above the organic film. This meant
that the IRRAS measurements could not distinguish the residues left at low temperatures from background noise. Figure S13
in the Electronic Supplement shows an example of IRRAS data from an ozonolysis experiment on INTER.

2.3 Materials

*d*₃₄-oleic acid was used (one batch custom-synthesised by the ISIS Deuteration Facility and one batch purchased from
Sigma-Aldrich at 98 % Atom D; 99.9 %); the half-deuterated *d*₁₈-oleic acid was produced by the ISIS Deuteration Facility;
140 O₃ was produced for the reaction using a commercial pen-ray ozoniser (UVP Ltd, Cambridge) to ozonise a stream of O₂
(99.999 %; BOC) regulated to a flow of 1.2 L min⁻¹ (20 cm³ s⁻¹) using an electronic mass flow controller to an O₃
concentration of $(1.43 \pm 0.05) \times 10^{13}$ cm⁻³; the ozoniser was calibrated offline using UV-Vis absorption at 254 nm and an
absorption cross-section value of 1.13×10^{-17} cm⁻² (Daumont et al., 1992). Mixing ratios of ozone in the chamber were in the
range 126 – 2010 ppb.

145 3 Results and Discussion

Prior to the ozonolysis studies we characterised the stability of the oleic acid monolayers at room and reduced temperatures
(see Section S1 of the Electronic Supplement with π -A isotherms presented as Figures S1 and S2). After confirming the
reactant film's stability, we exposed the monolayers to ozone following the reaction by neutron reflectometry and IRRAS in
the conditions described below.

150 3.1 Pure Water Subphase – Room Temperature

At room temperature, on a pure water subphase, we found that the removal of deuterated material from the surface is
consistent with complete oxidation. The remaining reflectivity signal is not reliably distinguishable from zero and cannot be
fitted except by using a fixed background. This is consistent with the results of Voss et al. (2007), but not with those of King
et al. (2009), where a stable product film was reported.

155 Figure 1 shows a time series of fitted ρr values (proportional to surface concentration) for 120 s time slices of the reaction,
with an O₃ concentration of 323 ± 9 ppb introduced at $t = 0$ s. The absence of points after ca. 800 s indicates that the
numerical fits fail to converge after this point, demonstrating that the reflectivity is not consistent with an adsorbed surface
layer (i.e. not measurably different from the background). Figure S3 in the Electronic Supplement illustrates this as a pair of



before/after R vs Q reflectivity curves. The figure also shows data for a salt subphase reaction, which will be discussed
160 below.

This result of no measurable residue was reproducible across 11 different ozonolysis runs carried out across an $[O_3]$ range of
126 ± 15 to 2010 ± 238 ppb as parts of three different beamline experiments at two different neutron facilities (ISIS INTER
RB 1810793 and RB 1710483; ILL FIGARO 9-10-1518).

3.2 Salt Water Subphase – Room Temperature

165 Sea spray aerosol will naturally be salty, and a simple monovalent common salt, sodium chloride (aq; 36 g L⁻¹) was used as a
rough model of sea spray for this experiment.

At room temperature, the reaction also proceeded to completion, with no residual deuterated material detectable at the
interface. King et al. (2009) found that there was no detectable difference in the nature of the reaction between a room
temperature pure water subphase and a room temperature salted subphase (across a wider variety of salts than studied here),
170 and these results support that comparative conclusion (though King et al. actually measured a residual layer in both
conditions while the present study has measured no residual layer in either condition; this experiment supports their finding
that no *difference* between the reaction in the two conditions is detectable using this method). Figure 1 shows the results in
these conditions as a time series of 120 second time slices (a lack of points indicates no convergence in the numerical fit; a
pair of before/after R vs Q reflectivity curves can be found as Figure S4 in the Electronic Supplement).

175 3.3 Atmospheric Temperature Conditions: Pure Water Subphase

Experiments were then undertaken to determine if the reaction proceeds in a similar manner at atmospherically more relevant
temperatures of 3 ± 1 °C. A clear difference between this reaction and the reaction at room temperature is observable. At the
lower temperature, the neutron reflectometry data clearly show a residual signal from deuterated material at the interface
after the initial reaction of oleic acid and ozone. On heating the subphase to room temperature, this residue disappears. This
180 is inferred from the fact that, after heating, the reflectivity signal is consistent with that for a null reflecting water surface,
meaning that no deuterated material remains at the surface (or so little that it cannot be distinguished from this background
condition;¹ the reflectivity data for such a null reflecting air–water interface are included in the electronic supplement (Figure
S11).

The kinetics of the reaction, however, do not seem to differ markedly in the two temperature conditions. A fuller treatment
185 of the kinetics of the reaction (in which we confirm no significant difference in 2nd-order rate coefficients for the two
temperature conditions) will follow later.

¹ The exact value of this cut-off point varies depending on measurement conditions and count time, but SLD*thickness
values as low as 5 × 10² cm⁻¹, corresponding to ca. 5 % of the oleic acid concentration spread initially, have been reliably
measured with this experimental setup.



Figure 2 shows a time evolution plot for these conditions. It demonstrates that a stable residual layer remaining after ozonolysis for more than one hour can be measured and fitted over 120-s counting periods, and that this is no longer the case after heating to 20 °C. The figure also shows data from a salt subphase reaction, which will be discussed below. Figure 3 draws particular attention to the distinction between the situation after ozonolysis and the situation after heating by showing R vs Q reflectivity curves before ozonolysis, after ozonolysis and after heating (the analogous plot for the salt water condition is included in the electronic supplement as Figure S5).

This measurable residue after ozonolysis is reproducible across 18 experiments carried out with a wide $[O_3]$ range from 126 ± 15 ppb to 2010 ± 238 ppb. The lower end of this range is close to mixing ratios of 100 ppb that have been observed in polluted conditions (Warneck, 1999) and thus approaches atmospherically realistic concentrations as far as feasible within the time constraints of beamtime experiments for such a rigorous study.

Twelve of these runs (those obtained at the high-flux instrument FIGARO at ILL; experiment 9-10-1518) were carried out to determine the kinetic behaviour of this reaction, and were therefore performed using a high dQ/Q fast (5 s per measurement) chopper and slit setup optimised for kinetic measurements of the fast reactions afforded by high $[O_3]$. These runs were used to measure 2nd-order rate constants for the reaction (this is discussed in a later section) rather than to precisely quantify the residual material; the setup is not conducive to precise quantitative measurements of the rather weak reflectivity signals produced by the residual layer. Therefore, these 12 runs support the qualitative conclusion that a residue remains after ozonolysis, but were not used to quantify this residue.

Four runs (INTER; experiment RB 1810793) were carried out with the precise and reproducible temperature control system and with the neutron reflectometry setup optimised to facilitate precise measurement of a low intensity reflectivity signal (low dQ/Q ; long count times facilitated by Event Mode data collection). These were assumed to be sampling from a Gaussian distribution of residue intensities, and on that basis a mean deuterated residue fraction of 11.1 % of the initial spread material was calculated, with a 95 % confidence interval of ± 1.9 % (absolute).

3.4 Atmospheric Ageing Simulation

In order to provide further assurance that the measured residue was a genuine product monolayer and not, for example, a temperature-dependent fitting artefact (perhaps due to a shift in roughness due to the temperature change), an experiment was performed in which, after ozonolysis of an oleic acid monolayer, more oleic acid was added and another ozonolysis reaction carried out, and then yet more oleic was added, and a third ozonolysis reaction carried out. If the measured residual reflectivity is due to a product monolayer, then this should build-up over multiple spreading and ozonolysis cycles. This was indeed observed, adding further weight to the conclusion that the measured residual reflectivity stems from the presence of a product monolayer that is impervious to further ozonolysis.

Figure 4 shows a time series representing reflectivity from the air–water interface at 120-s time slices throughout this process, and clearly demonstrates the gradual build-up of a product monolayer. As well as illustrating that this is a real product, not a temperature-dependent measurement artefact, this represents a possible process in the real atmosphere, in



220 which reactive species could be repeatedly adsorbed to the surface and engage in reactions which leave small amount of unreactive material behind, gradually building up an unreactive monolayer. The atmospheric implications of this, which are potentially significant, are discussed in the *Wider Atmospheric Implications* section.

Figure 5 further illustrates this as a series of R vs Q reflectivity curves for each spreading and ozonolysis (as well as for a final heating step; data for 2nd and 3rd spreading steps are omitted and only fits shown as all three data series heavily overlap), and Figure S6 in the Electronic Supplement focuses in on the build-up of the product monolayer by excluding the spreading R vs Q curves from the plot and zooming in on the post-ozonolysis reflectivity data. In Figure 5, the data points for the spreading of additional material (two series) are removed for clarity (they very closely overlap the initial spreading data), and only the fits are shown.

3.5 Atmospheric Temperature Conditions: Salt Water Subphase

230 Ozonolysis reaction was also carried out on the simple monovalent sea salt solution model subphase. At the same temperatures where a residue was observed on pure water ($3 \pm 1^\circ\text{C}$), a residue was not reliably measurable for the salt-water subphase: only one out of five runs carried out with the temperature control setup produced a measurable residue, and it is possible that this residue was not stable, but was still slowly disappearing – see discussion below on the unexpected kinetics of the reaction in these conditions. This could be because no residue remains under these conditions, or because whatever residue does remain is close to the detection limit for this technique.

However, at still colder temperatures not accessible on a pure water subphase ($-2 \pm 1^\circ\text{C}$), a residue is reliably measurable. Figure 2 shows a time evolution for a reaction in these conditions, and Figure S5 in the Electronic Supplement shows the corresponding R vs Q plots for spreading, ozonolysis, and heating.

This result was produced in duplicate (INTER experiment RB 1810793). Using the same assumption of sampling from a Gaussian distribution of measured residues as a fraction of initially deposited deuterated material as used in the pure water at $3 \pm 1^\circ\text{C}$, the mean deuterated residue fraction of 7.3 % was calculated, with a 95 % confidence interval of $\pm 0.45\%$ (absolute). The upper confidence bound of this mean lies below the lower confidence bound of the mean for the pure water at $2 \pm 1^\circ\text{C}$. This supports the conclusion that a little less product monolayer remains at the interface in the salt water at $-2 \pm 1^\circ\text{C}$ condition than in the pure water at $3 \pm 1^\circ\text{C}$ condition.

240 A basic visual appraisal of the time evolution of this reaction (see Figure 2) also suggests a considerable difference in the kinetics of the reaction compared with those seen at room temperature, and on pure water at low temperatures. Instead of the linear-to-exponential decay (either to no signal, or to a residual signal) seen under other conditions, the reaction appears to follow a linear-to-exponential decay at first, before switching to a much slower roughly linear decay to the final residual monolayer. This shape was reproducible across three runs under these conditions, as well as in five runs with the salt subphase at $3 \pm 1^\circ\text{C}$. One of these five runs in which a residue was detectable may have simply been a slow linear decay that was not allowed to run to completion – as this arresting of exponential decay and replacement with a much slower linear



decay was unexpected, it was initially difficult to distinguish from the stable residual monolayer, as seen in pure water at 3 ± 1 °C and after the slow linear decay in salt water at -2 ± 1 °C.

We can currently only speculate about what exactly is causing this deviation from expected stretched exponential decay in
255 the low temperature salt water conditions. The most likely explanation seems to be that some deuterated products are
building up on the surface throughout the reaction and then slowly partitioning away from the interface (in a process which
goes to completion at 3 ± 1 °C but not at -2 ± 1 °C).

3.6 Atmospheric Product Elucidation With Partially Deuterated Reactants: Pure Water Subphase

In order to understand what the atmospheric impacts of this product monolayer are likely to be, it is important to understand
260 its composition. The ozonolysis of oleic acid (see Scheme 1) produces four initial products: nonanoic acid, nonanal, azelaic
acid and 9-oxononanoic acid.

Nonanoic acid is the most obviously amphiphilic product, and thus the prime candidate picked out in the past for possible
membership in a post-ozonolysis monolayer (King et al., 2009). Nonanal has been reported as partitioning to the gas phase
upon oxidation of methyl oleate monolayers (McNeill et al., 2007). The surfactant activity of azelaic acid is under debate,
265 with Voss *et al.* suggesting no surfactant activity (Voss et al., 2007) and Tuckermann taking the opposite view (Tuckermann,
2007). The solubility of azelaic acid (2.4 g L^{-1} (Tuckermann, 2007)) is much higher than that of nonanoic acid (0.28 g L^{-1}
(Gilman et al., 2004)), so, in a reaction producing both products, azelaic acid is more likely to partition into the bulk rather
than to the interface, although there is no conclusive evidence that it does not partition to the interface. King et al. (2009)
suggest that it most likely partitions to the bulk. 9-Oxononanoic acid is not as well studied as the other products, and
270 therefore is the hardest to predict as regards to its partitioning. King et al. (2009) suggest tentatively that it does not partition
to the interface.

From the results discussed so far and knowledge of the volatility, solubility, and amphiphilicity of the candidate species, it is
reasonable to dismiss nonanal from consideration due to its measured partition to the gas phase in a very similar reaction,
and due to the lack of any obvious significant amphiphilicity in the structure of the molecule. The results discussed so far do
275 not allow discernment between nonanoic acid, azelaic acid and 9-oxononanoic acid, all of which, if present as product
monolayers, could produce the observed results.

However, the use of a partially deuterated form of oleic acid allows for some discernment between possibilities. Deuteration
of only the tail-side of the double-bond of the oleic acid molecule (shown in teal in Scheme 1) facilitates an ozonolysis
reaction in which two of the products (nonanal and nonanoic acid) will be deuterated (and thus detectable via neutron
280 reflectometry) and the other two (9-oxononanoic acid and azelaic acid) will not be deuterated (and thus will not be detectable
via neutron reflectometry).

Depending on the makeup of the product monolayer, the measured residue (as a fraction of initial deuterated material) will
vary from nothing (signifying a product monolayer made up entirely of azelaic acid and/or 9-oxononanoic acid) to twice the



relative amount (the same absolute amount if the same initial surface concentration of oleic acid is assumed) as in the d_{34} case (signifying a product monolayer made up entirely of nonanoic acid).

This experiment was carried out on a pure water subphase at 3 ± 1 °C and the result was intermediate between these two possible extremes. The fraction of deuterated material remaining at the interface was calculated for five ozonolysis reactions and the mean deuterated residue fraction was 9.8 %, with a 95 % confidence interval (assuming sampling from a Gaussian distribution as before) of ± 2.0 % (absolute). The confidence interval here heavily overlaps with the confidence interval for the mean deuterated residue fraction for the d_{34} experiment, so the two values are not significantly different. Indistinguishable fractional deuterated residue means that, from the same oleic acid surface concentration starting point, the deuterated residue present in a d_{18} experiment is half of what it is in a d_{34} experiment. This implies a product monolayer made up of roughly equal molar amounts of nonanoic acid and azelaic and/or 9-oxononanoic acids (the ratio between these latter two cannot be determined by this method, as both are deuterated in a d_{34} experiment and non-deuterated in a d_{18} experiment).

Figure 6 shows a representative example of a time series of 120-s time slices for this reaction on pure water, as well as the reaction on a salt subphase. The absolute amount of deuterated material in the residue is about half of that seen for the d_{34} experiment in the same conditions (see Figure 2), and this comes close to the detection limit for 120-s count times in this neutron reflectometry setup. This results in many non-converging fits for the product monolayer, making its identification via this method of analysis alone difficult. However, taking longer time slices allows for a reliable discernment of a product monolayer, as the quality of the reflectivity statistics scales with the square root of count time (assuming a constant neutron flux). This is also illustrated in the stage-by-stage R vs Q reflectivity plots displayed in Figure S7 in the Electronic Supplement.

A topping-up and re-oxidisation experiment was also carried out with d_{18} -oleic acid, and the results were analogous to those for the d_{34} -oleic acid experiment (except scaled down by a factor of two). This demonstrates that both the nonanoic acid and azelaic/9-oxononanoic acid components of the product monolayer can be built up over time (if only nonanoic acid were to build up, then the build-up of fractional deuterated residue would be faster in the d_{18} experiment; if only azelaic/9-oxononanoic acid were to build up, then no build-up would be observed in the d_{18} experiment). These data are included in the electronic supplement (Figures S9 and S10).

3.7 Atmospheric Product Elucidation With Partially Deuterated Reactants: Salt Water Subphase

A series of d_{18} experiments was also run for the salt water subphase at -2 ± 1 °C in which measurable residue was observed for d_{34} -oleic acid ozonolysis. This allowed investigation of the likely makeup of the product monolayer in the same way as under the pure water 3 ± 1 °C conditions. However, the yet lower absolute amounts of residual deuterated material in this experiment posed sensitivity problems for this method of measuring the residue, and therefore the conclusions that can be drawn about the composition of the product monolayer in the salt water -2 ± 1 °C conditions are less secure than those that can be drawn about the composition of the product monolayer on pure water at 3 ± 1 °C discussed above.



In two out of three runs, a residue was detected. This could be because the residue was genuinely absent in the third run, or because it was simply below the detection threshold. Treating the run in which no residue was measurable as a measurement of zero residue yields a mean fractional deuterated residue of 5.6 % with a 95 % confidence interval of ± 2.9 % (absolute) for this system. This may be a slight underestimate of the true value due to the treatment of below-threshold residue as zero residue.

What can be said is that the product monolayer is not composed of all or almost-all nonanoic acid, as that would produce a significantly higher fractional deuterated residual in the d_{18} case than in the d_{84} case which can be ruled out by our data. It is not possible to say with confidence that the composition of this product monolayer is similar to that observed in the pure water $3 \pm 1^\circ\text{C}$ conditions (a roughly equal mixture of nonanoic acid and azelaic/9-oxononanoic acids), as the data are also consistent with somewhat lower relative levels of nonanoic acid (though not none at all, as that would produce no measurable residue).

It must be noted that, in this particular case, an assumption had to be made that the reaction would have proceeded to completion within 4000 s, and that anything measured after that point was a stable residue. This is because the residue was, in all these d_{18} salt water $-2 \pm 1^\circ\text{C}$ cases, below the detection threshold for a 120-s count time. This meant that the reaction could not be followed to ascertain at which point the system was stable in order to define a period over which the residue could be more accurately measured using a single reflectivity curve compiled over a long count time. As the saltwater trace in Figure 2 (low temperature) shows, the reaction on salt water at low temperatures proceeds to completion over a much longer time frame than the pure water equivalent.

In order to measure the stable residue, the 120 second interval time series graph is first prepared, and the slope of that graph is then used to determine at what point a stable residue has formed, and the time period during which that graph is flat is then averaged over to create the single “after ozonolysis” reflectivity curve which is shown in the R vs Q reflectivity graphs and used to determine the fractional deuterated residue values. For instance, Figure 2 shows that the signal is no longer declining after 4000 s, so the time period used for the “after ozonolysis” reflectivity curve in Figure S4 is 4000 – 4500 s (heating began at 4500 s). For all fractional deuterated residue calculations except these last (for d_{18} salt water $-2 \pm 1^\circ\text{C}$), the 120 second time series interval graphs have been able to guide the time integration ranges for the step-by-step R vs Q reflectivity curves (see Fig. S7 in the Electronic Supplement).

However, for the d_{18} salt water $-2 \pm 1^\circ\text{C}$ experiment, the absolute signal from the residue was so low that 120-s count times were not sufficient. As a result, the reaction was assumed to have completed by 4000 s (longer than any observed reaction times), and signal was averaged from this point until heating in order to quantify the residue.

Figures 6 and S8 (in the Electronic Supplement) show a time series and R vs Q reflectivity plots for these conditions. The time series plot demonstrates that any residue is below the detection limit for 120 seconds of counting, however, the 500 seconds over which the “after ozonolysis” reflectivity curve is calculated affords good enough data to discern a residue.



3.8 Atmospheric Product Stability: Temperature Threshold

350 It has been demonstrated that a residue impervious to further ozonolysis remains at the interface after ozonolysis of an oleic acid monolayer by gas phase ozone at 3 ± 1 °C on a pure water subphase and at -2 ± 1 °C on a 36 g L^{-1} NaCl aqueous solution. However, it would be useful to establish across what ranges of temperature this product monolayer persists.

For the salt water subphase, no residue can be observed at 3 ± 1 °C. This does not mean there is certainly no residue, as it could simply be below our detection limit. For the pure water subphase it is already clear, with easily measurable residue at 3 ± 1 °C (and more of it than on salt water at -2 ± 1 °C), that the product monolayer is more stable at higher temperatures than on salt water. In order to investigate how stable it is, a product monolayer was gradually heated to see if there was a critical ‘threshold temperature’ above which it would be rapidly removed from the interface.

This experiment was performed on the FIGARO reflectometer at the ILL (experiment 9-10-1518) and showed that the product film was stable at up to 7 ± 1 °C, though there was a slight linear decay in product monolayer surface concentration with increasing temperature. On further heating to 12 ± 1 °C, no ‘threshold temperature’ was observed but, at this higher temperature, the linear decay ran into the detection limits of the neutron reflectometry setup. This could mean that the monolayer is not stable at or above 12 ± 1 °C, or it could mean that it simply continues to gradually linearly decay with rising temperature above 12 ± 1 °C, but passed the detection limit of the setup used for this experiment. Either way, the product monolayer is certainly stable up to 7 ± 1 °C, but definitely not above 12 ± 1 °C (upper limit).

365 It is important to note that a monolayer produced at 3 ± 1 °C and then being stable at up to around 12 ± 1 °C does not mean that a reaction carried out at 12 ± 1 °C would definitely produce a stable monolayer. However, this temperature ramping experiment at least provides a hint for the range of temperatures over which these product monolayers might persist. Most of the troposphere is below 10 °C, so these conditions are highly atmospherically relevant.

Hung and Tang (2010) suggested that the physical state of products from the ozonolysis of solid state oleic acid particles by O_3 might be temperature-dependent across a $4 - 9$ °C temperature range, and it is worth considering whether the effect we report in present work is linked to this phenomenon, as there is overlap between this transition temperature range and the $6 - 13$ °C transition range we observe.

Figure 7 shows the temperature-ramping experiment in detail. The temperature of the subphase is controlled by varying the temperature of a coupled coolant bath. For the experiments discussed thus far, the temperature of the subphase can be measured before each experiment, allowing the offset between bath and subphase to be measured and an accurate assessment of the subphase temperature via direct measurement used for each experiment. For this ramping experiment, it was not practical to measure the subphase temperature directly for every step. Instead, the relationship between bath and subphase temperatures were used to define a linear relationship between bath and subphase temperatures that was deemed sufficiently accurate given the existing ± 1 °C uncertainty. Diurnal temperature variations that could have disturbed this relationship were largely eliminated using air conditioning to maintain the temperature of the experimental area at around 15 °C, which was also key in reducing the impact of condensation. The bath was set to -1 °C for ozonolysis, then increased by 1 °C at $t =$



1035 s and every 300 s following until 5°C (corresponding to a measured subphase temperature of 7 °C) was reached after 2535 s. A single step to a bath temperature of 11 °C, which corresponds to a subphase temperature of around 12 °C was performed at $t = 3260$ s.

385 3.9 Kinetic Analysis of Oleic Acid Ozonolysis

Experiments were performed on the FIGARO reflectometer at the ILL (experiment 9-10-1518) to elucidate the effect of temperature changes on the kinetics of the reaction. The ozonolysis reaction was performed with $[\text{O}_3]_{\text{gas}}$ ranging between 126 ± 15 and 1005 ± 119 ppb. A pseudo-1st-order rate coefficient (k_1) for each reaction was calculated by fitting a modified exponential developed in previous work by this group in order to account for the fact that $[\text{O}_3]_{\text{gas}}$ initially builds up in the reaction chamber and thus rises steeply at the start of the reaction as initial mixing occurs within the chamber (Pfrang et al., 2014). The traditional 1st-order exponential equation that describes a 2nd-order reaction occurring with an excess of one reactant (in this case, O_3) is modified to (Pfrang et al., 2014):

$$390 \quad \Gamma(t) = \Gamma_0 e^{-k_1 \left(t - \frac{v}{f} \left(1 - e^{-\frac{f}{v} t} \right) \right)} \quad (3)$$

The expected exponential relationship between surface concentration (Γ) and time (t) is modified by the inclusion of a second exponential function that includes constants for the gas flow rate (f), which is $20 \text{ cm}^3 \text{ s}^{-1}$ for these experiments, and chamber volume (v), which is $2.1 \times 10^3 \text{ cm}^3$, but which requires replacement with an ‘effective chamber volume’. The derivation of Eq. (3) is presented in previous work (Pfrang et al., 2014).

It is important to note that this analytical treatment is not a complete description of the processes at work throughout the reaction. Transient reaction products at the interface are, due to their deuterated nature, measured along with the reactant film throughout the reaction if and when they are present (this is why the technique is sensitive to a residual product film). As a result, fitting this analytical model to the data needs to take this into account. A number of assumptions have to be made about the precise way in which ozone mixes into the chamber. These are discussed in detail in Section S3 of the Electronic Supplement. Here, we present and discuss the results of this fitting procedure.

Figure 8 displays fitted k_1 values for reactions under a variety of $[\text{O}_3]_{\text{surf}}$ conditions at 21 °C and 2 °C, and 95 % confidence intervals for fits of k_2 values ($k_2 = k_1/[\text{O}_3]_{\text{surf}}$) to these data.

$[\text{O}_3]_{\text{surf}}$ values were calculated from $[\text{O}_3]_{\text{gas}}$ values by using a Henry’s law solubility constant for O_3 in organics of $[\text{organic}]/[\text{gas}] = 11.7$ (unitless) and assuming the same layer thickness of 2 nm. This solubility constant is consistent with the value used previously in ozonolysis experiments by King et al. (2009) and is informed by the work of Smith et al. (2002). The error in each fitted k_1 value, as noted in Section S3 of the Electronic Supplement, is dominated by uncertainty in model fitting at the start of each reaction. Uncertainty in $[\text{O}_3]_{\text{surf}}$ arises from uncertainties in the calibration of the pen-ray ozoniser, which was performed using Beer-Lambert law UV absorbance at 254 nm using an extinction coefficient of $1.13 \times 10^{17} \text{ cm}^{-2}$ (Daumont et al., 1992).



- The fitted k_2 values for these two conditions (\pm a 95 % confidence interval) are $(2.2 \pm 0.4) \times 10^{-10} \text{ cm}^2 \text{ s}^{-1}$ and $(2.2 \pm 0.2) \times 10^{-10} \text{ cm}^2 \text{ s}^{-1}$ at 21 °C and 2 °C, respectively.
- 415 Our experiments observe either no difference, or a difference too small to be reliably detected (a difference of < 10 % might not be noticeable given the uncertainty in fitted k_1 parameters and $[\text{O}_3]$ calibration). This is a similar situation to that found by Hung and Tang (2010), who observed, for ozonolysis of liquid oleic acid, a very slight dependence on temperature based on their point estimates of reaction rate that was within their margins of error (although they observed a strong temperature-dependence for the ozonolysis of solid oleic acid).
- 420 It is important to note that, as this reflectivity-based method for calculating surface concentration of oleic acid is not sensitive only to oleic acid, but also to reaction products that may remain at the interface, it is possible that the rate of reaction does differ across this temperature range, but that changes in product build-up and distribution conspire to entirely mask this, leading to a similar trend in total adsorbed deuterated material at the interface. It seems highly unlikely that counterbalancing effects would conspire to so well balance each other out across a range of $[\text{O}_3]$ conditions. In any case,
- 425 from an atmospheric perspective, the key question is not how fast oleic acid reacts, but how fast the monolayer is removed from the interface. These experiments confirm that changing the temperature from room temperature to a more atmospherically realistic near-freezing temperature does not notably alter the rate of monolayer removal from the interface. Figures 9 shows time series of the product of SLD and thickness for the lowest and highest $[\text{O}_3]_{\text{surf}}$ concentrations used at the two temperatures studied, to provide a clearer visual confirmation of the similar rates of the two reactions.
- 430 It can be seen from these two comparisons that the rates of these reactions do not differ appreciably. Indeed, the offset between the two curves is due in both cases to slight differences in starting concentration. These plots also further corroborate the main result of this study – that a residue remains after ozonolysis at near-freezing temperature but not at room temperature.
- The rate coefficients determined here are ca. three times higher than those previously reported for ozonolysis of oleic acid monolayers (King et al., 2009). Significant variability between experiments to determine rates for these heterogeneous reactions is not unprecedented. When Hung and Tang (2010) investigated heterogeneous ozonolysis of liquid oleic acid they measured a rate coefficient that was three times higher than the highest value they could find in previous work (Moise and Rudich, 2002) and up to 10 times higher than the lowest. For solid state ozonolysis, the discrepancy was up to a factor of 40 (Hung and Tang, 2010).
- 440 Despite the limitations/uncertainties discussed above in our method for deriving a rate coefficient from these data, we believe it is still the best method available at this time. The most important conclusions here, however, are not the absolute rate coefficients measured but the fact that there is not a notable difference between them. Despite the qualitative differences between the ozonolysis of an oleic acid monolayer at room temperature and more atmospherically relevant near-freezing temperatures (namely the presence of a residual monolayer in the latter case), the kinetics of the reaction does not appear to
- 445 be altered substantially in these two conditions.



4 Conclusions

4.1 Atmospheric Surface Chemistry

Based on our neutron reflectometry data, we conclude that the ozonolysis of an oleic acid monolayer on a pure water subphase (a basic model of an atmospheric water droplet) does not leave behind a product at the interface at room
450 temperature, but does leave such a residual product film at more atmospherically relevant near-freezing temperatures, and may do so at temperatures of up to $7 - 12$ °C. Data from an experiment involving re-deposition and re-ozonolysis of oleic acid showing the build-up of this product monolayer convinces us that this is a genuine product of the reaction.

Further to this, we conclude that the ozonolysis of an oleic acid monolayer film on a 36 gL^{-1} NaCl aqueous solution subphase (a basic model of a sea spray droplet) does not leave a product film at the interface at room temperature, but does leave such
455 a residual product film behind at temperatures below freezing. Such a residual product film probably is not left behind after ozonolysis at the 3 ± 1 °C temperature condition at which stable product films were observed on pure water.

Based on data from experiments performed with a partially deuterated form of oleic acid together with a knowledge of the expected major products of the ozonolysis, we conclude that, for the pure water subphase, this product film is roughly half nonanoic acid, with the other half being azelaic acid or 9-oxononanoic acid, or a mixture of the two. For the salt subphase
460 case, the data are less conclusive on the ratio between these components, though very high or very low fractions of nonanoic acid can be ruled out.

Experiments performed at a variety of O_3 concentrations demonstrate that the rate of monolayer removal does not differ significantly between the two temperatures studied, despite the clear qualitative differences in the end state of the reaction; rate coefficients were determined to be $(2.2 \pm 0.4) \times 10^{-10} \text{ cm}^2 \text{ s}^{-1}$ and $(2.2 \pm 0.2) \times 10^{-10} \text{ cm}^2 \text{ s}^{-1}$ at 21 ± 1 °C and 2 ± 1 °C,
465 respectively.

4.2 Wider Atmospheric Implications

Almost regardless of the chemical nature of the surface film, the result from an atmospheric physics perspective is very similar: a film remains at the surface after ozonolysis of an oleic acid monolayer at atmospherically realistic temperatures. The presence of such a film means that the physical effects of a surface monolayer, such as reduced water uptake, reduced
470 surface pressure, and reduced evaporation, will still be present, albeit not to the same extent, as they were in the original oleic acid-coated aerosol droplet. This means the fact that an oleic acid film will oxidise in the atmosphere does not render such a film irrelevant to the physical properties of the droplet in the long term, as would be the case if no residual film remained after ozonolysis.

Furthermore, our re-oxidation experiments demonstrate that an inert product film may build up during the droplet ageing
475 process in the atmosphere, even if only ordinarily short-lived reactive species (such as oleic acid and other unsaturated compounds) were initially emitted into the atmosphere. It is entirely possible that, given suitably cold conditions, an entirely saturated ‘full’ monolayer could be built up by repeated deposition and ozonolysis of entirely unsaturated precursor



surfactants. More generally, long-lived inert films could develop even if only short-lived reactive species are emitted, provided a suitable processing mechanism is available. The ozonolysis of oleic acid studied here is such a mechanism, therefore emissions of oleic acid and similar unsaturated fatty acids may well result in the build-up of saturated monolayers inert to further ozonolysis. This provides a way to reconcile the observation that anthropogenic activity emits significant quantities of unsaturated fatty acids (Shrivastava et al., 2007) with the observation that aerosol particles collected from the atmosphere seem to host monolayers entirely inert to ozonolysis (Jones et al., 2017).

The presence of these long-lived films is atmospherically significant. The surface pressure reduction in particular may have an impact on cloud lifetimes via the stabilisation of lower diameter droplets associated with this change under Köhler theory (Ambaum, 2010). Other possible effects include: reduced water uptake (and therefore growth) of the droplet; inhibited evaporation from the droplet; reduced transfer of species between the droplet and the wider atmosphere (alternative processes leading to this effect have been discussed in earlier work by this research group and others (King et al., 2004; Pfrang et al., 2014, 2017)); and modified surface solubility of other atmospheric species (Barnes, 1997; Benjamin, 1996; Cohen Stuart et al., 1996; Gaines, 1966; Garrett, 1971; Gilman et al., 2004; La Mer, 1962, 1964; Mmereki et al., 2003; Mmereki and Donaldson, 2002; Ray et al., 1991; Rideal, 1924; Tomoaia-Cotisel and Cadenhead, 1991).

In summary, this work provides evidence that even the emission of reactive surfactant species such as unsaturated fatty acids could alter the physical properties of water droplets in the atmosphere (including in clouds) over a much longer timeframe than the atmospheric lifetime of these species would suggest, via the build-up of inert monolayers on the surface of such droplets composed of the products of the oxidative processing of such fatty acids in the atmosphere.

Author contributions

CP and MWAS initiated the research project. CP, MWAS and BW designed the experiments and carried them out. BW analysed the data with support from MWAS and CP. AM (Maestro) provided support during the FIGARO beamtime. AM (Milsom) supported the work during beamtime experiments and off-line calibrations. JT synthesised deuterated oleic acid. BW, CP and MWAS prepared the manuscript.

Data availability

The data presented in this manuscript can be obtained from the corresponding author upon request. The underlying data are archived at ILL and ISIS.



Acknowledgements

505 The authors acknowledge the following people for their contributions to this work: S. Ayscough (University of Edinburgh) and E. Hartmane (University of Reading) for assistance on beamline experiments at ILL and ISIS; Dr P. Gutfreund (ILL) for help with the FIGARO beamline operation; S. Wood (ILL) for technical assistance on the FIGARO beamline; J. Simms (ISIS) for reaction chamber design and assembly partnership; R. Haynes (ISIS) for support of the reaction chamber design, assembly, and deployment, plus technical assistance on the INTER beamline; J. Crawford (ISIS) for assistance with the
510 reactor chamber assembly; J. Vine (ISIS), T. Crawford (ISIS) and A. Church (ISIS) for technical assistance on the INTER beamline.

References

- Allan, J. D., Williams, P. I., Morgan, W. T., Martin, C. L., Flynn, M. J., Lee, J., Nemitz, E., Phillips, G. J., Gallagher, M. W. and Coe, H.: Contributions from transport, solid fuel burning and cooking to primary organic aerosols in two UK cities, Atmos. Chem. Phys., 10(2), 647–668, doi:10.5194/acp-10-647-2010, 2010.
- Ambaum, M. H. P.: Thermal Physics of the Atmosphere, 1st ed., Wiley-Blackwell, Reading, UK., 2010.
- Barnes, G. T.: Permeation through monolayers, Colloids Surf. Physicochem. Eng. Asp., 126(2–3), 149–158, doi:10.1016/S0927-7757(96)03926-X, 1997.
- Benjamin, I.: Chemical Reactions and Solvation at Liquid Interfaces: A Microscopic Perspective Chemical Reactions and Solvation at Liquid Interfaces: A Microscopic Perspective, Chem. Rev., 96(4), 1449–1476, doi:10.1021/cr950230, 1996.
- 525 Chen, Y., Zhang, Y., Lambe, A. T., Xu, R., Lei, Z., Olson, N. E., Zhang, Z., Szalkowski, T., Cui, T., Vizuete, W., Gold, A., Turpin, B. J., Ault, A. P., Chan, M. N. and Surratt, J. D.: Heterogeneous Hydroxyl Radical Oxidation of Isoprene-Epoxydiol-Derived Methyltetrol Sulfates: Plausible Formation Mechanisms of Previously Unexplained Organosulfates in Ambient Fine Aerosols, Environmental Science & Technology Letters, 7(7), 460–468, doi: 10.1021/acs.estlett.0c00276, 2020.
- 525 Cohen Stuart, M. A., Wegh, R. A. J., Kroon, J. M. and Sudhölter, E. J. R.: Design and Testing of a Low-Cost and Compact Brewster Angle Microscope, Langmuir, 12(11), 2863–2865, doi:10.1021/la9507592, 1996.
- Daumont, D., Brion, J., Charbonnier, J. and Malicet, J.: Ozone UV spectroscopy I: Absorption cross sections at room temperature, J. Atmos. Chem., 15, 135–155, 1992.
- Donaldson, D. J. and Vaida, V.: The influence of organic films at the air-aqueous boundary on atmospheric processes, Chem. Rev., 106(4), 1445–1461, doi:10.1021/cr040367c, 2006.
- 530 Ellison, G. B., Tuck, A. F. and Vaida, V.: Atmospheric processing of organic aerosols, J. Geophys. Res., 104(D9), 11633–11641, doi:10.1029/1999JD900073, 1999.
- Fu, P. Q., Kawamura, K., Chen, J., Charrière, B. and Sempéré, R.: Organic molecular composition of marine aerosols over the Arctic Ocean in summer: contributions of primary emission and secondary aerosol formation, Biogeosciences, 10(2),
535 653–667, doi:<https://doi.org/10.5194/bg-10-653-2013>, 2013.



- Gaines, G. L.: Insoluble Monolayers at the Liquid Gas Interface, Interscience Publishers, 1966.
- Gallimore, P. J.; Griffiths, P. T.; Pope, F. D.; Reid, J. P. and Kalberer, M.: Comprehensive modeling study of ozonolysis of oleic acid aerosol based on real-time, online measurements of aerosol composition, *J. Geophys. Res. Atmos.*, 122, 4364–4377, doi:10.1002/2016JD026221, 2017.
- 540 Garrett, W. D.: Retardation of Water Drop Evaporation with Monomolecular Surface Films, *J. Atmos. Sci.*, 28(5), 816–819, doi:10.1175/1520-0469(1971)028<0816:rowdew>2.0.co;2, 1971.
- Geřard, V.; Noziere, B.; Fine, L.; Ferronato, C.; Singh, D. K.; Frossard, A. A.; Cohen, R. C.; Asmi, E.; Lihavainen, H.; Kivekař, N.; Aurela, M.; Brus, D.; Frka, S.; Kuřan, A. C.: Concentrations and Adsorption Isotherms for Amphiphilic Surfactants in PMI Aerosols from Different Regions of Europe, *Environ. Sci. Technol.*, 53, 21, 12379–12388, 2019.
- 545 Gill, P. S.; Graedel, T. E. and Weschler, C. J.: Organic films on atmospheric aerosol particles, fog droplets, cloud droplets, raindrops, and snowflakes, *Rev. Geophys.*, 21(4), 903, doi:10.1029/RG021i004p00903, 1983.
- Gilman, J. B.; Eliason, T. L.; Fast, A. and Vaida, V.: Selectivity and stability of organic films at the air-aqueous interface., *J. Colloid Interface Sci.*, 280(1), 234–43, doi:10.1016/j.jcis.2004.07.019, 2004.
- Gross, S.; Iannone, R.; Xiao, S. and Bertram, A. K.: Reactive uptake studies of NO₃ and N₂O₅ on alkenoic acid, alkanooate, and polyalcohol substrates to probe nighttime aerosol chemistry. *Phys. Chem. Chem. Phys.*, 11, 7792–7803, 2009.
- 550 Grotjahn, R.: General Circulation of the Atmosphere | Mean Characteristics, in *Encyclopedia of Atmospheric Sciences (Second Edition)*, edited by G. R. North, J. Pyle, and F. Zhang, pp. 73–89, Academic Press, Oxford, 2015.
- Hung, H.-M.; Katrib, Y. and Martin, S. T.: Products and mechanisms of the reaction of oleic acid with ozone and nitrate radical. *J. Phys. Chem. A*, 109(20), 4517–4530, doi:10.1021/jp0500900, 2005.
- 555 Hung, H.-M. and Tang, C.-W.: Effects of Temperature and Physical State on Heterogeneous Oxidation of Oleic Acid Droplets with Ozone, *J. Phys. Chem. A*, 114(50), 13104–13112, doi:10.1021/jp105042w, 2010.
- Jones, S. H.; King, M. D.; Ward, A. D.; Rennie, A. R.; Jones, A. C. and Arnold, T.: Are organic films from atmospheric aerosol and sea water inert to oxidation by ozone at the air-water interface?, *Atmos. Environ.*, 161, 274–287, doi:10.1016/J.ATMOSENV.2017.04.025, 2017.
- 560 King, M. D.; Thompson, K. C. and Ward, A. D.: Laser Tweezers Raman Study of Optically Trapped Aerosol Droplets of Seawater and Oleic Acid Reacting with Ozone: Implications for Cloud-Droplet Properties, *J. Am. Chem. Soc.*, 126(51), 16710–16711, doi:10.1021/ja044717o, 2004.
- King, M. D.; Rennie, A. R.; Thompson, K. C.; Fisher, F. N.; Dong, C. C.; Thomas, R. K.; Pfrang, C. and Hughes, A. V.: Oxidation of oleic acid at the air-water interface and its potential effects on cloud critical supersaturations., *Phys. Chem. Chem. Phys.*, 11(35), 7699–7707, doi:10.1039/b906517b, 2009.
- 565 Knopf, D. A.; Anthony, L. M. and Bertram, A. K.: Reactive uptake of O₃ by multicomponent and multiphase mixtures containing oleic acid. *J. Phys. Chem. A*, 109, 5579–5589, 2005.
- Krořlic, A.; Frka, S.; Simmel, M.; Wex, H.; Grgic, I.: Size-Resolved Surface-Active Substances of Atmospheric Aerosol: Reconsideration of the Impact on Cloud Droplet Formation. *Environ. Sci. Technol.*, 52 (16), 9179–9187, 2018.



- 570 La Mer, V. K.: Retardation of Evaporation by Monolayers: Transport Processes, Academic Press Inc., London, 1962.
La Mer, V. K.: The transport of water through monolayers of long-chain n-paraffinic alcohols, *J. Colloid Sci.*, 19(8), 673, 1964.
- Last, D. J., Nájera, J. J., Wamsley, R., Hilton, G., McGillen, M., Percival, C. J. and Horn, A. B.: Ozonolysis of organic compounds and mixtures in solution. Part I: Oleic, maleic, nonanoic and benzoic acids. *Phys. Chem. Chem. Phys.*, 11(9), 1427-1440, doi:10.1039/b815425b, 2009.
- Li, S., Cheng, S., Du, L. and Wang, W.: Establishing a model organic film of low volatile compound mixture on aqueous aerosol surface, *Atmos. Environ.*, 200, 15–23, doi:10.1016/j.atmosenv.2018.11.052, 2019.
- Lu, J. R., Thomas, R. K. and Penfold, J.: Surfactant layers at the air/water interface: structure and composition, *Adv. Colloid Interface Sci.*, 84(1–3), 143–304, doi:10.1016/S0001-8686(99)00019-6, 2000.
- 580 Mmereki, B. T. and Donaldson, D. J.: Laser induced fluorescence of pyrene at an organic coated air-water interface, *Phys. Chem. Chem. Phys.*, 4(17), 4186–4191, doi:10.1039/b204754c, 2002.
- Mmereki, B. T., Chaudhuri, S. R. and Donaldson, D. J.: Enhanced Uptake of PAHs by Organic-Coated Aqueous Surfaces, *J. Phys. Chem. A*, 107(13), 2264–2269, doi:10.1021/jp027361g, 2003.
- Moise, T. and Rudich, Y.: Reactive Uptake of Ozone by Aerosol-Associated Unsaturated Fatty Acids: Kinetics, Mechanism, and Products, *J. Phys. Chem. A*, 106(27), 6469–6476, doi:10.1021/jp025597e, 2002.
- 585 Nelson, A.: Co-refinement of multiple-contrast neutron/X-ray reflectivity data using MOTOFIT, *J. Appl. Crystallogr.*, 39(2), 273–276, doi:10.1107/S0021889806005073, 2006.
- Nozieře, B., Baduel, C., Jaffrezo, J.-L.: The dynamic surface tension of atmospheric aerosol surfactants reveals new aspects of cloud activation. *Nat. Commun.*, 5, 3335, 2014.
- 590 Ovadnevaite, J., Zuend, A., Laaksonen, A., Sanchez, K. J., Roberts, G., Ceburnis, D., Decesari, S., Rinaldi, M., Hodas, N., Facchini, M. C., Seinfeld, J. H., O’ Dowd, C.: Surface tension prevails over solute effect in organic-influenced cloud droplet activation. *Nature*, 546 (7660), 637–641, 2017.
- Pfrang, C., Shiraiwa, M. and Poschl, U.: Chemical ageing and transformation of diffusivity in semi-solid multi-component organic aerosol particles, *Atmos. Chem. Phys.*, 11(14), 7343–7354, doi:10.5194/acp-11-7343-2011, 2011.
- 595 Pfrang, C., Sebastiani, F., Lucas, C. O. M., King, M. D., Hoare, I. D., Chang, D. and Campbell, R. A.: Ozonolysis of methyl oleate monolayers at the air–water interface: oxidation kinetics, reaction products and atmospheric implications, *Phys. Chem. Chem. Phys.*, 16(16), 13220–13228, doi:10.1039/c4cp00775a, 2014.
- Pfrang, C., Rastogi, K., Cabrera-Martinez, E. R., Seddon, A. M., Dicko, C., Labrador, A., Plivelic, T. S., Cowieson, N. and Squires, A. M.: Complex three-dimensional self-assembly in proxies for atmospheric aerosols, *Nat. Commun.*, 8(1), 1724, doi:10.1038/s41467-017-01918-1, 2017.
- 600 Ray, A. K., Devakottai, B., Souyri, A. and Huckaby, J. L.: Evaporation characteristics of droplets coated with immiscible layers of nonvolatile liquids, *Langmuir*, 7(3), 525–531, doi:10.1021/la00051a019, 1991.

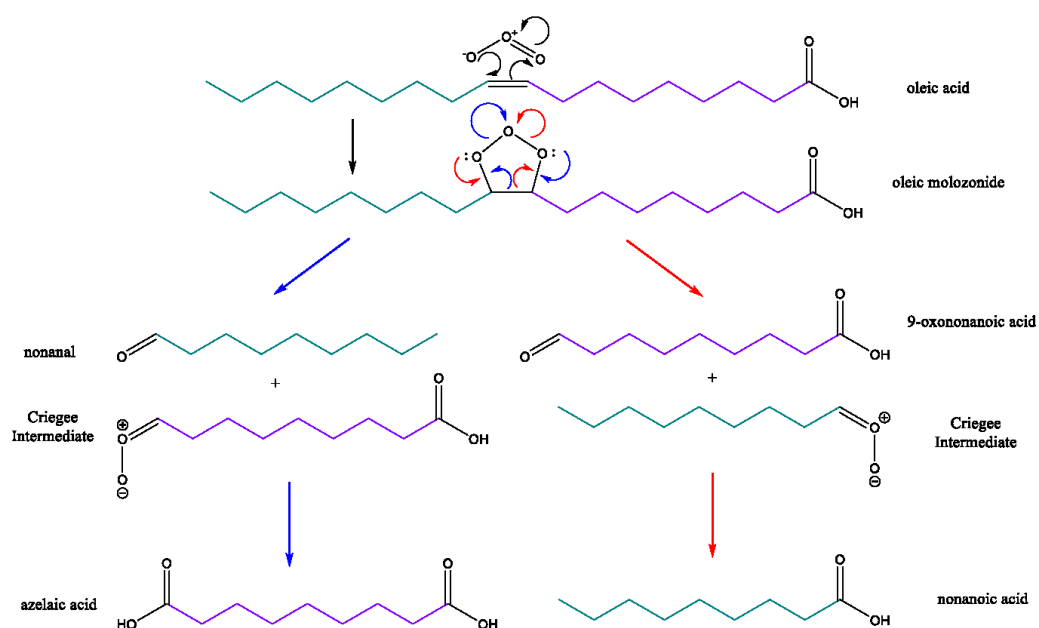


- Rideal, E. K.: On the Influence of Thin Surface Films on the Evaporation of Water, *J. Phys. Chem.*, 29(12), 1585–1588, doi:10.1021/j150258a011, 1924.
- 605 Ruehl, C. R., Davies, J. F., Wilson, K. R.: An interfacial mechanism for cloud droplet formation on organic aerosols. *Science*, 351 (6280), 1447–1450, 2016.
- Sareen, N., Schwier, A. N., Lathem, T. L., Nenes, A., McNeill, V. F.: Surfactants from the gas phase may promote cloud droplet formation. *Proc. Natl. Acad. Sci. U. S. A.*, 110 (8), 2723–2728, 2013.
- Sebastiani, F., Campbell, R. A. and Pfrang, C.: Complementarity of neutron reflectometry and ellipsometry for the study of
610 atmospheric reactions at the air–water interface, *RSC Adv.*, 5(129), 107105–107111, doi:10.1039/C5RA22725A, 2015.
- Sebastiani, F., Campbell, R. A., Rastogi, K. and Pfrang, C.: Night-time oxidation of surfactants at the air–water interface: effects of chain length, head group and saturation, *Atmos. Chem. Phys.*, 18, 3249–3268, 2018.
- Shrivastava, M. K., Subramanian, R., Rogge, W. F. and Robinson, A. L.: Sources of organic aerosol: Positive matrix factorization of molecular marker data and comparison of results from different source apportionment models, *Atmos.*
615 *Environ.*, 41(40), 9353–9369, doi:10.1016/j.atmosenv.2007.09.016, 2007.
- Skoda, M. W. A., Thomas, B., Hagreen, M., Sebastiani, F. and Pfrang, C.: Simultaneous neutron reflectometry and infrared reflection absorption spectroscopy (IRRAS) study of mixed monolayer reactions at the air-water interface, *RSC Adv.*, 7(54), 34208–34214, doi:10.1039/C7RA04900E, 2017.
- Smith, G. D., Woods, E., DeForest, C. L., Baer, T. and Miller, R. E.: Reactive uptake of ozone by oleic acid aerosol
620 particles: Application of single-particle mass spectrometry to heterogeneous reaction kinetics, *J. Phys. Chem. A*, 106(35), 8085–8095, doi:10.1021/jp020527t, 2002.
- Stevens, B. and Feingold, G.: Untangling aerosol effects on clouds and precipitation in a buffered system., *Nature*, 461(7264), 607–613, doi:10.1038/nature08281, 2009.
- Tervahattu, H., Juhanoja, J. and Kupiainen, K.: Identification of an organic coating on marine aerosol particles by TOF-
625 SIMS, *J. Geophys. Res. Atmospheres*, 107(D16), ACH 18-1-ACH 18-7, doi:10.1029/2001JD001403, 2002.
- Tomoaia-Cotisel, M. and Cadenhead, D. A.: The interaction of procaine with stearic acid monolayers at the air/water interface, *Langmuir*, 7(5), 964–974, doi:10.1021/la00053a025, 1991.
- Tuckermann, R.: Surface tension of aqueous solutions of water-soluble organic and inorganic compounds, *Atmos. Environ.*, 41(29), 6265–6275, doi:10.1016/j.atmosenv.2007.03.051, 2007.
- 630 McNeill, V. F.; Wolfe, G. M. and Thornton, J. A.: The Oxidation of Oleate in Submicron Aqueous Salt Aerosols: Evidence of a Surface Process, *J. Phys. Chem. A*, 111(6), 1073–1083, doi:10.1021/JP066233F, 2007.
- Voss, L. F., Bazerbashi, M. F., Beekman, C. P., Hadad, C. M. and Allen, H. C.: Oxidation of oleic acid at air/liquid interfaces, *J. Geophys. Res.*, 112(D6), D06209, doi:10.1029/2006JD007677, 2007.
- Warneck, P.: *Chemistry of the Natural Atmosphere, Volume 71 - 2nd Edition*, [online] Available from:
635 <https://www.elsevier.com/books/chemistry-of-the-natural-atmosphere/warneck/978-0-12-735632-7>, 1999.

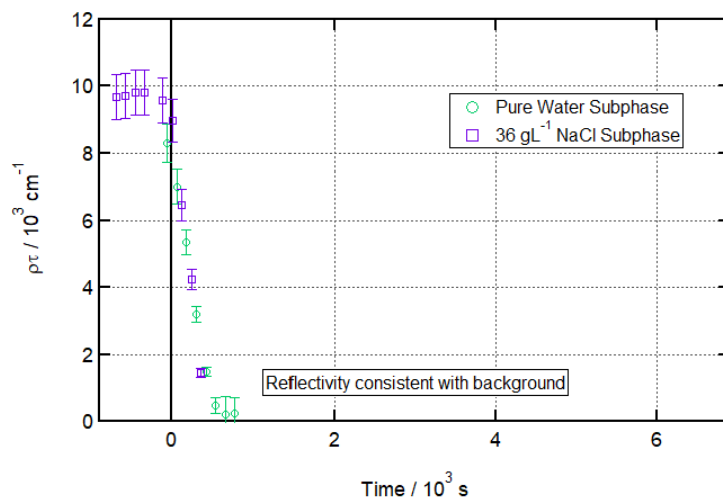


Woden, B., Skoda, M. W. A., Hagreen, M. and Pfrang, C.: Night-Time Oxidation of a Monolayer Model for the Air–Water Interface of Marine Aerosols—A Study by Simultaneous Neutron Reflectometry and in Situ Infra-Red Reflection Absorption Spectroscopy (IRRAS), *Atmosphere*, 9(12), 471, doi:10.3390/atmos9120471, 2018.

Zahardis, J. and Petrucci, G. A.: The oleic acid-ozone heterogeneous reaction system: products, kinetics, secondary chemistry, and atmospheric implications of a model system – a review, *Atmos. Chem. Phys.*, 7, 1237–1274, 2007.

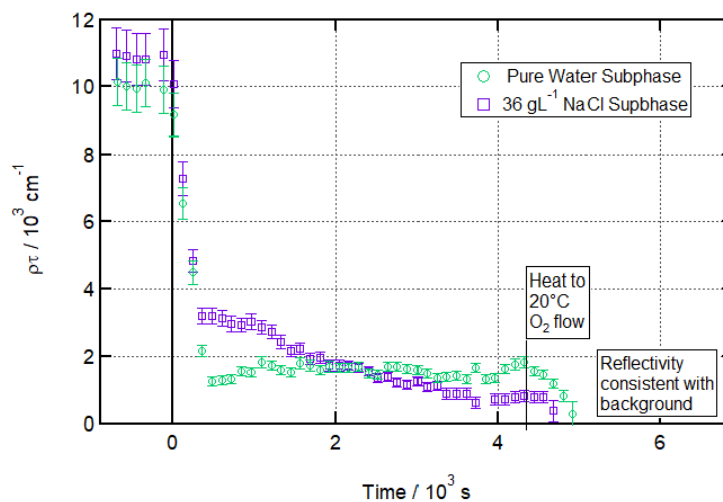


645 **Scheme 1: Oleic acid ozonolysis reaction scheme.** We used both fully and half-deuterated oleic acid samples, granting us the ability to create different contrasts for analysis by neutron reflectometry. In the fully deuterated (d_{34}) variant of oleic acid, both the head portion (purple) and tail portion (teal) of the molecule are deuterated. In the partially deuterated (d_{18}) variant of oleic acid, only the tail portion (teal) is deuterated. The colouring of the products and intermediates indicates the fate of the two portions of the oleic acid molecule, and demonstrates that, when d_{18} -oleic acid is oxidised, two products (nonanal and nonanoic acid) are deuterated, and two (ozelaic acid and 9-oxononanoic acid) are not.



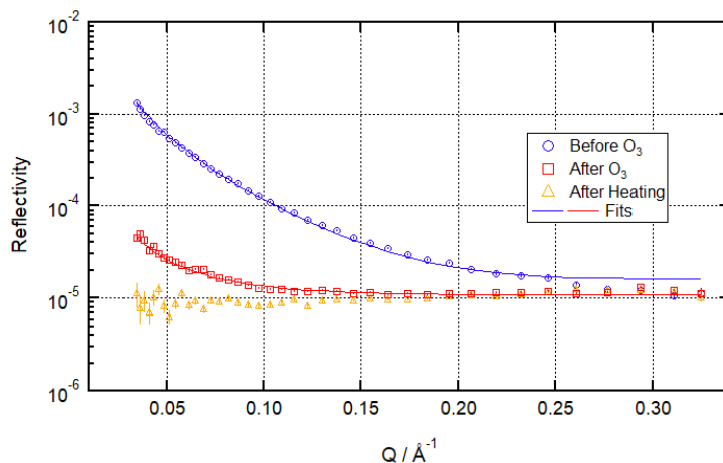
650

Figure 1: Ozonolysis of an oleic acid monolayer floating on pure vs salt water. Time evolution plot for ozonolysis of $29 \mu\text{L } 1.0 \text{ g L}^{-1} d_{34}\text{-OA}$ (CHCl_3 spread. sol) on pure water (green circles) and $25 \mu\text{L } 1.0 \text{ g L}^{-1} d_{34}\text{-OA } 36 \text{ g L}^{-1} \text{NaCl(aq)}$ (purple squares) subphases by $323 \pm 29 \text{ ppb O}_3$ introduced at $t = 0 \text{ s}$ at $21 \pm 1 \text{ }^\circ\text{C}$.

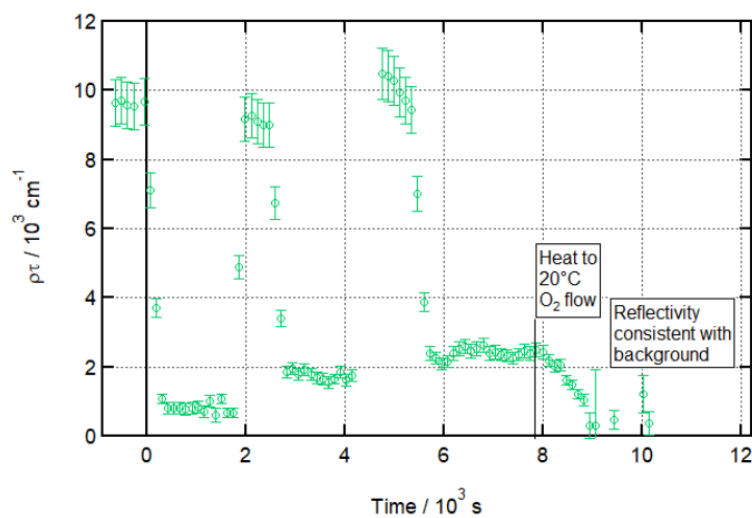


655

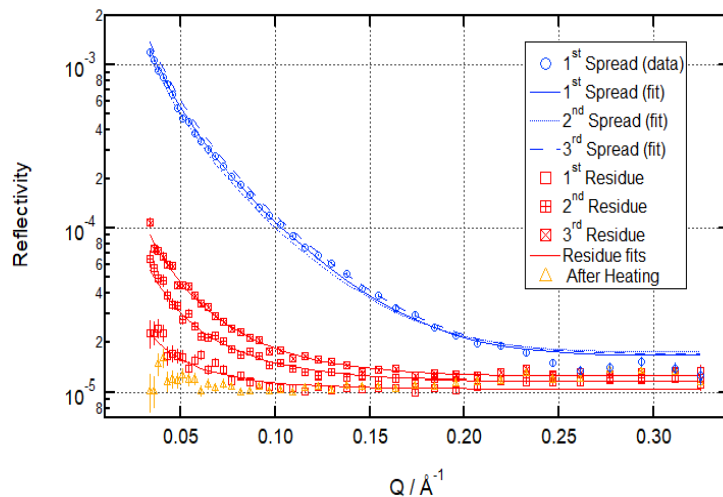
Figure 2: Ozonolysis of an oleic acid monolayer at low temperatures floating on pure vs salt water. Time evolution plot for ozonolysis of $25 \mu\text{L } 1.0 \text{ g L}^{-1} d_{34}\text{-OA}$ (CHCl_3 spread. sol) on pure water (green circles) and $36 \text{ g L}^{-1} \text{NaCl(aq)}$ (purple squares) subphases by $323 \pm 29 \text{ ppb O}_3$ introduced at $t = 0 \text{ s}$ at $3 \pm 1 \text{ }^\circ\text{C}$ (pure water) or $-2 \pm 1 \text{ }^\circ\text{C}$ (salt water).



660 **Figure 3:** Neutron reflectivity signal from the air–water interface before ozonolysis (blue circles - signal from the pristine oleic acid monolayer), after ozonolysis (red squares - clear signal remaining) and after heating (orange triangles - no measurable signal) for ozonolysis of 25 μL 1.0 g L^{-1} $d_{34}\text{-OA}$ (CHCl_3 spread. sol.) on pure water subphase by 323 ± 29 ppb O_3 introduced at $t = 0$ s at 3 ± 1 $^\circ\text{C}$.



665 **Figure 4:** Experiment mimicking an aqueous aerosol droplet exposed to multiple cooking emission peaks and demonstrating the associated build-up of an inert organic film at the air–water interface at low temperatures. Time evolution plot for ozonolysis of 25 μL 1.0 g L^{-1} $d_{34}\text{-OA}$ (CHCl_3 spread. sol.) on pure water subphase by 323 ± 29 ppb O_3 introduced at $t = 0$ s and after two additional spreadings of 25 μL 1.0 g L^{-1} $d_{34}\text{-OA}$ at 3 ± 1 $^\circ\text{C}$.



670 **Figure 5: Neutron reflectivity signal from the air–water interface before ozonolysis (blue circles (data only shown for first spreading; fits shown for all three spreadings - clear and consistent signal from the oleic acid monolayers across the three simulated cooking emission peaks), after ozonolysis (red squares - demonstrating the build-up of organic residue at the air–water interface during repeated exposure to cooking emission) and after heating (orange triangles - removal of organic residue at room temperature) for the multi-ozonolysis reaction shown as a time evolution plot in Figure 4.**

675

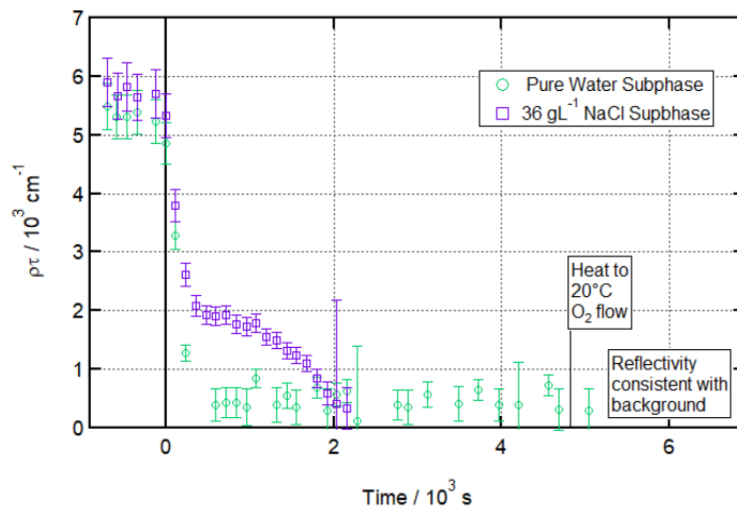
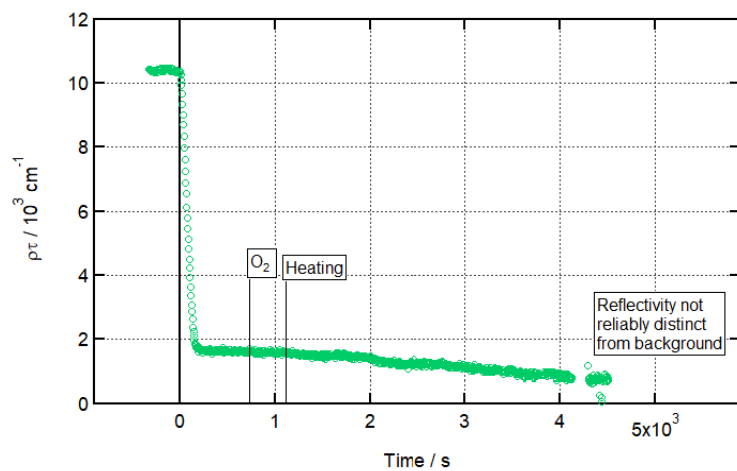
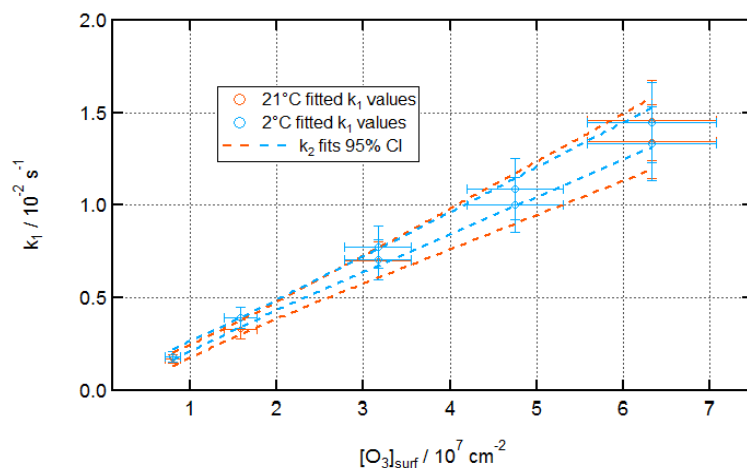


Figure 6: Ozonolysis of a partially deuterated oleic acid monolayer floating on pure vs salt water. Time evolution plot for ozonolysis of $17 \mu\text{L } 1.3 \text{ g L}^{-1} d_{18}\text{-OA}$ (CHCl_3 spread. sol.) on pure water (green circles) and $36 \text{ g L}^{-1} \text{NaCl(aq)}$ (purple squares) subphases by $323 \pm 29 \text{ ppb O}_3$ introduced at $t = 0 \text{ s}$ at $3 \pm 1^\circ\text{C}$ (pure water) or $-2 \pm 1^\circ\text{C}$ (salt water).



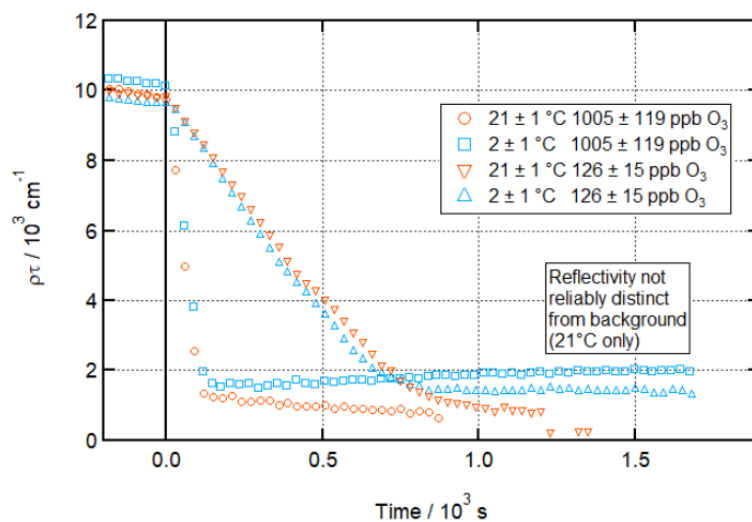
680

Figure 7: Gradual loss of residue due to increase in temperature. Time evolution plot for ozonolysis of $29 \mu\text{L } 1.0 \text{ g L}^{-1} d_{34}\text{-OA}$ (CHCl_3 spread. sol.) on pure subphase by $754 \pm 89 \text{ ppb O}_3$ introduced at $t = 0 \text{ s}$ at $2 \pm 1^\circ\text{C}$, with temperature ramping (described in detail in the text) from $t = 1035 \text{ s}$; error bars are omitted for visual clarity.



685

Figure 8: Kinetics of ozonolysis of the oleic acid monolayer on pure water at room and low temperatures. Fitted k_1 pseudo-1st-order rate constants against $[O_3]_{surf}$ at 21 ± 1 °C (orange) and 2 ± 1 °C (aqua).



690 Figure 9: Comparison of time-dependent loss of material from the air–water interface during oleic acid ozonolysis at room and low temperatures and at highest and lowest $[O_3]$. Time evolution plot for ozonolysis of $39 \mu\text{L } 0.75 \text{ g L}^{-1} \text{ } \alpha\text{-OA}$ (CHCl_3 spread, sol.) on pure subphase by O_3 introduced at $t = 0 \text{ s}$ at 21 ± 1 °C (orange) and 2 ± 1 °C (aqua); error bars are omitted for visual clarity.

Electronic Supplementary Information

Ozonolysis of fatty acid monolayers at the air–water interface: organic films may persist at the surface of atmospheric aerosols.

- 5 Ben Woden^{1,2}, Max W. A. Skoda², Adam Milsom³, Armando Maestro⁴, James Tellam² and Christian Pfrang^{3,5}.

¹Department of Chemistry, University of Reading, Whiteknights, Reading, RG6 6AD, UK

²ISIS Neutron and Muon Source, Science and Technology Facilities Council, Rutherford Appleton Laboratory, Didcot, OX11 0QX, UK.

- 10 ³School of Geography, Earth and Environmental Sciences, University of Birmingham, Edgbaston, Birmingham, B15 2TT, UK

⁴Institut Laue Langevin (ILL), 71 Avenue des Martyrs, Grenoble, 38000, France.

⁵Department of Meteorology, University of Reading, Whiteknights Road, Reading, RG6 6BG, UK.

Correspondence to: Christian Pfrang (c.pfrang@bham.ac.uk)

15 Section S1 – Monolayer Characterisation at Low Temperature

- In order to ensure that the system could effectively be modelled as a monolayer for neutron reflectometry data fitting, and to find an optimum spreading volume that packs in a similar manner across the temperature ranges studied (to ensure that temperature effects alone, rather than effects due to monolayer phase, were studied), monolayers of oleic acid were spread on pure water, 0.6 M NaCl solution, and 0.6 M CaCl₂ solution subphases at room temperature, just above freezing point, and
20 just below freezing point (not accessible for pure water) and Wilhelmy tensiometric measurements were performed using a Langmuir trough equipped with a NIMA surface pressure sensor and control software. π -A isotherms were recorded and are shown below in Figures S1 and S2.

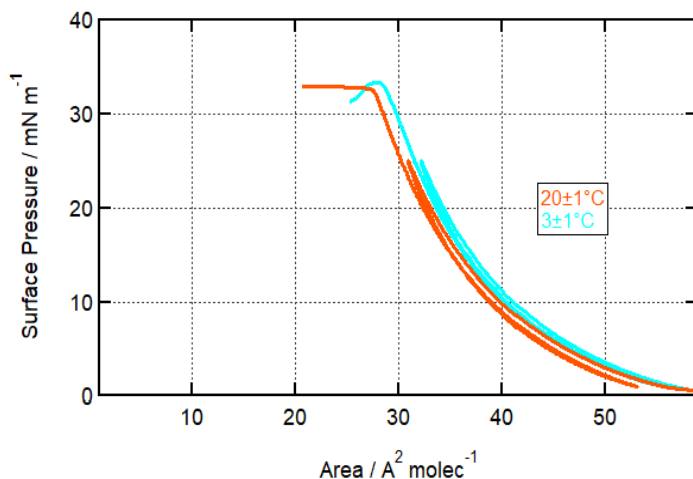


Figure S1: π -A Isotherm for oleic acid on pure water at 3 °C (aqua) and 20 °C (orange).

- 25 These tensiometry experiments showed that the system could be described as a well-behaved monolayer over the temperature range of interest on pure water and NaCl solution. On CaCl₂, the results were less reproducible. The CaCl₂ system was physically more difficult to handle, with the high viscosity of the subphase at low temperatures posing a problem, and the initial impact on the surface tension of the system caused by the addition of the first droplet of oleic acid solution proving so great as to occasionally spill subphase out of the trough purely by the force of the surface waves created.
- 30 Preliminary neutron reflectometry (ISIS INTER reflectometer; RB 1710483) carried out with an early prototype of the apparatus on such a system also showed an unusual R vs Q curve not characteristic of a monolayer. For these reasons, further work was conducted only on the pure water and NaCl solution subphases.

The impact of temperature on the π -A isotherm for oleic acid was not large, and indeed was not reliably distinguishable from zero by our apparatus and method. Due to this, the target surface area per molecule of 30 Å² used for previous experiments at 35 room temperature was deemed suitable for use at the lower temperature as well. This choice of initial surface concentration

maximises initial signal for neutron reflectometry and infrared spectroscopy measurements without risking film breakage.

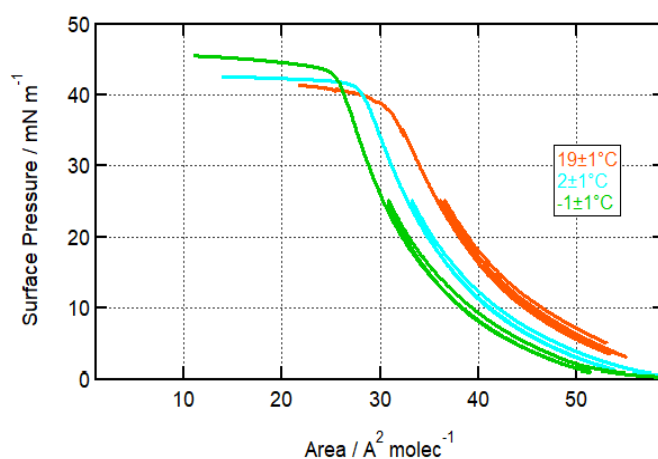
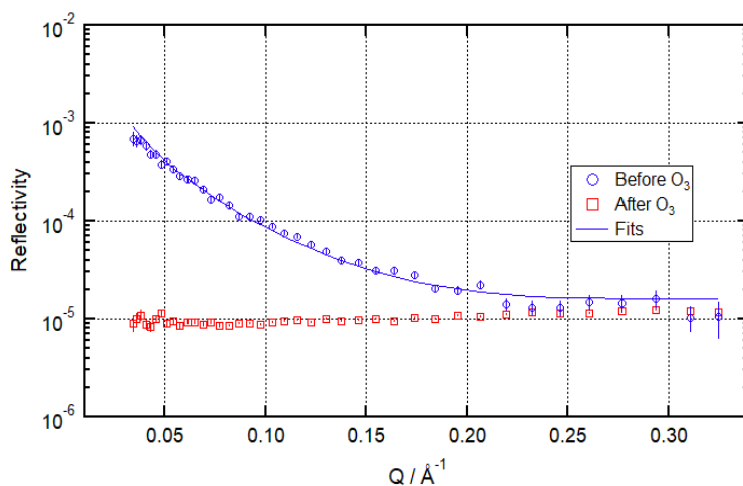


Figure S2: π -A Isotherm for oleic acid on 36 g L⁻¹ NaCl at -1 °C (green), 2 °C (aqua) and 19 °C (orange).

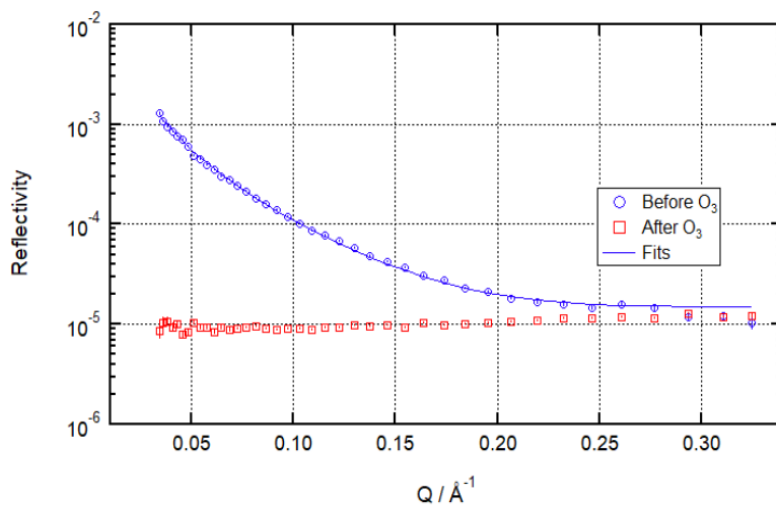
The situation on the NaCl solution subphase was somewhat different. Compared with the pure water condition, significantly
40 higher surface pressure regimes are accessible before the breaking of the monolayer at all temperatures and these are
associated in the low temperature conditions with slightly higher surface concentrations. There is an observable trend of
lower surface pressure with lower temperature at a given surface concentration, and this trend does not appear to be linear.
Based on these results, the target surface area per molecule of 30 Å² used for the pure water condition was extended to the
NaCl solution condition at all temperatures. Preserving consistency across conditions and maximising observable signal
45 were considered highly important, and the slight risk of overspreading in the room temperature NaCl solution condition
(which was not observed during experiments) was deemed acceptable to achieve this, particularly as preliminary neutron
reflectometry data gathered with an early prototype of the apparatus (ISIS INTER reflectometer; RB 1710483) had suggested
that this was the least interesting of the new conditions under study.

Section S2 – Reflectivity Curves



50

Figure S3: Reflectivity before ozonolysis (blue circles), and after ozonolysis (red squares) for ozonolysis of 29 μL 1.0 g L^{-1} $d_{34}\text{-OA}$ (CHCl_3 spread. sol.) on pure water subphase by 323 ± 29 ppb O_3 introduced at $t = 0$ s at 21 ± 1 $^\circ\text{C}$.



55

Figure S4: Reflectivity before ozonolysis (blue circles), and after ozonolysis (red squares) for ozonolysis of 25 μL 1.0 g L^{-1} $d_{34}\text{-OA}$ (CHCl_3 spread. sol.) on 36 g L^{-1} NaCl(aq) subphase by 323 ± 29 ppb O_3 introduced at $t = 0$ s at 21 ± 1 $^\circ\text{C}$.

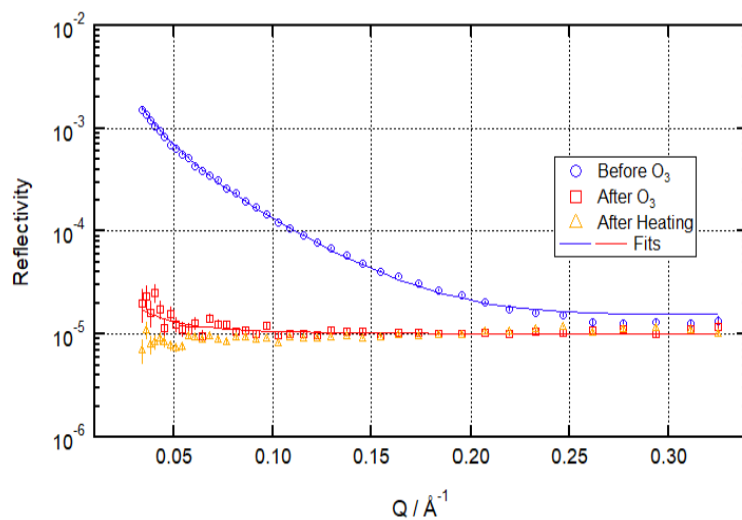
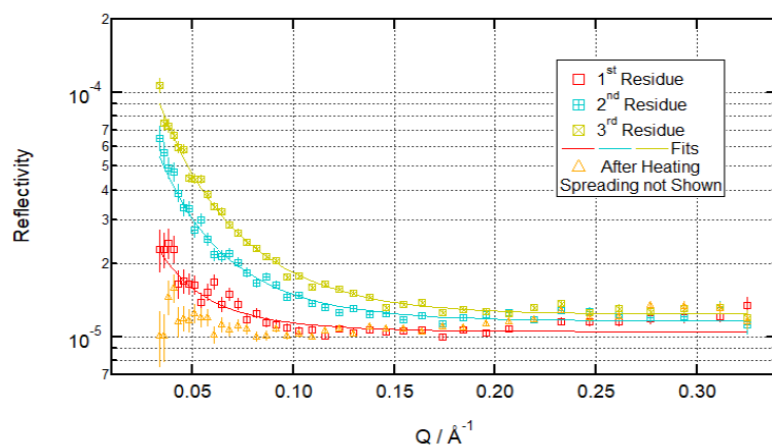


Figure S5: Reflectivity before ozonolysis (blue circles), after ozonolysis (red squares) and after heating (orange triangles) for ozonolysis of $25 \mu\text{L } 1.0 \text{ g L}^{-1} d_{34}\text{-OA}$ (CHCl_3 spread. sol.) on $36 \text{ g L}^{-1} \text{NaCl(aq)}$ subphase by $323 \pm 29 \text{ ppb O}_3$ introduced at $t = 0 \text{ s}$ at $-2 \pm 1 \text{ }^\circ\text{C}$.



60

Figure S6: Reflectivity after ozonolysis from the first (open red squares), second (teal squares with an upright cross), and third (olive squares with a diagonal cross) ozonolysis steps, and after heating (orange triangles) for the multi-ozonolysis reaction shown in Figures 4 and 5 (main paper).

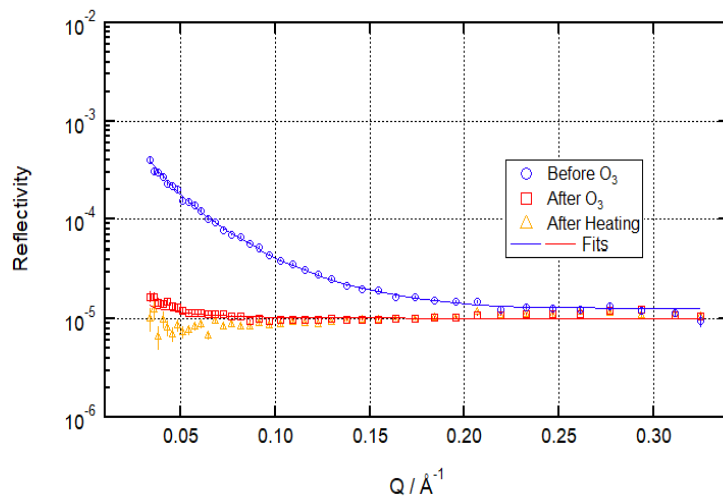
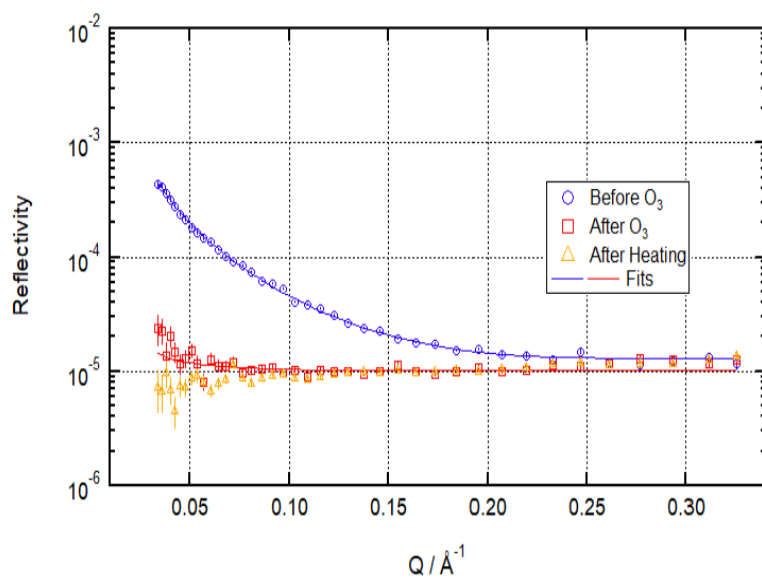
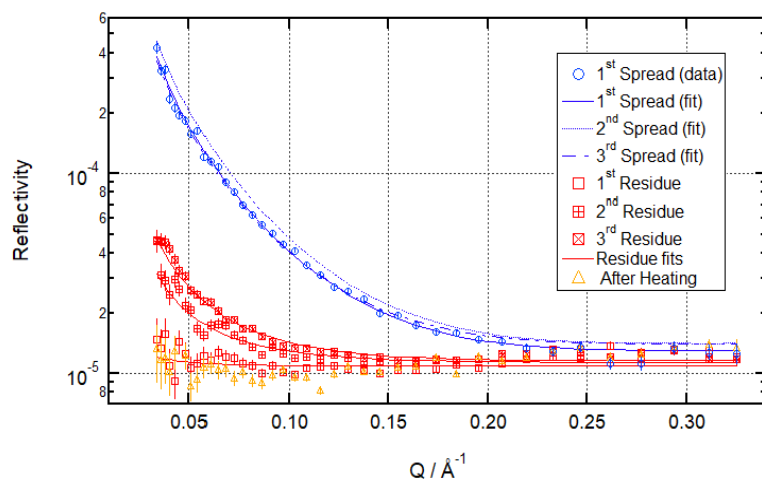


Figure S7: Reflectivity before ozonolysis (blue circles), after ozonolysis (red squares) and after heating (orange triangles) for ozonolysis of $17 \mu\text{L } 1.3 \text{ g L}^{-1} d_3+OA$ (CHCl_3 spread. sol.) on pure water subphase by 323 ± 29 ppb O_3 added at $t = 0$ s at 3 ± 1 °C.



70 **Figure S8:** Reflectivity before O_3 (blue circles), after O_3 (red squares) and after heating (orange triangles) for ozonolysis of $17 \mu\text{L } 1.0 \text{ g L}^{-1} d_{34}\text{-OA}$ (CHCl_3 spread. sol.) on $36 \text{ g L}^{-1} \text{NaCl(aq)}$ subphase by $323 \pm 29 \text{ ppb } O_3$ added at $t = 0 \text{ s}$ at $3 \pm 1 \text{ }^\circ\text{C}$.



75 **Figure S9:** Reflectivity before ozonolysis (blue circles (data only shown for first spreading; fits shown for all three spreadings), after ozonolysis (red squares) and after heating (orange triangles) for a multi-ozonolysis reaction (analogous to that shown in Figures 4 and 5 (main paper) and S6) of $17 \mu\text{L } 1.0 \text{ g L}^{-1} d_{34}\text{-OA}$ at $3 \pm 1 \text{ }^\circ\text{C}$.

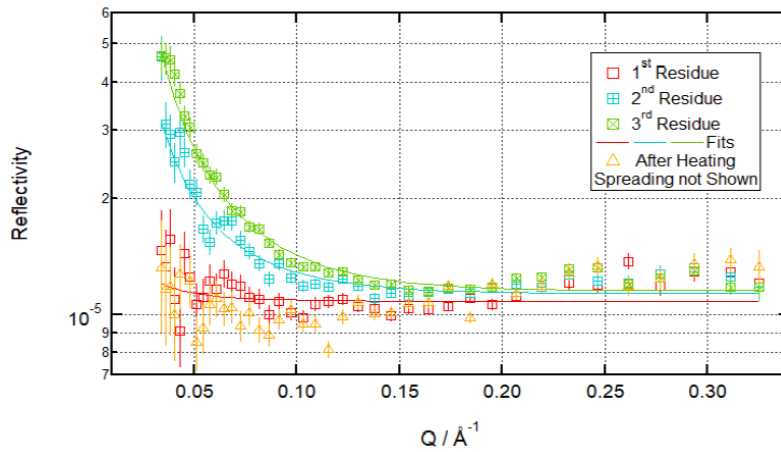
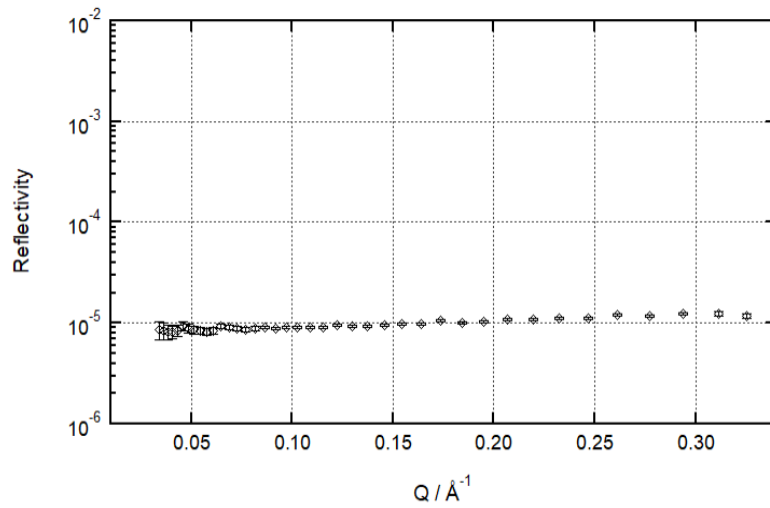


Figure S10: Reflectivity after ozonolysis from the first (open red squares), second (teal squares with an upright cross), and third (olive squares with a diagonal cross) ozonolysis steps, and after heating (orange triangles) for the multi-ozonolysis reaction shown in Figure S9.



80

Figure S11: Reflectivity for a pure null-reflecting air-water interface.

Section S3 – Kinetic Fitting

In the latter stages of the reaction, reflectometry signal from products is likely to be a significant or even dominant contributor to reflectivity. Indeed, the primary case made in this paper is that we can use residual reflectivity that cannot be depressed by further ozonolysis at low temperatures to infer the presence of a residual monolayer of reaction products. As a result, we do not attempt to fit data for lower surface coverage values than 10^{14} cm⁻² (as calculated by fitting reflectivity curves and assuming all reflectivity is due to oleic acid). This represents approximately the final third of the reaction in terms of reflectivity, and was chosen as it is at this point that significant deviations from a smooth, regular function are observed from a basic visual appraisal of the data. However, even before this point, some of the measured reflectivity will be due to the presence of reaction products at the interface (whether or not they are sufficiently stable to persist at the end of the reaction), meaning that calculations of oleic acid surface coverage will be over-estimations to some degree as soon as the reaction begins, and to a greater and greater extent as the reaction progresses. As a result, fitted pseudo-1st-order rate constants are likely to be slight under-estimations, even when the latter third of the reaction is excluded from the fitting.

Another complication involves the mixing of O₃ into the chamber at the very start of the reaction. The model presented in equation 1 assumes that [O₃]_{gas} is uniform throughout the reaction chamber. This is, in reality, not the case. O₃ is introduced to the chamber through a long tube running down one side of the chamber just above the air/water interface with holes of varying diameters drilled along its length. This oxidant gas ingress system was designed by a previous member of this research group in order to achieve even distribution of the oxidant gas with respect to the long edge of the interface (it is unavoidably still the case that there is a concentration gradient across the short edge) and the precise sizes of the drilled holes were tuned in order to achieve even mixing based on fluid dynamics simulations (Sebastiani, 2014; Sebastiani et al., 2015). The mixing time for the cell is estimated as around 60 s. As a result of this, [O₃]_{gas} will rise much more quickly in a boundary layer just above the air/water interface at around the height of the ingress pipe than it will in the chamber as a whole. It is, of course, the [O₃]_{gas} just above the interface that is relevant for the progress of the reaction. This boundary layer constitutes an ‘effective volume’ for the reaction which is significantly lower than the total volume of the reaction chamber. Determining the volume of this boundary layer is not experimentally possible, and its value is unfortunately something of a fudge factor in fitting rate constants to these data. Assuming too high an effective volume will mean that the model underestimates the time it takes for the reaction to ‘get up to speed’, meaning that too high a rate constant will be fitted to compensate. Usefully, this effect scales with [O₃]_{gas}. Choosing too high an effective volume (for instance by using the entire chamber volume of 2.1×10^3 cm³) results in very poor fitting at higher values of [O₃]_{gas}, and causes fitted k_1 values to show a superlinear relationship with [O₃]_{surf}, meaning no 2nd-order rate constant can be determined. Choosing too low an effective volume results in very poor fitting at lower values of [O₃]_{gas} and a sublinear relationship between k_1 and [O₃]_{surf}. It is possible, therefore, to estimate a boundary layer volume by appraising both the quality of fits between model and data at various values of [O₃]_{surf}, and by assessing the relationship between k_1 and [O₃]_{surf}, which should be linear (due to the 2nd-

order nature of the reaction). As long as the same boundary layer is used, fitted parameters from different experiments will
115 be meaningfully comparable.

For this work, a boundary layer volume of 35 cm³ (or a boundary layer height above the interface of 2 mm) was used, as it
was appraised to produce a reasonable quality of fit for experimental data across the range of [O₃]_{gas} conditions studied, and
produced suitably linear relationship between k_1 and [O₃]_{surf} in order for a 2nd-order rate constant (k_2) to be calculated.

This is further complicated due to experimental uncertainty regarding the exact time of the start of the reaction. The reaction
120 is started by manually uncovering part of the UV lamp inside the ozoniser, and the moment at which this action is performed
is treated as t_0 for that reaction. However, this manual process is only as precise and reproducible as the finger movements
required to perform it. Sometimes, the lamp might be uncovered more slowly than others. Sometimes, the sheath might stick
slightly, delaying the uncovering of the lamp by a second or two. Sometimes, the experimenter might overshoot the desired
sheath position, uncovering slightly more of the lamp than intended for a fraction of a second. The situation is yet further
125 complicated by the fact that the 'head' of O₃ produced still has to travel a few metres down the tube before it enters the
chamber.

When fitting this kind of exponential function, the first few points exercise a high degree of leverage over the whole fit.
However, it is exactly these first few points (reflectivity data are collected in 5 second frames for these experiments) that
suffer from this uncertainty over the precise start time of the reaction. In order to overcome this difficulty, the first three
130 points (15 seconds) of each reaction are not fitted, and a time offset parameter is added to the model (each instance of " t " on
the right-hand-side of equation 2 is replaced by a " $(t-t_{\text{offset}})$ " term). This produces the problem that t_{offset} is somewhat
correlated with Γ_0 – the reaction can be modelled to have started arbitrarily far back into the past before the fitted data as
long as the starting surface coverage is raised to correspondingly high and physically unrealistic values. In order to avoid
this, Γ_0 is measured before the reaction begins (under a stream of O₂ containing no O₃) and the parameter is fixed for each
135 fitting based on this measurement. Fitting then proceeds by allowing k_1 and t_{offset} to vary, and fits are achieved by this method
that tend to converge on values of t_{offset} (generally 10 – 20 s) that make physical sense.

Variation in the assumptions outlined above result in good agreement between model and data for each experiment and
produce k_1 values that differ by as much as 15 % from the values produced via the fitting methods settled upon. This error
(which is far greater than the error associated with reflectivity fitting at each individual point, and therefore dominates the
140 error in fitted k_1 values) is reflected in our final calculated values for the 2nd-order rate constant.

This error due to model subjectivity turned out to have a much greater effect on the robustness of the fitted k_1 values than did
the first problem discussed here (that of deciding what portion of the end of the reaction to discard from fitting due to
overbearing influence on fitted surface coverage values of reflectivity due to reaction products). The choice of where to stop
fitting made much less difference to the resultant fit than did the choice of where to start fitting and what boundary layer
145 volume to use.

This analytical fitting process does involve the piling of several epicycles upon the basic model of a 2nd-order reaction in
which one component in excess, producing a series of pseudo-1st-order reactions with rate constants proportional to the

concentration of the excess component. Particularly with regard to the $[O_3]_{\text{gas}}$ gradient at the start of the reaction, these
epicycles are somewhat arbitrary and depend on human judgement in terms of assessing linearity of the 2nd-order plot and
150 goodness of fit of the 1st-order plots. The problem could be avoided by using a numerical model to explicitly represent the
surface concentrations of oleic acid and all likely deuterated products and intermediates and the rates at which those products
and intermediates are produced, decay, and partition away from the surface into the bulk phase or gas phase, as well as to
explicitly represent the spatial and temporal gradients of $[O_3]_{\text{gas}}$ within the chamber. Several numerical models focusing on
155 layers) are under development by this research group in collaboration with others, and their use has already yielded
significant contributions in the field of aerosol kinetics (Pfrang et al., 2010, 2011; Sebastiani et al., 2018; Shiraiwa et al.,
2010, 2012).

However, a full investigation of the detailed kinetics of this reaction is considered out of scope for this study, as it has been
studied before (King et al., 2009), and the primary purposes of this work is to investigate differences between the reaction at
160 room temperature and at a more atmospherically realistic near-freezing temperature. As is made clear in the presentation of
the results of this kinetic fitting in the main text, this simpler analytic approach demonstrates that there is not a significant
difference in the kinetics of the reaction between these two temperature conditions. As a result, it was not considered
worthwhile to deploy the numerical model in order to attempt to account for the slight systematic bias towards
underestimation of rate constants present in the analytical model, as it would be exceedingly unlikely to uncover anything of
165 further interest.

Figure S12 shows an example of equation 2 fitted to a kinetic time series as described above.

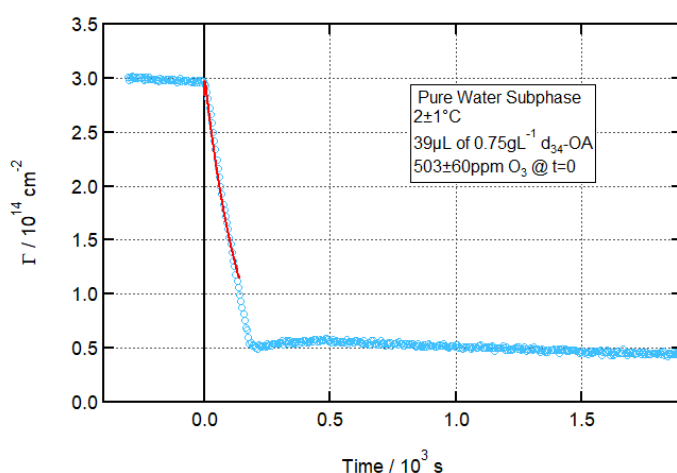


Figure S12: Time evolution plot for ozonolysis of 39 μL 0.75 g L^{-1} d_{34} -OA (CHCl_3 spread. sol) on pure water subphase by 503 \pm 60 ppb O_3 introduced at $t = 0$ s at 2 ± 1 °C showing Eq. (2) (main paper) fitted to the data; error bars omitted for visual clarity.

170 Section S4 – IRRAS Data

As mentioned in the method section, this work was carried out in a reaction chamber designed for the integration of simultaneous *in situ* IRRAS measurements on a neutron reflectometry beamline. This equipment was deployed and used for the experiments carried out on INTER, but could not be deployed on FIGARO due to space restrictions. IRRAS integration is primarily intended to facilitate the study of mixed monolayers, in which one component can be deuterated (for neutron reflectometry) and the other left non-deuterated (and thus easily measurable by IRRAS). As the work discussed here focused entirely on single-component monolayers, the IRRAS data did not provide any additional insight. IRRAS can also measure deuterated components (the IR absorbance bands are shifted to a lower wavenumber, distinguishing them from the absorbance bands associated with non-deuterated components), but the sensitivity in this region is much lower, as these bands are weaker and more affected by atmospheric interference. This means that IRRAS measurements cannot distinguish the residues left at low temperatures from background noise. Figure S13 shows an example of IRRAS data from an ozonolysis experiment on INTER.

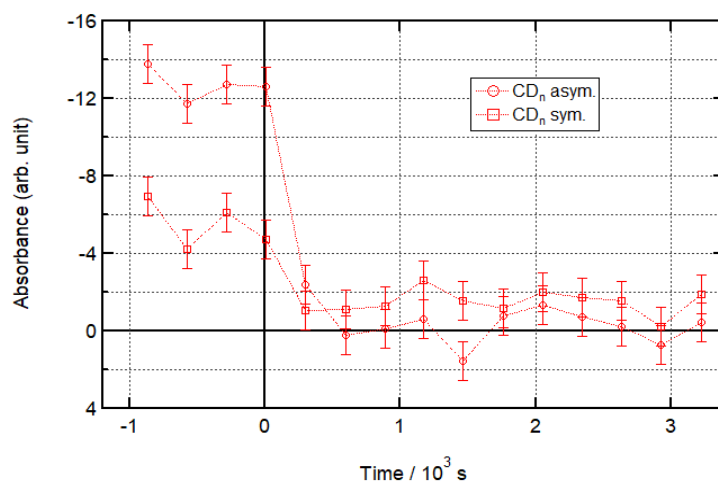
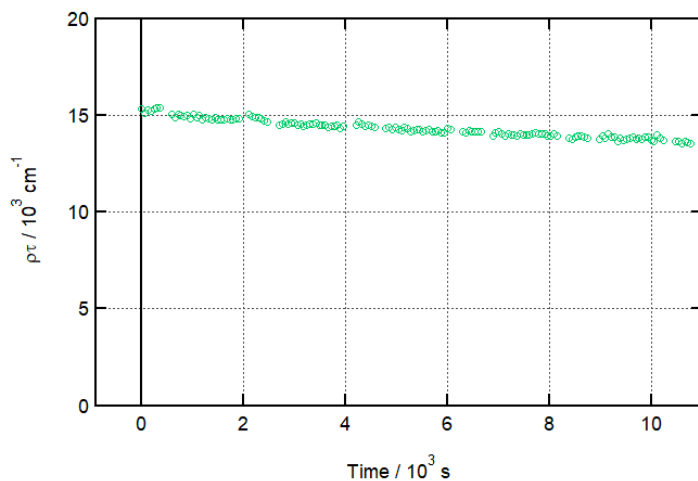


Figure S13: Time evolution plot for ozonolysis of 29 μL 1.0 g L^{-1} $\text{d}_{34}\text{-OA}$ (CHCl_3 spread. sol.) on pure subphase by 323 ± 29 ppb O_3 introduced at $t = 0$ s at 21 ± 1 $^\circ\text{C}$ showing integrated IR absorbance for CD_n asymmetric (circles) and symmetric (squares) bands.

185 Section S5 – Stability Run

In order to ensure that the monolayer was stable at low temperatures, and that the reactions observed were chemical oxidation on the introduction of O_3 , and not confounded by significant loss of material through physical or chemical processes unrelated to ozonolysis, a long exposure of an oleic acid to a pure O_2 flow was performed, and the results are shown in Figure S14 below.



190

Figure S14: Stability run; time evolution plot for 30 μL 1.2 g L^{-1} d_{34} -OA (CHCl_3 spread. sol.) at 3 ± 2 $^\circ\text{C}$ on pure water subphase under pure O_2 flow; error bars omitted for visual clarity.

References

- King, M. D., Rennie, A. R., Thompson, K. C., Fisher, F. N., Dong, C. C., Thomas, R. K., Pfrang, C. and Hughes, A. V.:
 195 Oxidation of oleic acid at the air-water interface and its potential effects on cloud critical supersaturations, *Phys. Chem. Chem. Phys.*, 11(35), 7699–7707, doi:10.1039/b906517b, 2009.
- Pfrang, C., Shiraiwa, M. and Pöschl, U.: Coupling aerosol surface and bulk chemistry with a kinetic double layer model (K2-SUB): oxidation of oleic acid by ozone, *Atmos. Chem. Phys.*, 10(10), 4537–4557, doi:https://doi.org/10.5194/acp-10-4537-2010, 2010.
- 200 Pfrang, C., Shiraiwa, M. and Pöschl, U.: Chemical ageing and transformation of diffusivity in semi-solid multi-component organic aerosol particles, *Atmos. Chem. Phys.*, 11(14), 7343–7354, doi:10.5194/acp-11-7343-2011, 2011.
- Sebastiani, F.: Neutron reflectometry and Ellipsometry applied to ATmospheric Night-time Oxidation, University of Reading, PhD thesis, 2014.
- Sebastiani, F., Campbell, R. A. and Pfrang, C.: Complementarity of neutron reflectometry and ellipsometry for the study of
 205 atmospheric reactions at the air–water interface, *RSC Adv.*, 5(129), 107105–107111, doi:10.1039/C5RA22725A, 2015.
- Sebastiani, F., Campbell, R. A., Rastogi, K. and Pfrang, C.: Night-time oxidation of surfactants at the air–water interface: effects of chain length, head group and saturation, *Atmos. Chem. Phys.*, 18, 3249–3268, 2018.

- Shiraiwa, M., Pfrang, C. and Pöschl, U.: Kinetic multi-layer model of aerosol surface and bulk chemistry (KM-SUB): the influence of interfacial transport and bulk diffusion on the oxidation of oleic acid by ozone, *Atmos. Chem. Phys.*, 10(8), 210 3673–3691, doi:<https://doi.org/10.5194/acp-10-3673-2010>, 2010.
- Shiraiwa, M., Pfrang, C., Koop, T. and Pöschl, U.: Kinetic multi-layer model of gas-particle interactions in aerosols and clouds (KM-GAP): linking condensation, evaporation and chemical reactions of organics, oxidants and water, *Atmos. Chem. Phys.*, 12(5), 2777–2794, doi:<https://doi.org/10.5194/acp-12-2777-2012>, 2012.

Chapter 6 – Ozonolysis of Mixed Monolayers of Oleic and Stearic Acids

6.1 – Introduction

The initial motivation behind combining neutron reflectometry (NR) with Fourier transform infra-red reflection-absorption spectroscopy (FT-IRRAS) was the study of mixed monolayers. The first mixed system selected for study with our combined NR/FT-IRRAS apparatus was a binary mixture of oleic and stearic acids. Oleic acid (OA) has been studied extensively in the past^{1,2}; stearic acid (SA) is the saturated analogue of oleic acid, and so provides the most similar feasible unreactive co-component. It was considered useful to measure with a saturated co-component, as saturated compounds are commonly found in sea-spray aerosol³ and recent work has suggested that such compounds make up the majority of the monolayers on atmospheric water aerosols⁴.

Work on this mixed system dominated early experiments, but was later relegated in terms of importance within the research project compared with the work on galactocerebroside monolayers and low temperature pure oleic acid monolayers (see Chapters 4 and 5, respectively). This was because data from these mixed monolayers proved initially somewhat confounding to interpret, and required a lot more conceptual work to properly understand than the data for the other systems studied. Several cycles of formulating a hypothesis to explain the unexpected behaviour that was initially observed, performing an experiment, processing the data, rejecting the hypothesis, returning to the literature, and formulating another hypothesis, etc., had to be performed in order to produce a full understanding of the processes at play and the difficulties for our measurement techniques that this particular system was posing. These cycles take a long time when each new set of experiments to test the most recent hypothesis has to be performed on a separate beamline experiment, which are generally scheduled many months apart. Of the eight distinct beamline experiments performed across the course of the work behind this thesis, only three focused on this mixed system in particular, but every single one involved at least a few experimental runs focused on furthering our understanding of this system by testing a hypothesis that purported to explain the more confounding results and help make sense of the data.

This chapter brings together data from all eight beamline experiments in order to finally make sense of the apparently anomalous behaviour of the system and present a description of the ozonolysis of a mixed OA/SA monolayer and how it differs from the ozonolysis of a pure OA monolayer, both in terms of the partitioning of reaction products to the interface and in terms of reaction kinetics. All experiments in this chapter were carried out at room temperature unless otherwise noted.

The chapter is presented in a more narrative format than the preceding results chapters (Chapters 4 and 5), explaining the steps that were undertaken to gradually converge on a satisfactory explanation of all experimental data. This body of work may be repurposed into a paper for publication after the submission of this thesis. In that case, it would gain an introduction and methods section of a similar style to that seen in the those chapters, which briefly cover the material laid out in the introduction and methods chapters of this thesis (Chapters 1 and 2) in a manner which focuses on the justifications for studying this particular system. Such an introduction and methods section are not included here, as this would only duplicate material from earlier in the thesis.

6.2 – Initial Results

Mixtures of d_{34} -OA and h-SA in various molar ratios were oxidised at room temperature by ozone at various ozone concentrations on the INTER beamline at ISIS (RB 1520459 and RB 1620451). In this deuteration configuration, NR was sensitive to OA surface concentration, and FT-IRRAS provided complementary qualitative information with regards to SA surface concentration (via C–H bands) as well as OA concentration (via C–D bands). C–D bands from OA were often weak, as C–D bands are weaker than C–H bands (see Chapter 2), and unsaturated and therefore disordered molecules like OA produce weaker bands than saturated, well-ordered molecules like SA. The combination of disorder and deuteration for d_{34} -OA produces the weakest bands. Experiment RB 1520459 was performed with an early prototype of the NR/FT-IRRAS apparatus that was not able to detect C–D bands for unsaturated components; later prototypes of the apparatus, including that used for experiment RB 1620451, were typically able to detect these bands, though the signal was weak and noisy (signal-to-noise ratios as poor as 2:1 were sometimes observed). The FT-IRRAS is primarily integrated into the NR setup in order to provide information on non-deuterated components via C–H bands; the C–D bands provide qualitative information on the deuterated components that are already quantitatively analysed with high precision by NR, so the absence or weakness of the information from these IR bands is not a concern.

The NR data produced from these experiments was as expected, showing the same linear-to-exponential decay trace seen in our experiments on pure OA ozonolysis (see Figure 6.1). However, the FT-IRRAS data was somewhat confounding. SA, as it lacks a double-bond, is impervious to ozonolysis, at least via the mechanism that oxidises OA, and so, over the timescales studied, should be inert. However, the C–H bands associated with SA were observed to disappear upon the introduction of O_3 into the reaction and analysis chamber on a similar timescale to the removal of OA as measured by NR (see Figure 6.2). Furthermore, this result was not consistently reproducible. The C–H bands did not disappear over a reproducible timescale (sometimes persisting for several minutes after the completion of OA removal as measured by NR). On more than one occasion, the bands were seen to disappear and reappear seemingly at random after the introduction of O_3 (see Figure 6.3 for an example). It was observed that disturbing the monolayer slightly after ozonolysis by removing and replacing the chamber lid often prompted the C–H bands to appear or disappear. These experiments were repeated off the beamline (with an h-OA/ d_{35} -SA mixture, substituted for the original mixture due to the high cost of d_{34} -OA) and the presence or absence of IR bands assigned to SA (in this offline case, C–D bands) continued to be variable and inconsistent after ozonolysis of the mixed monolayer.

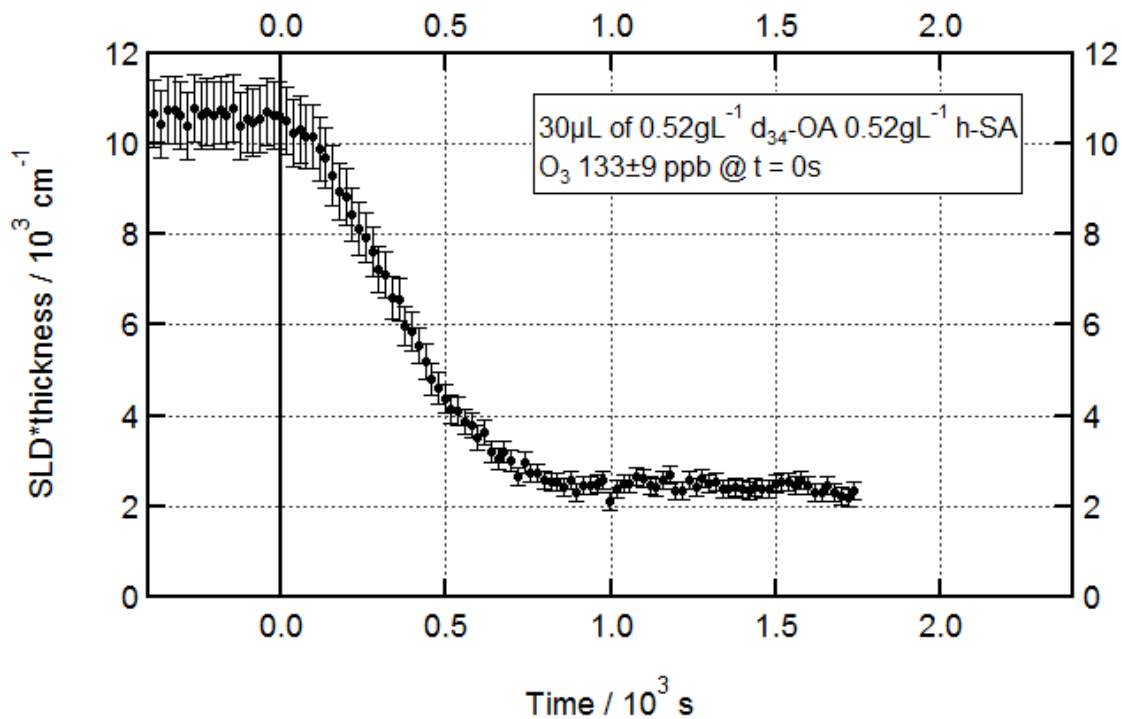


Figure 6.1 – Ozonolysis of d_{34} -OA in a mixed monolayer with h-SA; 30 μL of 0.52 g L^{-1} d_{34} -OA/ 0.52 g L^{-1} h-SA; O_3 introduced at $t = 0 \text{ s}$ at $133 \pm 9 \text{ ppb}$; neutron reflectometry fitted time series.

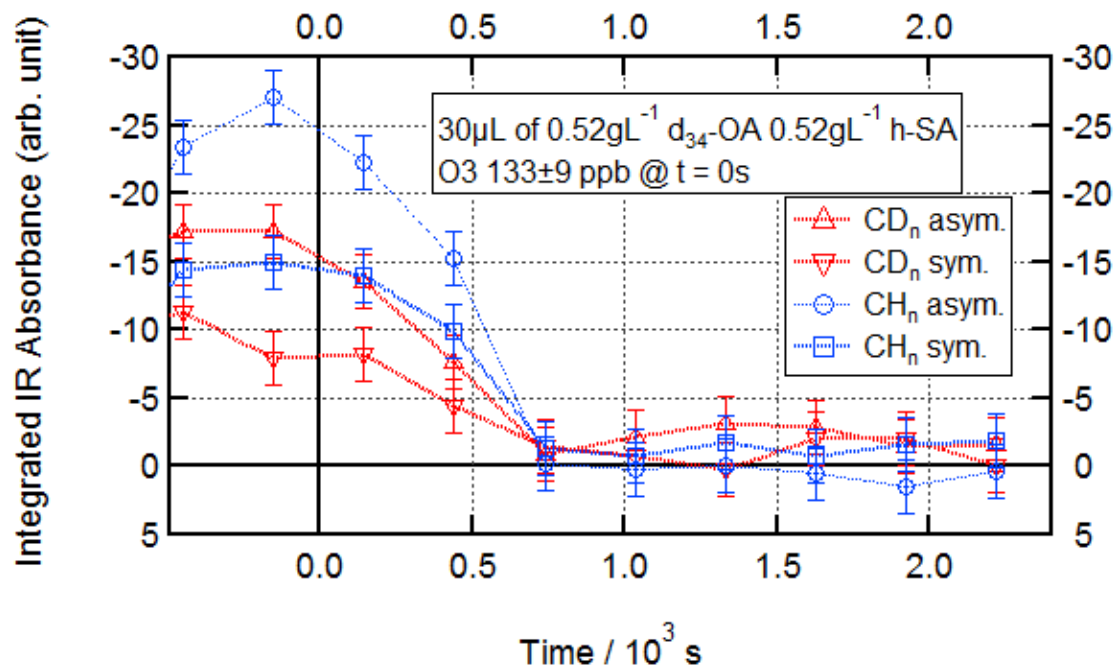


Figure 6.2 – Ozonolysis of d_{34} -OA in a mixed monolayer with h-SA; 30 μL of 0.52 g L^{-1} d_{34} -OA/ 0.52 g L^{-1} h-SA; O_3 introduced at $t = 0 \text{ s}$ at $133 \pm 9 \text{ ppb}$; infra-red spectroscopy integrated time series.

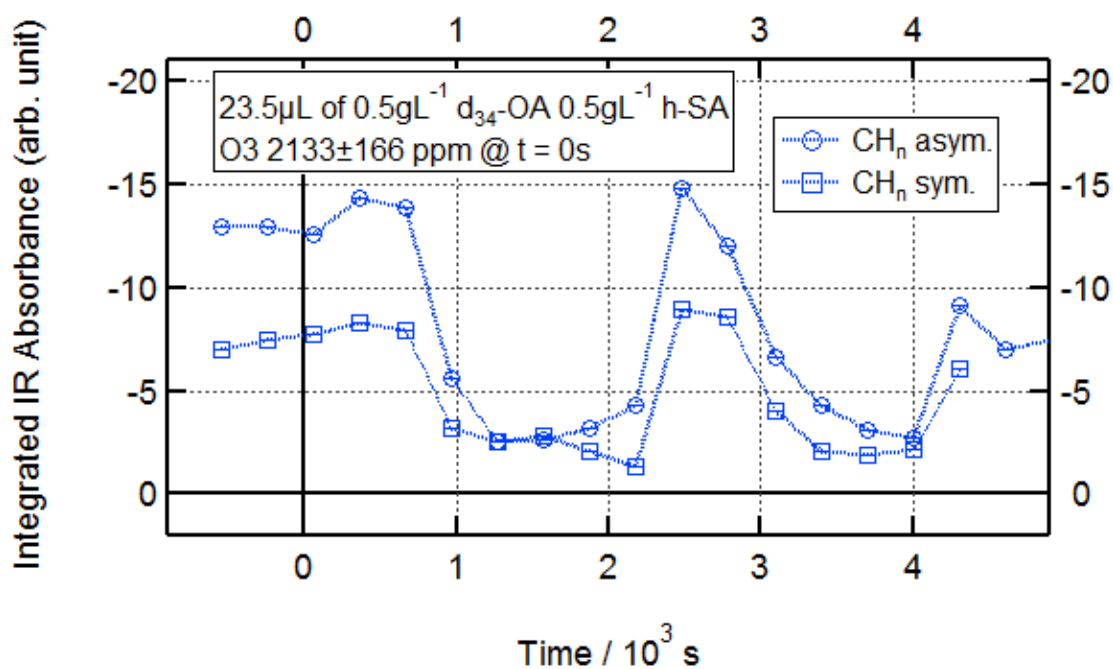


Figure 6.3 – Ozonolysis of d_{34} -OA in a mixed monolayer with h-SA; 23.5 μL of 0.5 g L^{-1} d_{34} -OA/0.5 g L^{-1} h-SA; O_3 introduced at $t = 0$ s at 2133 ± 166 ppb; infra-red spectroscopy integrated time series for h-SA over an extended measurement showing inconsistent absorbance.

In order to probe this issue further, and attempt to determine whether the disappearance of SA as observed by FT-IRRAS was real or simply a measurement problem, ozonolysis experiments on h-OA/ d_{35} -SA mixed monolayers were performed with full NR/FT-IRRAS measurement (INTER RB 1520459 and RB 1610500). In this deuteration configuration, NR was sensitive to SA, and FT-IRRAS was sensitive to OA (C–H bands) and SA (C–D bands).

The FT-IRRAS data produced was consistent with offline experiments performed with the same deuteration configuration and with the data shown in Figures 6.2 and 6.3 (except with the C–H and C–D bands reversed), showing disappearance of bands attributable to OA (C–H) upon ozonolysis as expected (and in agreement with NR data for the d_{34} -OA/h-SA deuteration configuration) and inconsistent behaviour of bands attributable to SA (C–D).

The NR data was of most interest for this configuration, as if it agreed with the FT-IRRAS data (by showing a decline in reflectivity concomitant with the decline in C–D band intensity) it would suggest that SA really was being removed from the interface by an as-yet unknown mechanism, whereas, if it remained constant throughout exposure of the monolayer to O_3 (as originally expected due to the lack of a double-bond for ozonolysis and as observed for pure d_{35} -SA monolayers under O_3 (INTER RB 1620451; see Figure 6.4), it would suggest that the FT-IRRAS measurements were being affected by some measurement artefact or other.

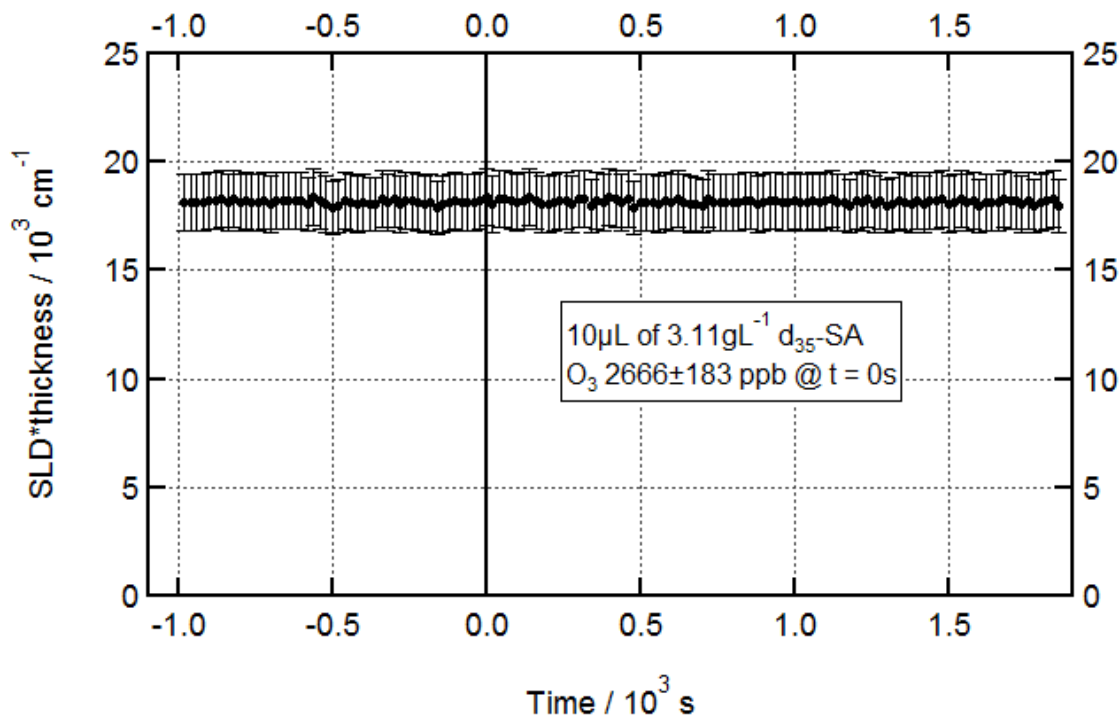


Figure 6.4 – Exposure of a pure d_{35} -SA monolayer to O_3 ; $10 \mu\text{L}$ of $3.11 \text{ g L}^{-1} d_{35}$ -SA; O_3 introduced at $t = 0 \text{ s}$ at $2666 \pm 183 \text{ ppb}$; neutron reflectometry fitted time series showing no ozonolysis; compare with Figure 6.5.

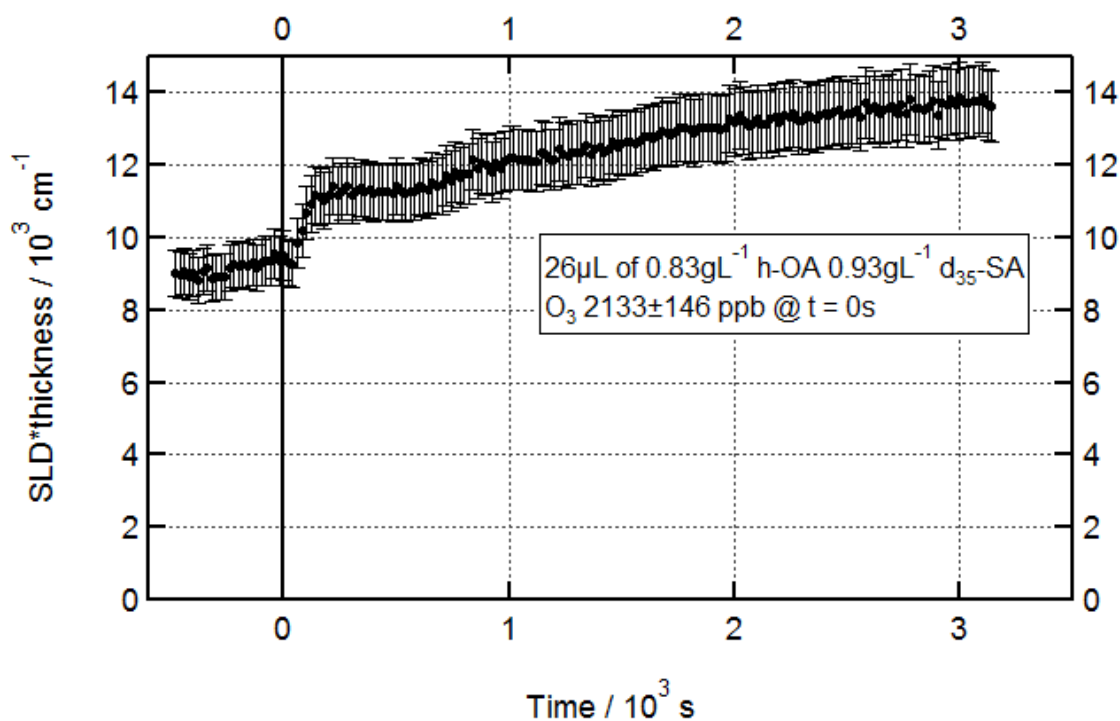


Figure 6.5 – Ozonolysis of h -OA in a mixed monolayer with d_{35} -SA; $26 \mu\text{L}$ of $0.83 \text{ g L}^{-1} h$ -OA/ $0.93 \text{ g L}^{-1} d_{35}$ -SA; O_3 introduced at $t = 0 \text{ s}$ at $2133 \pm 146 \text{ ppb}$; neutron reflectometry fitted time series showing unexpected increase in signal, as if more d_{35} -SA somehow appeared at the interface upon oxidation of h -OA; compare with Figure 6.4.

In a result more confounding than the original unexpected FT-IRRAS results, the NR data for this ozonolysis reaction showed an *increase* in SA concentration at the surface upon ozonolysis of the mixed monolayer (see Figure 6.5). It was immediately recognised that this was very unlikely to represent a real phenomenon: There is simply nowhere for the additional SA to come from. The consistent NR response of increasing SA signal regardless of whether the FT-IRRAS data showed the persistence or disappearance of bands attributable to SA (C–D) suggested that this FT-IRRAS data inconsistency was not caused by a genuine inconsistency in the reaction, in which SA was sometimes removed from the interface and sometimes not, for reasons and by a mechanism unknown, but rather by some property of the post-ozonolysis experimental state that rendered the FT-IRRAS measurement itself inconsistent. Similarly, the NR measurements either before or after the introduction of ozone are overwhelmingly likely to be affected by the same or a connected property, as it is not credible to take both at face value and infer that the reaction has created additional SA. Attention was then turned to discerning what could cause these measurement discrepancies.

6.3 – Explaining the Anomaly

Initially, it was hypothesized that the microscale structure of the mixed layer might result in unexpectedly high roughness, but this, as mentioned in the *RSC Advances* paper introducing the NR/FT-IRRAS combined reaction and analysis chamber (see section 3.1), was rejected as predicted enhanced off-specular scattering was not observed⁵. We then hypothesised in that paper that the explanation may involve problems in correctly assigning a scaling factor to the mixed layer, due to surface inhomogeneity that had previously been identified on a monolayer of this composition⁶. However, this was later ruled out after experiments with a d₃₄-OA/d₃₅-SA monolayer (INTER RB 1620451), which should have eliminated this effect, did not. Instead a simple additive signal of the effects seen for d₃₄-OA and d₃₅-SA in monolayers with h-SA and h-OA respectively was seen (a decrease in signal due to OA ozonolysis overlaid with the same mysterious increase in SA signal; see Figure 6.6). A third hypothesis, in which the two components were theorised to form a structure better modelled by a multilayer, was rejected after experiments on a D₂O subphase (INTER RB 1710483), which would have produced NR data characteristic of a bilayer were this hypothesis correct, failed to produce this result.

Attention then turned to attempting to appraise what changes in the lateral structure of the surface were likely to be occurring during the ozonolysis of the mixed monolayer. Brewster angle microscopy (BAM) allows for visual appraisal of surface structure in monolayers of this sort, so was carried out on OA, SA, and mixed monolayers. Unfortunately, the requirement for BAM that the objective lens be positioned within a few millimetres of the interface made it practically infeasible to observe an ongoing ozonolysis reaction with BAM. Furthermore, the bulkiness of the BAM apparatus, and the fragility of the monolayers in question, made it impracticable to either bring a BAM to a post-reaction monolayer, or bring a post-reaction monolayer to a BAM. To overcome this limitation, pure SA monolayers were studied with BAM in order to simulate the expected residual monolayer after ozonolysis of a mixed monolayer.

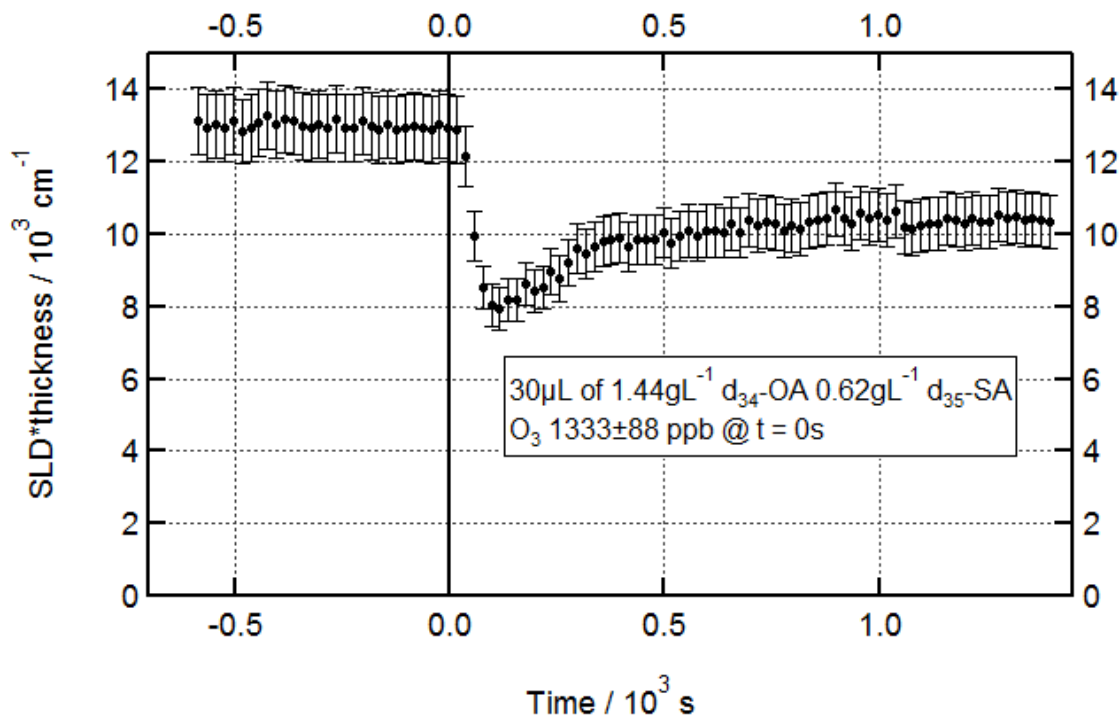


Figure 6.6 – Ozonolysis of d_{34} -OA in a mixed monolayer with d_{35} -SA; 30 μL of 1.44 g L^{-1} d_{34} -OA/0.62 g L^{-1} d_{35} -SA; O_3 introduced at $t = 0$ s at 1333 \pm 88 ppb; neutron reflectometry fitted time series showing total reflectivity due to both deuterated components.

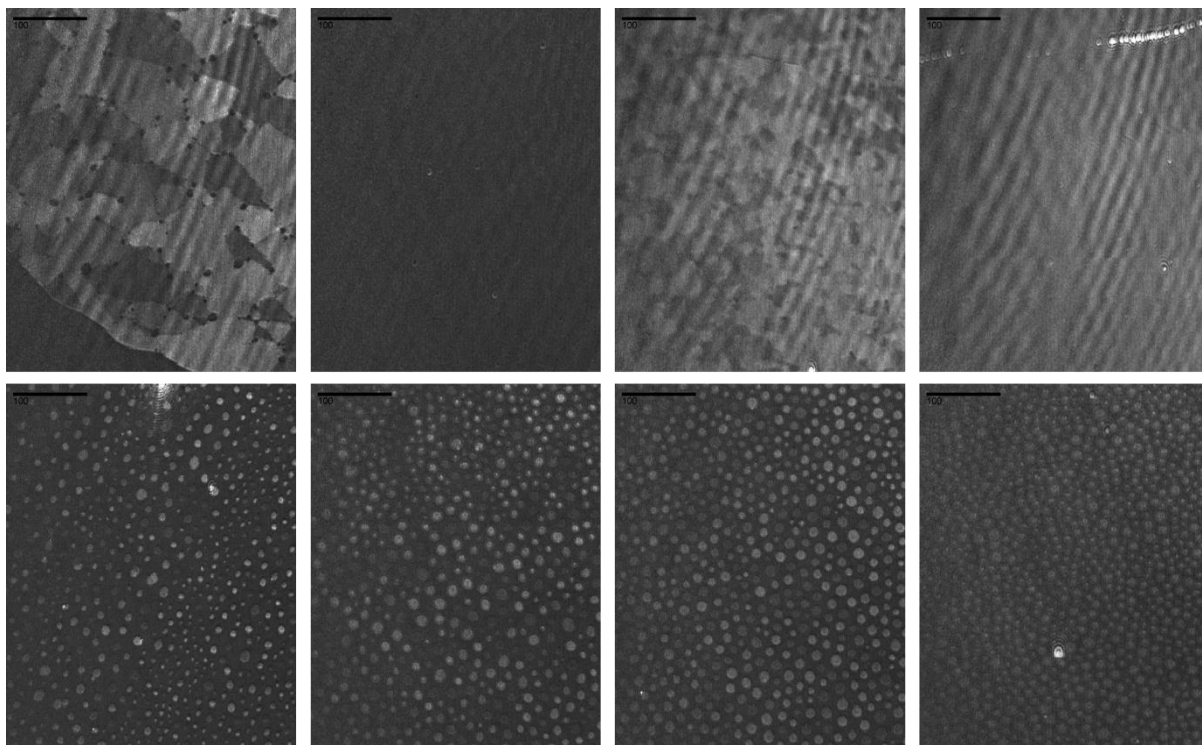


Figure 6.7 – BAM images. Top row: SA. From left to right: 0 mN m^{-1} (region with material); 0 mN m^{-1} (region with no material); 13 mN m^{-1} ; 30 mN m^{-1} . Bottom row: OA/SA 1:1 molar ratio. From left to right: 0 mN m^{-1} ; 7 mN m^{-1} ; 16 mN m^{-1} ; 30 mN m^{-1} . All scale-bars (top left corner of each image) are 100 μm ; tight banding across SA images is due to a small deformity in the BAM objective lens which causes this artefact in some circumstances.

For a complete set, monolayers of OA, SA, and an OA/SA mixture were studied with BAM at a variety of surface pressures (corresponding to a variety of surface concentrations; see Figure 6.7). OA monolayers were featureless and uniform throughout compression cycles. Mixed monolayers showed the

microscale surface inhomogeneity previously observed⁶. This microscale inhomogeneity is consistent with less than ideal mixing (any given molecule of OA or SA is more likely to be in contact with another molecule of the same species than with a molecule of the other species). Some previous research had observed macroscale inhomogeneities in OA/SA mixtures⁷, but this was in supersaturated surfaces in which OA and SA were essentially competing for surface adsorption sites. SA, being more amphiphilic, preferentially adsorbed to the surface in these conditions, and macroscale islands of OA were observed above the SA monolayer. This is not in contradiction with these results, which observe a subsaturated surface in which there is no excess surfactant and therefore no competition between surfactant species for adsorption sites, and observes microscale inhomogeneity within the surface monolayer itself.

The key finding was that SA monolayers, though uniform at high surface pressures/concentrations corresponding to a 2D-solid phase, showed significant inhomogeneity on the scale of 10 to 100 μm at intermediate surface pressures/concentrations corresponding to a 2D-liquid phase. Further, at low surface pressures/concentrations corresponding to a 2D-gas phase, the SA monolayers showed significant additional inhomogeneity on a much larger scale, with large areas of the surface appearing completely devoid of material. These low surface pressures/concentrations are in line with the surface concentrations of SA that would have been present at the interface after the ozonolysis of mixed films. The size of these islands of material and areas of monolayer-free surface was hard to ascertain, as they were significantly larger than the BAM field of view. It was estimated, based on ongoing observation of the surface as the islands moved around (probably due to slight air currents in the BAM chamber), that the size of the islands is of the order of a few millimetres to a few centimetres.

This large-scale inhomogeneity explains the inconsistency in the FT-IRRAS data collected from the SA left behind after the ozonolysis of OA in a mixed monolayer. Like the BAM field of view, the IR beam is focused sharply on a small area of the interface, measuring perhaps a few square millimetres. The kind of large-scale inhomogeneity observed in the BAM images would precipitate a situation in which the FT-IRRAS is sometimes sampling a part of the interface at which SA is adsorbed, and sometimes sampling a clean interface. This would result in exactly the inconsistency observed. Furthermore, the previously puzzling observation that removal and replacement of the reaction and analysis chamber lid often prompted a transition between observing and not observing IR bands attributable to SA can now be explained by the fact that such an interference would produce air currents inside the chamber, which would likely move the SA islands around the interface, sometimes prompting a transition from a state in which an island is in the IR footprint to a state in which the IR footprint is sampling clean interface, or the reverse.

This inhomogeneity in low surface concentration SA also explains the increase in NR signal upon ozonolysis of an h-OA/d₃₅-SA monolayer. Fitting NR data to a monolayer assumes lateral uniformity, and deviations from that uniformity on a length scale longer than the neutron coherence length are theorised to result in an overestimation of surface concentration by a model that assumes uniformity⁸. In a simplified model of surface inhomogeneity in which material is either present or not present at every point of the interface, and the fractional coverage of the interface is denoted Θ^p , a uniform monolayer model overestimates surface concentration by a factor of $1/\Theta$.

Estimating the neutron coherence length is not trivial, but other work in somewhat similar experimental setups suggests that, for these setups, it is on the order of tens of μm ⁹⁻¹¹. Certainly, the inhomogeneity of the low concentration SA system is sufficiently large-scale to precipitate this effect. However, the inhomogeneity of the mixed system is of the scale of 10 μm or lower, which is small enough that it could

^p Lu *et al.* use the lower-case θ , but the upper-case Θ is used here to avoid confusion with θ as used for potential temperature in section 1.4 and for angles in various other contexts.

well be smaller than the coherence length of the neutron, and therefore essentially be beyond the spatial resolution of the neutron, which would ‘see’ a smeared-out uniform layer.

If this situation were to obtain, then reflectivity from d_{35} -SA in an h-OA/ d_{35} -SA mixed monolayer would not be correctly interpreted by a uniform monolayer model before ozonolysis. However, once ozonolysis had removed the h-OA and left a low concentration d_{35} -SA ‘layer’ (which would more accurately be described as a collection of islands) behind, the reflectivity from the d_{35} -SA would be higher, and thus the surface concentration overestimated by a model assuming a uniform layer. This would result in exactly the apparent increase in surface concentration that we observed in this situation.

In order to test this, we performed a multi-trough experiment (INTER RB 1910615) in which a series of pure and mixed OA and SA monolayers of various concentrations were spread in adjacent troughs and NR data collected sequentially. The results are presented in Table 6.1.

Table 6.1 – NR data from various OA and SA surface concentrations.

Trough	Sample	Total OA spread /nmol	Total SA spread /nmol	Fitted SLD @ 2 nm Monolayer Thickness
1	d_{35} -SA	0	33	5.16
2	d_{35} -SA	0	65	6.78
3	d_{34} -OA	32	0	2.49
4	d_{34} -OA	70	0	4.64
5	h-OA/ d_{35} -SA	34	34	3.30
6	d_{34} -OA/ d_{35} -SA	33	32	5.07
7	d_{34} -OA/h-SA	35	34	2.57

As this data demonstrates, d_{34} -OA is relatively well-behaved and shows a near-linear relationship between fitted SLD and quantity spread onto the interface (an error of around $\pm 10\%$ is expected due to dilution errors, difficulty in spreading precisely the correct volume, and other general experimental errors) and shows no great change in reflectivity when co-deposited with h-SA. Conversely, d_{35} -SA shows significant deviation from the linear behaviour that would be expected from a uniform monolayer, with the lower concentration run of pure d_{35} -SA showing far more reflectivity (resulting in a far higher fitted SLD) than would be expected based on such a model. This is what I predicted based on the idea of enhanced reflectivity due to large-scale surface inhomogeneity as proposed by Lu *et al.*⁸. Crucially, this enhanced reflectivity effect is not seen for d_{35} -SA in a mixed monolayer with h-OA, which supports my claim that the inhomogeneity observed with BAM is, in this case, too small-scale to affect reflectivity in the same manner.

The increase in neutron reflectivity observed during the ozonolysis of an h-OA/ d_{35} -SA monolayer is therefore explained as due to a transition between inhomogeneity regimes with respect to the distribution of d_{35} -SA. In the pre-ozonolysis regime, inhomogeneity manifests on a small enough length scale so as not to enhance neutron reflectivity and result in overestimation of surface concentration by a reflectivity fitting model that assumes a uniform monolayer. In a post-ozonolysis regime, due to the absence of h-OA, this inhomogeneity manifests on a significantly larger length scale. Critically, it manifests on a scale that is larger than the coherence length of the neutron and therefore enhances neutron reflectivity and results in overestimation of surface concentration by a reflectivity fitting model that assumes a uniform monolayer. The inconsistency in FT-IRRAS data observed for the post-ozonolysis period of the same ozonolysis is due to the same phenomenon of large-scale SA inhomogeneity, which is on a length scale similar to or even larger than the IR footprint.

6.4 – Compression/Annealing Experiments

Further evidence that inhomogeneity in the surface distribution of SA leads to increased reflectivity compared with a uniform monolayer was gathered by performing a compression/annealing experiment. The combined NR/FT-IRRAS reaction and analysis chamber used for the majority of this work does not permit adjustment of the surface area of the system (see Chapter 3) but, if no gas-phase oxidants are to be introduced, and no FT-IRRAS measurements are required, a Langmuir trough can be deployed onto a suitable neutron reflectometry beamline, allowing for manipulation of the surface area of a system while collecting surface pressure and neutron reflectometry data. Such an experiment was performed on the SURF reflectometer at ISIS (RB 1540015).

Previous BAM/tensiometry work had suggested that the large-scale surface inhomogeneity was largely a feature of the 2D-gas phase of SA, with limited smaller-scale inhomogeneity (though possibly still large-scale enough to produce an enhanced reflectivity effect) in the 2D-liquid phases, and a homogenous surface in the 2D-solid phase. See Figure 6.7 for BAM images; see Figure 6.8 for a pressure-area isotherm with phases labelled. This work had also suggested that ‘annealing’ the surface, by compressing into the 2D-solid phase and then relaxing back into the 2D-gas phase, might reduce the extent of the inhomogeneity in the 2D-gas phase. An annealing effect can clearly be seen in the pressure-area isotherm in Figure 6.8; the first compression shows higher surface pressure at a given surface area, with subsequent compressions and expansions settling into a more reproducible relationship. Appraising the surface at 0 mN m^{-1} after the first compression cycle suggested that this annealing cycle might have decreased surface inhomogeneity to some degree; as previously mentioned, the BAM field of vision is not nearly wide enough to systematically assess the degree of inhomogeneity or fractional surface coverage in this state, but simply watching through the microscope over time suggested that this effect had occurred. This tentative observation was the rationale behind performing this compression/annealing NR experiment, which tested this hypothesis quantitatively.

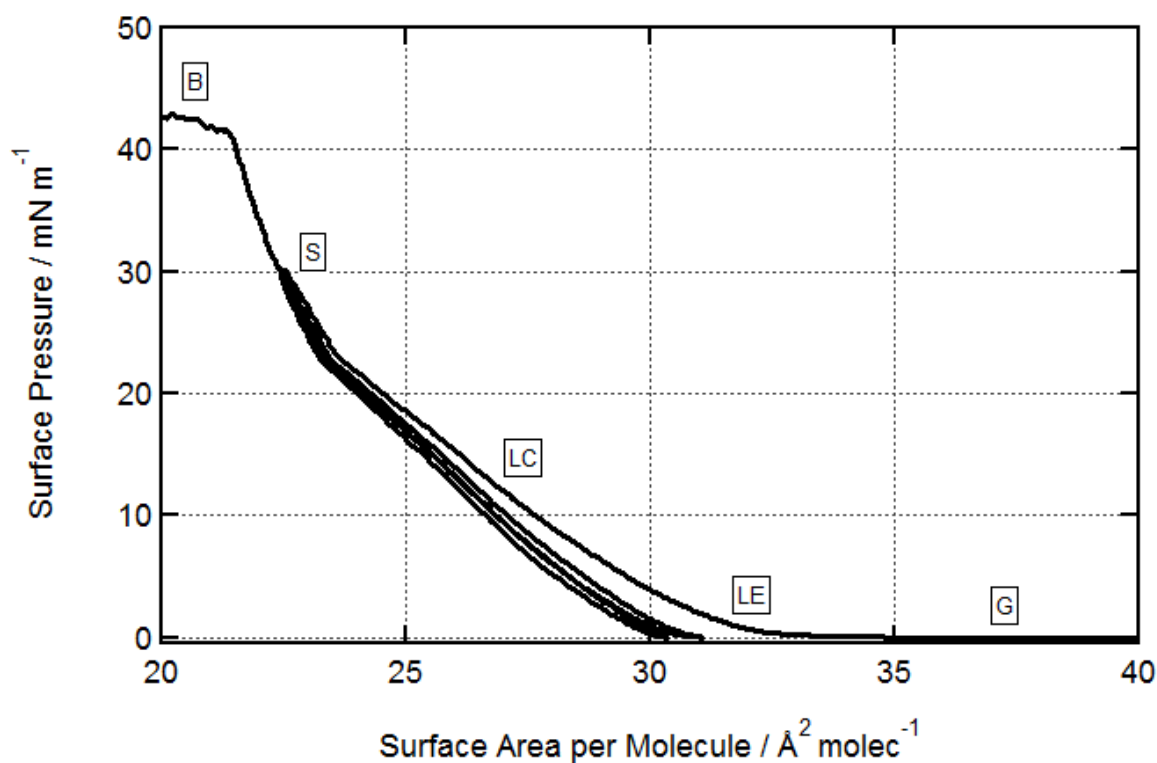


Figure 6.8 – Stearic acid pressure-area isotherm on pure water collected by compression from low-area spreading to 30 mN m^{-1} , two cycles between 30 and 0 mN m^{-1} , and a final compression to break. G = 2D-gas; LE = 2D-liquid expanded; LC = 2D-liquid compressed; S = 2D-solid; B = broken monolayer. Boundaries of LE phase are somewhat indistinct.

In this experiment, d_{35} -SA was spread to a target of $70 \text{ \AA}^2 \text{ molec}^{-1}$, and reflectivity was measured. An annealing cycle was then performed by compressing to a target surface pressure of 25 mN m^{-1} (taking the monolayer into the 2D-solid phase) and then expanding to the original $70 \text{ \AA}^2 \text{ molec}^{-1}$. The reflectivity was measured again and was lower (see Figure 6.9), suggesting that the degree of inhomogeneity (and thus reflectivity enhancement) was lower after annealing. A second compression cycle produced a much smaller decrease in reflectivity, which is concomitant with the pressure-area isotherm data in suggesting that the majority of the difference is made by the first compression cycle. This second cycle also acts as an internal control, demonstrating that a compression cycle results in negligible loss of material, strengthening the case that the loss of reflectivity from the first compression cycle is a result of a surface annealing effect.

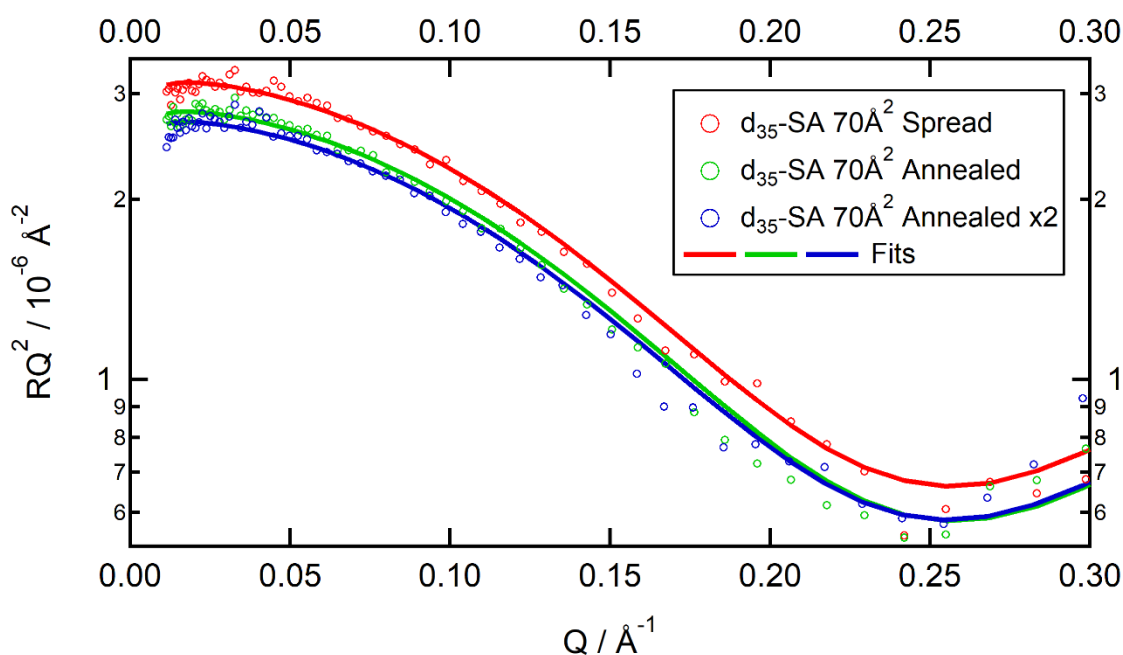


Figure 6.9 – Annealing of a pure d_{35} -SA monolayer; spread to $70 \text{ \AA}^2 \text{ molec}^{-1}$; RQ^2 vs Q reflectivity plots after spreading and after each of two annealing cycles.

Further to this, the twice-annealed layer was compressed to 60 , 51 , and $47 \text{ \AA}^2 \text{ molec}^{-1}$. This corresponds to a linear series in surface concentration, which has a hyperbolic relationship with surface area per molecule. The increase in reflectivity with increasing surface concentration (decreasing surface area) was far weaker than that which would be predicted by a uniform monolayer model. This demonstrates that the behaviour of an SA ‘monolayer’ in the 2D-gas phase is not well described by a model in which a uniform monolayer simply decreases in density at lower surface concentrations, and may in fact be better represented by a model in which islands of SA simply drift further apart at lower surface concentrations. A single compression cycle was also performed on a d_{35} -SA layer spread to a target of $50 \text{ \AA}^2 \text{ molec}^{-1}$ and compressed once to 25 mN m^{-1} before being expanded back to $50 \text{ \AA}^2 \text{ molec}^{-1}$, and the same annealing effect was observed.

6.5 – Implications

The implications of these conclusions are twofold. For one, it appears that the use of FT-IRRAS as a complementary technique to NR is somewhat limited in cases where large-scale surface inhomogeneity is likely to play a part, due to the small measurement footprint. Low surface concentrations of molecules such as saturated fatty acids, which experience strong van der Waals interactions and easily cluster together on the surface, are prime candidates for displaying this inhomogeneity, so care should be taken when applying this technique to these systems.

By the same token, quantitative use of NR to determine surface concentration for these systems is ill-advised if there is a reasonable chance that the system will transition between inhomogeneity regimes or display a poorly-defined or hard-to-measure level of inhomogeneity at any point where quantitative NR data is desired.

More encouragingly for this work, this does not mean that using NR to quantitatively track OA in a mixed OA/SA monolayer is problematic. As the data in Table 6.1 demonstrates, OA is reasonably well-behaved and does not suffer the same changes in reflectivity dependent on co-deposited material as does SA. Due to its double-bond, which introduces a bend into the main fatty acid chain, it does not easily form ordered stacks, and instead forms a disordered uniform monolayer in every case that was investigated. All three of our earlier hypotheses for the anomalous behaviour of our mixed monolayers (roughness, scale factor, and bilayers) would have, if true, cast doubt on the usefulness of the NR data for d₃₄-OA in a mixed layer with h-SA. The hypothesis which we now believe to be correct, which is laid out at the end of section 6.3, essentially places the entirety of the blame for the anomalous data on the behaviour of SA, and provides no reason why NR cannot be used to quantitatively measure the surface concentration of d₃₄-OA in a mixed monolayer with h-SA, despite the difficulties with measuring the reverse deuteration configuration. The usefulness of the FT-IRRAS data gathered through a combined NR/FT-IRRAS study of this system, however, is of limited use, as the FT-IRRAS cannot reliably inform us about the SA, as had originally been hoped.

6.6 – Kinetics

The notion that NR can effectively be used to quantitatively measure d₃₄-OA in the presence of h-SA implies that such data from the ozonolysis of these monolayers can be used to calculate a 2nd-order rate constant for the reaction of OA with O₃ in these conditions. Experiments on INTER (RB 1620541) for d₃₄-OA/h-SA mixtures of 1:1 and 1:3 mass ratios exposed to O₃ concentrations of 133±9 and 533±37 ppb were performed (see Figure 6.10). Pseudo-1st-order rate constants were fitted to each reaction using a modified exponential function that takes into account the evolution of [O₃] (ozone concentration) inside the reaction and analysis chamber during the reaction (which starts at zero, and climbs towards the target value quickly enough to allow most of the reaction to proceed at the target [O₃]_{gas}, but slowly enough to cause the reaction to start more slowly than would be predicted from a simple exponential decay in constant [O₃]_{gas} model). This model relates the surface concentration of OA (Γ) over time (t) to the initial surface concentration of OA (Γ₀), the pseudo-1st-order rate constant (k₁), the volume of the chamber (v = 2100 cm³) and the gas flow rate through it (f = 1200 cm³ min⁻¹) via a modified exponential pseudo-1st-order reaction rate equation thus:

$$\Gamma(t) = \Gamma_0 e^{-k_1 \left(t - \frac{v}{f} \left(1 - e^{-\frac{f}{v}t} \right) \right)}$$

Equation 6.1

The chapter on OA kinetics at low temperatures (Chapter 5) explains in detail the limitations of this model, how some limitations can be overcome and others cannot, and the limitations thereby implied for the uses to which the fitted values can be put. All should be taken to apply to this data as well. Due to the longer distance between ozoniser and reaction and analysis chamber on INTER (as opposed to FIGARO at the ILL) t_{offset} values are higher (~1 min) for reactions on INTER.

The fitted k₁ values are then plotted against [O₃]_{surf} (see Figure 6.11). [O₃]_{surf} values were calculated from [O₃]_{gas} values by using a Henry's law solubility constant for O₃ in organics of [gas]/[organic] = 11.7 and assuming the same layer thickness of 2 nm. This solubility constant is consistent with the value used previously by this group and others² and is informed by the work of Smith *et al.*¹².

Fitting the relationship between k_1 and $[O_3]_{surf}$ to a straight line gives a 2nd-order rate constant (k_2) of $2.3 \pm 0.8 \times 10^{-10} \text{ cm}^2 \text{ s}^{-1}$ ($\pm 95\%$ confidence interval). This is precisely in line with that observed for pure OA ozonolysis with this same apparatus and data processing methods. The rate of reaction was not observed to differ within experimental error between the 1:1 and 1:3 mixtures (the result reported here is, as a result of this, a combined value using data from both mixtures).

This suggests that the presence of SA does not alter the kinetics of the ozonolysis of OA in a monolayer at the air/water interface, at least not to a degree measurable by our apparatus.

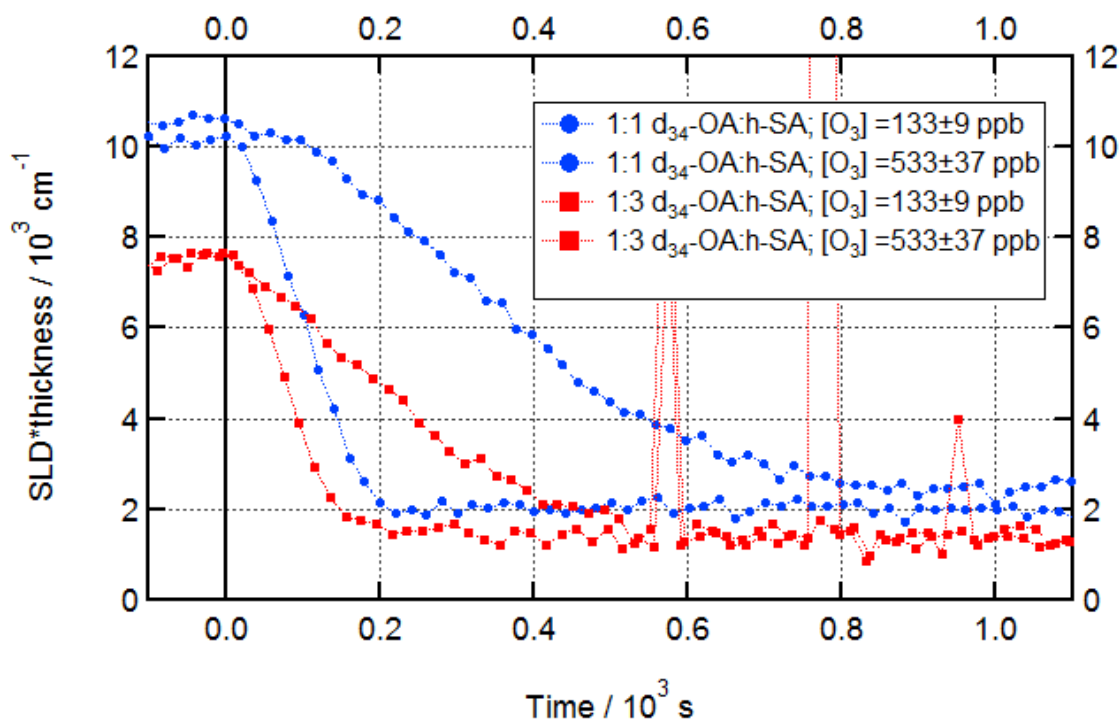


Figure 6.10 – Ozonolysis of d_{34} -OA in a mixed monolayer with h-SA; two spreading ratios; O_3 introduced at $t = 0 \text{ s}$ at two $[O_3]$; neutron reflectometry fitted time series.

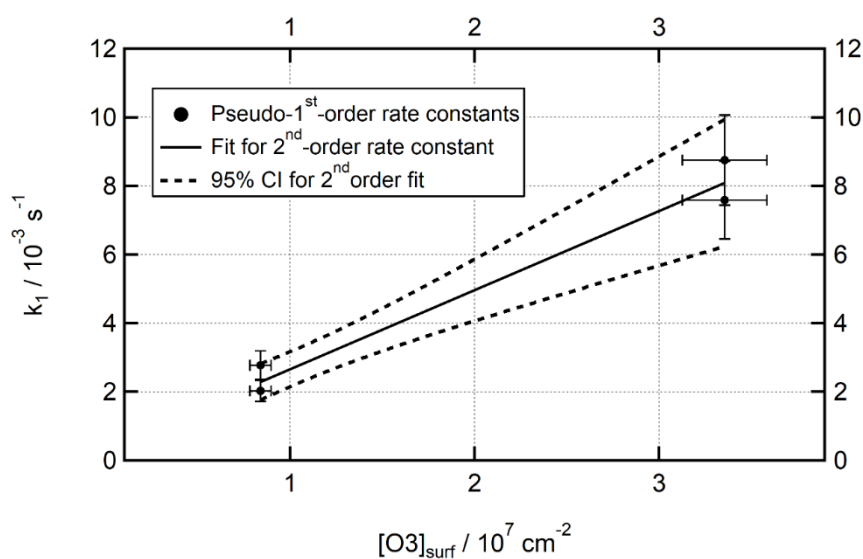


Figure 6.11 – 2nd-order rate plot for the reactions shown in Figure 6.10.

6.7 – Residual Product Monolayers

Despite this lack of impact on reaction kinetics, a qualitative difference is seen between the ozonolysis of OA in a pure monolayer and in a mixed monolayer with SA: In the latter case, a residue is left behind after oxidation. Work on pure OA monolayer ozonolysis at low temperatures showed that a residue remained after oxidation at 2 °C but not at room temperature (see Chapter 5). These experiments showed that the presence of co-deposited SA in the OA monolayer provides a set of conditions in which a residual monolayer is retained at room temperature. Furthermore, the average fractional reflectivity signal remaining after ozonolysis (an average of 17% from seven experiments ranging from 14% to 22%) was greater than had been observed for low temperature pure OA (an average of 10% from four experiments ranging from 7% to 16%), though the ranges of observed values overlapped slightly. Figure 6.12 shows the reflectivity curves for an example system before and after ozonolysis, with a null-reflecting water surface included as an indication of the curve obtained from the total absence of reflective material at the interface.

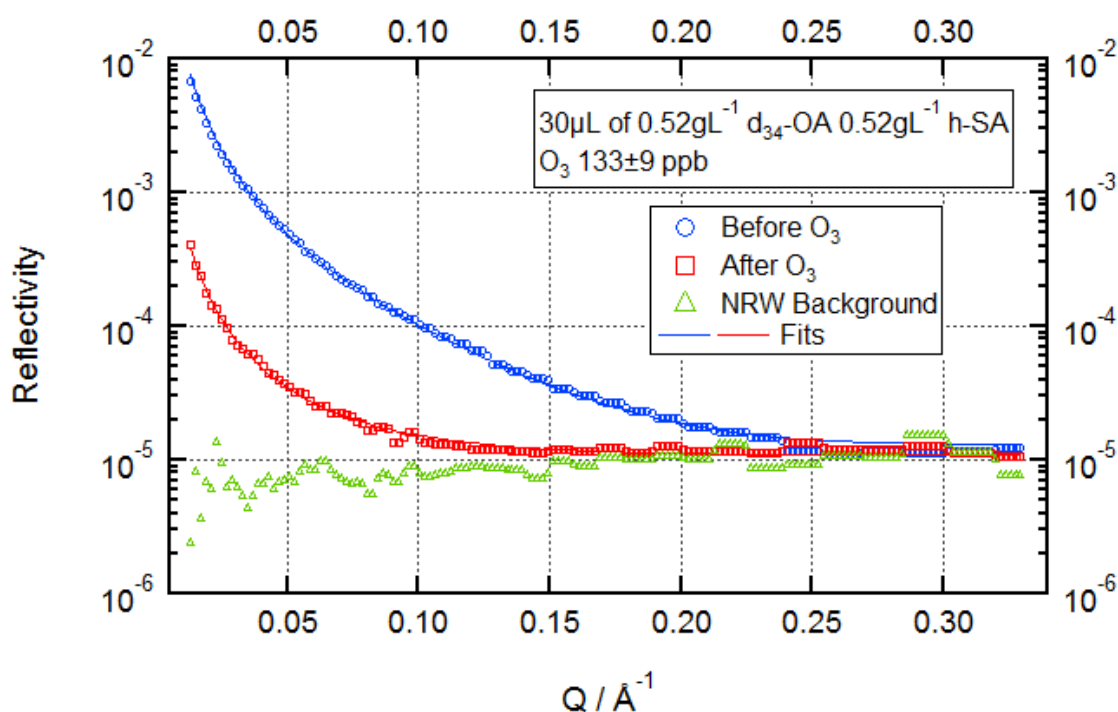


Figure 6.12 – Ozonolysis of d_{34} -OA in a mixed monolayer with h-SA; 30 μL of 0.52 g L^{-1} d_{34} -OA/ 0.52 g L^{-1} h-SA; $[\text{O}_3] = 133 \pm 9 \text{ ppb}$; room temperature; R vs Q reflectivity plots before and after oxidation; air/NRW background shown for comparison.

The observation that the mixing of SA into an OA monolayer does not measurably affect the ozonolysis kinetics (see section 6.6) and that decreasing the temperature of the OA monolayer to 2 °C similarly does not measurably affect the ozonolysis kinetics (see Chapter 5) suggests that measuring the kinetics of mixed monolayers at low temperatures is unlikely to prove the most fruitful of endeavours. Two condition changes that do not individually affect a reaction are unlikely to do so when combined (though this is far from impossible). The difference in behaviour of the pure OA and mixed monolayers at room temperature with regards to the production of residual product monolayers, and the difference in the behaviour of pure OA monolayers at different temperatures in this regard does, however, suggest that further study of mixed monolayers at low temperatures would be useful.

6.8 – Preliminary Low Temperature Experiments

A little preliminary data on this has been collected during experiments on INTER (RB 1810793 and RB 1910615) focused on studying other systems at low temperatures. Intriguingly, preliminary experiments on a 1:1 mole fraction mixed monolayer at 3 °C were unable to distinguish any possible residual monolayer from background noise. This may be because the mixed monolayer behaves in the opposite manner to the pure OA monolayer (i.e. it leaves a residue after ozonolysis at room temperature but *not* at near-freezing temperatures) or because residue was present, but below our detection limit (i.e. the absolute amount of residue from a mixed layer would be less than from a pure OA monolayer if the mixed layer behaved in the same way as the pure OA layer at low temperatures, purely because there is less OA in the mixed monolayer to begin with). Future work on this system should extend the Q range under observation, which would lower the detection threshold.

A preliminary experiment on a 4:1 mole fraction mixed d_{34} -OA/h-SA monolayer (chosen as it represents a system more similar to OA) behaved more like a pure OA monolayer at 3 °C, leaving a strong (17%) residual monolayer. This residual monolayer was heated (a process which drove away residual monolayers from oxidation of pure OA at this temperature; see Chapter 5) and this reduced the reflectivity to levels indistinguishable from the background (see Figure 6.13).

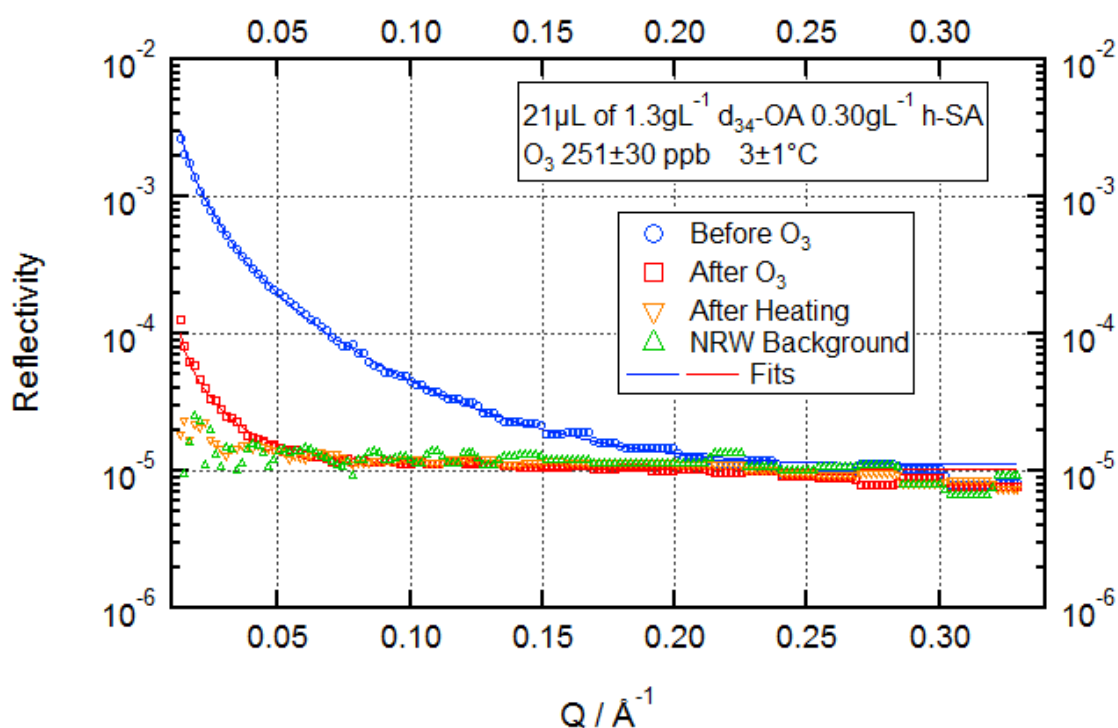


Figure 6.13 – Ozonolysis of d_{34} -OA in a mixed monolayer with h-SA; 21 μL of 1.3 g L⁻¹ d_{34} -OA/0.30 g L⁻¹ h-SA; [O₃] = 251 ± 30 ppb; low temperature; R vs Q reflectivity plots before and after oxidation and after heating; air/NRW background shown for comparison.

These preliminary experiments suggest that there is more to be discovered in terms of the ozonolysis of OA in mixed monolayers with SA at low temperatures. The kinetics of the reaction are unlikely to differ measurably from those already measured for the pure OA monolayer in both temperature conditions and for the mixed monolayer at room temperature. However, the atmospherically important issue of whether a residual monolayer remains at the interface after ozonolysis, and the unintuitive behaviour of the systems with respect to this outcome implied by these preliminary experiments, provide a strong incentive for further work. Further study of the combination of SA co-deposition and reduced

temperature effects on OA ozonolysis would be a good way to link together the insights provided in this chapter and in Chapter 5, and would be a logical next step for this research.

6.9 – Conclusions and Future Work

As mentioned in section 6.5, our explanation for the initially confounding FT-IRRAS data gathered (and NR for the reverse deuteration condition), which focuses on the significant inhomogeneity of 2D-gas phase SA, implies that FT-IRRAS data gathered during ozonolysis of these systems is not particularly useful. This somewhat strikes at the heart of the justification for building this apparatus in the first place. However, this should only apply to species that have such a proclivity for aggregating when present in low concentrations at the interface. The use of FT-IRRAS to track a co-deposited non-deuterated component should still be possible as long as that component behaves more like OA. It is likely to be saturated species, with their rigid regular rod-like shape and strong van der Waals interactions, that display this behaviour. Similarly, NR cannot reliably quantitatively determine the surface concentrations of these species if significant surface inhomogeneity obtains.

The fact that these issues do not affect OA mean that the NR data from d_{34} -OA/h-SA monolayers was useful for studying the behaviour of OA in these systems, and our kinetic study showed that the reaction rate was not different from that of OA in a pure monolayer. Our study of the residue left behind after the reaction, however, showed a difference in behaviour from the pure OA case, and an interesting one.

Initially, it might not seem so important to have discovered that some products from the ozonolysis of OA remain at the interface in a mixed monolayer with SA. After all, SA is itself a saturated fatty acid, and so the addition of a small amount of extra saturated material, impervious to further ozonolysis, does not greatly matter to the surface properties of the system in the same way that the presence at the interface of reaction products from pure OA ozonolysis (as seen at low temperatures; see Chapter 5) matters to what would, without these products, be a clean water surface.

However, the incomplete removal of OA (in terms of total material at the interface) by ozonolysis at room temperature if SA is also present suggests that re-deposition and re-ozonolysis of OA could build up saturated OA ozonolysis products at the interface until it becomes 'full', resulting in an entirely saturated monolayer impervious to any ozonolysis. The result from the low temperature OA work (see Chapter 5) in which OA ozonolysis products are stable at the interface at low temperatures hints at a situation in which this could happen without any 'seed' saturated material at all. If enough saturated material can be built up at low temperatures from ozonolysis of OA (and such a re-deposition and re-ozonolysis experiment was performed, and did result in the build-up of a product layer over time), then this product monolayer may act like SA did in this work, and stabilise further OA ozonolysis products even at higher temperatures. This is very speculative and depends on OA ozonolysis products playing the same stabilisation role as we have observed SA to play here, but is certainly an idea worth pursuing.

This may provide something of an explanation as to why, despite OA and other unsaturated fatty acids being emitted significantly by anthropogenic activity¹³, recent work on aerosol particles collected from the atmosphere has shown that their surfaces host entirely inert monolayers⁴. A model in which an initially mixed saturated/unsaturated monolayer (or even, possibly, a fully unsaturated monolayer) is gradually transformed into a fully saturated monolayer through the repeated deposition and ozonolysis of unsaturated species, makes sense of both of these findings.

The preliminary low temperature work discussed here is worth following up properly. The preliminary result that a product monolayer is *not* seen for h-OA/ d_{34} -SA ozonolysis at low temperatures is hard to explain; why would two factors (the presence of SA and the low temperature) that individually induce OA ozonolysis products to stabilise at the interface not induce that stabilisation together? It should be stressed that these results are very preliminary, and it may simply be that, due to the limited Q range over which the experiment was run and the short count time allowed, the residue was just below our

detection limit. Repeating this experiment with a longer count time, and utilising the full Q range available at INTER, would be a good start. The experiment with a 4:1 mole ratio between d_{34} -OA and h-SA was performed using INTER's full Q range, and did show a residual monolayer. A full suite of residue-detection experiments for a variety of ratios at low temperatures would be a logical next step. It does not seem particularly important to make a detailed kinetic study under those conditions, as neither the change in temperature (see Chapter 5) nor the presence of SA (see section 6.6) changed the reaction rate observed for OA ozonolysis.

Also worth investigating would be what the threshold for SA presence in the mixed monolayer is to induce stabilisation of OA ozonolysis products. Residues have been observed at 1:1 and 1:3 mass ratios; it would be interesting to see at what point the SA no longer has this stabilising effect.

Furthermore, an experiment similar to the one performed for low temperature OA ozonolysis (see Chapter 5) in which more OA is added and then another ozonolysis step is performed multiple times in order to build up a product monolayer should be performed for the mixed system at room temperature. If the same result were to be seen, then the idea that mixed saturated/unsaturated systems gradually progress to fully saturated systems, by repeated deposition and ozonolysis of unsaturated species, would gain further credibility.

It would also be instructive to determine what other co-components can also stabilise reaction products. Is SA special, or will any saturated fatty acid do? Perhaps most importantly, will the saturated reaction products from OA ozonolysis, such as nonanoic acid, which remain at the interface after ozonolysis of a pure OA monolayer at low temperatures (see Chapter 5), suffice to stabilise further OA ozonolysis reaction products even at room temperature? If so, a full monolayer coating of saturated material could be built up from only OA deposition and ozonolysis, as long as sufficient deposition and ozonolysis occurred at low temperatures in order to 'seed' the interface with enough saturated material to stabilise further ozonolysis products at higher temperatures.

To investigate this, it would be helpful to explore the mechanism of this stabilisation. Is it purely intermolecular, mediated by van der Waals forces, or does SA involve itself chemically in the ozonolysis of OA, perhaps reacting with Criegee intermediates in order to form large saturated oxidised products that are more stable at the interface than the basic OA ozonolysis products are?

These are just a few ideas for taking research on mixed saturated/unsaturated systems further, and they demonstrate that, despite the limited ability of FT-IRRAS to contribute as much as had been hoped to the study of this sub-type of mixed fatty acid systems, NR still has a significant role to play in improving our understanding of how these monolayers form and develop. There is a lot more work to be done.

6.10 – Bibliography (Mixtures)

- 1 L. F. Voss, M. F. Bazerbashi, C. P. Beekman, C. M. Hadad and H. C. Allen, *Journal of Geophysical Research*, 2007, **112**, D06209.
- 2 M. D. King, A. R. Rennie, K. C. Thompson, F. N. Fisher, C. C. Dong, R. K. Thomas, C. Pfrang and A. V. Hughes, *Physical Chemistry Chemical Physics*, 2009, **11**, 7699–7707.
- 3 E. Adams and H. Allen, *Atmosphere*, 2013, **4**, 315–336.
- 4 S. H. Jones, M. D. King, A. D. Ward, A. R. Rennie, A. C. Jones and T. Arnold, *Atmospheric Environment*, 2017, **161**, 274–287.
- 5 M. W. A. Skoda, B. Thomas, M. Hagreen, F. Sebastiani and C. Pfrang, *RSC Advances*, 2017, **7**, 34208–34214.
- 6 F. Sebastiani, PhD Thesis, University of Reading, 2014.
- 7 A. I. Feher, F. D. Collins and T. W. Healy, *Australian Journal of Chemistry*, 1977, **30**, 511–519.
- 8 J. R. Lu, R. K. Thomas and J. Penfold, *Advances in Colloid and Interface Science*, 2000, **84**, 143–304.
- 9 M. Sferrazza, C. Xiao, R. A. L. Jones, D. G. Bucknall, J. Webster and J. Penfold, *Physical Review Letters*, 1997, **78**, 3693–3696.
- 10 R. M. Richardson, J. R. P. Webster and A. Zarbakhsh, *Journal of Applied Crystallography*, 1997, **30**, 943–947.
- 11 C. F. Majkrzak, C. Metting, B. B. Maranville, J. A. Dura, S. Satija, T. Udovic and N. F. Berk, *Physical Review A*, 2014, **89**, 033851.
- 12 G. D. Smith, E. Woods, C. L. DeForest, T. Baer and R. E. Miller, *The Journal of Physical Chemistry A*, 2002, **106**, 8085–8095.
- 13 M. K. Shrivastava, R. Subramanian, W. F. Rogge and A. L. Robinson, *Atmospheric Environment*, 2007, **41**, 9353–9369.

Chapter 7 – Oxidation of Linoleic Acid Monolayers including Fatty Acid and Methyl Ester Mixtures

7.1 – Introduction

In the last few months of this PhD project, another beamline experiment at ISIS (INTER RB 1910615) was undertaken in order to explore a few new possibilities for research using our apparatus and provide a way forward from the project to future work. A few experiments pertinent to oleic and stearic acid (OA/SA) mixtures were carried out on this beamline experiment, and these are discussed in Chapter 6. The main focus of the experiment, however, was to utilise the apparatus that has been under development throughout this project for a new group of systems, namely linoleic acid (LOA) monolayers.

LOA represents a logical next step for investigations, as it is a poly-unsaturated analogue of OA, with two double-bonds. This allows for ozone-initiated autoxidation (a radical self-oxidation process initiated by ozone) as well as traditional ozonolysis^{1,2}. This investigation was not originally intended as part of this PhD project, but, as the relevant experiment ended up being conducted during the project's write-up phase, some processing and analysis of the data has been performed in tandem with the write-up of the core work, and some resultant data is presented here as something of a primer for future work in this domain. Along with the questions left unanswered in the OA/SA mixed monolayers investigation, it provides a motivation for future applications of the apparatus developed over the course of this project in the domain of air/water interface oxidation studies.

The core of the experiment involved studying the oxidation of d_{32} -LOA as a pure monolayer, and in mixed monolayers with h-oleic acid (h-OA) and h-methyl oleate (h-MO; the methyl ester analogue of oleic acid) at both room temperature and a more atmospherically realistic temperature of 3 ± 1 °C. The OA/LOA system was also studied in a reverse deuteration configuration (d_{34} -OA/h-LOA) in both these temperature conditions. This facilitates more of a study of the ozonolysis of OA in the presence of LOA, and dovetails appropriately with the work on OA/SA systems discussed in Chapter 6. Some preliminary data from d_{32} -LOA/h-SA mixed monolayers was also gathered.

7.2 – Oleic Acid Ozonolysis with Linoleic Acid

As mentioned in section 7.1, the study of this experiment's reverse deuteration configuration mixed monolayer (d_{34} -OA/h-LOA) facilitates the study by neutron reflectometry of the impact of LOA as a co-deposited film component on the ozonolysis of OA, in a manner analogous to the study of the effects of SA discussed in Chapter 6. Figures 7.1 and 7.2 show the ozonolysis of a d_{34} -OA/h-LOA monolayer at a variety of ozone concentrations at room temperature and 3 ± 1 °C, respectively. Figure 7.3 shows ozonolysis under the two temperature conditions overlaid, displaying only the highest and lowest ozone concentrations for clarity. As these figures make clear, the change in temperature did not notably affect the rate of reaction.

Pseudo-1st-order rate constants were fitted to these neutron reflectometry time series using the stretched exponential analytical model employed in Chapters 5 and 6 and described in detail in the former. Figure 7.4 shows a 2nd-order plot for this reaction (omitting data from the highest ozone concentration, as these reactions were judged too fast to fit, given the limitation of 20 second time resolution). Fitting a 2nd-order rate constant to this data gives a value of $2.0\pm 0.4 \times 10^{-10} \text{ cm}^2 \text{ s}^{-1}$. This is

slightly lower than for pure OA, but the error bars overlap significantly, so this technique is not able to firmly claim a difference in rate.

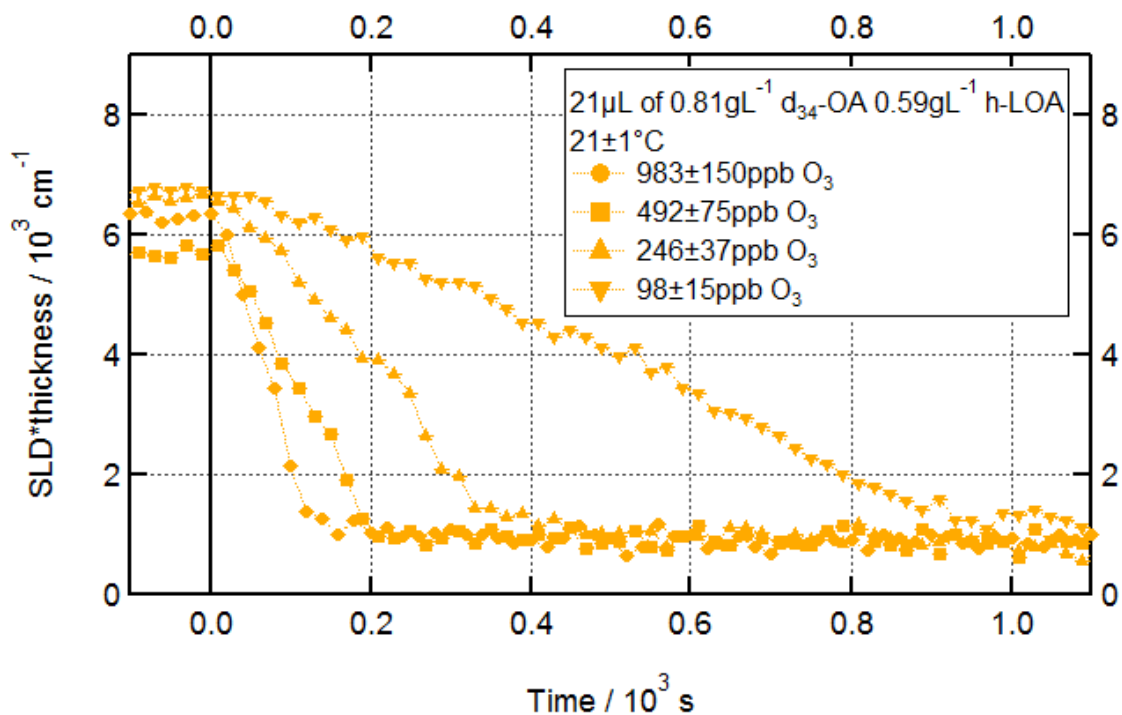


Figure 7.1 – Oxidation of d_{34} -OA in a mixed monolayer with h-LOA; 21 μL of 0.81 g L^{-1} d_{34} -OA/ 0.59 g L^{-1} h-LOA; O_3 introduced at $t = 0\text{ s}$ at various $[\text{O}_3]$; room temperature; neutron reflectometry fitted time series.

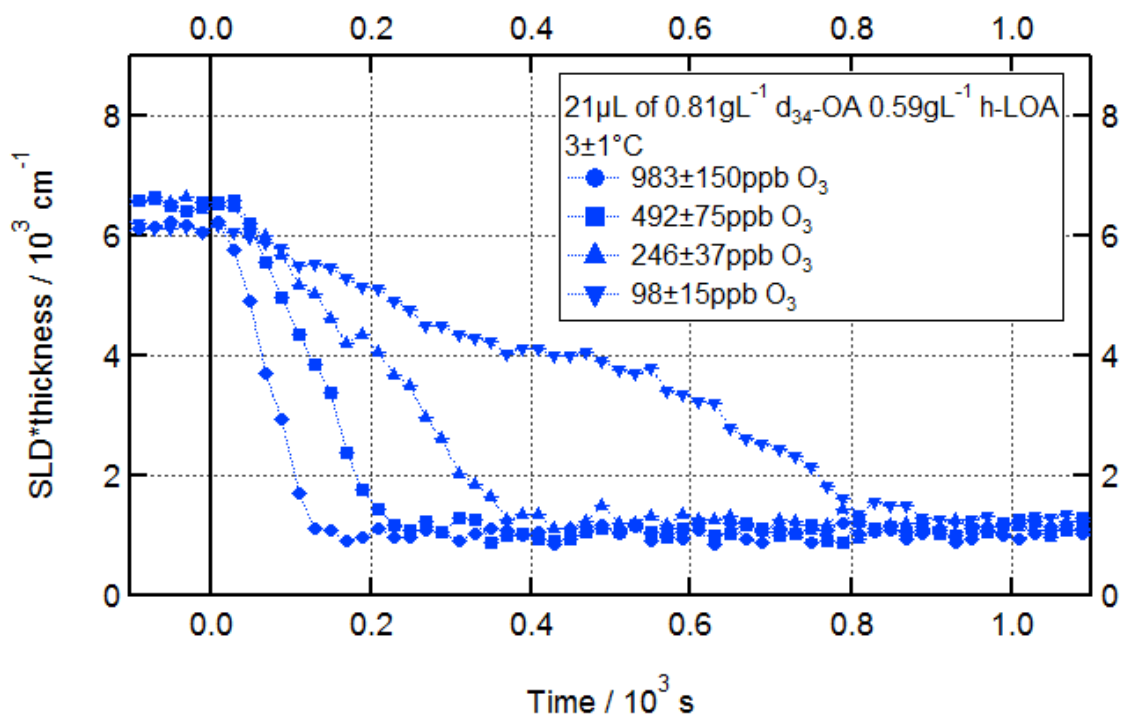


Figure 7.2 – Oxidation of d_{34} -OA in a mixed monolayer with h-LOA; 21 μL of 0.81 g L^{-1} d_{34} -OA/ 0.59 g L^{-1} h-LOA; O_3 introduced at $t = 0\text{ s}$ at various $[\text{O}_3]$; low temperature; neutron reflectometry fitted time series.

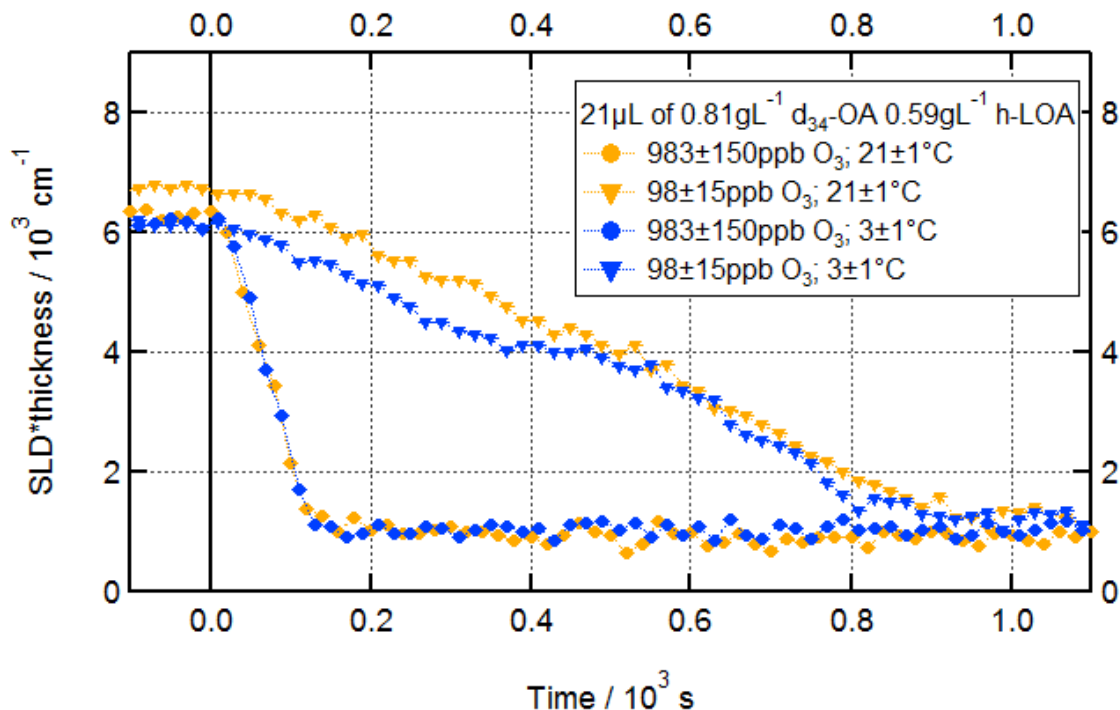


Figure 7.3 – Oxidation of d_{34} -OA in a mixed monolayer with h-LOA; $21 \mu\text{L}$ of $0.81 \text{ g L}^{-1} d_{34}\text{-OA}$ / $0.59 \text{ g L}^{-1} \text{ h-LOA}$; O_3 introduced at $t = 0 \text{ s}$ at two $[\text{O}_3]$; two temperatures; neutron reflectometry fitted time series.

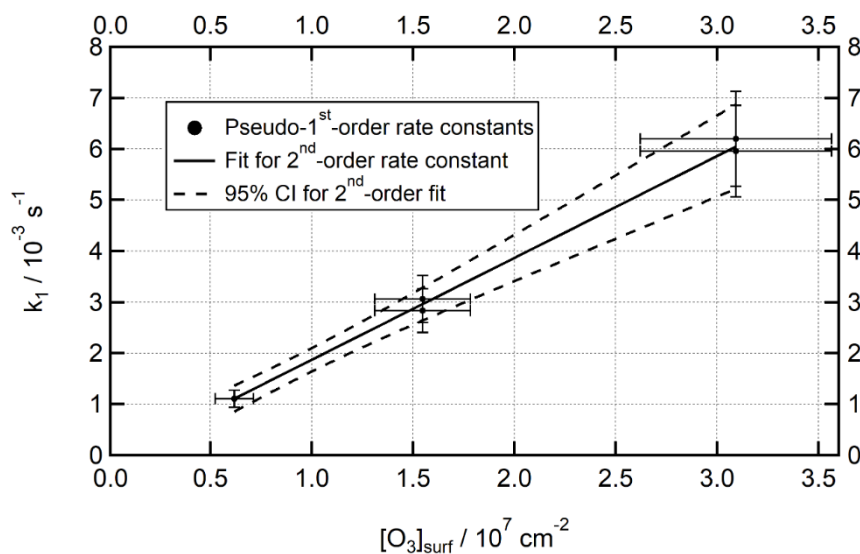


Figure 7.4 – 2^{nd} -order rate plot for the reactions shown in Figures 7.1 and 7.2.

An experiment was performed in which neutrons were collected over the full Q range accessible to INTER, in order to quantify any residue left behind after ozonolysis (as seen for low temperature ozonolysis of a pure OA monolayer and for room temperature ozonolysis of an OA/SA mixed monolayer in Chapters 5 and 6, respectively). Figure 7.5 shows reflectivity curves before and after oxidation at $3 \pm 1 \text{ }^\circ\text{C}$: A residue can clearly be seen. Fitting monolayer parameters to these reflectivity curves to quantify the absolute amount of deuterated material adsorbed at the interface determined that 13% of such material present before ozonolysis remained afterward. This is within the range seen for pure OA monolayers at these temperatures (see Chapter 5).

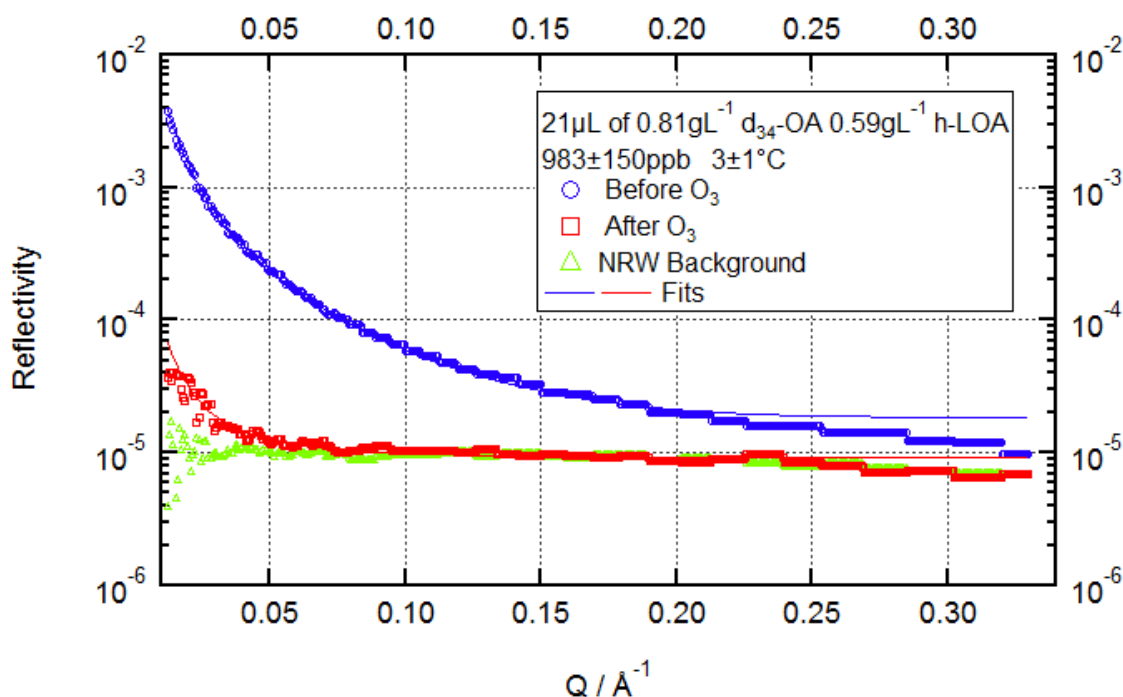


Figure 7.5 – Ozonolysis of d_{34} -OA in a mixed monolayer with h-LOA; 21 μL of 0.81 g L^{-1} d_{34} -OA/0.59 g L^{-1} h-LOA; $[\text{O}_3] = 983 \pm 150$ ppb; low temperature; R vs Q reflectivity plots before and after oxidation; air/NRW background shown for comparison.

Due to time restrictions, no analogous experiment was performed at room temperature. However, the kinetic data shown in Figures 7.2 to 7.4 (collected across a restricted Q range and therefore not suitable for precise absolute quantification of small amounts of material) suggests that a similar residual monolayer remains. An extended Q range experiment at room temperature would be a logical next step to test this more completely.

It is notable in Figure 7.5 that the fit to the data collected before the reaction deviates slightly from that data at high Q values. This is because the background on INTER is not quite Q-independent, but the fitting model in MOTOFIT expects it to be. Where there is very little signal, background is particularly important, and this can cause deviation from an ideal fit. This can be avoided by using a fixed background parameter derived from a clean air/NRW measurement, and, indeed, this is the procedure used for fitting most of the data in this thesis. This does, however, mean assuming that the background will not change across the conditions studied (including temperature variations). Therefore, when doing experiments specifically to quantify post-oxidation residue under various conditions, in which distinguishing genuine residue from background signal is particularly important, this fixed-background method was avoided, as it somewhat begs the question.

7.3 – Oxidation of Linoleic Acid

The primary focus of this beamline experiment was to study the oxidation of linoleic acid (which can be achieved via ozonolysis or ozone-initiated autoxidation) as a monolayer at the air/water interface, and the effects of temperature and co-deposited film components on that oxidation process. To this end, pure d_{32} -LOA monolayers and mixed monolayers containing h-OA and h-MO were oxidised under a variety of ozone concentrations at room temperature and at 3 ± 1 °C. Figures 7.6 to 7.11 show time series neutron reflectometry data for these reactions. Figures 7.12 to 7.14 overlay the temperature conditions, displaying only the highest and lowest ozone concentrations for clarity. Figure 7.15 shows a 2nd-order plot for this reaction, and Table 7.1 shows fitted 2nd-order rate constants for the three monolayer types in the two temperature conditions, as well as rate constants for each monolayer type (treating

temperature as irrelevant), for each temperature (treating monolayer type as irrelevant), and for all data combined. As Table 7.1 makes clear, neither the change in temperature nor the introduction of a co-deposited film component alongside d_{32} -LOA consistently affects the rate of reaction of LOA with ozone.

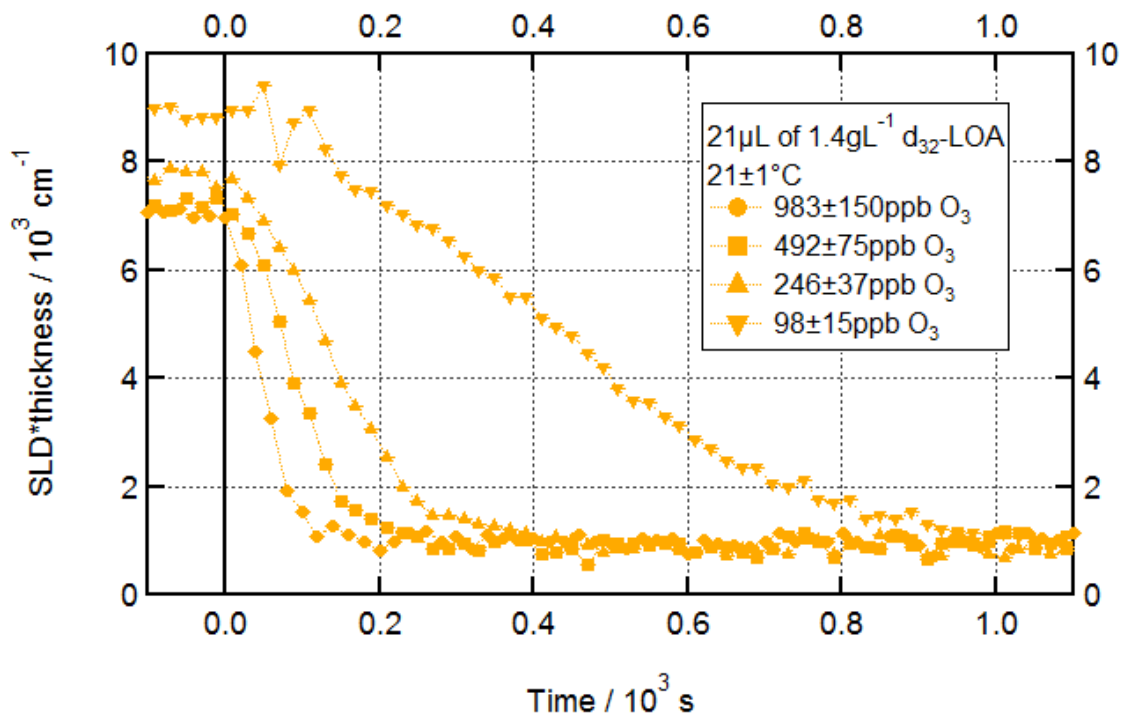


Figure 7.6 – Oxidation of a pure d_{32} -LOA monolayer; 21 µL of 1.4 g L⁻¹ d_{32} -LOA; O₃ introduced at $t = 0$ s at various [O₃]; room temperature; neutron reflectometry fitted time series.

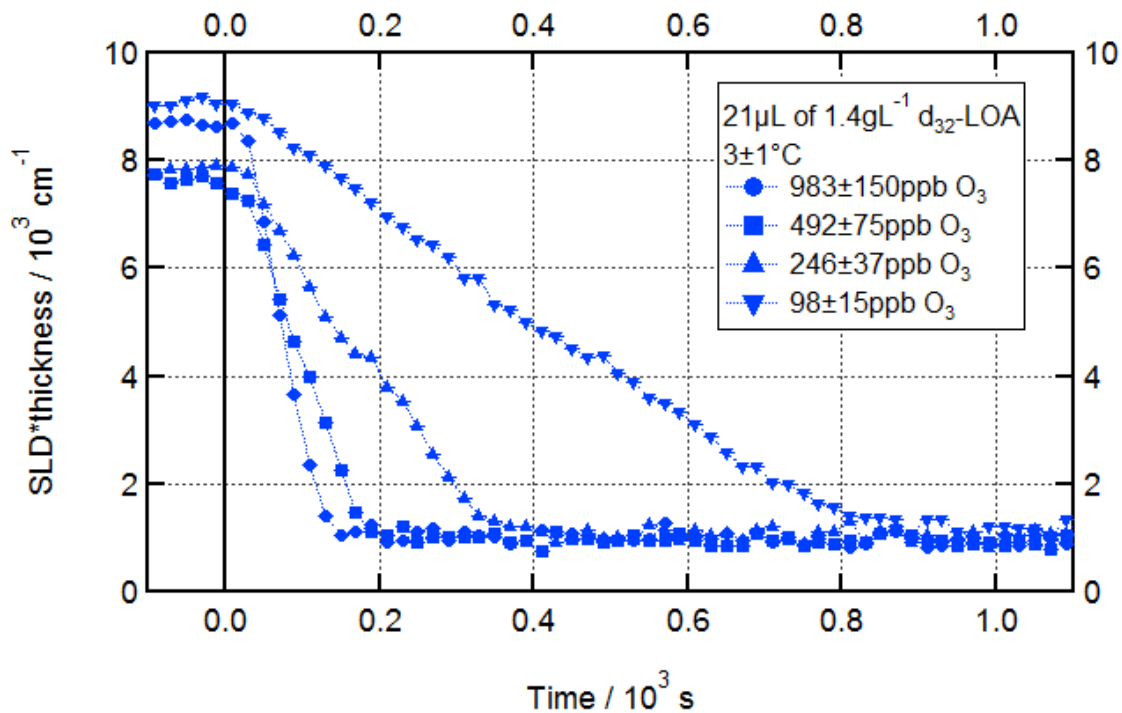


Figure 7.7 – Oxidation of a pure d_{32} -LOA monolayer; $21 \mu\text{L}$ of $1.4 \text{ g L}^{-1} d_{32}$ -LOA; O_3 introduced at $t = 0 \text{ s}$ at various $[\text{O}_3]$; low temperature; neutron reflectometry fitted time series.

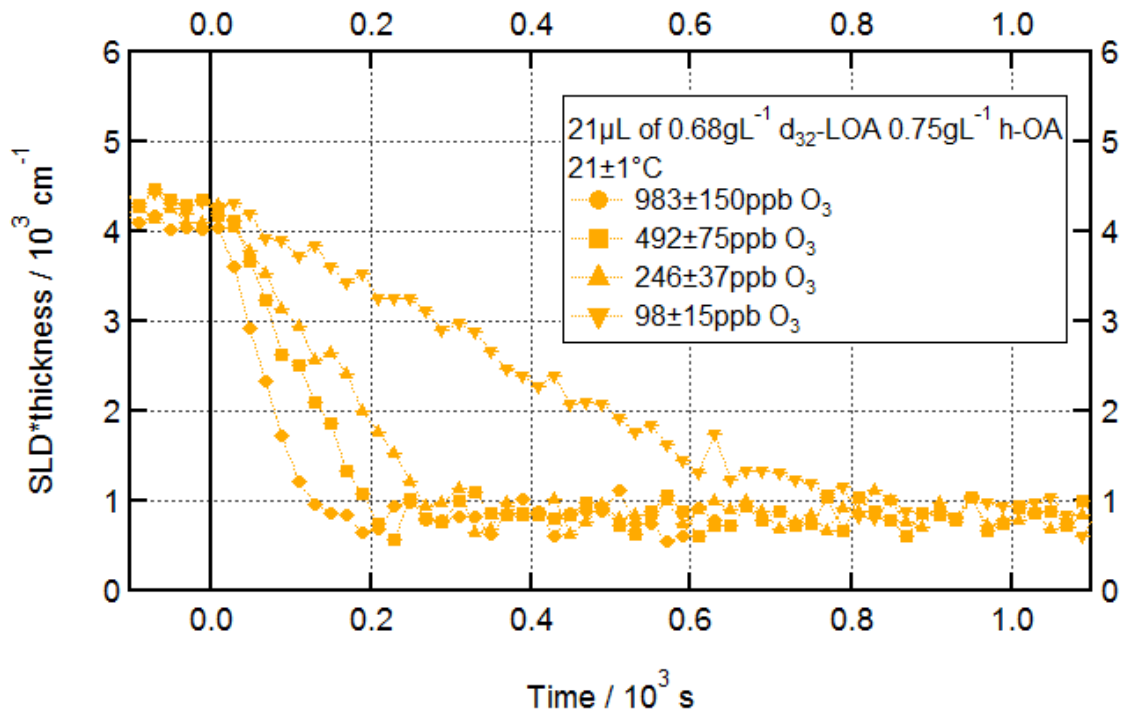


Figure 7.8 – Oxidation of d_{32} -LOA in a mixed monolayer with h -OA; $21 \mu\text{L}$ of $0.68 \text{ g L}^{-1} d_{32}$ -LOA/ $0.75 \text{ g L}^{-1} h$ -OA; O_3 introduced at $t = 0 \text{ s}$ at various $[\text{O}_3]$; room temperature; neutron reflectometry fitted time series.

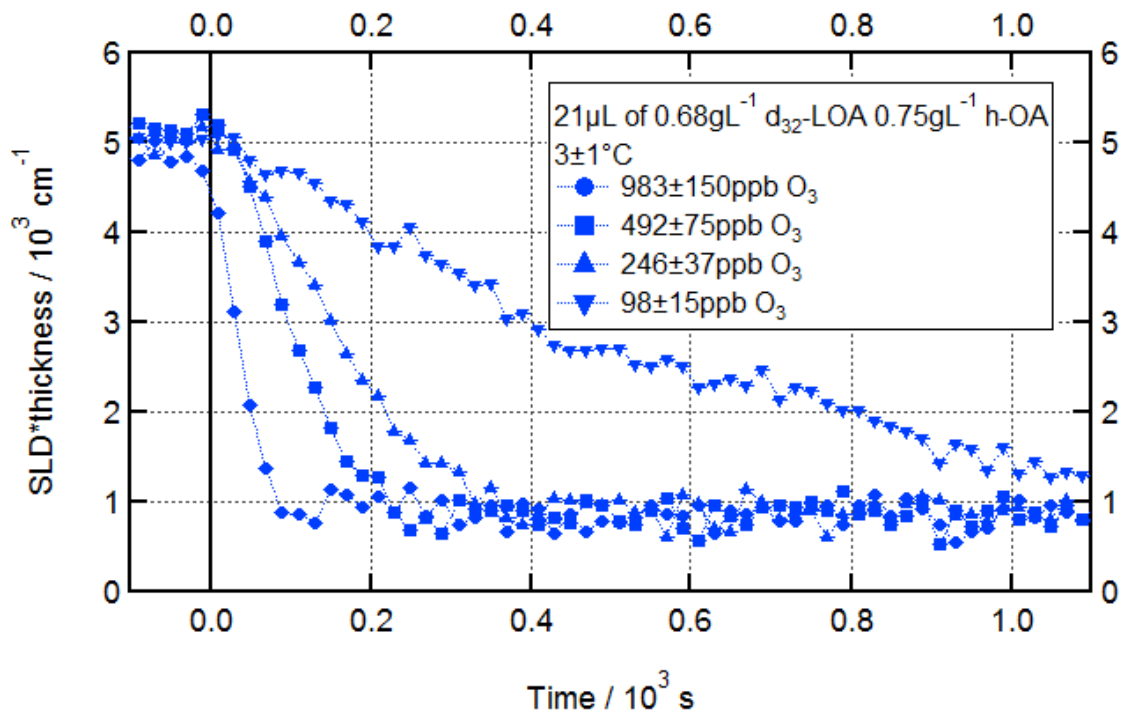


Figure 7.9 – Oxidation of d_{32} -LOA in a mixed monolayer with h-OA; $21 \mu\text{L}$ of $0.68 \text{ g L}^{-1} d_{32}$ -LOA/ $0.75 \text{ g L}^{-1} \text{ h-OA}$; O_3 introduced at $t = 0 \text{ s}$ at various $[\text{O}_3]$; low temperature; neutron reflectometry fitted time series.

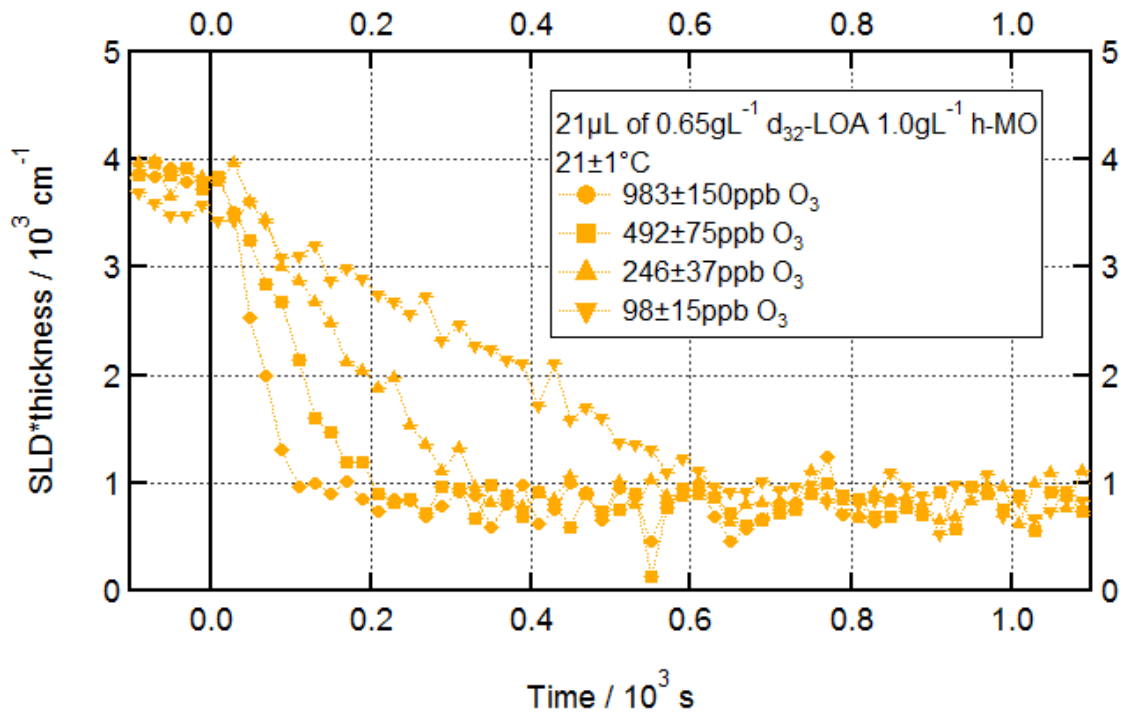


Figure 7.10 – Oxidation of d_{32} -LOA in a mixed monolayer with h-MO; $21 \mu\text{L}$ of $0.65 \text{ g L}^{-1} d_{32}$ -LOA/ $1.0 \text{ g L}^{-1} \text{ h-MO}$; O_3 introduced at $t = 0 \text{ s}$ at various $[\text{O}_3]$; room temperature; neutron reflectometry fitted time series.

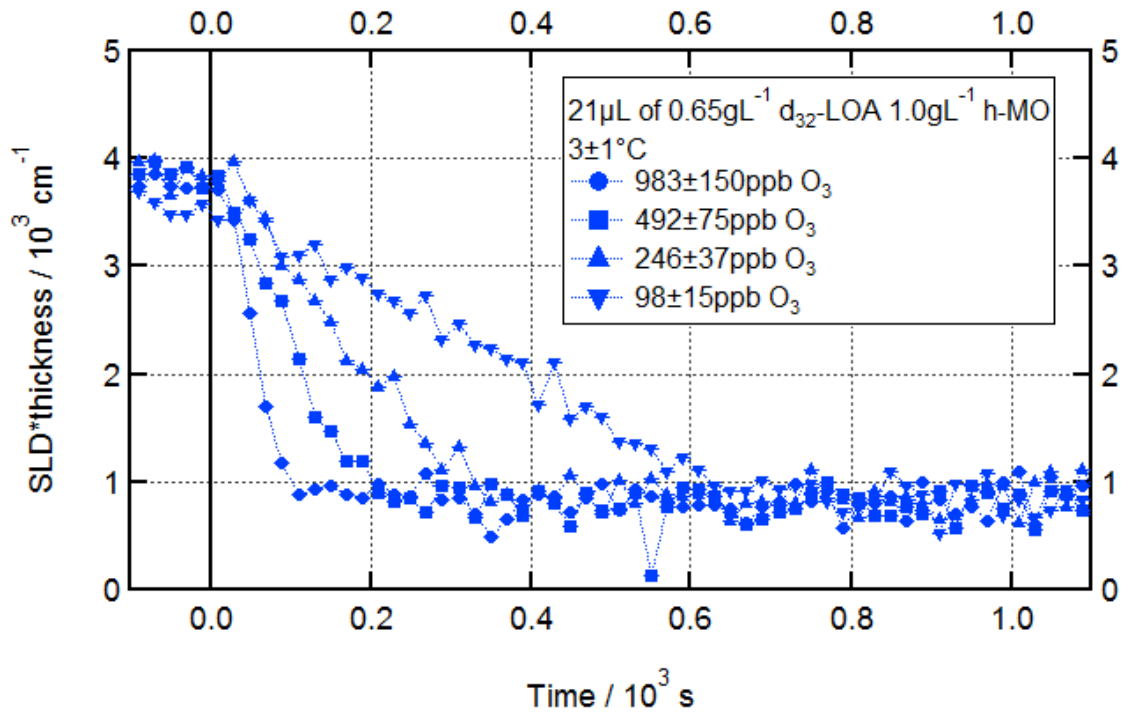


Figure 7.11 – Oxidation of d_{32} -LOA in a mixed monolayer with h-MO; $21 \mu\text{L}$ of $0.65 \text{ g L}^{-1} d_{32}\text{-LOA}/1.0 \text{ g L}^{-1} \text{ h-MO}$; O_3 introduced at $t = 0 \text{ s}$ at various $[\text{O}_3]$; low temperature; neutron reflectometry fitted time series.

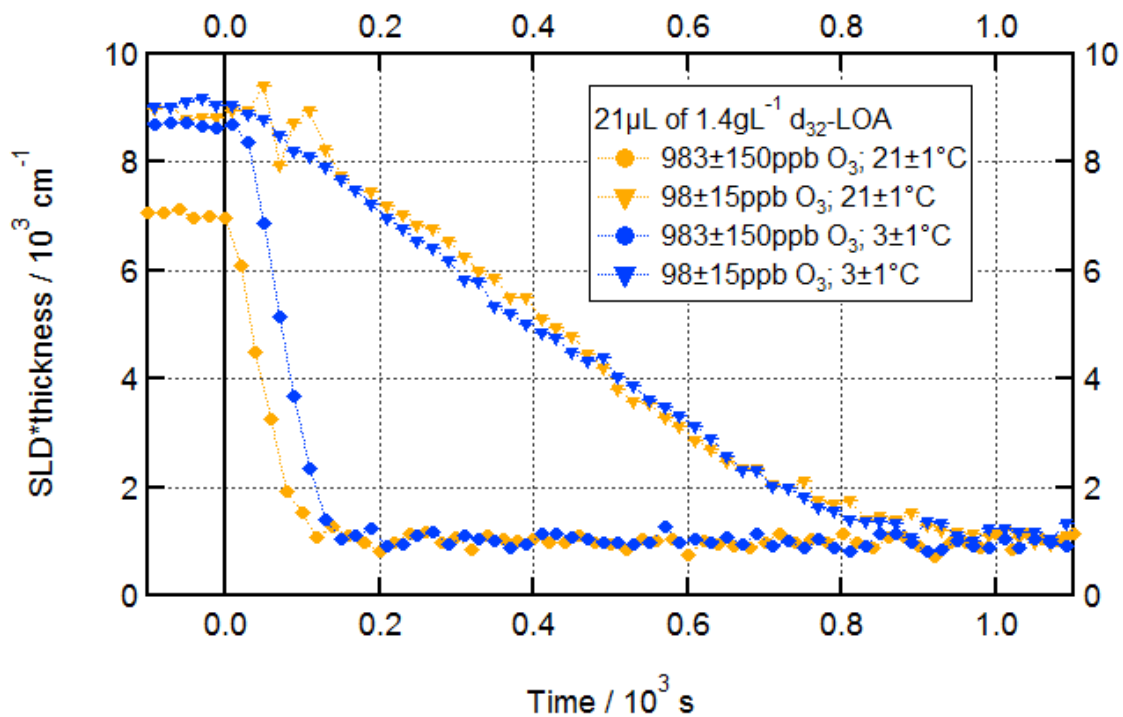


Figure 7.12 – Oxidation of a pure d_{32} -LOA monolayer; $21 \mu\text{L}$ of $1.4 \text{ g L}^{-1} d_{32}\text{-LOA}$; O_3 introduced at $t = 0 \text{ s}$ at two $[\text{O}_3]$; two temperatures; neutron reflectometry fitted time series.

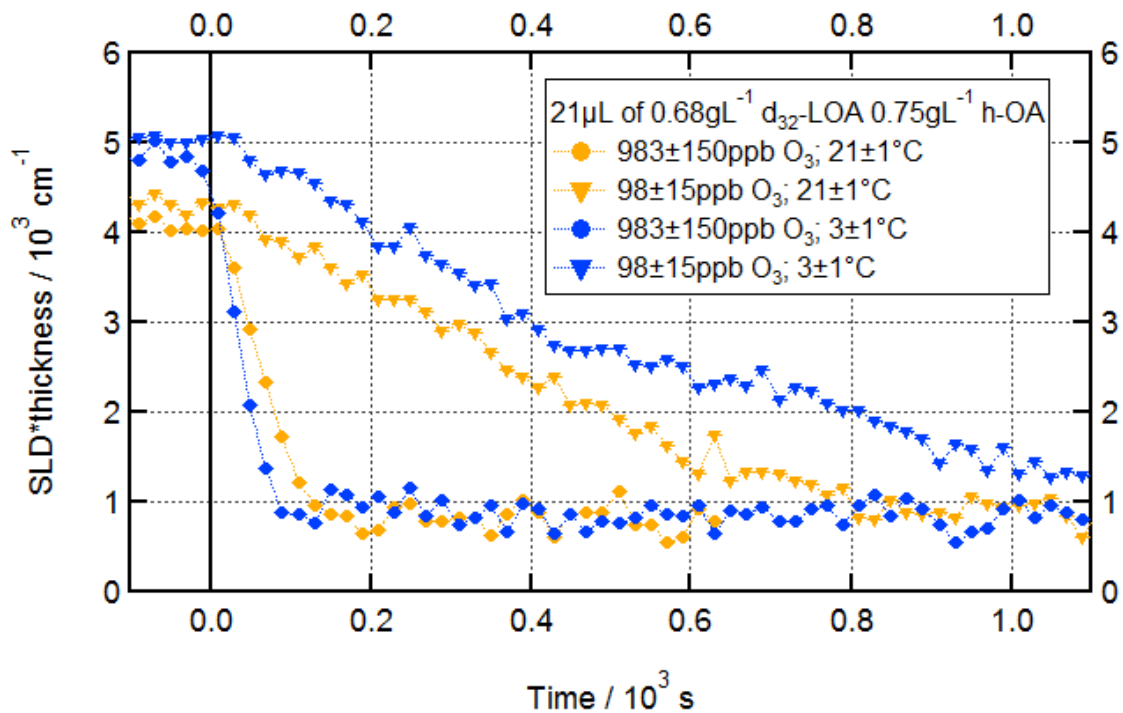


Figure 7.13 – Oxidation of d_{32} -LOA in a mixed monolayer with h-OA; 21 μL of $0.68 \text{ g L}^{-1} d_{32}$ -LOA/ $0.75 \text{ g L}^{-1} h$ -OA; O_3 introduced at $t = 0 \text{ s}$ at two $[\text{O}_3]$; two temperatures; neutron reflectometry fitted time series.

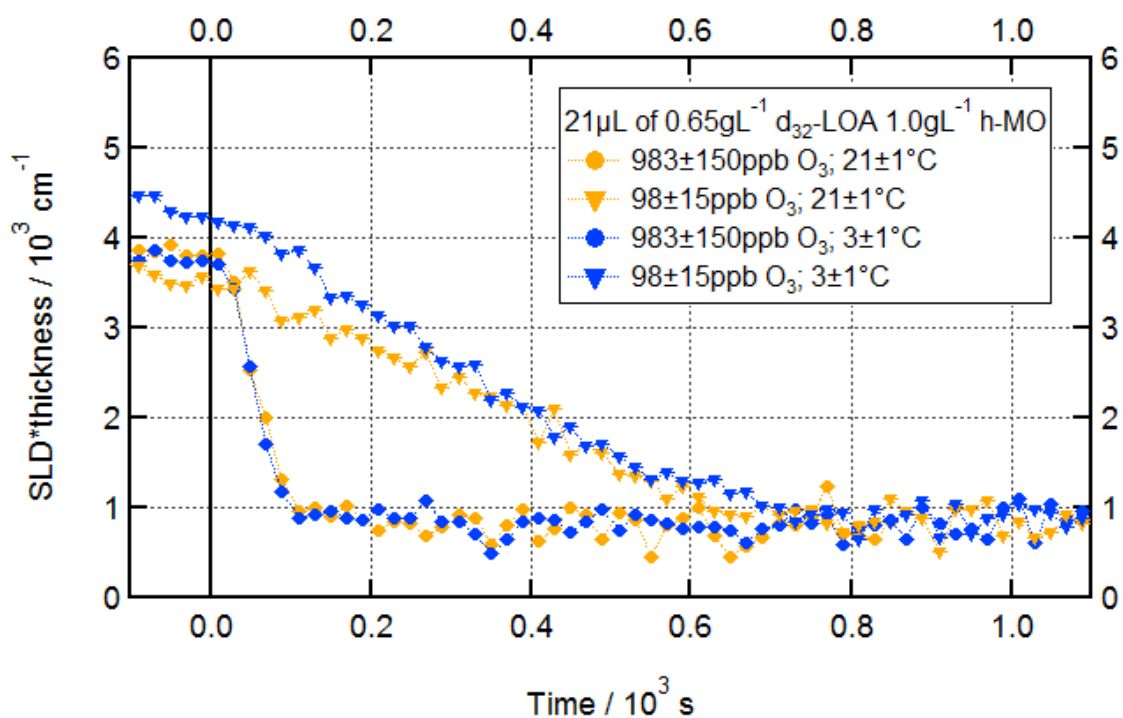


Figure 7.14 – Oxidation of d_{32} -LOA in a mixed monolayer with h-MO; 21 μL of $0.65 \text{ g L}^{-1} d_{32}$ -LOA/ $1.0 \text{ g L}^{-1} h$ -MO; O_3 introduced at $t = 0 \text{ s}$ at two $[\text{O}_3]$; two temperatures; neutron reflectometry fitted time series.

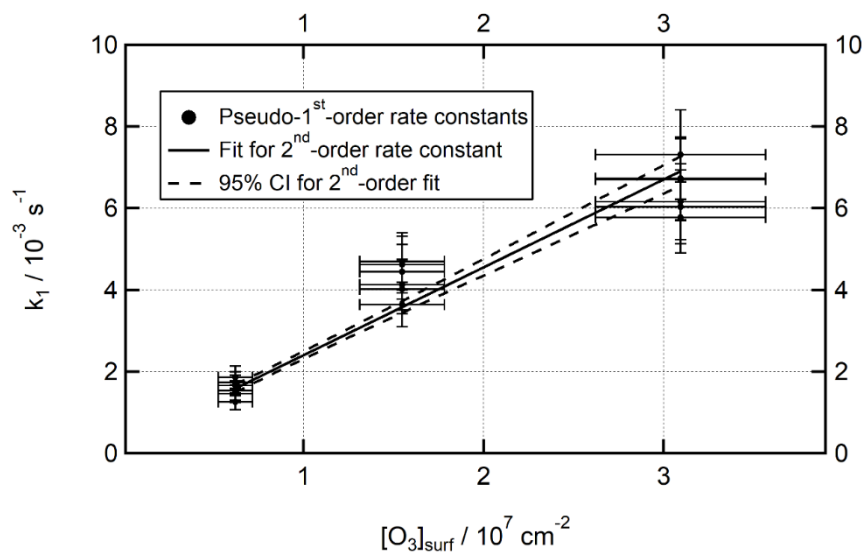


Figure 7.15 – 2nd-order rate plot for the reactions shown in Figures 7.6 to 7.11.

Table 7.1 – 2nd-order rate constants for d₃₂-LOA alone and in two mixed systems; two temperatures. Combined rate constants for each temperature (combining all mixture configurations), each mixture (combining both temperature conditions) and all data also shown. 95% confidence intervals included as ± figures. Confidence intervals estimated for individual mixture/temperature pairs; confidence intervals calculated statistically for all combined conditions.

Rate Constants /10 ⁻¹⁰ cm ² s ⁻¹	21±1 °C	3±1 °C	Combined Data
d ₃₂ -LOA	2.1±0.7	2.0±0.7	2.0±0.4
d ₃₂ -LOA/h-OA	2.0±0.7	2.5±0.7	2.3±0.4
d ₃₂ -LOA/h-MO	1.9±0.7	2.5±0.7	2.0±0.4
Combined Data	2.0±0.2	2.3±0.3	2.1±0.2

These rates are fast compared with those measured by He *et al.* in 2017³. However, this study uses a very different morphology (monolayer at the air/water interface) to that used by He *et al.* when measuring their rate constants. Furthermore, the He *et al.* study uses much higher ozone concentration than this study (~10 ppm compared with ~100 to ~1000 ppb in this study) and Chan *et al.* have warned that, due to the competing mechanisms for this reaction that dominate under different conditions, extrapolating from high ozone concentrations values downwards is likely to be problematic¹. Other studies on this heterogenous reaction have mostly reported uptake coefficients, rather than rate constants, and these have varied by around an order of magnitude as reviewed by He *et al.*³. The use of an uptake coefficient, which is more dependent on reaction conditions and geometry than is a rate constant, makes these studies less useful as a guide for what to expect in this study, which uses a monolayer at the air/water interface rather than particulate phase or film-coated flow tube setups. Differences in mechanism (discussed in more detail later in this chapter) may also be driving some of this discrepancy.

An experiment analogous to that for d₃₄-OA/h-LOA discussed in section 7.2 was performed in order to quantify any post-oxidation residue. Again, only the low temperature was studied due to time restrictions. Figures 7.16 to 7.18 show reflectivity curves before and after oxidation at 3±1 °C for d₃₂-LOA, d₃₂-LOA/h-OA, and d₃₂-LOA/h-MO respectively. For d₃₂-LOA as a pure monolayer, a residue is observed, and fitting monolayer parameters quantifies this as 7% of the initial adsorbed deuterated material. For d₃₂-LOA in a mixed monolayer with h-OA, a residue is also observed, and quantified as 11% of the initial adsorbed deuterated material.

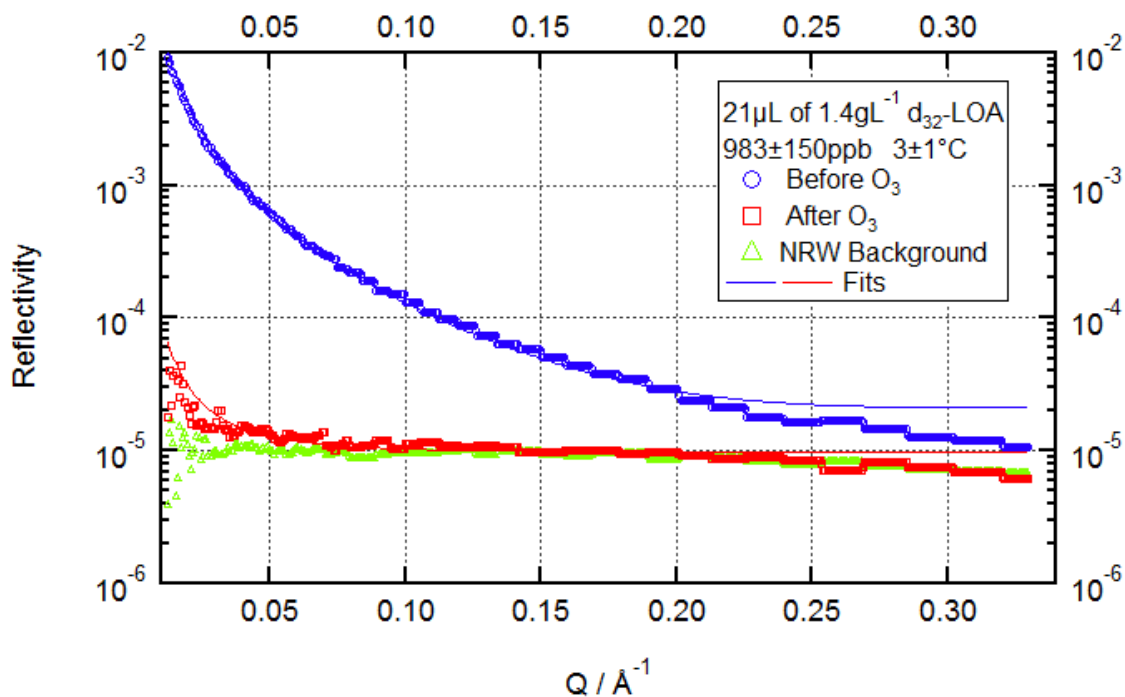


Figure 7.16 – Oxidation of a pure d_{32} -LOA monolayer; $21 \mu\text{L}$ of 1.4 g L^{-1} d_{32} -LOA; $[\text{O}_3] = 983 \pm 150 \text{ ppb}$; low temperature; R vs Q reflectivity plots before and after oxidation; air/NRW background shown for comparison.

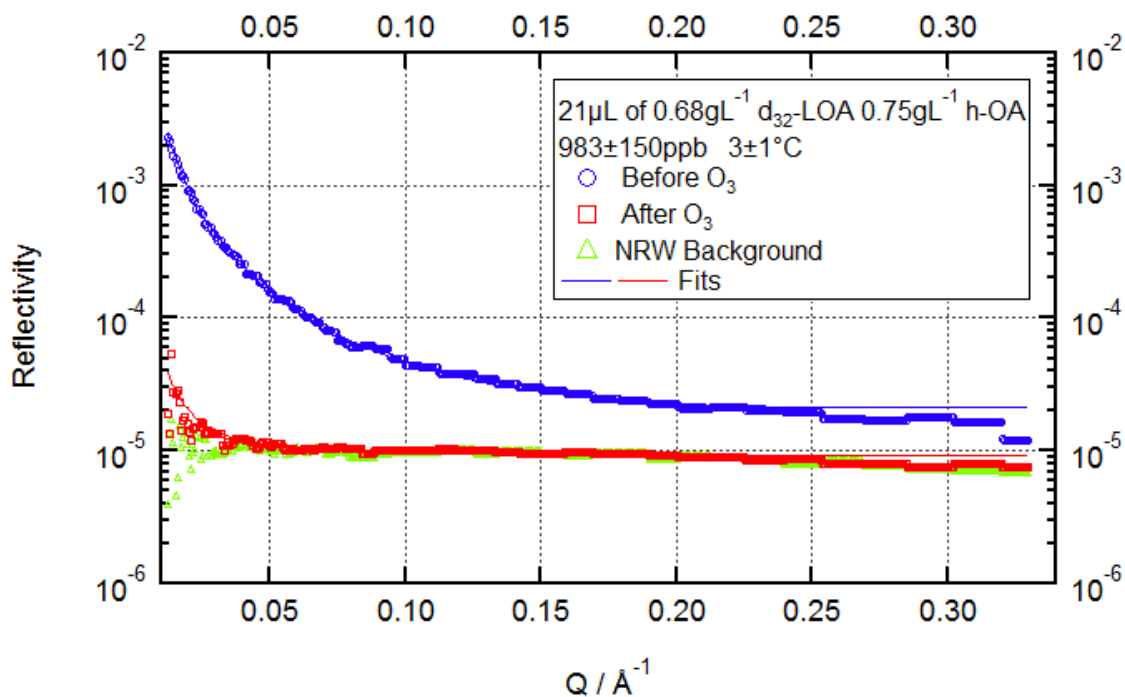


Figure 7.17 – Oxidation of d_{32} -LOA in a mixed monolayer with h -OA; $21 \mu\text{L}$ of 0.68 g L^{-1} d_{32} -LOA/ 0.75 g L^{-1} h -OA; $[\text{O}_3] = 983 \pm 150 \text{ ppb}$; low temperature; R vs Q reflectivity plots before and after oxidation; air/NRW background shown for comparison.

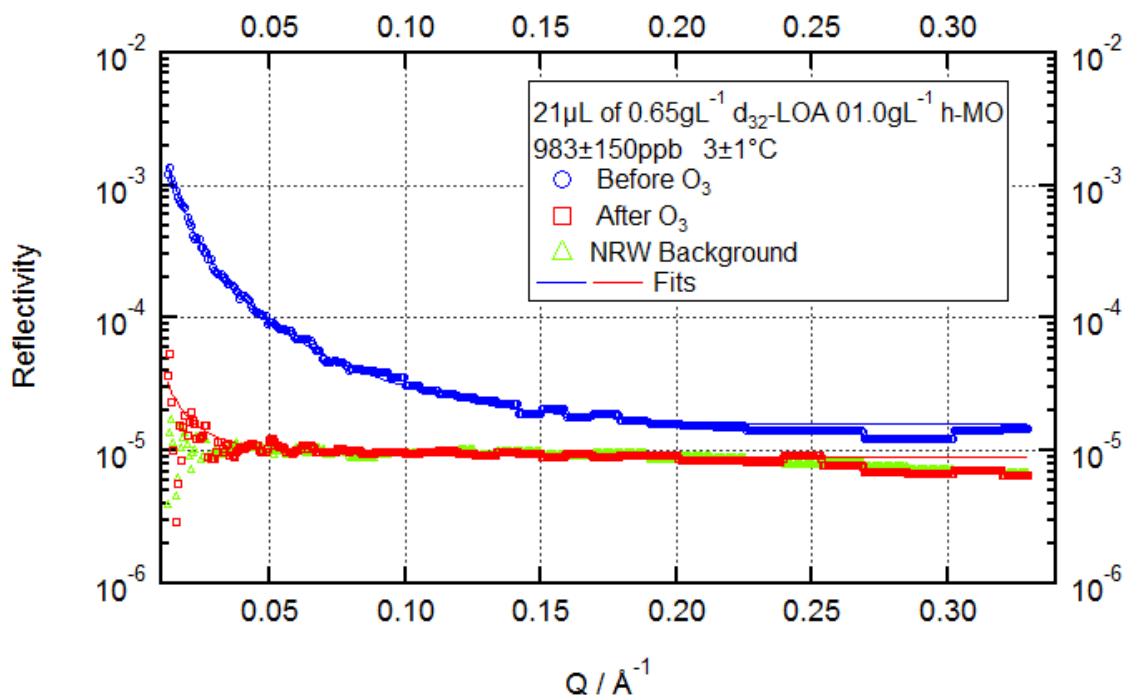


Figure 7.18 – Oxidation of d_{32} -LOA in a mixed monolayer with h-MO; 21 μL of 0.65 g L^{-1} d_{32} -LOA/ 1.0 g L^{-1} h-MO; $[\text{O}_3] = 983 \pm 150 \text{ ppb}$; low temperature; R vs Q reflectivity plots before and after oxidation; air/NRW background shown for comparison.

The data for d_{32} -LOA in a mixed monolayer with h-MO is slightly more difficult to interpret. The fitting process used throughout this work to fit monolayer parameters to reflectivity data does successfully converge and fit a curve (shown on the graph as a red line) that, if genuine, would represent 13% of the initial adsorbed deuterated material. However, a visual appraisal of Figure 7.18 suggests strongly that no residue remains, as the post-oxidation reflectivity curve differs only from a null-reflecting water background in that it is unusually noisy at very low Q. The fit to the data is also visually very poor. This is probably a result of the unexpected noisiness at low Q and the fact that several points are below background. As mentioned in section 7.2, the INTER background at very low and high Q is sometimes not entirely Q-independent, and this may be what is causing this issue; air/NRW background runs often also show this oscillation at low Q (see Figures 7.16 to 7.18), so this is likely the source of the similar oscillation after oxidation in this case. This may be confusing the fitting algorithm, resulting in the spurious fit. This experiment should be repeated to make sure, but it seems likely from this data alone that no measurable residual monolayer remains under these conditions, and that the fit achieved by MOTOFIT in this case is illusory.

As well as repeating the low temperature residue quantification experiment for d_{32} -LOA/h-MO, future work on this system could perform analogous room temperature experiments. As for the OA ozonolysis in the presence of LOA discussed in section 7.2, the kinetic data collected over a limited Q range suggests that similar residual monolayers are present, but a full Q range characterisation would be necessary to confirm this.

The mechanism for LOA oxidation is more complex than for OA oxidation; the former involves multiple competing pathways of ozonolysis and ozone-initiated autoxidation that result in different products. One mechanism or the other has previously been observed to dominate depending on ozone concentration and relative humidity¹. The linear increase in pseudo-1st-order reaction rate with increasing ozone concentration suggests that one dominant mechanism is being observed across the range of ozone concentrations used in this work (~100 to ~500 ppb for kinetic studies; ~1000 ppb for

residue). Chu *et al.* noted that higher ozone concentrations (above 250 ppb) inhibited the build-up of autoxidation products, as did higher relative humidity¹. All this work is carried out with ozone dissolved in a stream of dry oxygen, so the relative humidity will be close to 0%. Based on the range of ozone concentrations we employed and the low relative humidity of our system, it seems likely that we observed only autoxidation, and did not reach conditions necessary for ozonolysis to dominate. The autoxidation mechanism is complex and, particularly since it seems premature to claim with certainty that it is the mechanism we have observed (as we are only inferring from conditions in comparison to other work, not using any direct measurement technique to distinguish autoxidation from ozonolysis), it is not presented in full here. A detailed explanation can be found in Chu *et al.*¹. Further work to modify our experimental apparatus in order to control the relative humidity would be a logical next step for investigations into LOA oxidation.

Some preliminary experiments on the effect of co-deposited SA on LOA monolayer oxidation were also carried out. Figure 7.19 shows the oxidation of a d₃₂-LOA/h-SA monolayer at two ozone concentrations at two temperatures. This was not enough data to reliably calculate a 2nd-order rate constant, but a visual appraisal of the data suggests that temperature once again does not exert a significant effect on the reaction rate. As far as the effect of SA on the reaction rate goes, however, this preliminary data suggests that there may be an impact. Figure 7.20 shows the room temperature data overlaid with analogous data for d₃₂-LOA/h-OA oxidation. It does appear that the reaction is faster in the presence of SA. Further work is necessary to see whether this effect is reproducible, as there is a reasonable degree of inter-run variability (as shown in Figure 7.15).

A full Q range residue quantification experiment was performed for the d₃₂-LOA/h-OA system, and the results are shown in Figure 7.21. The post-oxidation reflectivity is not different from the air/NRW background barring an intriguing oscillation at low Q. In a similar manner as for d₃₂-LOA/h-MO, MOTOFIT is able to fit a curve to this, but this time the fit is clearly illusory. This is in line with the effect suggested in Chapter 6 for OA, in which a residue exists for the pure monolayer at low temperature but not for the mixed layer with SA. That data needs confirmation with a larger Q range experiment, however, and this experiment could do with being repeated, and the oscillation further investigated if it is observed again. As with all other systems discussed in this chapter, a full Q range residue quantification experiment at room temperature would also be very useful, perhaps more so for the d₃₂-LOA/h-OA system than for any of the others presented in this chapter, as we have previously found strong evidence (see Chapter 6) that the presence of SA can stabilise products from OA ozonolysis at room temperature, so it would be interesting to see if the same holds for LOA autoxidation or ozonolysis.

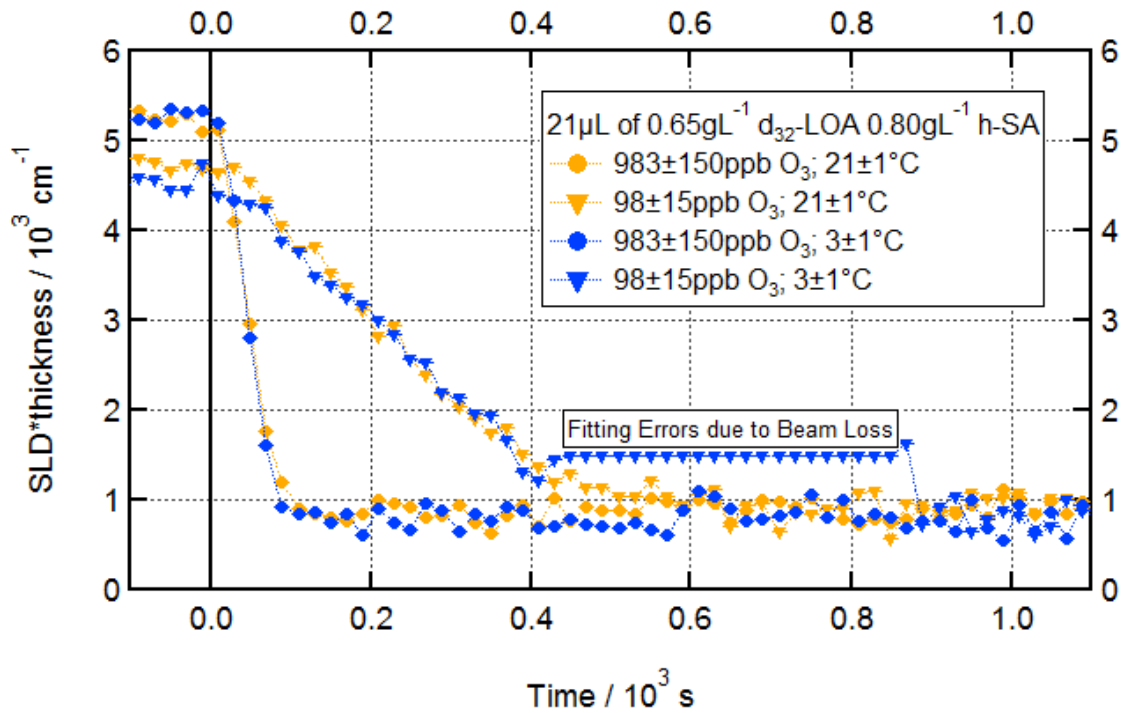


Figure 7.19 – Oxidation of d_{32} -LOA in a mixed monolayer with h-SA; 21 μL of $0.65 \text{ g L}^{-1} d_{32}$ -LOA/ $0.80 \text{ g L}^{-1} h$ -SA; O_3 introduced at $t = 0 \text{ s}$ at two $[\text{O}_3]$; two temperatures; neutron reflectometry fitted time series.

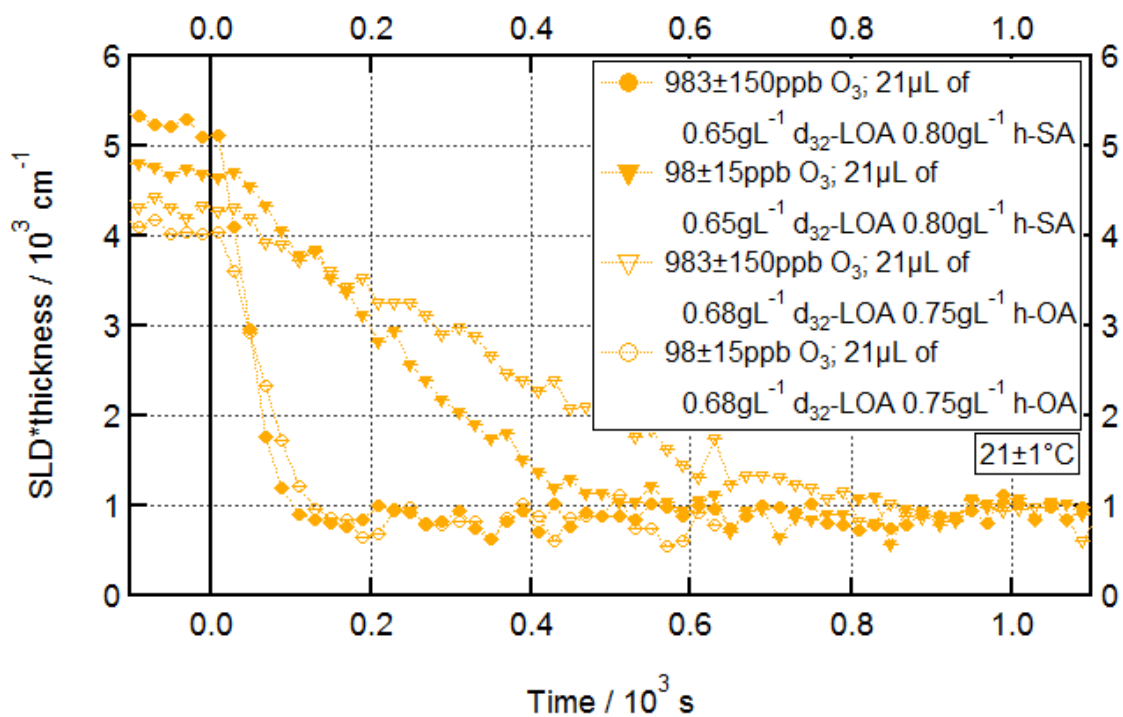


Figure 7.20 – Oxidation of d_{32} -LOA in mixed monolayers with h-OA or h-SA; 21 μL of $0.68 \text{ g L}^{-1} d_{32}$ -LOA/ $0.75 \text{ g L}^{-1} h$ -OA or $0.65 \text{ g L}^{-1} d_{32}$ -LOA/ $0.80 \text{ g L}^{-1} h$ -SA; O_3 introduced at $t = 0 \text{ s}$ at two $[\text{O}_3]$; room temperature; neutron reflectometry fitted time series.

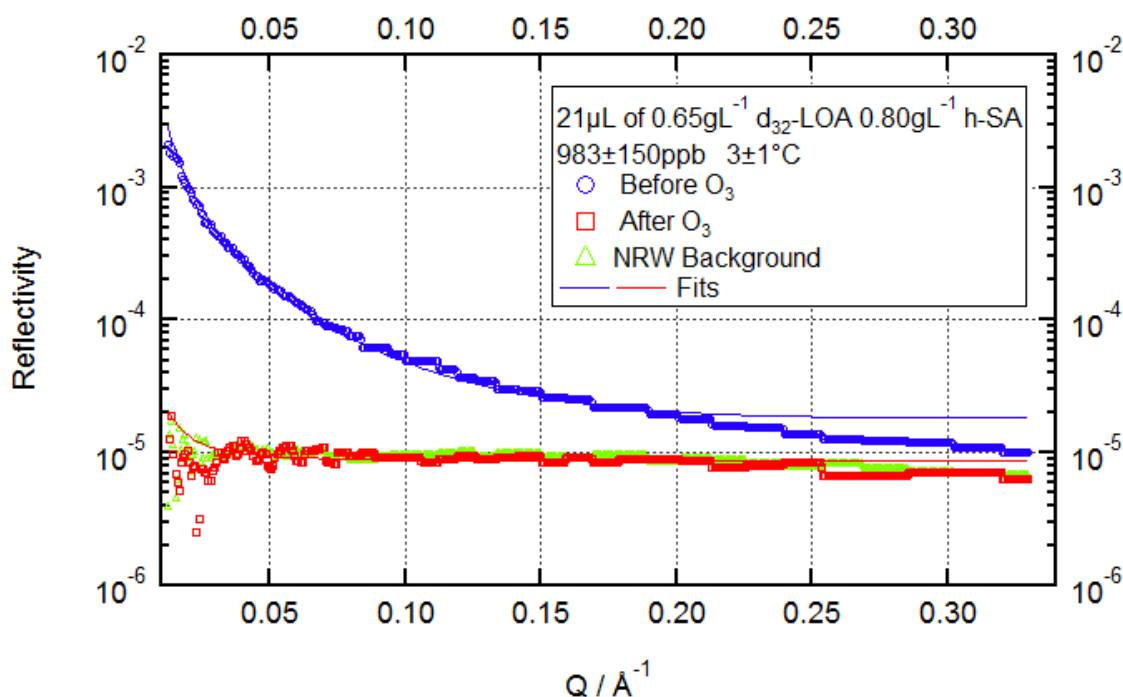


Figure 7.21 – Oxidation of d_{32} -LOA in a mixed monolayer with h-SA; $21 \mu\text{L}$ of 0.65 g L^{-1} d_{32} -LOA/ 0.80 g L^{-1} h-SA; $[\text{O}_3] = 983 \pm 150 \text{ ppb}$; low temperature; R vs Q reflectivity plots before and after oxidation; air/NRW background shown for comparison.

7.4 – Future Work

This preliminary investigation of the data from experiment RB 1910615 on INTER provides a good foundation for further investigations into the oxidation of LOA. As mentioned in sections 7.2 and 7.3, residue quantification experiments at room temperature across the full Q range accessible at INTER, as well as repeats of the low temperature experiments detailed in sections 7.2 and 7.3 (some of which have produced unclear results) would be a logical next step.

The films also need to be characterised and studied offline more fully in order to ensure that the initial surface phase is well understood for any more detailed experiments that follow this introductory study, and that any apparent differences in behaviour between the pure system and the various mixed systems are in fact due to mixing effects, and not due to differing surface phase behaviour. As linoleic acid, oleic acid, and methyl oleate are all unsaturated fatty acids with broadly similar physical properties, it is likely that they mix well at the interface, and it is also likely that linoleic acid and stearic acid mix poorly, as do oleic and stearic acids (see Chapter 6). Due to this similarity to systems already studied and due to the very limited timeframe available to work with linoleic acid for this exploratory study, offline characterisation (for instance via BAM and Wilhelmy plate tensiometry) was not performed in the work displayed here, but such investigations would form a useful part of any further, more detailed work to investigate some of the phenomena illuminated by this initial study.

The kinetic data presented in Table 7.1 is somewhat speculative, as only three data points are used for each of the six individual conditions. Data was collected under four ozone concentration conditions, but pseudo-1st-order rate constants could not be fitted for the highest, as the reaction was too fast to fit at a 20 second time resolution. Fitting pseudo-1st-order and 2nd-order rate constants to this data is not trivial, as discussed in detail in Chapter 5. In order to achieve a reliable 2nd-order rate constant, one has to deal with offsetting at the start of the reaction and find an appropriate ‘effective volume’ to achieve a good 1st-order fit across a range of ozone concentration values and achieve linearity in the 2nd-order fit. This is challenging with four or five ozone concentration values, and very speculative with only three.

This might also explain the very slight negative intercept value seen in the two 2nd-order fits in Figures 7.4 and 7.15. A zero-intercept is within the 95% confidence interval of the fit, so this may simply be chance, but, if it is a genuine effect of the fit, then this deviation from true 2nd-order behaviour could be due to the problems in fitting in this manner with only 3 different ozone concentration conditions.

These issues could be solved by collecting more data across a greater variety of [O₃] values. Reactions at [O₃]_{gas} ≈ 500 ppb produced data that could be fitted at a 20 second time resolution, but reactions at [O₃]_{gas} ≈ 1000 ppb were too fast, so care would have to be taken about extending the range to higher [O₃]. It could be possible to push the time resolution a little lower, which might make data collected at [O₃]_{gas} ≈ 1000 ppb useful for kinetic study after all. This could be investigated by re-processing some of the data already collected under those conditions. Alternatively, one could make use of the 5 second time resolution available on FIGARO, due to the higher neutron flux at that instrument, though this would make FT-IRRAS integration impossible due to the more restricted sample environment.

The most fruitful approach for further kinetic study would be to move to lower ozone concentrations. This would extend the range of data available for 2nd-order fitting, and the new data produced would be easier to fit at the 1st-order level, increasing the robustness of the fitted parameters. Furthermore, lower ozone concentrations would be more atmospherically relevant. The reason that such high ozone concentrations were used for this study is that, as this was an exploratory study, the aim was to test as many different mixtures and temperature conditions as possible in the short timeframe of a beamline experiment. Higher ozone concentration means faster reactions, greatly increasing the number of systems that could be studied. Now that this exploratory study has identified fruitful areas for possible future work, any future kinetic studies would be most useful if the ozone concentration range were extended to lower values (~25 to ~250 ppb would be a reasonable starting point, compared with ~100 to ~1000 ppb as used in this exploratory study).

The effect of SA on the oxidation of LOA, which was only very briefly studied in this experiment, certainly merits further investigation. As Figure 7.20 shows, the preliminary data suggests a possible significant and measurable effect on the reaction rate.

The FT-IRRAS data from this experiment also bears deeper study than has been feasible in the time available for this initial investigation, as, in some d₃₂-LOA/h-OA oxidation runs, the FT-IRRAS was able to see a non-deuterated residue remaining after the reaction (see Figure 7.22 for an example).

In sum, another beamline experiment is necessary for the picture sketched out with regards to LOA oxidation to come fully into focus. The stage is set for the combined NR/FT-IRRAS apparatus developed across the course of this project to continue to produce exciting results across a wide range of applications in the field of monolayer oxidation studies.

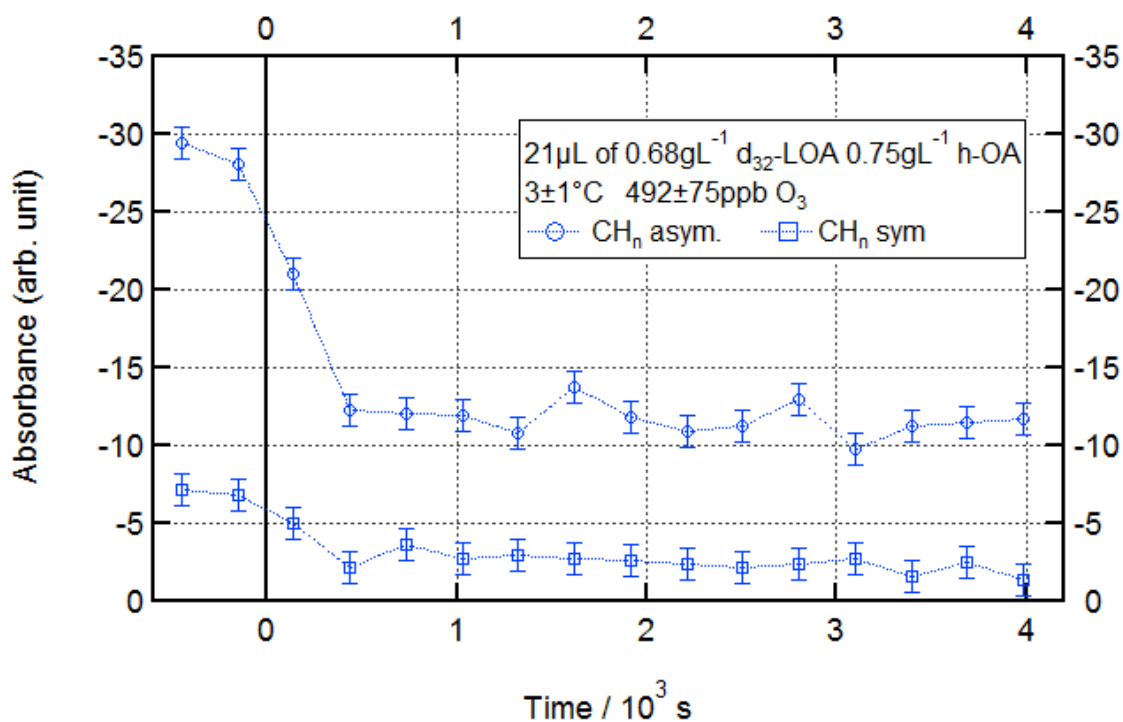


Figure 7.22 – Ozonolysis of h-OA in a mixed monolayer with d₃₂-LOA; 21 μL of 0.68 g L⁻¹ d₃₂-LOA/0.75 g L⁻¹ h-OA; O₃ introduced at t = 0 s at 492 ± 75 ppb; infra-red spectroscopy integrated time series. Peaks from residual h-OA visible.

7.5 – Bibliography (Linoleic)

- 1 Y. Chu, T. F. Cheng, M. Gen, C. K. Chan, A. K. Y. Lee and M. N. Chan, *ACS Earth and Space Chemistry*, 2019, **3**, 779–788.
- 2 U. Molteni, M. Simon, M. Heinritzi, C. R. Hoyle, A.-K. Bernhammer, F. Bianchi, M. Breitenlechner, S. Brilke, A. Dias, J. Duplissy, C. Frege, H. Gordon, C. Heyn, T. Jokinen, A. Kürten, K. Lehtipalo, V. Makhmutov, T. Petäjä, S. M. Pieber, A. P. Praplan, S. Schobesberger, G. Steiner, Y. Stozhkov, A. Tomé, J. Tröstl, A. C. Wagner, R. Wagner, C. Williamson, C. Yan, U. Baltensperger, J. Curtius, N. M. Donahue, A. Hansel, J. Kirkby, M. Kulmala, D. R. Worsnop and J. Dommen, *ACS Earth and Space Chemistry*, 2019, **3**, 873–883.
- 3 X. He, C. Leng, S. Pang and Y. Zhang, *RSC Advances*, 2017, **7**, 3204–3213.

Chapter 8 – Summary

8.1 – Introduction

The layout of the thesis so far has been by area of enquiry. This final chapter attempts to tie the various topics together into a summary and present the work in a chronological, narrative fashion that makes clear the interweaving of scientific problem-solving and technique development that drove this work forwards. It is the nature of a PhD project based in a technique like neutron scattering to be based around a small number of significant experiments, and so those beamline experiments will serve as the structure for this chapter.

8.2 – Early Exploratory Phase: INTER RB 1510605 and RB 1520459

The first beamline experiment of the project, RB 1510605 on INTER at ISIS, took place before my PhD programme had started, and mostly formed a proof of concept for the idea of combining FT-IRRAS with NR in order to study the oxidation of surfactant monolayers at the air/water interface. Some data from this beamline experiment can be seen in the *RSC Advances* paper presented in section 3.1.

I began working on the project in September 2015, shortly after this beamline experiment, and started to familiarise myself with the FT-IRRAS equipment and the wet techniques required to work with and spread surfactant monolayers. My first beamline experiment, RB 1520459 took place in November 2015. This beamline experiment still used a basic version of the combined NR/FT-IRRAS equipment adapted from commonly available NR sample environment equipment, with many FT-IRRAS mirrors essentially free-floating in the environment.

Progress on this beamline experiment was slow, due to the cumbersome and sensitive nature of the FT-IRRAS equipment, but some good data was gathered. The most obviously promising area of research opened up by the combination of techniques was mixed monolayers, and so this beamline experiment focused on OA/SA monolayers. Some results from this beamline experiment are presented in Chapter 6, including the result that defied adequate explanation until years later: the increase in NR signal upon oxidation of an h-OA/d₃₅-SA monolayer.

Further FT-IRRAS work off the beamline on mixed monolayers followed on from RB 1520459 and backed up some of the data gathered during the main experiment, but it became clear that the sample environment was too fragile and difficult to use to make good progress, and so attention turned to developing a new reaction and analysis chamber and FT-IRRAS beam path manipulation system.

8.3 – Focus on GCB: INTER RB 1610500

A proposal for an experiment focusing on the oxidation of GCB alone and in mixed monolayers with palmitic acid had been submitted shortly after I began working on the project, and beamline access was awarded for July 2016. Preparatory experiments off the beamline showed that GCB would be a more challenging surfactant to work with than fatty acids, both in terms of wet technique and FT-IRRAS signal strength and consistency.

Work began on designing and building the first completely bespoke sample environment system for NR/FT-IRRAS monolayer oxidation studies around the start of 2016, and the first build was completed in time for INTER RB 1610500 in July, during which GCB monolayer studies were undertaken. This version of the reaction and analysis chamber was spotlighted in the *RSC Advances* paper (section 3.1), and the results of the GCB experiments were published in the *Atmosphere* paper (section 4.1).

The discovery that the GCB monolayer remained largely intact throughout oxidation, losing only the unsaturated branch of the tail (which was the part of the molecule that least well modelled marine

aerosol normally observed) and not even that in some cases, provided few avenues for promising further study. This part of the research, along with some offline Brewster angle microscopy (BAM) work on the same monolayer systems, therefore stands somewhat separately from the main body of work on fatty acid monolayers, which have proven much more interesting and unpredictable in their behaviour. Attention returned to these systems (especially given the unexplained data from h-OA/d₃₅-SA oxidation) following RB 1610500.

As Chapter 3 reports, RB 1610500 was challenging from an equipment point of view, and work immediately began on rectifying some of the shortcomings of the first build before the next beamline experiment.

8.4 – Focus on Mixtures: INTER RB 1620451 and RB 1710483

The trough height adjustment system described in Chapter 3 was deployed for INTER RB 1620451 in March 2017, which returned the focus of the project firmly to mixed fatty acid monolayers, particularly the OA/SA combination. RB 1620451 was one of the most productive beamline experiments of the project in terms of data output. The improved reaction and analysis chamber and sample environment setup functioned admirably, and a large variety of OA/SA mixtures were reacted with ozone at a variety of concentrations.

Scientifically, though, this was one of the most frustrating beamline experiments. The working hypothesis that best explained the data we'd seen so far (that it was difficult to assign a meaningful scale factor due to surface inhomogeneity and the apparent increase in signal was a modelling anomaly due to this problem) was contradicted by our first d₃₄-OA/d₃₅-SA monolayer experiments, which should have behaved more conventionally if this were the case, but still behaved anomalously.

The issue is discussed in detail in Chapter 6, but the consequence of this uncertainty was that data was collected fairly blind, with the experiment run under a variety of conditions, with the hope that some of the data would turn out to be useful in determining kinetic parameters and explaining the OA/SA interaction, but with work still to do on getting to the bottom of the problem.

A few experiments on a D₂O subphase performed at the start of the next beamline experiment (RB 1710483 in September 2017) disproved another working hypothesis (multi-layer formation) that had seemed like a promising explanation of the confusing OA/SA data, leaving the project with a wealth of NR and FT-IRRAS data on OA/SA mixture oxidation, but very little in the way of a coherent explanatory framework for it, or much idea of what was going on.

8.5 – Focus on Temperature: INTER RB 1710483 and RB 1810793; FIGARO 9-10-1518

While the discussion on mixtures continued, the idea of studying temperature variation was proposed and agreed. Following INTER RB 1620451 in early 2017, work began on modifying the reaction and analysis chamber by including liquid cooling apparatus. RB 1710483 in September 2017 saw the first iteration of a temperature-controlled chamber deployed, and the beamline experiment proceeded as something of a mirror image of the prolific but frustrating RB 1620451.

RB 1710483 was very technically challenging. The first iteration of the cooling system worked poorly and inhibited the operation of other chamber components. Details of these problems, and how they were solved, are included in Chapter 3. However, through the poor quality and low volume of data produced, an exciting possibility was glimpsed: It seemed like, at low enough temperatures, a pure OA monolayer wasn't being entirely removed from the surface, but something was left behind, which disappeared on heating.

At this point, two years in, the research project was at a serious crossroads. Incomplete oxidation, or a stable residual product monolayer, would have important atmospheric implications (it would mean that unsaturated fatty acid emissions could affect the physical properties of atmospheric water droplets for far longer than would be implied simply by the atmospheric lifetime of the emitted surfactant itself), but better controlled experiments would have to be run to reproduce the finding, which would mean significant focus on improving the temperature control system.

On the other hand, plenty of data on mixed monolayers, the original focus of the project and the primary justification for combining NR and FT-IRRAS measurements in the first place, was left without a clear framework for interpretation. There was data from RB 1610451 that could be used to calculate kinetic parameters for the reaction of OA/SA monolayers with ozone (that collected using d_{34} -OA/h-SA monolayers), but, without a clear explanation of why data from the h-OA/ d_{35} -SA and d_{34} -OA/ d_{35} -SA experiments demonstrated the anomalous behaviour that it did, it would be unwise to assume that we could interpret the d_{34} -OA/h-SA as if our modelling and assumptions were correct.

The project clearly had to choose a primary direction at this point, and I decided to focus on solving the technical issues around temperature control, with a view to following up the suggestion that OA monolayers were behaving somewhat differently at low temperatures.

The next six months saw progress on the temperature control issues, detailed in Chapter 3, which culminated in a far improved chamber for RB 1810793 in April 2018. This experiment focused completely on studying pure OA monolayers at low temperatures, and so the FT-IRRAS side took less of a leading role (though ongoing incremental improvements to the beam path and increased experience in alignment helped produce the highest quality FT-IRRAS data yet). The NR signal from the residue was slight, but given long run times, detection right down to the background at high Q, and the flexibility of INTER's Event Mode data collection system, it was detectable and demonstrably differentiable from background scattering.

I had already started drafting what would become the *ACP* paper, based on the scant data from RB 1710483, and the far better data from RB 1810793 ended up forming the crux of its argument that OA monolayers leave behind a stable residue when they oxidise at low temperatures, and that this residue can be built up through repeated depositions and re-oxidations.

A few last technical problems still remained on RB 1810793, and it was unclear whether these could be solved in time for the next beamline experiment, 9-10-1518 on the ILL's FIGARO at the very start of July, barely two months after the end of RB 1810793, and the other side of the English Channel. The fix was obvious (this was the switch to a single baseplate/trough piece detailed in Chapter 3) but the timelines were compressed. I took the decision to proceed, and final adjustments were made to the trough in the ILL workshop, the night before 9-10-1518 began.

FIGARO's sample environment lacks the size and flexibility of INTER's, and could not accommodate the FT-IRRAS apparatus, meaning this was a pure NR experiment. What it lacks in flexibility, though, FIGARO makes up for in neutron flux. This made it ideal for kinetic measurements. Experiment 9-10-1518 was therefore able to provide a complementary dataset to RB 1810793. While INTER allowed us to probe fine distinctions at high Q over variable time slicing regimes in order to qualitatively investigate the residual monolayer that was the focus of our paper, a large number of fast, high-flux experiments on FIGARO allowed us to test whether the kinetics of the reaction were affected notably by the same temperature shift that stabilised the residue.

It turned out that the answer was no: There was no notable difference in the kinetics between room temperature and near-freezing. This data formed part of the *ACP* paper, as well as providing a host of extra runs to back up the primary residue finding.

8.6 – The Final Piece of the Puzzle: SURF RB 1540015 and INTER RB 1910615

Following 9-10-1518 on FIGARO, attention turned to analysing and writing up the data from that beamline experiment and from INTER RB 1810793, and then to a number of side projects, including a secondment. When I returned to write up in January 2019, I approached the still confounding OA/SA mixtures data with a fresh outlook and a better understanding of the fundamentals of neutron scattering than I had in the early stages of the project. I formulated another hypothesis, which claimed the pre-oxidation inhomogeneity that we knew existed from the BAM data and that had driven our thinking up to that date was too fine-grained to cause NR interpretation problems, and that in fact the problem was a much more coarse-grained post-oxidation inhomogeneity in the remaining SA monolayer.

This hypothesis explained all the NR and FT-IRRAS data we had so far gathered, and its central thesis, that a pure SA monolayer well below surface saturation concentration would cluster and that this would cause NR fitting based on a uniform monolayer model to overestimate its surface concentration, could be tested. It was tested in a short beamline experiment on SURF, which has less flux and flexibility than INTER but enough to perform an experiment like this, as it didn't require the tracking of a fast reaction or any additional sample environment equipment besides a standard Langmuir trough. This was RB 1540015, performed in June 2019.

RB 1540015 used compression cycling, and demonstrated the predicted effect but with somewhat uncertain magnitude. A further experiment on INTER at the start of RB 1910615 the following month completed the puzzle, comparing various SA and OA/SA monolayers in side-by-side troughs and demonstrating the overestimation of SA monolayer concentration due to inhomogeneity when present as a partial monolayer alone, but not when present as part of an OA/SA monolayer.

The details of this experiment are covered in Chapter 6. From a narrative perspective, these two small experiments were the most consequential of any performed throughout the project. They allowed the data from previous experiments (RB 1520459, RB 1620451, and RB 1710483 on INTER) to be appraised in a new light, and finally understood properly.

This meant that the wealth of data on OA/SA monolayers from RB 1620451 in March 2017 could finally be utilised properly and used to calculate kinetic parameters for the ozonolysis of OA in the presence of SA. Once again, the kinetic data implied a null result: The presence of SA does not significantly alter the kinetics of OA ozonolysis. What is potentially much more interesting is that OA ozonolysis does seem to leave a product monolayer behind when SA is present, just as it does by itself at low temperatures.

This last finding opens the door for future studies on the way that the mixture and temperature effects interact. Preliminary experiments on low temperature ozonolysis of OA/SA mixtures suggested that the residual product monolayer seen with low temperature OA and room temperature OA/SA does *not* show up in this case, though this was just one run and the data was somewhat noisy, so certainly warrants more investigation.

8.7 – New Frontiers: INTER RB 1910615

The rest of RB 1910615 involved opening up the project to a brand new fatty acid: LOA. With the reaction and analysis chamber and FT-IRRAS integration now working well, a large variety of preliminary studies were conducted on pure LOA monolayers as well as OA/LOA, LOA/MO, and LOA/SA mixtures. The details of these experiments are included in Chapter 7, and are too many and varied to list here, but many combinations showed interesting potential for further study in terms of residual monolayers and kinetics (the first hint of a change in kinetics for a reaction based on a change in conditions was observed: LOA may react with ozone when SA is present in the monolayer).

RB 1910615 was the first experiment carried out using exactly the same reaction and analysis chamber and trough as a previous experiment (9-10-1518 on FIGARO). Equipped with well-functioning cooling that no longer impedes standard operation, the currently standing apparatus is ready to continue expanding our knowledge of surfactant monolayer oxidation, though there are some possible improvements that could yet be made, which are outlined in Chapter 3.

8.8 – Key Findings

In its totality, this project should be viewed as having produced both physical and knowledge products. The final iteration of the reaction and analysis chamber, FT-IRRAS beam path equipment, and reaction trough represents a significant advance over what was available at the start of the project, and should allow other projects of a similar nature to proceed with much greater speed and flexibility.

The knowledge products are summed up in detail in the papers and thesis chapters that precede this narrative summary, but the headline findings are outlined here.

Galactocerebroside oxidation by nitrate radicals:

- Nitrate radical oxidation does not remove a GCB monolayer from pure water or CaCl_2 (aq);
- The unsaturated tail branch is removed, but not for a GCB/PA monolayer on CaCl_2 (aq);
- This implies that glycolipid monolayers on marine aerosol persist through night-time.

Effect of temperature on oleic acid ozonolysis:

- At near-freezing temperatures, OA ozonolysis leaves a residual product monolayer;
- This residue is likely partly nonanoic acid, partly 9-oxononanoic or azelaic acids;
- This residue is stable up to 7 to 12 °C;
- Re-deposition and re-ozonolysis of OA leads to build-up of this product layer;
- Changes in temperature over this range do not affect OA ozonolysis kinetics.

Effect of stearic acid as a monolayer co-component on oleic acid ozonolysis:

- Despite problems using NR to measure SA, NR measurements of OA in the presence of SA using standard uniform monolayer models are reliable;
- OA ozonolysis in a binary mixed monolayer with SA leaves a residual product monolayer;
- Further analysis of the interaction between this effect and the temperature effect is needed;
- The presence of SA does not affect the kinetics of OA ozonolysis.

The single headline result, implied from both the temperature effect and the SA co-component effect, is this: Unsaturated fatty acid emissions could affect the physical properties of water droplets in the atmosphere longer than implied by their atmospheric lifetimes.

If OA monolayers form at low temperatures, or if they form in the presence of SA as a monolayer co-component even at higher temperatures, then ozonolysis will not remove all surfactant material but will leave a residual product monolayer behind. If SA is taken to be a model for saturated fatty acids, and OA for unsaturated, then a situation could obtain where, as long as some 'seed' saturated material is present (either through direct deposition or as residue from a low temperature ozonolysis of unsaturated material), repeated deposition and re-oxidation of unsaturated material could result in the gradual build-up of a saturated monolayer impervious to ozonolysis, as has been observed in real-life aerosol samples, despite the feedstock material being mostly or maybe even wholly unsaturated material. Unsaturated, reactive emissions could lead to saturated, stable monolayers.

Appendices

Appendix 1 – Process Code

A.1.1 – Introduction

As discussed in Chapter 2, data processing for the work detailed in this thesis was carried out using: MantidPlot¹, a Python plotting and data handling environment designed explicitly for working with neutron scattering data; COSMOS, a neutron reflectometry data handling package that forms part of the LAMP² software suite for neutron scattering data; and MOTOFIT³, a neutron reflectometry fitting tool for the data analysis environment Igor Pro.

Across the course of the project, I composed simple software tools to assist with my analysis. One of these was a function within MantidPlot that modified existing scripts used for Event Mode data reduction and packaged them into a basic wrapper that could iterate over a run and break it down into time slices of a defined length. This was used extensively for the early phase of data reduction, in which raw Event Mode data is processed into R vs Q reflectivity curves.

The other tool was an Igor procedure designed to run after MOTOFIT batch fitting. The output from MOTOFIT batch fitting is produced in terms of scattering length density, and is displayed and stored in a somewhat inconvenient manner. Furthermore, multiple batch fitting instances simply append their results to the same dataset. The Igor procedure I wrote takes the output from a MOTOFIT batch fit, translates it into a more usable format (surface concentration and scattering length coverage, rather than simply scattering length density, which is not particularly informative alone as it depends on modelled layer thickness; see Chapter 2 for a full explanation), and graphs it in a manner appropriate for further processing or pseudo-1st-order rate constant fitting. It then cleans the MOTOFIT batch fitting output data so that the next batch fit produces a separate dataset.

A.1.2 – MantidPlot

The MantidPlot function definitions are included here. “EventRef...” functions are slightly modified versions of functions regularly in use at ISIS that were not originally written by me. “ProcessRun” is my wrapper for those functions. The liberal use of print statements is intended to allow me to monitor the progress of the function and ensure it is running properly, as MantidPlot is not completely stable. The function was intended for local use, so file paths are hard coded.

```
def EventRefLoQ(runno, stop, start=0, latest=0):
    runno=str(runno)
    Load(Filename=runno, OutputWorkspace=runno, LoadMonitors=True)
    angle=0.8

    w1=mtd[runno]
    total = w1.getRun().getLogData('gd_prtn_chrg').value

    FilterByTime(InputWorkspace=runno,
OutputWorkspace=runno+'_filter', StartTime=start, StopTime=stop)
    wt=mtd[runno+'_filter']
```

```

slice = wt.getRun().getLogData('gd_prtn_chrg').value
fraction = slice/total

duration = wt.getRun().getLogData('duration').value

print 'Processing Slice ' +str(start) + ' to ' + str(stop) + ' of
total ' + str(duration) + ' of run ' + str(runno)

if latest==1:
    start=int(duration-stop)
    stop=int(duration)

Scale(InputWorkspace=runno+'_monitors',Factor=fraction,OutputWorkspace
='mon_slice')

Rebin(InputWorkspace=runno+'_filter',
OutputWorkspace=runno+'_'+str(start)+'_'+str(stop),
Params='0,100,100000', PreserveEvents=False)

Rebin(InputWorkspace='mon_slice', OutputWorkspace='mon_rebin',
Params='0,100,100000', PreserveEvents=False)

AppendSpectra(InputWorkspace1='mon_rebin',
InputWorkspace2=runno+'_'+str(start)+'_'+str(stop),
OutputWorkspace=runno+'_'+str(start)+'_'+str(stop), MergeLogs=True)

ReflectometryReductionOneAuto(InputWorkspace=runno+'_'+str(start)+'_'+
str(stop), FirstTransmissionRun='TRANS_SM',
OutputWorkspace=runno+'_'+str(start)+'_'+str(stop)+'_ref',\

OutputWorkspaceWavelength=runno+'_'+str(start)+'_'+str(stop)+'_lam',
OutputWorkspaceBinned=runno+'_'+str(start)+'_'+str(stop)+'_binned',
Params='0.03,-0.07,0.33', ProcessingInstructions='3',
WavelengthMin=1.5, \

    WavelengthMax=17, ThetaIn=angle, StrictSpectrumChecking=False,
CorrectionAlgorithm='None',MomentumTransferStep=0.07)

Rebin(runno+'_'+str(start)+'_'+str(stop)+'_ref',Params='0.012,-
0.06,0.08',OutputWorkspace=runno+'_'+str(start)+'_'+str(stop)+'_ref')

def EventRefHiQ(runno,stop,start=0,latest=0):
    runno=str(runno)
    Load(Filename=runno, OutputWorkspace=runno, LoadMonitors=True)
    angle=2.3

```

```

w1=mtd[runno]

total = w1.getRun().getLogData('gd_prtn_chrg').value

FilterByTime(InputWorkspace=runno,
OutputWorkspace=runno+'_filter', StartTime=start, StopTime=stop)

wt=mtd[runno+'_filter']

slice = wt.getRun().getLogData('gd_prtn_chrg').value
fraction = slice/total

duration = wt.getRun().getLogData('duration').value

print 'Processing Slice ' +str(start) + ' to ' + str(stop) + ' of
total ' + str(duration) + ' of run ' + str(runno)

if latest==1:
    start=int(duration-stop)
    stop=int(duration)

Scale(InputWorkspace=runno+'_monitors',Factor=fraction,OutputWorkspace
='mon_slice')

Rebin(InputWorkspace=runno+'_filter',
OutputWorkspace=runno+'_'+str(start)+'_'+str(stop),
Params='0,100,100000', PreserveEvents=False)

Rebin(InputWorkspace='mon_slice', OutputWorkspace='mon_rebin',
Params='0,100,100000', PreserveEvents=False)

AppendSpectra(InputWorkspacel='mon_rebin',
InputWorkspace2=runno+'_'+str(start)+'_'+str(stop),
OutputWorkspace=runno+'_'+str(start)+'_'+str(stop), MergeLogs=True)

ReflectometryReductionOneAuto(InputWorkspace=runno+'_'+str(start)+'_'+
str(stop), FirstTransmissionRun='TRANS',
OutputWorkspace=runno+'_'+str(start)+'_'+str(stop)+'_ref',\

OutputWorkspaceWavelength=runno+'_'+str(start)+'_'+str(stop)+'_lam',
OutputWorkspaceBinned=runno+'_'+str(start)+'_'+str(stop)+'_binned',
Params='0.03,-0.07,0.33', ProcessingInstructions='3',
WavelengthMin=1.5, \

WavelengthMax=17, ThetaIn=angle, StrictSpectrumChecking=False,
CorrectionAlgorithm='None',MomentumTransferStep=0.07)

Rebin(runno+'_'+str(start)+'_'+str(stop)+'_ref',Params='0.033,-
0.06,0.33',OutputWorkspace=runno+'_'+str(start)+'_'+str(stop)+'_ref')

def ProcessRun(runnumber,angle,slicelength,runlength):

```

```

numberofslices=runlength/slicelength
for jj in range(0,numberofslices):
    if angle=='Lo':
        print 'Processing at Lo Angle'
        EventRefLoQ(runnumber, (jj+1)*slicelength, jj*slicelength)
        fname='C://Nexus Storage (No Cloud Mirror)/1810793/ASCII
Dump/' + str(runnumber) + '_' + str(jj*slicelength) + '_' +
str((jj+1)*slicelength)+'.txt'
        print 'Saving ASCII file ' + fname

SaveANSTOAscii(str(runnumber)+'_'+str(jj*slicelength)+'_'+str((jj+1)*s
licelength)+'_ref',fname)

        fname='C://Nexus Storage (No Cloud Mirror)/1810793/Kinetic
Slice Processing/' + str(runnumber) + '_' + str(jj*slicelength) + '_'
+ str((jj+1)*slicelength)+'.nxs'
        print 'Saving NEXUS file ' + fname

SaveNexus(str(runnumber)+'_'+str(jj*slicelength)+'_'+str((jj+1)*slicel
ength),fname)

        fname='C://Nexus Storage (No Cloud Mirror)/1810793/Kinetic
Slice Processing/' + str(runnumber) + '_' + str(jj*slicelength) + '_'
+ str((jj+1)*slicelength)+'_lam.nxs'
        print 'Saving NEXUS file ' + fname

SaveNexus(str(runnumber)+'_'+str(jj*slicelength)+'_'+str((jj+1)*slicel
ength) + '_lam',fname)

        fname='C://Nexus Storage (No Cloud Mirror)/1810793/Kinetic
Slice Processing/' + str(runnumber) + '_' + str(jj*slicelength) + '_'
+ str((jj+1)*slicelength)+'_ref.nxs'
        print 'Saving NEXUS file ' + fname

SaveNexus(str(runnumber)+'_'+str(jj*slicelength)+'_'+str((jj+1)*slicel
ength) + '_ref',fname)

        fname='C://Nexus Storage (No Cloud Mirror)/1810793/Kinetic
Slice Processing/' + str(runnumber) + '_' + str(jj*slicelength) + '_'
+ str((jj+1)*slicelength)+'_binned.nxs'
        print 'Saving NEXUS file ' + fname

SaveNexus(str(runnumber)+'_'+str(jj*slicelength)+'_'+str((jj+1)*slicel
ength) + '_binned',fname)

        print 'Deleting slice workspaces'

```

```
DeleteWorkspace(str(runnumber)+'_'+str(jj*slicelength)+'_'+str((jj+1)*slicelength)+'_binned')
```

```
DeleteWorkspace(str(runnumber)+'_'+str(jj*slicelength)+'_'+str((jj+1)*slicelength)+'_ref')
```

```
DeleteWorkspace(str(runnumber)+'_'+str(jj*slicelength)+'_'+str((jj+1)*slicelength) + '_lam')
```

```
DeleteWorkspace(str(runnumber)+'_'+str(jj*slicelength)+'_'+str((jj+1)*slicelength))
```

```
    elif angle=='Hi':
```

```
        print 'Processing at Hi Angle'
```

```
        EventRefHiQ(runnumber, (jj+1)*slicelength, jj*slicelength)
```

```
        fname='C://Nexus Storage (No Cloud Mirror)/1810793/ASCII  
Dump/' + str(runnumber) + '_' + str(jj*slicelength) + '_' +  
str((jj+1)*slicelength)+'.txt'
```

```
        print 'Saving ASCII file ' + fname
```

```
SaveANSTOAscii(str(runnumber)+'_'+str(jj*slicelength)+'_'+str((jj+1)*slicelength)+'_ref',fname)
```

```
        fname='C://Nexus Storage (No Cloud Mirror)/1810793/Kinetic  
Slice Processing/' + str(runnumber) + '_' + str(jj*slicelength) + '_' +  
+ str((jj+1)*slicelength)+'.nxs'
```

```
        print 'Saving NEXUS file ' + fname
```

```
SaveNexus(str(runnumber)+'_'+str(jj*slicelength)+'_'+str((jj+1)*slicelength),fname)
```

```
        fname='C://Nexus Storage (No Cloud Mirror)/1810793/Kinetic  
Slice Processing/' + str(runnumber) + '_' + str(jj*slicelength) + '_' +  
+ str((jj+1)*slicelength)+'_lam.nxs'
```

```
        print 'Saving NEXUS file ' + fname
```

```
SaveNexus(str(runnumber)+'_'+str(jj*slicelength)+'_'+str((jj+1)*slicelength) + '_lam',fname)
```

```
        fname='C://Nexus Storage (No Cloud Mirror)/1810793/Kinetic  
Slice Processing/' + str(runnumber) + '_' + str(jj*slicelength) + '_' +  
+ str((jj+1)*slicelength)+'_ref.nxs'
```

```
        print 'Saving NEXUS file ' + fname
```

```
SaveNexus(str(runnumber)+'_'+str(jj*slicelength)+'_'+str((jj+1)*slicelength) + '_ref',fname)
```

```

        fname='C://Nexus Storage (No Cloud Mirror)/1810793/Kinetic
Slice Processing/' + str(runnumber) + '_' + str(jj*slicelength) + '_'
+ str((jj+1)*slicelength)+'_binned.nxs'

        print 'Saving NEXUS file ' + fname

SaveNexus(str(runnumber)+'_'+str(jj*slicelength)+'_'+str((jj+1)*slicel
ength) + '_binned',fname)

        print 'Deleting slice workspaces'

DeleteWorkspace(str(runnumber)+'_'+str(jj*slicelength)+'_'+str((jj+1)*
slicelength)+'_binned')

DeleteWorkspace(str(runnumber)+'_'+str(jj*slicelength)+'_'+str((jj+1)*
slicelength)+'_ref')

DeleteWorkspace(str(runnumber)+'_'+str(jj*slicelength)+'_'+str((jj+1)*
slicelength) + '_lam')

DeleteWorkspace(str(runnumber)+'_'+str(jj*slicelength)+'_'+str((jj+1)*
slicelength))

        else:

                print 'Angle not set'

        print 'Deleting run workspaces'

        DeleteWorkspace(str(runnumber))

        DeleteWorkspace(str(runnumber) + '_filter')

        DeleteWorkspace(str(runnumber) + '_monitors')

        DeleteWorkspace('mon_rebin')

        DeleteWorkspace('mon_slice')

##Now updated to work with Mantid 3.12.1

##Fixes included new syntax for ReflectometryReductionOneAuto function
and a few changes to name handling to make it all work out properly
plus saving and deleting the new *_binned workspaces

##Bleed of run (rather than slice) workspaces fixed

##LoQ and HiQ variants of EventRef from EventRef.py have been defined
separately

##Defining Angle and Trans no longer necessary

##Angle set to 0.8 for LoQ variant and 2.3 for HiQ variant in function
definitions

```

```

##Trans set to TRANS_SM for LoQ variant and TRANS for HiQ variant in
function definitions

##ProcessRun looks at an angle set and loops the relevant EventRef
over the defined timescale

##ProcessRun takes Run Number, Angle ('Hi' or 'Lo'), Slice Length
(seconds) and Run Length (seconds)

##Save location is part of the definition so need to redefine for new
location

```

A.1.3 – Igor

The Igor procedure is included here. I also wrote a modified version that can deal with a co-deposited stable deuterated component. This version simply accepts a few extra parameters regarding the stable component and corrects the surface concentration calculations accordingly. The modified procedure did not end up being used for any graphs that were included in the thesis, and it is not reproduced here as it is identical to the following single component procedure in almost every way.

```

#pragma rtGlobals=3          // Use modern global access method and
strict wave access.

Function OneComponent()

    Variable timestep //declare timestep parameter
    Variable scatlengthfm //declare scatlength fm parameter
    Variable numpts //declare number of points for output graph
    String runid //declare runid parameter

    Prompt timestep "Enter Experiment Timestep in seconds "
    //input timestep parameter

    Prompt scatlengthfm "Enter Film Component Scattering Length in
fentometres " //input reactive component scattering length fm
parameter

    Prompt numpts "Enter Number of Data Points for Model" //input
numpts parameter

    Prompt runid "Enter Run ID" //input runid parameter

    DoPrompt "Set Parameters", scatlengthfm, timestep, numpts, runid
//wait for user input

    If (V_Flag) //check if user cancelled
        return 0 //abort process
    endif //return to function

    NewDataFolder root:$runid //create data folder for this run
    SetDataFolder root:$runid //set data folder for this run

```

```

Duplicate/O/R=[*][7,7]
root:packages:motofit:motofit_batchfits:concat_coef SLD //create SLD
wave

Duplicate/O/R=[*][7,7]
root:packages:motofit:motofit_batchfits:concat_coef_sigma SLD_sigma
//create SLD error wave

Duplicate/O/R=[0,0][6,6]
root:packages:motofit:motofit_batchfits:concat_coef Modthickwave
//create temporary thickness wave

Duplicate SLD SLC //create SLC wave

Duplicate SLD_sigma SLC_sigma //create SLC error wave

Duplicate SLC Coverage //create Coverage wave

Duplicate SLC_sigma Coverage_sigma //create Coverage error wave

Redimension/N=-1
SLD,SLC,Coverage,SLD_sigma,SLC_sigma,Coverage_sigma //redimension all
data waves

Variable/G Modthickcm //create thickness centimetres variable

Variable/G SLengthcm //create scattering length cm variable

Variable/G Graphlength //create graph length variable

String/G SLDlabel //create SLD graph label variable

String/G GraphBox //create graph box variable

String/G SLDGraphName //create SLD graph name variable

String/G SLCGraphName //create SLC graph name variable

String/G CoverageGraphName //create Coverage graph name variable

SetScale/P x 0,timestep,"",
SLD,SLD_sigma,SLC,SLC_sigma,Coverage,Coverage_sigma; //set scaling of
waves to data spacing of experiment

Modthickcm = Modthickwave*(10^-8) //set thickness centimetres
variable

SLengthcm = scatlengthfm*(10^-13) //set scattering length cm
variable

Graphlength = numpts //set graph length variable

SLDlabel = "SLD /10\\S-6 \\MA\\S-2 \\Mat " +
num2str(modthickcm*(10^8)) + " A model layer" //set graph label
variable

GraphBox = "Run " + runid //set graph box variable

SLDGraphName = "Run" + runid + "SLD" //set SLD graph name
variable

SLCGraphName = "Run" + runid + "SLC" //set SLC graph name
variable

```

```

CoverageGraphName = "Run" + runid + "Coverage" //set Coverage
graph name variable

SLC = (SLD*(10^10))*Modthickcm //calculate SLC
SLC_sigma = (SLD_sigma*(10^10))*Modthickcm //calculate SLC error
Coverage = SLC/SLengthcm //calculate Coverage
Coverage_sigma = SLC_sigma/SLengthcm //calculate Coverage error
KillWaves Modthickwave //kill temporary thickness wave

Display/N=$SLDGraphName SLD //display SLD graph
DoWindow/T $SLDGraphName "Run " + runid + " SLD" //set SLD graph
title
ErrorBars SLD Y,wave=(SLD_sigma,SLD_sigma) //add SLD error bars
ModifyGraph mode=3,marker=19,msize=1.5,rgb=(0,0,0) //SLD graph
markers
SetAxis/A/N=1/E=1 left //SLD axis cleanup
SetAxis/A/N=1/E=1 bottom //SLD axis cleanup
ModifyGraph highTrip=10,notation=1 //SLD axic cleanup
Label bottom "Time /s" //SLD axis label
Label left SLDlabel //SLD axis label
TextBox/C/N=text0/A=MC GraphBox //Set Graph Box
ModifyGraph standoff=0 //SLD axis standoff
Display/N=$SLCGraphName SLC //display SLC graph
DoWindow/T $SLCGraphName "Run " + runid + " SLC" //set SLC graph
title
ErrorBars SLC Y,wave=(SLC_sigma,SLC_sigma) //add SLC error bars
ModifyGraph mode=3,marker=19,msize=1.5,rgb=(0,0,0) //SLC graph
markers
SetAxis/A/N=1/E=1 left //SLC axis cleanup
SetAxis/A/N=1/E=1 bottom //SLC axis cleanup
ModifyGraph highTrip=10,notation=1 //SLC axis cleanup
Label left "SLC /cm\\S-1" //SLC axis label
Label bottom "Time /s" //SLC axis label
TextBox/C/N=text0/A=MC GraphBox //Set Graph Box
ModifyGraph standoff=0 //SLC axis standoff
Display/N=$CoverageGraphName Coverage //display Coverage graph

```

```

    DoWindow/T $CoverageGraphName "Run " + runid + " Coverage" //set
Coverage graph title

    ErrorBars Coverage Y,wave=(Coverage_sigma,Coverage_sigma) //add
Coverage error bars

    ModifyGraph mode=3,marker=19,msize=1.5,rgb=(0,0,0) //Coverage
graph markers

    SetAxis/A/N=1/E=1 left //Coverage axis cleanup
    SetAxis/A/N=1/E=1 bottom //Coverage axis cleanup
    ModifyGraph highTrip=10,notation=1 //Coverage axis cleanup
    Label left "Coverage /cm\\S-2" //Coverage axis label
    Label bottom "Time /s" //Coverage axis label
    TextBox/C/N=text0/A=MC GraphBox //Set Graph Box
    ModifyGraph standoff=0 //Coverage axis standoff

    DeletePoints graphlength+1,100000,
SLD,SLD_sigma,SLC,SLC_sigma,Coverage,Coverage_sigma //truncate graphs

    DoWindow/K concatenatedcoefs //window cleanup
    DoWindow/K batchdata //window cleanup
    DoWindow/K concatenatedparameters //window cleanup
    SetDataFolder :: //return to root folder

    KillDataFolder root:packages:motofit:motofit_batchfits //cleanup
temporary waves

End

```

Appendix 2 – Oleic Acid Brewster Angle Microscopy

Brewster angle microscopy (BAM) images were taken for every system studied in the course of the project, excepting the linoleic acid systems discussed in Chapter 7, as work on those systems is just getting underway. Many hundreds of images were taken, and the best examples of the relevant images are included at various points in the thesis as relevant. At several points, reference is made to the featureless nature of BAM images of pure oleic acid monolayers, but these are not shown, as there is very little to see. Such an image is reproduced in Figure A.1 here for completeness. Several other images were taken, but they all look like this. The banding is an artefact caused by a flaw in the BAM objective lens. The small oval in the top right is a fleck of dust flitting past the objective lens. The speck of dust is out of focus, hence the rings around it.

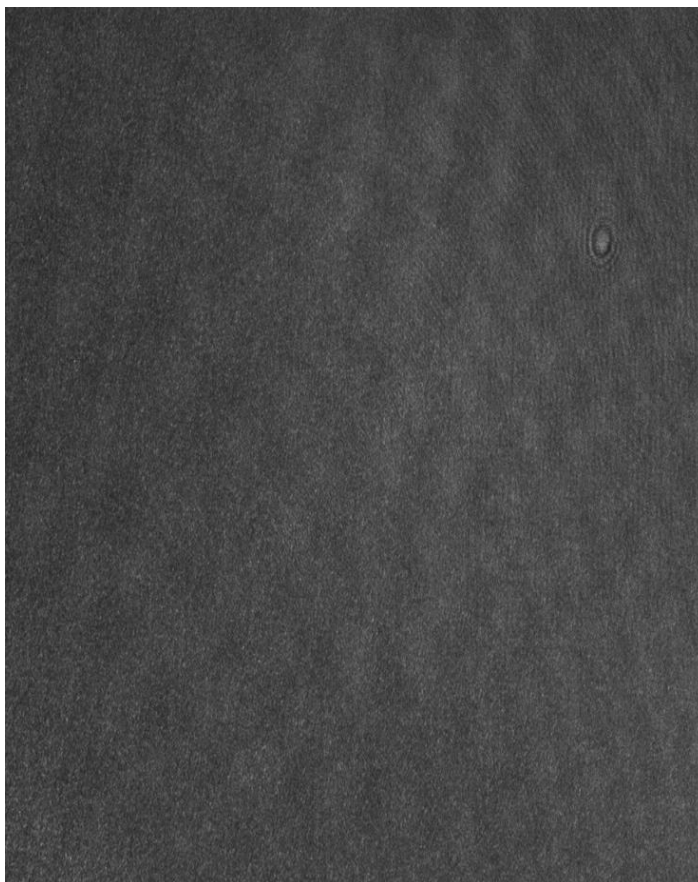


Figure A.1 – BAM image of a pure oleic acid monolayer on a pure water subphase at 23 mN m^{-1} surface pressure.

Bibliography (Appendices)

- 1 O. Arnold, J. C. Bilheux, J. M. Borreguero, A. Buts, S. I. Campbell, L. Chapon, M. Doucet, N. Draper, R. Ferraz Leal, M. A. Gigg, V. E. Lynch, A. Markvardsen, D. J. Mikkelsen, R. L. Mikkelsen, R. Miller, K. Palmen, P. Parker, G. Passos, T. G. Perring, P. F. Peterson, S. Ren, M. A. Reuter, A. T. Savici, J. W. Taylor, R. J. Taylor, R. Tolchenov, W. Zhou and J. Zikovsky, *Nuclear Instruments and Methods in Physics Research Section A: Accelerators, Spectrometers, Detectors and Associated Equipment*, 2014, **764**, 156–166.
- 2 D. Richard, M. Ferrand and G. J. Kearley, *Journal of Neutron Research*, 1996, **4**, 33–39.
- 3 A. Nelson, *Journal of Applied Crystallography*, 2006, **39**, 273–276.

Acknowledgements

Many individuals contributed to the production of this thesis or the undertaking of the underlying work or in some other way provided assistance or support. I would like to thank a few people specifically for the practical, academic, administrative, personal, or other forms of support they have offered throughout the process.

Dr Christian Pfrang and Dr Maximilian WA Skoda, my University of Reading (later Birmingham) and ISIS supervisors, respectively, conceived of and designed the project and provided supervision and support throughout. They both provided academic support and challenged me on my thinking throughout the project, as well as contributing some excellent ideas of their own. They both attended all my beamline experiments (bar the SURF experiment, which Max and I performed) and I had great fun discussing a wide variety of topics unrelated to the project through the night while the experiments were being well-behaved, which did happen from time to time.

Max also ran the INTER beamline for all our experiments there, and managed to teach me a lot about neutron reflectometry while doing so. I spent a lot of time at ISIS off the beamline performing various other pieces of analysis, and Max was always around to help out with troublesome analysis equipment, or rip my political ideology to shreds over lunch, both of which were very helpful in their own way. Much of the design of the early apparatus prototypes is as much the product of his thought as of mine, and he also deserves thanks for conducting my transfer viva.

Dr Roger Bennett stepped in as my nominal supervisor at Reading after Dr Pfrang transferred to the University of Birmingham, and provided the administrative support involved in overseeing my submission and examination.

My wife, Rebecca Wōden, proofread my thesis and supported me personally throughout the project, and was always willing to talk over some of the fine points of my work, which was hugely helpful, especially when I was struggling to keep it all straight in my head myself.

Dr Adam Squires conducted my transfer examination (along with Dr Skoda), and acted as the head of the monitoring committee in the first half of the project. His feedback after the first year was incredibly helpful in building my confidence in the data I had so far, and Chapter 6 in particular is better for it.

Prof Ann Chippindale acted as my internal examiner, provided a host of detailed corrections, and oversaw the corrections and sign-off process. The final product is more coherent and readable than it would have been without her involvement.

Prof Martin King acted as my external examiner and provided incredibly rigorous scrutiny of the ideas outlined in the thesis, before suggesting a variety of clarifications and extra content.

Prof Georg Held acted as the head of the monitoring committee in the latter half of the project, and kindly signed off on my request for extra time and funding, without which I'd have had precious little of use to say in the preceding pages!

Dr Kunal Rastogi, Dr Matthew Hageen, Dr Edna Rocio Cabrera-Martinez, Evita Hartmane, Curtis Gubb, Adam Milsom, and Sophie Ayscough attended a variety of beamline experiments and provided valuable practical support ranging from making up spreading solutions in the lab to keeping me awake until I needed to perform a sample change.

Dr James Tellam performed synthesis of some of the deuterated materials used throughout.

Dr Armando Maestro and Dr Phillip Gutfreund ran the FIGARO beamline.

Jacob Simms produced technical drawings for manufacture of parts for the experimental apparatus, translating from my hand-waving and terrible drawings in PowerPoint into CAD drawings for manufacturers, and assisted with the manufacture and assembly of that apparatus.

Richard Haynes assisted with the manufacture and assembly of the apparatus, provided technical support for beamline experiments, and just generally helped me out with sourcing and modifying equipment at ISIS.

Richard Haynes, John Crawford, Andy Church, Tom Charleston, Jeff Vine, and Simon Wood provided technical support for beamline experiments, which was particularly useful early in the design of the temperature-control apparatus, when at one point we seemed to be simultaneously using every type of adapter and tube in the facility. Jeff, Andy, Richard, and Tom also regularly helped me out on offline experiments with piecing together test versions of the apparatus out of handy equipment, and setting up large amount of ISIS equipment I generally seemed to require. Richard and John also helped with apparatus assembly. I'd have got very little experimental work done without their help and guidance.

Dr Luke Clifton was always around at ISIS and taught me a lot of the practical skills needed to work with surface-active lipids. He's also something of a BAM master, and helped me out of a bind with that and the FT-IRRAS work on a number of occasions.

Prof Rainer Cramer lent me a PC when mine failed at a critical juncture, which I used for most of the analysis for my first beamline experiment.

Dr Jana Geßner provided modelling support behind tensiometry experiments and assistance with tensiometry data interpretation.

Jill Hazelton, Claire Morris, and Wendy Neale administered the SCENARIO DTP at various points; I kept each of them very busy with unusual requests and problems, and they were all incredibly helpful.